Metamorphic petrology of glacial clasts from the Byrd Glacier drainage: Implications for the crustal history of East Antarctica

A Thesis
SUBMITTED TO THE FACULTY OF
UNIVERSITY OF MINNESOTA
BY

Amy Laureen Radakovich

IN PARTIAL FULFILLMENT OF THE REQUIREMENTS
FOR THE DEGREE OF
MASTER OF SCIENCE

Dr. John Goodge

January 2013

Acknowledgements

First and foremost, I want to express enormous thanks to my advisor, Dr. John Goodge, for his excellent mentoring and teaching which helped me complete this thesis. His dedication and excitement are always evident and inspiring, and his consistent patience was much appreciated.

My committee members Dr. Vicki Hansen and Dr. Paul Siders have provided invaluable assistance throughout my time at UMD, both with coursework and research. Vicki – thank you for providing a phenomenal example of a strong woman scientist…it is appreciated more than you might know. I would also like to thank Bryan Bandli for his help with the SEM portion of my research, and for the time spent in the microscopy lab helping me play 'Name That Silicate.'

I'm very grateful to the Precambrian Research Center (PRC), particularly Dr. Jim Miller, for helping encourage my passion for Precambrian geology. I'm also thankful for the financial support they provided for this research. This research was primarily funded by NSF award #0944645, without which this work could not have been completed. Their financial support is crucial to the success of this and future Antarctic research.

I am also grateful to the National Science Foundation's GK-12 program for providing me with the opportunity to work as a scientist in a local 8th grade classroom while I completed my research. I'm so fortunate to have worked with my cooperating teacher, Lauri Severson who became an inspiration and a friend. I'm also very grateful to my co-workers at the USGS in Menlo Park for their support and input on my project.

I couldn't have made it through grad school without my wonderful fellow geologists and grad students. Avery Cota-Guertin and Meg Pierce always keeping me inspired, laughing, and well-caffeinated. I was fortunate to have a wonderful officemate and friend in Tanya Dreyer, who not only shared many lovely study dates with me at Caribou, but who also passed down her research project and her Antarctic rock collection to me. Another officemate Craig Caton was always there with good friendship and witty banter. And of course I can't forget the other two-thirds of our Dynamic Trio – Ben Brooker and Matt Chaffee. After sharing every class, most meals, and a large portion of every day for two years together, it's safe to say grad school wouldn't have been the same (nor nearly as entertaining) without you. And I would be lost without my favorite 'real-world' geologist, field camp roomie, and best friend Alli Vallowe.

Most importantly I am so incredibly grateful to my family, who has been my support system from day one. I truly think I'm the luckiest woman in the world to be blessed with such wonderful people in my life. Dad, you are a fantastic man and I'm lucky to call you my father and friend. Thanks for your encouragement and light-hearted humor through this process, and for never, ever doubting me. Mom – you've always been my cheerleader and my best friend. Your strength inspires me every day…thanks for always being there. Grandma and Grandpa, thank you for your encouragement and love through the years. Oh yeah, and thanks for the 'sisu', too!

Dedication

This thesis is dedicated to my grandpa, Carl Stengard.

Grandpa, I remember you walking me up the stairs to class on my first day of preschool – sorry I left you behind on the stairs and told my teacher "My grandpa's coming. He's slow." You told Mom you wanted to live long enough to see me start school, and here we both are as I'm finishing grad school 20 years later. You have been the biggest supporter for my education from the start. Your unwavering faith in me has meant more to me than you'll ever know. I've always looked up to you, Grandpa. You are a great man with a great heart. I hope I can live to be even half as sharp as you are at 96 years old.
I love you.

Abstract

The geology of the Precambrian East Antarctic shield remains enigmatic due to extensive ice-cover in continental East Antarctica. Understanding the nature of this large Precambrian shield is essential for understanding its assembly, which has bearing on past supercontinent cycles as well as modern ice sheet growth. Optical petrography and mineral chemical analysis of metamorphic glacial clasts collected from the Lonewolf Nunataks, Antarctica, reveal a complex metamorphic history representative of bedrock in the East Antarctic shield beneath the Byrd Glacier drainage.

Three lithologic groups were identified: (a) felsic gneisses, (b) mafic gneisses and amphibolites, and (c) schists. Both felsic gneisses and mafic gneisses and amphibolites include garnet-bearing and garnet-free varieties. Typical mineral assemblages consist of quartz + plagioclase ± microcline + biotite ± muscovite ± garnet ± scapolite in felsic gneisses, and quartz + plagioclase ± microcline + biotite ± muscovite ± garnet ± tschermakite ± hypersthene ± scapolite in mafic gneisses and amphibolites. Petrologic evidence, including the presence of garnet, tschermakitic Ca-amphibole, hypersthene and scapolite in relatively anhydrous mineral assemblages, indicate amphibolite- to granulite-facies metamorphism. Of 16 suitable garnet-bearing samples, eight show compositional zoning in garnet indicative of prograde metamorphism, 12 show evidence of retrograde metamorphism, and two display no discernable compositional zoning. *P-T* calculations give prograde to peak temperatures ranging from ~500 to ~800 °C, with all samples reaching peak metamorphic conditions of at least 600 °C. Metamorphic pressures are less well constrained due to a lack of pelitic mineralogy. In one pelitic gneiss sample, GASP

(garnet-aluminosilicate-silica-plagioclase) barometry indicates pressures of ~8-9 kbar. In five other samples of mafic gneiss and amphibolite, pressures determined from the Al content in calcic amphiboles give pressures of ~10-20 kbar.

Clasts from Lonewolf Nunataks exhibit petrographic and *P-T* similarities with Archean to Proterozoic metamorphic rocks in the Terre Adélie craton in East Antarctica, the Gawler craton in southern Australia, and the Nimrod Group in the Transantarctic Mountains (TAM). These correlations are consistent with continuation of the Proterozoic Mawson Continent into the vast area of East Antarctica underlying the Byrd Glacier drainage. Specifically, it is possible that a geographically widespread metamorphic/magmatic tectonic event produced metamorphism in all of these areas, but that *P-T* variations between them is the result of differing local tectonic environments. Previous studies indicate that metamorphism documented in the Terre Adélie craton, Gawler craton, and Nimrod Group resulted from the ~1.7 Ga Nimrod-Kimban orogenies. Although geochronologic data are lacking to confirm a correlation, this study indicates that similar high-grade metamorphic rocks extend well into the East Antarctic shield beneath the Byrd Glacier drainage. Combined with recent age-dating of igneous glacial clasts that confirm the presence of heterogeneous Proterozoic basement underlying the Byrd Glacier drainage, this study also provides further evidence consistent with an interpretation of a connection between East Antarctica and Laurentia during the time of Rodinia.

Table of Contents

List of Tables

List of Figures

List of Equations

1. INTRODUCTION

Almost all of continental East Antarctica's geology is covered by the East Antarctic ice sheet. With the exception of limited coastal areas and outcroppings in the Transantarctic Mountains (TAM), there is almost no outcrop of the bedrock of East Antarctica, which has a subcontinental area similar to that of the conterminous United States or Australia. Understanding the nature of the bedrock beneath the East Antarctic ice sheet is important because it will provide us with context for paleotectonic assembly of East Antarctica, a principal component of past supercontinents. Such an understanding can help define Antarctica's role in paleogeographic reconstructions of the supercontinents, necessary to determine their history of assembly. Additionally, the existence of the Antarctic continent played a vital role in formation of the ice sheet that now covers East Antarctica; not only did the existence of continental Antarctica provide the substrate for growth of the ice sheet, but its physical properties such as thickness and heat flow govern modern ice sheet stability. Despite its importance in past and present events, however, East Antarctica's geology remains elusive.

The large continental mass beneath the East Antarctic ice sheet is known as the East Antarctic shield (EAS). As with cratonic shields elsewhere, the EAS is a composite body that grew in stages beginning in early Precambrian time. The EAS is composed of Archean to Ordovician crystalline rocks that were episodically metamorphosed and intruded by igneous rocks, then subsequently overlain by Jurassic and Devonian sediments (Fig. 1; Fitzsimons, 2000). A central element of the craton, the Mawson Continent, forms the core of the EAS, and extends into now-distant south Australia (Oliver and Fanning, 2002; Fanning et al., 1995; Peucat et al., 1999; Boger, 2011; Payne

et al., 2009). Crust has been added to and removed from this central craton by Paleoproterozoic (1.7-1.6 Ga) accretion (Peucat et al., 1999; Goodge et al., 2001), Mesoproterozoic (~1.5-1.4 Ga) rifting and Grenville-age (~1.1 Ga) accretion (Fitzsimons, 2003; Boger, 2011), and Neoproterozoic (~700-650 Ma) rifting (Goodge et al., 2002, 2004; Wysoczanski et al., 2004). Earliest Cambrian plate convergence at ~540 Ma formed the root of the TAM during the Ross Orogeny (Goodge, 2007), essentially completing EAS amalgamation.

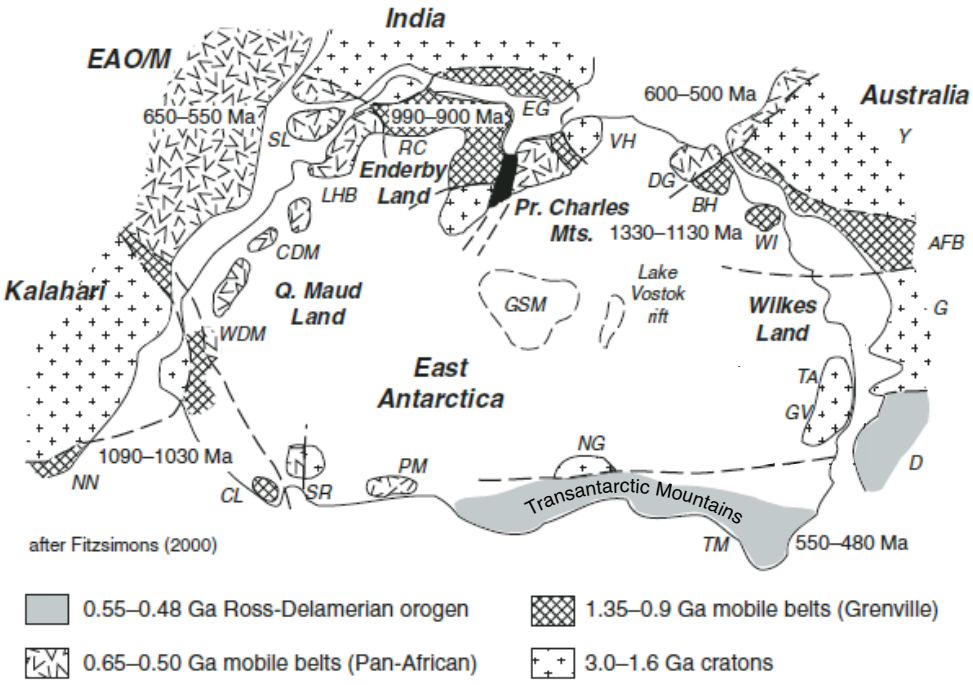

Figure 1. Generalized geological map and reconstruction of East Gondwana crustal elements in East Antarctica ca. 500 Ma (Goodge and Fanning, 2010). Location of study area in Byrd Glacier drainage is shown by box. Abbreviations: AFB, Albany-Fraser belt; BH, Bunger Hills; CDM, central Dronning Maud Land; CL, Coats Land; D, Delamerian Orogen; DG, Denman Glacier; EAO/M, East African Orogen/Mozambique belt; EG, Eastern Ghats; G, Gawler craton; GSM, Gamburtsev Subglacial Mountains; GB, George V coast; LHB, Lutzow-Holm Bay; NG, Nimrod Group, NN, Namaqua-Natal; PM, Pensacola Mountains; RC, Rayner Complex; SL, Sri Lanka; SR, Shackleton Range; TA, Terre Adélie; TM, Transantarctic Mountains; VH, Vestfold Hills; WDM, western Dronning Maud Land; WI, Windmil Island; Y, Yilgarn craton.

Bedrock of the East Antarctic shield likely reaches its farthest western extent (true geographic coordinates) as it abuts the Transantarctic Mountains, which, along with the Pensacola Mountains, Shackleton Range, and Theron Mountains (Moores, 1991), form a ~4000 km geographic and tectonic boundary between West and East Antarctica (Fig. 2). Basement to the modern TAM includes widespread sedimentary, igneous, and metamorphic rocks formed during the ~580-540 Ma Ross Orogeny (Goodge, 2007), which was the result of plate convergence along an active Neoproterozoic to early Paleozoic margin of East Antarctica. In the Miller and Geologists ranges near Nimrod Glacier, Archean and Paleoproterozoic igneous and metamorphic rocks are exposed, providing a rare window into the East Antarctic shield. Geochemical and isotopic evidence from Laurentian granites and TAM rift margin strata suggest that the TAM margin was connected to western Laurentia as a part of the supercontinent Rodinia in the Neoproterozoic (Goodge et al., 2008, 2010). The geology of the EAS abutting the TAM may therefore contain key information that can be used to gain insight into the development of this past supercontinent.

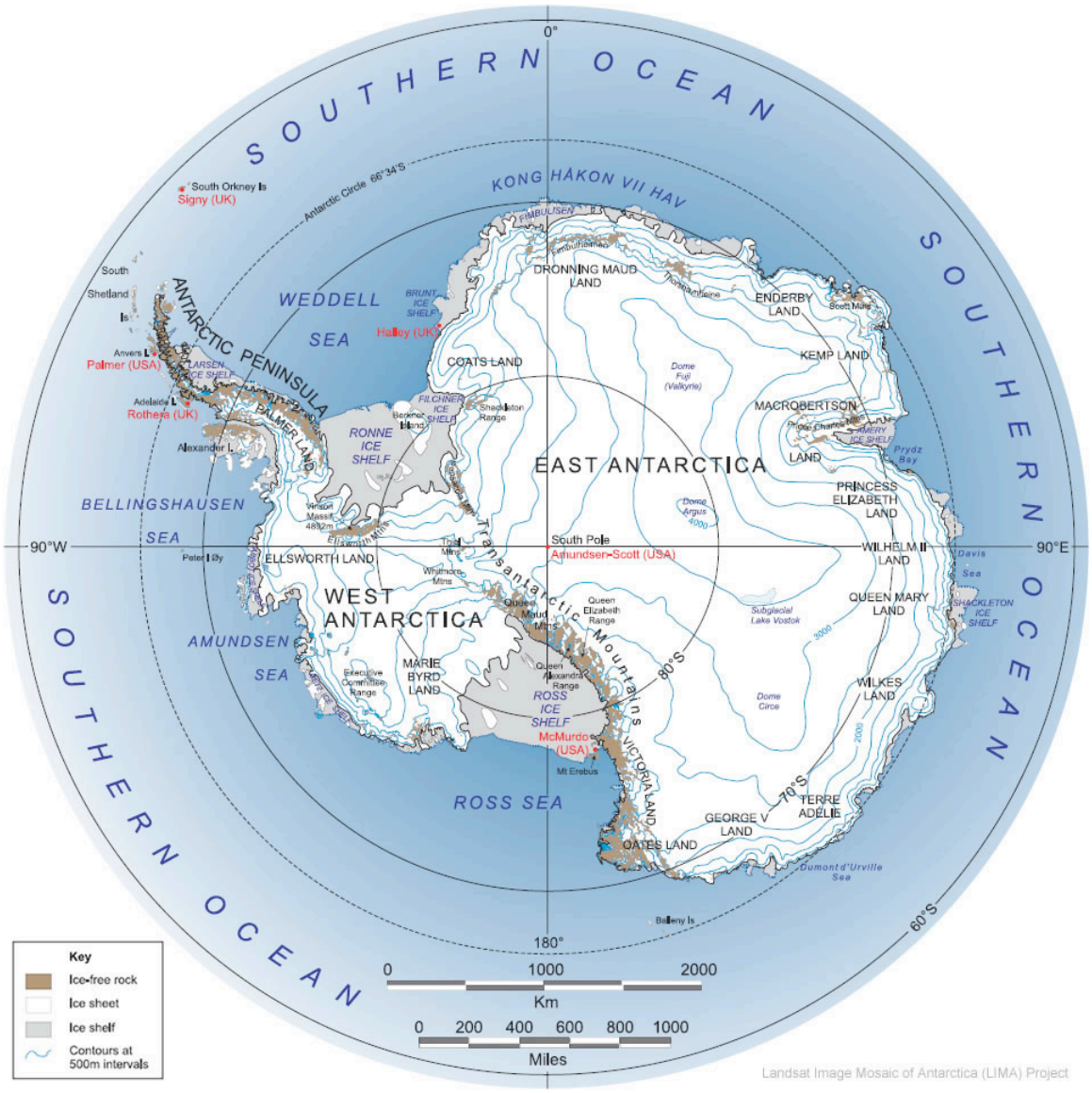

Figure 2. Map of the Southern Ocean and East Antarctica, including the Transantarctic Mountains. Note the extensive ice coverage of East Antarctica, with only a few locations where bedrock is exposed (brown) (Landsat Image Mosaic of Antarctica (LIMA) Project, 2012).

Minimal outcrops along the coast of East Antarctica from ~30 °W to ~160 °E indicate that the EAS is composed of Precambrian rocks (Harley, 2003). However, because direct outcrop sampling is impossible for most of the EAS, other methods of study must be employed. Drilling through the ice to bedrock is impractical and costly, and any drill core would provide information about the geology in a very limited area.

Geophysical surveys have helped characterize regional variations in East Antarctica's bedrock geology, but these are mostly restricted to narrow transects (Studinger et al., 2004; Ferraccioli et al., 2009, Goodge and Finn, 2010). These studies have correlated aeromagnetic anomalies with the Ross Orogen trends and in doing so have more precisely located known boundary of the EAS. An alternative way to study the bedrock lithology of the EAS is indirectly, through study of rock clasts entrained in glacial till deposited by movement of the East Antarctic Ice Sheet over the EAS bedrock. If glacially transported material is widely varied in composition it can provide information about numerous different petrologic units present beneath large glacial source areas.

Previous studies have successfully utilized glacially transported material to examine the sub-ice geology of the EAS (Peucat et. al., 2002; Brecke, 2007; Goodge et. al., 2008, 2010; Goodge and Fanning, 2010). These studies provided petrological, geochemical and isotopic evidence of Archean, Paleoproterozoic, and Neoproterozoic rocks in the Wilkes Land area of the EAS and of Archean terranes in the EAS inboard of Nimrod Glacier, as well as strengthened correlations with crustal rocks in southern Australia and western Laurentia. The present study uses similar principles to assess the basement composition and metamorphic history of the western EAS in the Byrd Glacier drainage. The metamorphic clasts examined in this study were collected from Pleistocene glacial moraines at Lonewolf Nunataks in the Byrd Glacier drainage of the East Antarctic ice sheet (Fig. 5). The Lonewolf Nunataks are ~60 km upstream from the TAM, so clasts from moraines at these nunataks likely reflect the character of the EAS rather than the TAM. The Byrd Glacier drainage is ideal for study because it is the fastest moving and the most spatially extensive ice catchment of the East Antarctic Ice Sheet (Bamber et al.,

2000; Lythe et al., 2000), so its till likely represents the composition(s) of an extensive area of the western EAS bedrock.

The purpose of this study is to better understand the pressure-temperature (*P-T)* history of metamorphic rocks in the western EAS basement in order to help correlate the development of the East Antarctic craton with past tectonic events. Paleogeographic reconstructions in the distant past rely upon, among other things, an accurate understanding of the timing and nature of tectonic events in Precambrian terranes. Rocks record tectonic events as they are metamorphosed, so understanding the *P-T* history of a rock can shed light on the tectonic environment in which it formed. This study explores the temperature and pressure evolution of the western EAS basement rocks through petrographic and mineral chemical analyses. Optical petrography was used to define mineralogy and textural characteristics of the metamorphic glacial clasts. This allows for the classification of several distinct suites of metamorphic rocks from the Byrd Glacier drainage. Compositional profiles of major cations in garnets in these different metamorphic suites reveal patterns of compositional zoning with changing *P-T* conditions. The compositions of minerals determined by quantitative analyses using energy-dispersive spectroscopy (EDS) are used in geothermobarometers to help refine the prograde and/or retrograde metamorphic history of the clasts. Comparison of these results with other studies, as well as planned age-dating of the metamorphic minerals, will help strengthen connections with past orogenic events affecting the EAS. Clarifying the tectonic history of the western EAS beneath the Byrd Glacier drainage will help provide insight into past supercontinent reconstructions involving East Antarctica.

2. GEOLOGIC BACKGROUND

2.1.Geologic setting of Antarctica

2.1.1 Crustal evolution of Antarctica and its role in supercontinent formation

East Antarctica has a Precambrian geologic history dating back to ~3.8 Ga, and a rich history of events spanning the Neoarchean and Proterozoic time periods. Because of extensive ice cover, much of what is known of East Antarctica's cratonal development is known from limited coastal and mountain outcrop (Fig. 2). Extrapolating across the continent from the margins, and inferring from areas that may have been previously connected to East Antarctica, leaves many questions about Antarctica's interior geology.

The East Antarctic shield (EAS) has experienced multiple periods of continental growth and rifting over its long existence. East Antarctica is thought to be composed of a central craton to which additional crustal materials were accreted throughout the Precambrian and earliest Cambrian (Fitzsimons, 2000). This central core of proto-East Antarctica is referred to as the so-called Mawson Continent, made up of the Terre Adélie region in East Antarctica and the Gawler craton in present-day Australia (Oliver and Fanning, 2002; Fanning et al., 1995; Peucat et al., 1999; Boger, 2011, Payne et al., 2009). The Mawson Continent is represented by 3.0-2.5 Ga gneisses and intrusive rocks that probably extend deep into the interior of East Antarctica, based on limited exposure of rocks in the Nimrod Glacier and Shackleton Range areas that have similar histories (Goodge et al., 2001; Will et al., 2010). Crust was added to this nucleus by igneous growth and collisional thickening in the late Paleoproterozoic (~1.7-1.6 Ga) at its eastern and western margins during the Nimrod-Kimban orogeny (Peucat et al., 1999; Goodge et al., 2001). A period of rifting in the Mesoproterozoic was then followed by Grenvillian-

aged collision with the Crohn craton to the west of the Pinjarra suture as a possible extension of the Pinjarra Orogeny in Australia. The Crohn craton is now thought to compose about one-third of the EAS hidden under the ice (Fig. 3, labeled as rocks with no known affinities) (Fitzsimons, 2003; Boger, 2011).

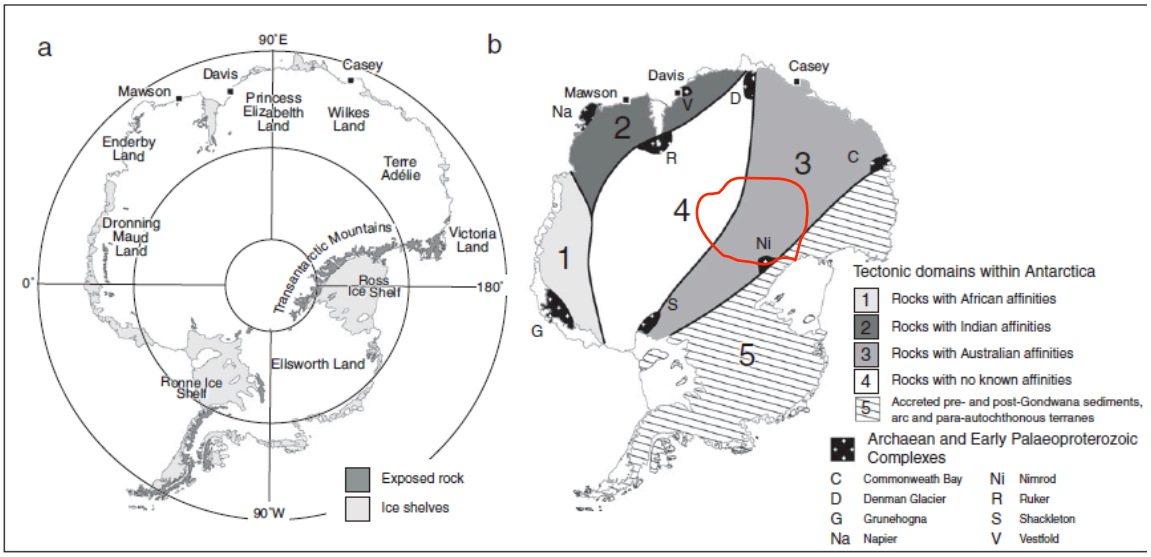

Figure 3. Antarctica showing major geographic regions (a) and known bedrock domains (b). Modified from Boger (2011). Red line indicates boundary of the Byrd Glacier drainage, from Rignot and Thomas (2002). Note that the majority of bedrock underlying Byrd Glacier is thought to have Australian affinities, while some is unknown.

Following the last major assembly stage during Grenville-age collision, East Antarctica was subject to Neoproterozoic (Ediacaran) rifting during the breakup of the supercontinent Rodinia. Rift-margin sedimentary successions and volcanic rocks indicate that a passive rift margin formed between about 700-650 Ma (Goodge et al., 2002, 2004; Wysoczanski et al., 2004; Cooper et al., 2011). Rifting along the present-day TAM margin of Antarctica coincided with collision against the Indian (Dharwar) and African (Kaapvaal) cratons in the Early Cambrian along the opposite side of Antarctica, in what would eventually form the new supercontinent Gondwana (Boger, 2011). Fragments of these cratons were added to Antarctica's current eastern margin between about 30 °W to

100 °E longitude (see Fig. 2). At about the same time, subduction was initiated along the paleo-Pacific margin of Antarctica, leading to development of the Ross Orogen in the present-day Transantarctic Mountains (Goodge, 2007). The Ross Orogen involved both high- and low-P/T metamorphism, as well as voluminous magmatism, as expressions of a convergent plate boundary akin to the modern Andean margin of South America. The last significant tectonic event associated with East Antarctica was the breakup of Gondwana through the sequential separation of Africa and South America, then India and Australia, and finally New Zealand, a process that spanned the Jurassic through Late Cretaceous (Reeves and de Wit, 2000). Throughout this storied development, the East Antarctic craton has been an important part of several past supercontinents, as discussed below.

2.1.1.1 East Antarctica-Australia connections in Gondwana

Despite the extensive ice cover of East Antarctica, direct evidence links it with the cratons of Australia, India, and southern Africa that once formed the core of East Gondwana (Fig. 3). The association of East Antarctica and Australia is especially straightforward and well-documented (Cande et al., 2000). In addition to an easily-visualized paleogeographic fit, East Antarctica and Australia are closely linked geologically. Neoarchean and Paleoproterozoic (2.8-1.6 Ga) exposures on the King George V and Terre Adélie coasts in East Antarctica contain rocks of similar type and age as the Gawler craton of southern Australia. This combined area is named the Mawson Continent (Oliver and Fanning, 2002; Fanning et al., 1995; Peucat et al., 1999). Further discussion of the East Antarctica-Australia connection is provided in the Discussion as it pertains to the results of the present study.

2.1.1.2 East Antarctica as a part of Rodinia and connections to Laurentia

The supercontinent Rodinia was assembled between ~1.3-0.9 Ga, preceding the assembly of Gondwana by at least 400 million years. East Antarctica and Laurentia were both key components of the former supercontinent Rodinia, and later of Gondwana (Antarctica) and Pangaea (Laurentia). East Antarctica and Laurentia are very distant from one another today, and it seems remarkable to think that they might have once been connected as part of the former supercontinent Rodinia. However, the largest amount of Precambrian rifted margin (~14,000 km at the edges of Laurentia as compared to other cratons) indicates that Laurentia was indeed a keystone in the late Precambrian supercontinent Rodinia. The formation of Rodinia occurred through periodic collision of continental blocks at Laurentia's margins. However, there is much debate about which Precambrian craton(s) were connected to the margins of Laurentia during the time of Rodinia, particularly along its western (present coordinates). Some suggestions include: Tasmania (Borg and DePaolo, 1994; Berry et al., 2005; Fioretti et al., 2005), based on the ages of metamorphic monazite and quartz syenite in Tasmania that connect an orogen from northwest Tasmania to Laurentia; South China (Li et al., 1995), based among other things on Neoproterozoic stratigraphic correlations; Siberia (Pisarevsky et al., 2008), based on paleomagnetic data; and Australia (most recently Karlstrom et al., 1999; Burrett and Berry, 2000), based on matching basement and sedimentary provenance. Li et al. (2008) provide a thorough review of existing ideas on the breakup of Rodinia and subsequent assembly of Gondwana.

Addressing this uncertainty regarding former conjugates to western Laurentia, Moores (1991) proposed a groundbreaking paleogeographic reconstruction that correlated

a Grenville-age orogenic belt present in East Antarctica with belts of similar age in the present-day Australian and Indian cratons and ultimately back to southern Laurentia. Specifically, his reconstruction suggested that the Wopmay orogenic belt in present-day northern Canada likely connected to Australia, which wrapped around the edge of the East Antarctic craton in Dronning Maud Land and continued as the Grenville orogenic belt in the southwest United States (Fig. 4). This reconstruction became known as the SWEAT (Southwest U.S.–East Antarctica) hypothesis. Moores based this reconstruction on stratigraphic correlations between Canada and Australia, as well as similar ages from rocks in the Nimrod Glacier region of Antarctica and the Yavapai-Mazatzal province in the southwestern U.S. The SWEAT hypothesis revolutionized concepts of paleogeographic reconstructions by providing geologic connections from Antarctica to other parts of Gondwana as well as to Laurentia.

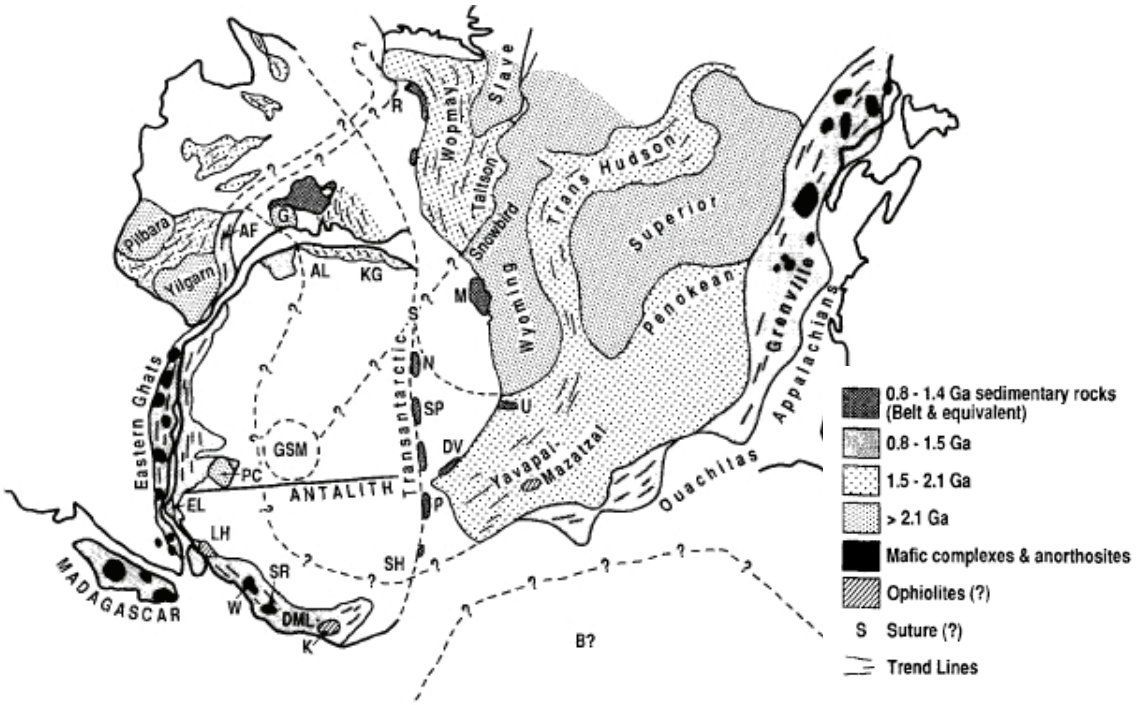

Figure 4. Schematic reconstruction depicting proposed continental fit of East Antarctica with western Laurentia, including connections to India and Australia, based on Grenville-age belts. From Moores (1991).

About the same time, Hoffman (1991) compared previous paleogeographic studies and concluded that a reconstruction of Rodinia in which Laurentia played a central role was highly likely. Hoffman suggested that Laurentia was connected at its northern, eastern, southern, and western margins to Siberia, Amazonia-Baltica, southern Africa, and Australia-Antarctica, respectively. The breakup of Rodinia was proposed to have occurred along rifts centered on these present-day margins of Laurentia. Hoffman determined that subsequent reassembly of these continental pieces into the Paleozoic supercontinent Gondwana was plausible and could have occurred through a 'scissor-like' separation from the western and eastern margins of Laurentia as Rodinia was inverted from inside out. The Proterozoic rift margins that developed in central Rodinia became the outer margins of Gondwana when it assembled in the Paleozoic as a remade supercontinent. Like Moores (1991), Hoffman called on the juxtaposition of Grenvillian age belts in Laurentia and East Antarctica as key evidence of the two continents' geographic association in Rodinia.

Borg and DePaolo (1994) affirmed the possibility of Moores' (1991) Australia-Antarctica-Laurentia connection with further modifications to restore possible displacement of allocthonous terranes, and they suggested a component of right-lateral translation between continents in order to provide a better match of observed structural characteristics. Borg and DePaolo predicted that if such a reconstruction was valid, there should be abundant Archean crust in East Antarctica like that in the Mojave province of Laurentia, and ~1.4 Ga rapakivi granites present in a juvenile Proterozoic crustal province in East Antarctica, just as there are in the southwestern United States.

Subsequent work has confirmed Borg and DePaolo's (1994) predictions and provided strong evidence in support of the SWEAT hypothesis. Goodge et al. (2008) collected a rapakivi-type glacial granitoid clast, named TNQ, sourced from the interior shield of East Antarctica. TNQ has Zr, Y, Nb, Ce, and $K_2O + Na_2O$ values similar to Mesoproterozoic A-type granites from the ~1.4 Ga Laurentian province (Anderson and Morrison, 2005; Anderson and Cullers, 1999). Sample TNQ shares several other key characteristics with the distinctive ~1.4 Ga granites of southwestern Laurentia, including: a) incompatible trace element patterns that resemble two-mica granites in southwest Laurentia; b) a U-Pb date of 1441 ± 6 Ma and an ε_{Hf} isotopic value that matches the Yavapi Province in Laurentia (Goodge & Vervoort, 2006); and c) an ε_{Nd} isotopic value that matches those of Laurentian granites (Bennett and DePaolo, 1987; Gleason et al, 1994).

Several other independent lines of evidence support the SWEAT hypothesis. First, Hf isotopes from ~1.4 Ga detrital zircons in Neoproterozoic rift-margin strata of the central TAM closely match the compositions of Laurentian A-type granites (Goodge and Vervoort, 2006). Additionally, ε_{Nd} values from these same rift-margin strata overlap those of similar age sedimentary rocks in southwestern Laurentia (Goodge et al., 2008), suggesting that these sediments were derived from equivalent Paleoproterozoic crust. These TAM sediments could not have been sourced from Laurentia, however, because by the time of Gondwana assembly in the Early Cambrian Laurentia had already drifted away from Antarctica. Therefore, the EAS must include a geologic province containing ~1.4 Ga granitic rocks similar to those found in Laurentia. Third, in the Nimrod Glacier area of the central TAM, high-grade gneisses, eclogites, and intermediate granites of the

Nimrod Group record metamorphism and magmatism between ~1730 and 1720 Ma, reflecting a period of continental assembly coeval with crustal growth and accretion in the Mojave Province of Laurentia (Goodge et al., 2001). Last, Antarctic rift-margin siliciclastic rocks of Neoproterozoic age contain abundant ~1.8 to 1.6 Ga detrital zircons, indicating that a significant source of Paleoproterozoic igneous and metamorphic crust is present in the EAS, just as in southwestern Laurentia (Goodge et al., 2004). Together these data show that there must be a Mesoproterozoic igneous belt present beneath the EAS ice sheet, as shown by the similar ages, isotopic signatures, and identical crustal sources as Proterozoic provinces of Laurentia. Any Neoproterozoic paleogeographic reconstruction must explain these close ties between southwestern Laurentia and the EAS. Figure 5 illustrates a modified SWEAT reconstruction proposed by Goodge et al. (2008).

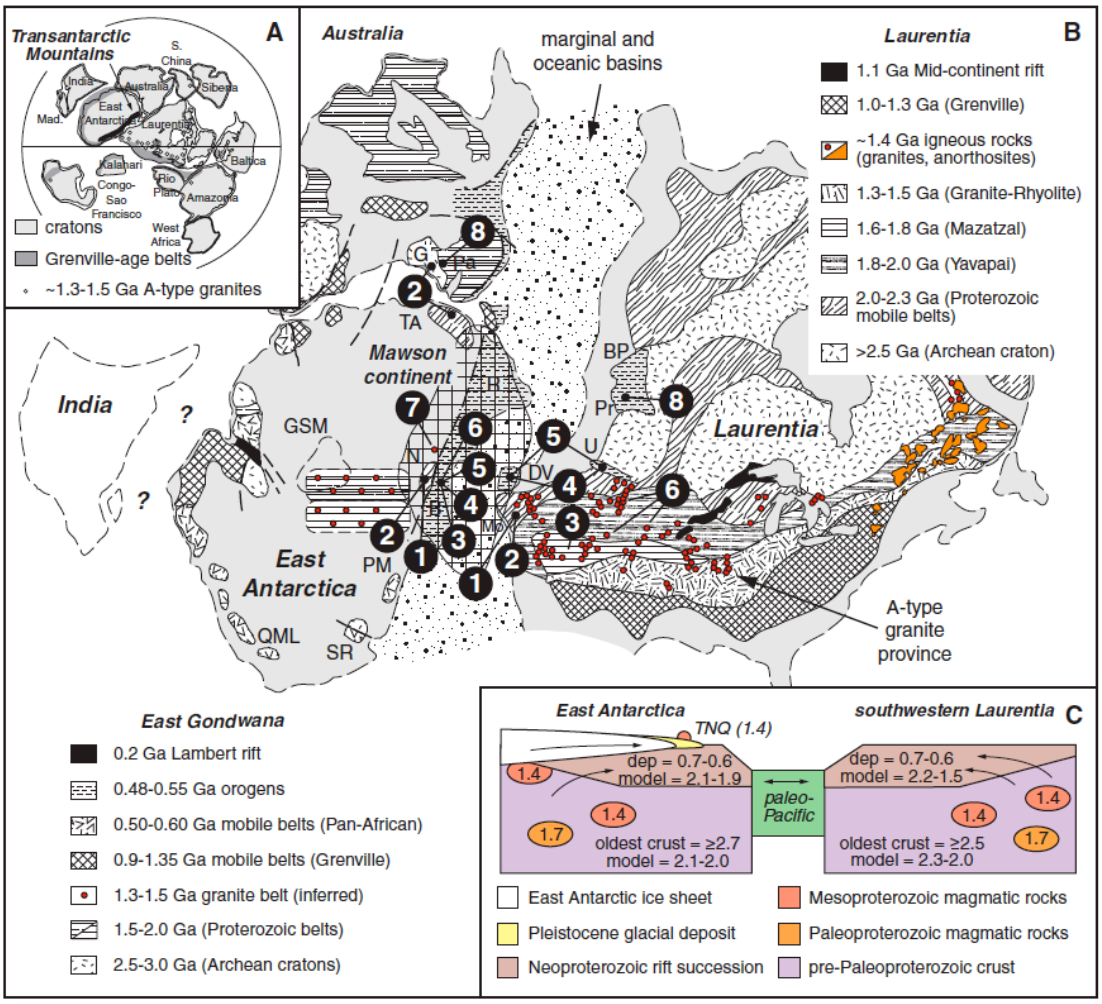

Figure 5. SWEAT fit of Laurentia and East Antarctica proposed by Goodge et al. (2008).

More recently, Goodge et al. (2010) obtained U-Pb zircon ages from igneous and metamorphic glacial clasts sampled in the central TAM, revealing igneous zircon cores of ~1065-1100 Ma (Grenville-age) and Ross Orogen (~500-550 Ma) metamorphic overgrowths. Some igneous clasts yielded Proterozoic ages of ~1460, ~1580, and ~1880 Ma. Other than the Ross-age overprint, none of these ages are known from geologic outcrop in the TAM, providing direct evidence of Proterozoic crystalline crust underlying the glacial drainage area that provides the source of moraine clasts. These ages are known from the Gawler craton in Australia, but they also correlate with known basement rocks

in Laurentia: the Paleoproterozoic ages match those in rocks of northern Idaho, and the Grenville ages with igneous rocks in western Texas. This evidence reinforces the idea of extending the Grenville belt from western Laurentia into central East Antarctica. All of the above evidence provides a compelling case for East Antarctica as a crucial part of the western Laurentian margin of Rodinia during the time of this past supercontinent.

Although its assembly is hotly debated, there is general agreement that Rodinia remained an intact supercontinent for a period of 200-400 million years. This large time discrepancy stems from the varying interpretations of when Rodinia was completely assembled and when it completely broke up. For example, Li et al. (2008) suggested that Rodinia was not fully assembled until 900 Ma. Other authors focus on 'peak' Rodinia assembly, which was ~1.1 Ga according to Dalziel (2010). Just as it assembled, Rodinia broke apart piece by piece, leaving the aforementioned ~14,000 km of rift margins in its wake. The western margin of Laurentia was the first part to rift, but the timing is largely uncertain. Paleomagnetic data and dating of mafic dikes suggest crustal extension began at as early as ~750 Ma (Li et al., 2008). However, rifting, as it is classically defined, involves more than crustal extension. Rifting involves the formation of a passive margin and eventual thermal subsidence. Depositional age and mixed provenance of Antarctic sedimentary deposits in the Beardmore Group suggest that deposition occurred in a platform or shoreline environment consistent with a rifted margin. A zircon age of 668 ± 1 Ma for igneous rocks in this succession reinforces a time of Rodinia rifting along the western margin of Laurentia/East Antarctica of ~680-650 Ma (Goodge et al., 2002). Though breakup may have been diachronous in different locales, the pieces rifted from western Laurentia had combined to form Gondwana by ~530 Ma (Li et al., 2008).

Antarctica's paleogeographic associations as a part of Gondwana are much more straightforward than those for Rodinia, as discussed above.

2.1.2 Geology of the Nimrod Group

Metamorphic rocks of the Nimrod Group in the central TAM provide unique and rare insight into the Precambrian geology of the EAS. Nimrod Group rocks experienced extensive geological activity periodically from the Archean to the early Paleozoic, as summarized by Goodge and Fanning (2002). Despite a definitive Precambrian ancestry, the Nimrod Group was very strongly overprinted by Ross-age metamorphism at ~500 Ma. SHRIMP U-Pb dating has identified the following periods of activity in the Nimrod group: a) juvenile magmatism at ~3150-3000 Ma (Goodge and Fanning, 1999); b) crustal metamorphism at 2955-2900 Ma (Borg et al., 1990; Borg and DePaolo, 1994; Goodge and Fanning, 1999); c) anatectic magmatism at ~2500 Ma; and d) magmatism, metamorphism, and eclogite formation at 1730-1700 Ma (Peacock and Goodge, 1995; Goodge and Fanning, 1999; Goodge et al., 2001). The final modification to the Nimrod Group was high-P/T metamorphism, deformation and orogenic magmatism from 540-520 Ma related to the Ross Orogeny (Goodge et al., 1993a), as shown by SHRIMP (sensitive high-resolution ion microprobe) and ID/TIMS (isotope dilution/thermal ionization mass spectrometry) geochronology (Goodge and Fanning, 1999; Goodge et al., 2001). These studies of the Nimrod Group provide significant knowledge about age and composition of the EAS, and serve as the basis for this study.

The Nimrod Group is a heterogeneous assemblage of layered gneisses, orthogneisses, and schists, including banded quartzofeldspathic to mafic gneiss, pelitic

schist, quartzite, amphibolite, granitic to gabbroic orthogneiss, migmatite, calc-silicate gneiss, marble, relict eclogites and pods of ultramafic rocks (Grindley et al., 1964; Grindley, 1972; Goodge et al., 1993a,b; Peacock and Goodge; 1995). Penetrative ductile deformation fabrics imparted during Ross orogenesis (Goodge et al., 1993a) are characteristic. Granitic plutons of the Granite Harbour series (Gunner, 1976; Borg et al., 1990) with ages of ~590-490 Ma (Goodge et al., 2012) are intrusive into the Nimrod Group.

2.1.2.1 Archean formation of the Nimrod Group

The first significant event in the history of the Nimrod Group is formation of protoliths to the existing layered gneisses from juvenile magmas in the Meso- to Neoarchean, as shown by U-Pb zircon ages of 3.29-3.02 Ga (Bennett and Fanning, 1993; Goodge and Fanning, 1999) and whole-rock Nd-model ages of 3.10-2.72 Ga (Borg et al., 1990; Borg and DePaolo, 1994). These studies established the importance of ~3100-3000 magmatism and metamorphism in the EAS. Due to its chemical and thermal robustness, zircon in some samples of gneiss preserve a composite history of Archean events at ~3000 Ma as well as younger growth stages at ~1720 Ma and ~530 Ma in the same rock (Goodge and Fanning, 1999), emphasizing East Antarctica's long history which correlates with other evidence described below.

2.1.2.2 Paleoproterozoic Nimrod Orogeny

A major Paleoproterozoic geological event affecting the Nimrod Group was a period of deep crustal metamorphism and magmatism at ~1.7 Ga. Despite thorough

reconstitution during later Ross Orogen deformation and metamorphism, evidence of older pre-Ross events at age ~1.7 Ga are preserved in the Geologists and Miller ranges. There, mafic blocks that occur in amphibolite- to granulite-facies lower crustal gneiss and schist show evidence of older eclogite-facies metamorphism that was not overprinted by amphibolite-facies Ross metamorphism. Such evidence includes: (a) plagioclase rims around garnet, which indicate that eclogite-facies garnet and clinopyroxene (Cpx) reacted to form plagioclase during decompression; (b) Cpx intergrowths replacing Na-rich pyroxene, which is stable in the eclogite facies; and (c) magnesian staurolite inclusions in pyrope-rich garnet, which form only at P ≥14 kbar and T ≥ 710-760 °C (Peacock and Goodge, 1995). This eclogite-facies metamorphism clearly pre-dated the ~540 Ma amphibolite-facies metamorphism, and the eclogitic blocks record unaltered metamorphic zircon growth. Subsequent U-Pb SHRIMP dating on these zircons gave ~ 1720 Ma ages (Goodge et al., 2001), penecontemporaneous with metamorphic zircon growth in gneisses and intrusion of granodioritic melts. This evidence points strongly to a deep-crustal metamorphic and magmatic event at this time, referred to by Goodge et al. (2001) as the Nimrod Orogeny. This is consistent with Peacock and Goodge's (1995) preferred of two models of eclogite emplacement, which shows that the eclogite formation probably occurred in the lower part of thick (40-90 km) continental crust at pressures from 12-25 kbar and temps of 600-900 °C, and was only partially re-equilibrated. This late Paleoproterozoic event was associated with significant crustal thickening, possibly related to collision.

This evidence of a significant ~1.72 Ga metamorphic event in the EAS strengthens links with the Laurentian Mojave province in western Laurentia, which also

records a key stage of crustal intrusion and metamorphism at ~1.7 Ga. A connection between the Nimrod and Mojave terranes provides key evidence in support of the SWEAT paleogeographic reconstruction. Furthermore, this Nimrod petrogenetic activity provides evidence of Archean and Paleoproterozoic geology on the Ross side of the EAS. Additionally, Archean rocks with late Paleoproterozoic overprints are also found in the Bunger Hills and Terre Adélie Land in Antarctica, as well as the Gawler craton in Australia. Although Rodinia formation is traditionally associated with Grenville-age events (1200-1000 Ma), the deep-crustal orogenesis associated with the Nimrod Group may represent the beginnings of proto-Rodinian assembly between East Antarctica, southern Australia, and southwestern Laurentia (Goodge et al., 2001; Boger, 2011).

2.1.2.3 Ross-age overprint of Nimrod Group

Despite zircon evidence of previous ~1.7 Ga magmatism and metamorphism, all of the presently observed textural and structural characteristics of the Nimrod Group are a result of Ross orogenic activity (Goodge et al., 1993b; Goodge and Dallmeyer, 1996). This later Ross Orogeny produced upper amphibolite to lower granulite facies metamorphism at high pressures of 8-12 kbar, equivalent to 25-40 km depth. This metamorphism overprinted most of the previously metamorphosed terrain between ~540-520 Ma (Goodge and Dallmeyer, 1992; Goodge et al., 1993b) and is recorded in the gneisses surrounding the eclogite-facies mafic blocks of the Nimrod Group (Peacock and Goodge, 1995). These petrologic and geothermobarometric characteristics are discussed in comparison with the results of this study in the Discussion.

2.1.3 Geology of Wilkes Land

Outcrops along George V Coast and Terre Adélie Land (Fig. 3) include Neoarchean and Paleoproterozoic high-grade gneiss and metaigneous rocks (Peucat et al., 1999; Oliver and Fanning, 1997, 2002; Ménot et al., 2005; Gapais et al., 2008). Together, these rocks comprise the Terre Adélie craton (TAC), which is correlated with the South Australian Gawler craton (GC) (Oliver and Fanning 1997, 2002; Hand et al. 2007; Payne et al., 2009). Rocks in the TAC include ~2.5 Ga gneisses (Monnier, 1995) and record a HT-LP metamorphic event at ~1.7 Ga. Further consideration of Wilkes Land geology is included in the Discussion as it pertains to results from this study.

2.2 Glacial geology of East Antarctica and the Byrd Glacier drainage

2.2.1 Glacial setting

Two major ice sheets – the East Antarctic ice sheet and the much smaller West Antarctic ice sheet – cover the vast majority of Antarctica (Fig. 4). These two ice sheets are separated from one another by the ~3,000 km-long Transantarctic Mountains (TAM). Glaciers and ice streams are responsible for transport of ice in a generally radial pattern from the center of the East Antarctic ice sheet to the surrounding ocean or through the TAM to the Ross Sea and Ross Ice Shelf. Most of the ice drained from the East Antarctic ice sheet to the Ross Sea and Ross Ice Shelf is funneled through outlet glaciers that transect the TAM. The fastest of these outlet glaciers is Byrd Glacier (Fig. 6), which is ~100 km long and ~20 km wide (Stearns and Hamilton, 2005). As it passes through the TAM, Byrd Glacier has an average velocity of ~825 m/yr. (Stearns et al., 2008). Other

major outlet glaciers also drain the central TAM, including the Nimrod and Skelton glaciers.

Byrd Glacier drains the largest geographical area of any single glacier crossing the TAM; its four tributaries reach over 1000 km inland from the TAM. Ice from its ~1,070,400 km^2 catchment area (Rignot and Thomas, 2002) converges to flow through the Byrd Glacier outlet to the Ross Ice Shelf. Flow in Byrd Glacier is "patterned enhanced flow," a combination of ice stream and ice sheet flows. Patterned enhanced flow is not uniform. Its primary mechanism of movement is by internal shear deformation, but it incorporates a component of basal slip, especially at the edges of ice divides (Rignot et al., 2011).

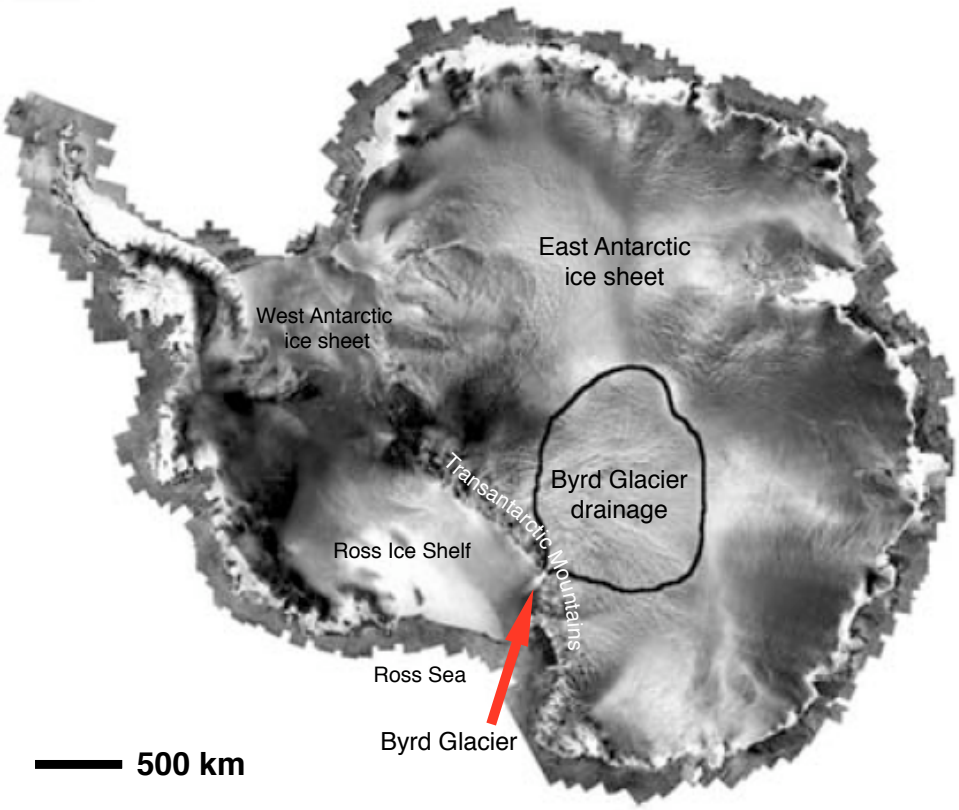

Figure 6. RADARSAT image of Antarctica. Thick black line shows extent of Byrd Glacier drainage. Image from Stearns and Hamilton (2005) and boundary from Rignot and Thomas (2002).

Ice velocity in Antarctica's ice sheets varies by up to five orders of magnitude depending on location. The fastest moving glaciers flow up to several km/yr, while ice velocity at drainage divides diminishes to only a few cm/yr. The slowest glacial movement is in East Antarctica, but a continent-wide average ice velocity is approximately 4-5 m/yr. Bedrock topography influences ice flow patterns, particularly by restricting ice flow over and around mountain ranges such as the TAM (Fig. 7). Flow rates in the Byrd Glacier drainage are as low as ~1.5 m/yr in the interior of the East Antarctic ice sheet (Rignot et al., 2011) to over 800 m/year (or ~2 m/day) in the Byrd Glacier proper (Stearns et al., 2008). Studies of flow in Byrd Glacier are vital to understanding the future state of the East Antarctic ice sheet because changes in Byrd Glacier flow will likely affect the mass balance of the ice sheet as well as the inflow to the Ross Ice Shelf (Stearns and Hamilton, 2005).

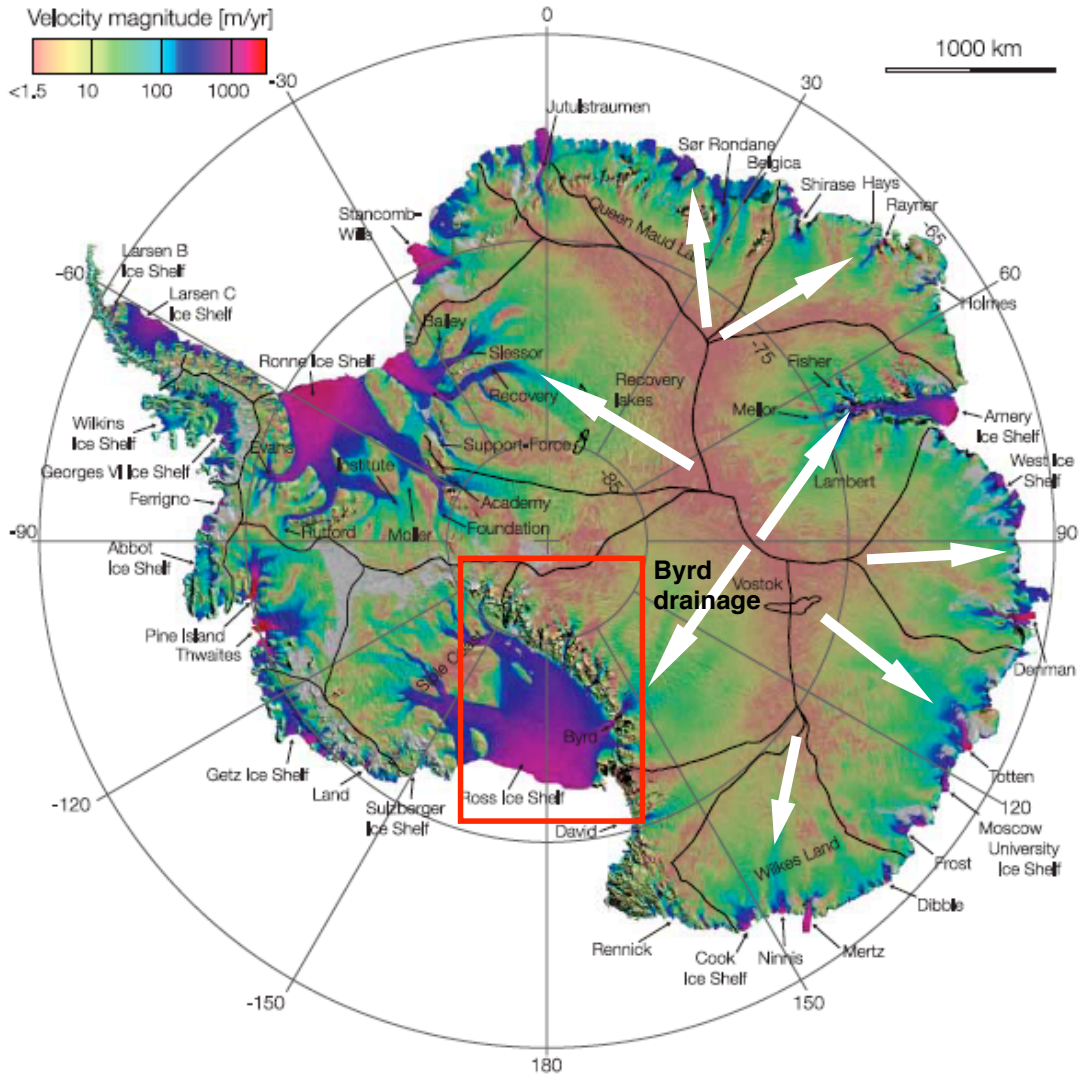

Figure 7. Antarctic ice velocity. Thick black lines are ice divides. Thin black lines are subglacial lakes. Red box indicates area shown in Fig. 8. White arrows are rough approximations of ice flow direction radially from center of ice sheet. Modified from Rignot et al. (2011).

2.2.2 Glacial entrainment, transport, and deposition

This study relies on the ability of a continental ice sheet to erode bedrock, transport debris for great distances, and deposit it in glacial moraines. Rocks may be plucked from the bedrock beneath a glacier and entrained at the bottom of the ice as basal

debris (Hambrey and Alean, 2004). From the site of erosion, rocks thus begin their journey toward the glacial margin.

Using similar logic, van Heeswijk et al. (1984) determined that the East Antarctic ice sheet was responsible for transporting numerous meteorites from all across the ice sheet to the outer ice-sheet margins. A dense concentration of meteorites of widely-varying ages located at Allan Hills, Antarctica, was likely not the result of a single fortuitous and geographically restricted meteor shower. Instead, the many meteorites likely fell all across the vast ice surface of Antarctica over many thousands of years and were transported to one location by ice movement. When the meteorites fell, they were entrained in the ice sheet's accumulation zone and traveled radially with ice flow to the margins of the continent (Figure 6). Because much of the East Antarctic ice sheet is surrounded by water, most meteorites entrained in the glaciers eventually end up in the ocean as the ice sheet begins to calve. However, because mountain ranges of the TAM near the Allan Hills acted as a physiographic barrier for ice flow, ablation of ice ponded behind the mountains left behind a glacial "lag" of debris that accumulated in nearby moraines. Over time, meteorites piled up at the base of the Allan Hills, resulting in the dense concentration van Heeswijk et al. (1984) described. This study applies the principles of glacial transport as described by van Heeswijk et al. (1984), and modeled by Whillans and Cassidy (1983), to bedrock clasts that may have been eroded at the glacial bed in the EAS and transported to glacial moraines.

2.2.3 Study area and site locations

As described above, ice of the East Antarctic ice sheet ponds in front of the TAM, and it either drains out to the Ross Ice Shelf or Ross Sea through small outlet glaciers or it is ablated by polar winds. In the process, the ice leaves behind rocks in morainal deposits at the base of the TAM. As a result, moraines inboard of the TAM may contain rock material transported from the central portions of East Antarctica. A UMD field team took advantage of this fact when selecting sample sites for glacial clasts.

All fieldwork done as a part of this study was completed in the 2010-2011 austral summer field season near the source areas of outlet glaciers in the TAM. Glacial samples were collected from ten sites (Fig. 8): WRA and WRB (Warren Range) to the north, AGA (Argo Glacier) and MRA (Miller Range), TNA (Turret Nunatak), LWA and LWB (Lonewolf Nunataks), MSA (Mt. Sirius), and SNA (Strickland Nunatak) and HBA (Hatcher Bluffs) from the Reedy Glacier area to the south. Samples used in this study are from the Lonewolf Nunataks sites LWA (152° 42.461'E /81° 20.186'S) and LWB (153° 01.445'E81° 19.545'S), located near the head of Byrd Glacier (Fig. 9). The Lonewolf Nunataks made particularly good candidates for study because there are no outcrops in the vicinity of the Byrd Glacier drainage to inform about the geology beneath it. Therefore, this study focuses only on clasts from the Lonewolf Nunataks.

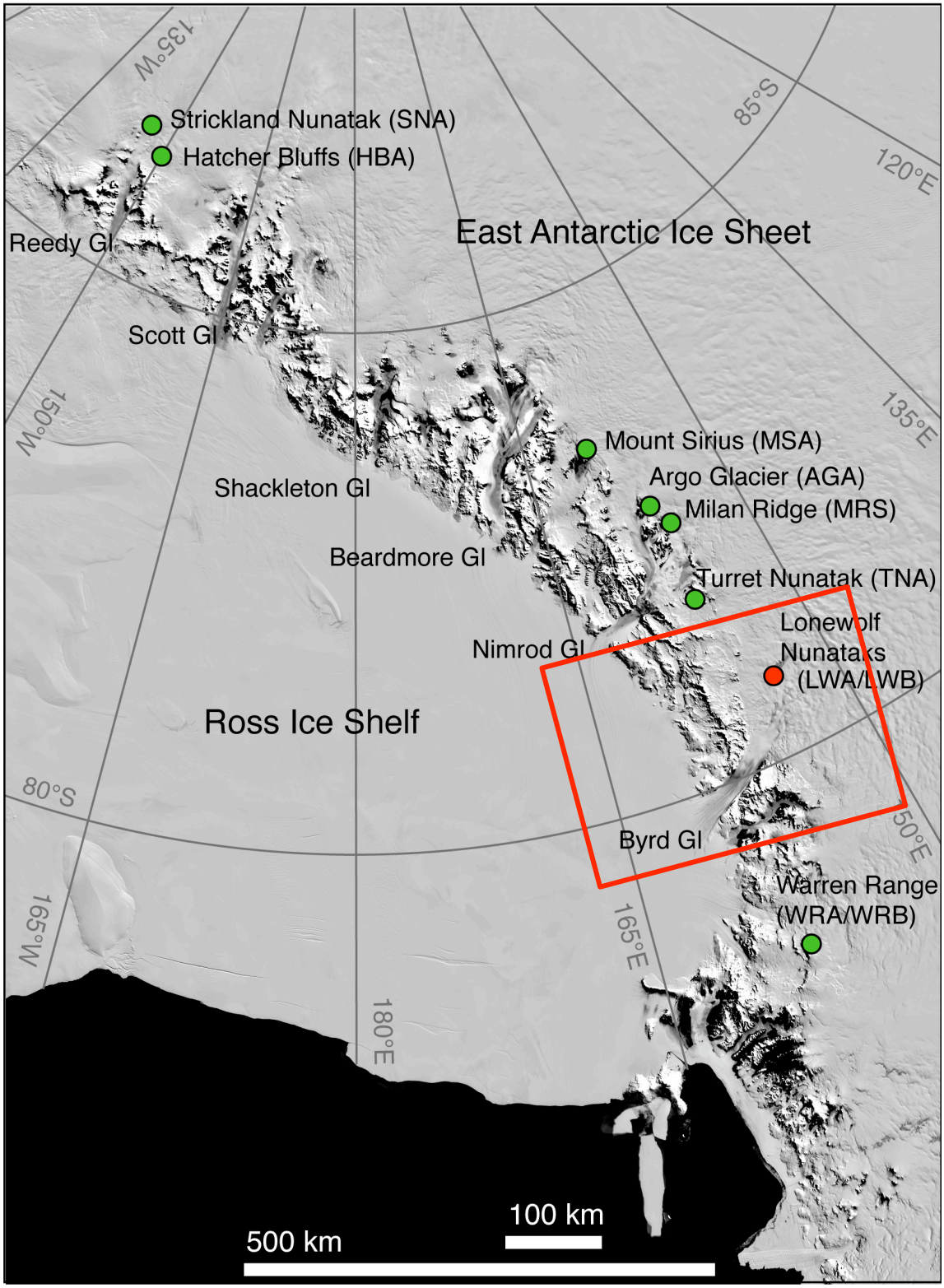

Figure 8. MODIS image of the Transantarctic Mountains, showing the location of all glacial moraine sample collection sites for the 2010-2011 austral field season. Red box shows approximate area shown in Figure 9.

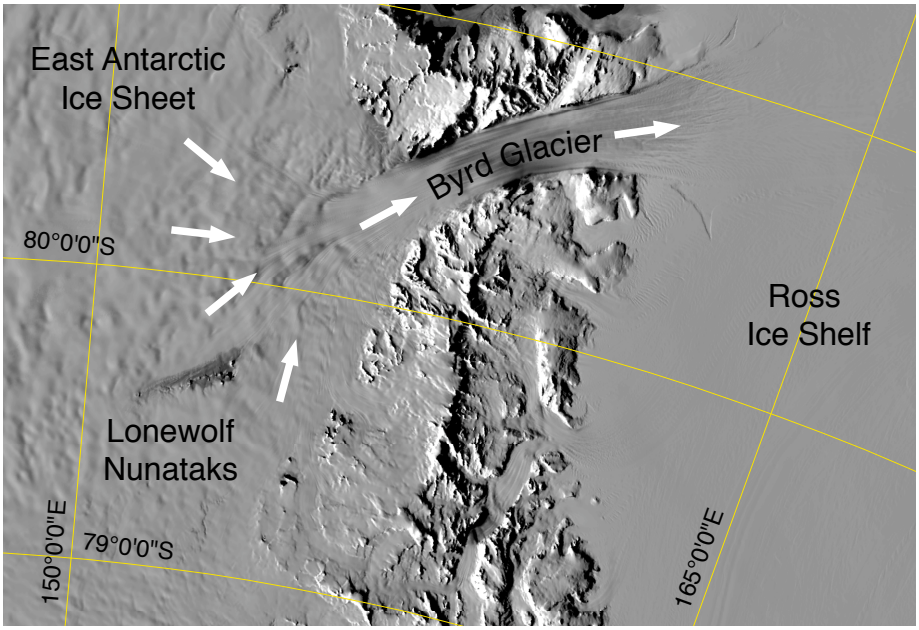

Figure 9. Location of Lonewolf Nunataks in relation to Byrd Glacier drainage. Image orientation is rotated ~180° from Figure 6 so that local north is up, as opposed to grid north in Fig. 8. Arrows show direction of ice flow.

2.3. Previous indirect study of the EAS

Because the vast East Antarctic ice sheet severely restricts the traditional geological investigations that can be used to study bedrock of the EAS, alternative methods of indirect study are used. These approaches include glaciomarine and terrestrial sediment provenance, glacial clast study, and potential-field geophysics. Studies of this type have proven useful in the identification and dating of parts of the EAS shield in the recent past.

2.3.1 Glaciomarine and terrestrial sediment study

Goodge and Fanning (2010) studied glaciomarine and terrestrial sediment as a proxy for the composition and age of the Wilkes Land interior of the East Antarctic shield. The various methods of investigation and results revealed important discoveries about the geological characteristics of Wilkes Land basement:

(1) Rock clasts collected from dredges of the ~100 km-wide Wilkes Land continental shelf give petrological information about the Wilkes Land basement, particularly Terre Adélie and George V areas. Clasts are mostly low-grade phyllites and psammites, with minor metamorphic and igneous clasts. U-Pb dating of selected clasts gave igneous zircon ages of ~500 Ma (Ross Orogen) and metamorphic zircon overgrowths with ages of ~670-780, 900-1300, 1740-2300, and > 2700 Ma. Interestingly, zircons with ages of 1400-1600 Ma were absent, suggesting the absence of Mesoproterozoic crust in Wilkes Land. These clasts show that the margin of Wilkes Land is composed primarily of Paleoproterozoic metamorphic basement with minor older and Grenville-age components.

(2) Detrital zircons from glaciomarine sediment cores show the presence of various age provinces that generally agree with those documented by U-Pb dating of the rock clasts.

(3) Detrital zircons from terrestrial Beacon Supergroup sandstones exhibit a different provenance, showing that the glaciogenic sedimentary deposits do not contain recycled Beacon inputs.

This indirect investigation reveals that the basement in the Wilkes Land region of the EAS contains rocks of distinct Neoproterozoic, Paleoproterozoic and Archean ages that were later either intruded by or partially melted to form Ross-age plutonic rocks. Importantly, this study supports a tectonic connection between rocks of South Australia's 1.7 Ga Gawler craton and the Terre Adélie craton of East Antarctica because basement of 1720-1740 Ma is a very important component of eastern Wilkes Land.

2.3.2 Geophysical investigations

Paleogeographic models of Rodinia are difficult to test because of a lack of paleomagnetic data from East Antarctica. Existing paleomagnetic data allow East Antarctica to be restored either next to southwest Laurentia or as much as 1400 km away if Australia was instead adjacent to southwest Laurentia (Torsvik, 2003). Regardless, geological and geophysical studies indicate that the EAS is a Precambrian craton modified by Proterozoic and Paleozoic events, making it possible to test cratonic correlations with potential-field methods like magnetics and gravity in order to image ice-covered basement.

Several recent geophysical studies have revealed more information about the sub-ice structure of the EAS, and the geographic extent of Ross Orogen basement.

Aeromagnetic surveys revealed an extensive aeromagnetic anomaly over the Matusevich Glacier area near Oates Coast that is thought to be associated with the Granite Harbour Intrusives and mafic/ultramafic rocks (Damaske et al., 2003). These rock units are associated with the Ross Orogeny, and thus extend the cratonic boundary of East Antarctica much farther west than previously thought – specifically, along the edge of the Wilkes Subglacial Basin, a 1400 km-long depression beneath the East Antarctic ice sheet inboard of the TAM (Damaske et al., 2003). Likewise, an aeromagnetic survey extending inland of Ross Island (Studinger et al., 2004) imaged an area from the TAM well into the EAS. Aeromagnetic anomaly patterns reveal the extent of TAM crust is as far west as 145 °E, or 400-500 km inland of exposed TAM outcrops.

Ferraccioli et al. (2009) conducted an aeromagnetic survey of the Wilkes Subglacial Basin and identified three distinct sub-basins. By comparison to the modern North American Cordillera these appear to be a broad backarc basin and multiple fold-and-thrust belts. As a part of the Wilkes Subglacial Basin, these elements mark the transition between Precambrian cratonic rocks and Ross Orogenic rocks. This basin is part of what has been identified in other studies as the Mawson Continent.

Most recently, Goodge and Finn (2010) reported an aeromagnetic survey that compared the geophysical signatures of Nimrod Group rocks in the Miller and Geologists ranges, the only Archean-Proterozoic rocks exposed for >3000 km in the TAM, to ice-covered basement beneath the inland East Antarctic ice sheet. The comparison revealed that the EAS in the study area is Archean craton, modified by Proterozoic magmatism as well as Paleozoic orogenic events. These authors, too, found that Ross Orogenic basement extended up to 100 km farther west than previously thought. Brecke (2007)

compared the magnetic susceptibilities of rocks in the Miller and Geologists ranges with the susceptibilities of glacial clasts collected in her study and was able to draw a correlation between the two.

A new compilation all of the geophysical investigations of Antarctica into a new ADMAP series is currently underway. This resource should help construct future models of geodynamic evolution of the Antarctic lithosphere as it pertains to the history of East Antarctica's involvement in Rodinia and Gondwana (Golynsky et al., 2012, in press).

2.3.3 Glacial transport of rock clasts

Indirect observation of the EAS through study of glacially transported rock clasts has been successfully completed by several groups. Previous studies (Peucat et al., 2002; Brecke, 2007; Goodge et al., 2008, 2010) have utilized the principles of glacial entrainment, transport, and deposition as a source for rocks from beneath the EAS, just as in the current study.

Peucat et al. (2002) completed petrological, geochemical, and geochronological studies on glacial clasts from moraines along the Terre Adélie margin in Wilkes Land, East Antarctica. The authors were able to positively correlate the presence of similar rock types and ages in both moraine samples and the Mesoproterozoic Gawler Volcanics in modern-day South Australia. The indirect nature of this study helped solidify cross-craton rock correlation.

Brecke (2007) took a similar approach in the study of moraine clasts from the Nimrod Glacier region. She used petrographic and metamorphic mineral compositions, whole-rock igneous geochemistry, and magnetic susceptibility data, to characterize material eroded from the EAS. These analyses helped Brecke correlate moraine samples

to mapped Archean rock units in the region of Nimrod Glacier. As a result, ties to Archean terranes in the ice-covered EAS in the Nimrod Glacier drainage were considerably strengthened. Finally, as discussed above in the review of the SWEAT hypothesis, Goodge et al. (2008, 2010) used the geochemical characteristics of glacial igneous and metamorphic clasts sourced from the EAS to make direct correlations with crustal rocks in western Laurentia.

These previous indirect studies serve as a template for the type of investigation undertaken here. Because clasts from the Lonewolf Nunataks are rounded, polished, and grooved, we can reasonably conclude that they were not locally sourced from the TAM but rather came from the bedrock beneath the ice sheet. Morainal material at Lonewolf Nunataks, which lie at the margin of Byrd Glacier (Fig. 9), could have come from the bedrock beneath any of the area covered by the Byrd Glacier drainage. This study aims to provide additional insight into the metamorphism of the EAS beneath the East Antarctic ice sheet that may or may not correlate with Laurentian rocks as conceived by the SWEAT hypothesis.

2.4 Goal of study

The goal of this study is to provide further information about the metamorphic crust that lies hidden beneath the central portions of the East Antarctic ice sheet. Study of metamorphic rock clasts sampled from glacial deposits at Lonewolf Nunataks along the southern margin of Byrd Glacier allows for characterization of the major rock types and quantitative assessment of the metamorphic temperatures and pressures experienced by bedrock of the EAS beneath the Byrd Glacier drainage. Metamorphic glacial clasts, along with igneous clast populations, can be used as a proxy for the composition of the bedrock sourced from within the Byrd Glacier drainage. This study provides a unique window into the composition and metamorphism of Antarctic bedrock hidden beneath miles of ice by using metamorphic glacial clasts.

3. FIELD AND LABORATORY METHODS

3.1 Sample collection and preparation

Fieldwork for this project was completed in Antarctica during the November 2010 – January 2011 field season by Dr. John Goodge, UMD Ph.D. student Tanya Dreyer, Mark Fanning (Australian National University), Jeff Vervoort (Washington State University), and field guide Dylan Taylor. In some cases the field team accessed sample sites by helicopter from McMurdo Station, and in other cases they established tent-camps with snowmobile and Twin Otter support to aid in sample collection. The field team collected outcrop samples from the Miller Range of the TAM as well as glacial clasts from Pleistocene and modern moraines (Fig. 10, 11) at ten different sites near major outlet glaciers that drain ice from the East Antarctic ice sheet through the TAM to the Ross Ice Shelf and/or Ross Sea (Fig. 8). All glacial sampling sites were located at the heads of the outlet glaciers, upstream of the TAM, in order to ensure, to the extent possible, that samples originated from the ice-covered basement of the EAS to the east. Sample collection focused on igneous and metamorphic glacial clasts that allow for both petrological, geochemical and isotopic analysis. In addition to the petrologic approach taken in this study, samples also will be used for U-Pb zircon dating, O-isotope analysis, and Lu-Hf isotopic analysis.

Figure 10. Ribbons of ice in a moraine along the southern edge of Byrd Glacier at Lonewolf Nunataks, showing clasts being transported along glacial edge. Largest boulders are about 1 m in size. View looking up-glacier. Note that some clasts may be displaced from the perched moraine on the hillslope to the left. The contrast in debris-rich and debris-free ice bands indicates the clasts are mostly exposed by sublimation of ice matrix. Photo by John Goodge.

Figure 11. Ribbons of ice along the southern edge of Byrd Glacier at Lonewolf Nunataks, showing clasts being transported along glacial edge. Largest boulders are about 1 m in size. Two members of the field team in the distance. View looking down-glacier. Photo by John Goodge.

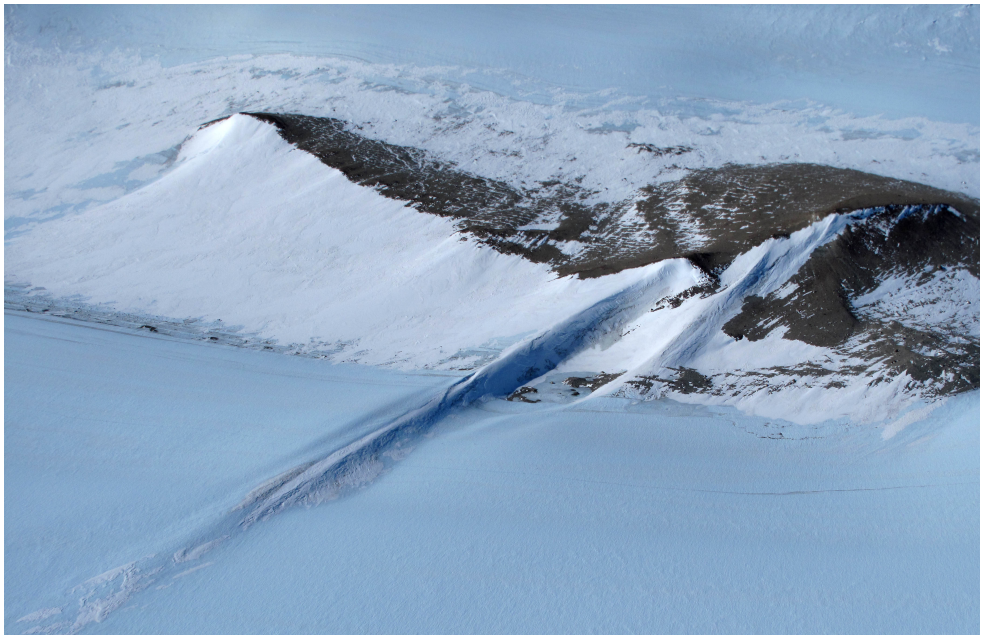

Figure 12. Aerial view of Lonewolf Nunataks, looking grid northwest along the southern edge of Byrd Glacier. High bench of dark, patterned ground is an older (Pleistocene?), stranded moraine. Samples for this study were collected from the streaky blue ice to the left (downstream) of the prominent wind ridge crossing the glacier. Photo by John Goodge.

Samples analyzed in this study are exclusively glacial clasts; no outcrop samples were analyzed. Analysis of the glacial clasts began with hand-sample descriptions where clasts were categorized into general lithologic groups. Nearly all of the samples collected in Antarctica were cut and slabbed, and most were made into polished thin sections. Of the ~375 glacial clasts collected, 152 metamorphic rocks and foliated igneous rocks were examined in this study because the goal was to gain insights into the metamorphic history of the EAS bedrock.

3.2 Optical petrography

Petrographic microscopes were used to study polished thin sections of metamorphic and deformed igneous glacial clasts from sample collection sites WRB, AGA, MRA, TNA, LWA, LWB, MSA, and HBA. Optical petrography established the primary mineralogical assemblages as well as textural relationships among minerals in the glacial clasts. This information was used to estimate each rock's protolith and assess its degree of metamorphism. Upon completion of optical petrography of all metamorphic and deformed igneous glacial clasts from all sample suites, 52 samples from sites LWA and LWB were selected for further study on the basis of: (1) their location ~60 km glacially upstream of the TAM effectively eliminated the possibility of any samples being TAM-sourced; (2) no previous studies of this type had been done on Lonewolf Nunatak clasts; (3) there was a great abundance of metamorphic clasts collected from these two sites; and (4) the sample sites were in close proximity to one another. All rocks discussed further as a part of this thesis are from LWA and LWB sites.

3.3 Mineral analysis and chemistry

3.3.1 Mineral compositions

Elemental analysis of minerals in 16 polished thin sections was conducted by energy dispersive x-ray spectroscopy (EDS) in the Research Instrumentation Laboratory at the University of Minnesota-Duluth. Data were collected using a JEOL JSM-6490LV scanning electron microscope equipped with an Oxford Instruments, xAct silicon-drift type detector. Spectral data were quantified to determine mineral chemistry using Oxford Instruments INCA™ software. All unknowns were analyzed simultaneously with and standardized to natural reference minerals from the Smithsonian Microbeam Reference Materials standard set. Table 1 lists the standards applied to all compositional measurements collected. Adequate standards were not available for Mn, Cr, or Cl, so internal standards were applied to those elements whenever they occurred. Data were collected over multiple sessions, and working conditions on the SEM were uniform at 15 kv accelerating voltage and a working distance of 10 mm during every session. Prior to data collection the vacuum and electron beam systems were allowed to stabilize for several hours. The average of three closely-spaced (~10 μm apart) point analyses (omitting any outliers or anomalous results) from a location on a mineral grain was taken to represent the composition of the mineral at that point.

Table 1. Standards used with quantitative compositional data

Element	Standard
Mg	Pyrope; Kakanui, New Zealand, NMNH143968
Al	Anorthite; Great Sitkin, AL, NMNH137041
Si	Anorthite; Great Sitkin, AL, NMNH137041
Ca	Anorthite; Great Sitkin, AL, NMNH137041
K	Microcline; Unknown Location, NMNH143966
Ti	Hornblende; Kakanui, New Zealand, NMNH143965
Fe	Fayalite; Rockport, MA, NMNH85276

3.3.2 Garnet profiles

Of the 21 garnet-bearing metamorphic clasts from the Lonewolf Nunataks, sixteen had garnets suitable for EDS compositional profiles. Compositional variations across single garnet grains were recorded by collecting EDS data in straight-line profiles of between 25-100 points. Two to three representative garnets were profiled in each of the 16 samples. Garnet profiles were not collected with reference to standards because the data were not used in geothermobarometry; profile data were used only to observe relative elemental concentrations across garnet grains that might reveal patterns of compositional zonation.

An effort was made to analyze garnets with the fewest cracks and inclusions, and those that exhibited the best crystal shape, i.e. the most 'robust' garnets available in each sample. In samples where all garnets had ragged edges and/or numerous inclusions, data were still collected on the best available garnets. Proximity of a garnet to minerals used in geothermobarometers was also taken into account when choosing garnets to profile. Preference was given to garnets which contained inclusions of biotite or amphibole, or which had biotite, amphibole, or pyroxene in close proximity to the garnet. In some

cases, two perpendicular profiles were analyzed within one garnet to determine whether any zoning was uniform throughout the garnet.

4. RESULTS

Thorough petrographic study of all metamorphic and deformed igneous glacial clasts from all sample locations allowed me to accurately identify and classify the rock samples. Hand sample observations facilitated initial groupings of glacial clasts based on rock type. Knowledge of rock compositions informed the choice of samples used in further study. In order to study glacial material most likely sourced from the central EAS in the Byrd Glacier drainage, I chose samples from Lonewolf Nunataks sites A and B for detailed study (hereafter LWA and LWB). Subsequent thin-section optical petrography provided more detailed mineralogical and textural descriptions of the samples. Finally, electron microbeam compositional analysis of mineral phases by EDS (energy dispersive spectrometer) permitted application of geothermobarometers to assess P-T conditions during formation of bedrock in the Byrd Glacier drainage.

4.1 Lithologic groups

Based on optical petrography I divided the Lonewolf Nunataks metamorphic clasts into three general compositional categories: (a) felsic gneisses (both garnet-bearing and garnet-free varieties); (b) mafic gneisses and amphibolites (including garnet-bearing and garnet-free varieties); and (c) schists. Table 2 lists the samples in each of these groups collected from the Lonewolf Nunataks A and B sites. The general attributes of each lithologic category are discussed below, and specific features are provided for those samples with notable mineralogy and/or textures. Figure 13 shows representative hand-sample photographs of the two types of felsic gneisses and the two types of mafic gneisses and amphibolites. An example from the schist group is not included in Figure 13 because schists were not a significant part of this study. Detailed descriptions of all 52

metamorphic samples from Lonewolf Nunataks, including clast photographs and thin section photomicrographs, are provided in Appendix A.

Table 2. Rock types among metamorphic glacial clasts at sites LWA and LWB.

Group		Sample No.	Rock name[a]
a	Quartzofeldspathic gneisses	LWA-1.2	Biotite gneiss
		LWA-1.4	Biotite gneiss
		LWA-1.5	Biotite gneiss
		LWA-1.6	Biotite gneiss
		LWA-1.7	Biotite gneiss
		LWA-2.1	Biotite-muscovite orthogneiss
		LWA-4.1	Biotite gneiss
		LWA-6.1	Biotite-muscovite orthogneiss
		LWA-6.2	Biotite-muscovite gneiss
		LWA-6.3	Biotite gneiss
		LWA-6.7	Biotite-muscovite gneiss
		LWA-10.1	Hornblende orthogneiss
		LWB-2.7	Biotite-gneiss
		LWB-4.4	Biotite-muscovite orthogneiss
		LWB-4.5	Biotite orthogneiss/deformed granodiorite
		LWB-4.6	Biotite orthogneiss/deformed diorite(?)
		LWB-4.7	Biotite-muscovite orthogneiss
		LWB-4.8	Muscovite-biotite orthogneiss
		LWB-5.1	Biotite-muscovite gneiss
		LWB-5.2	Muscovite gneiss
		LWB-5.3	Biotite gneiss
		LWB-5.4	Biotite-muscovite orthogneiss
		LWB-5.5	Biotite-muscovite gneiss
		LWB-5.6	Muscovite-biotite gneiss
		LWB-5.7	Biotite orthogneiss
		LWB-5.8	Biotite orthogneiss
	Quartzofeldspathic garnetiferous gneisses	LWA-1.1	Garnet-biotite gneiss
		LWA-1.3	Garnet-biotite gneiss
		LWA-2.2	Garnet-biotite gneiss
		LWA-2.3	Garnet-hornblende-biotite gneiss
		LWA-5.1	Hypersthene-garnet-hornblende gneiss
		LWB-1.2	Garnet-biotite-kyanite gneiss
		LWB-1.3	Garnet-biotite gneiss
		LWB-1.5	Garnet-biotite orthogneiss
		LWB-1.6	Garnet-biotite gneiss
		LWB-1.7	Garnet-muscovite leucogneiss
		LWB-2.3	Garnet gneiss
		LWB-4.3	Garnet-biotite orthogneiss
		LWB-6.4	Garnet-biotite gneiss
b	Mafic gneisses and amphibolites	LWB-2.2	Hornblende-biotite gneiss
		LWB-2.5	Hornblende amphibolite
		LWB-4.1	Hornblende-biotite orthogneiss

	Garnetiferous mafic gneisses and amphibolites	LWB-1.1	Garnet-tschermakite-biotite gneiss
		LWB-1.4	Garnet-biotite-hornblende gneiss
		LWB-2.4	Hornblende-hypersthene-garnet gneiss
		LWB-2.6	Tschermakite-biotite-garnet gneiss
		LWB-2.8	Garnet gneiss
		LWB-6.1	Garnet-tschermakite-scapolite gneiss
		LWB-6.2	Garnet-tschermakite amphibolite
		LWB-6.3	Garnet-tschermakite gneiss
c	Schists	LWA-3.1	Biotite-muscovite schist
		LWA-3.2	Muscovite-biotite schist

Notes: [a] full descriptions given in Appendix A.

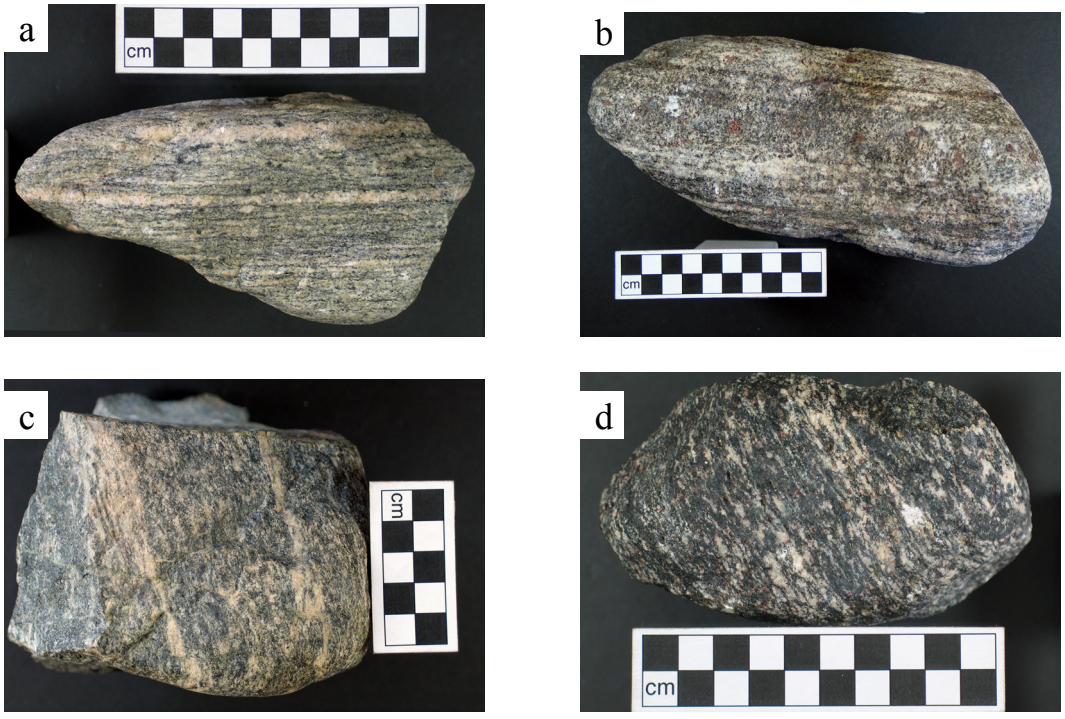

Figure 13. Representative felsic gneisses shown by (a) sample LWA-1.4 (garnet-free) and (b) sample LWB-1.6 (garnetiferous). Representative mafic gneisses shown by (c) sample LWB-2.5 (garnet-free) and (d) sample LWB-6.1 (garnetiferous).

In general, the felsic gneisses exhibit relict igneous mineralogy such as Qtz + Plag ± Kfs and relict textures such as large porphyroblasts of feldspar. There is also evidence of subsequent regional metamorphic deformation such as quartz ribbons, recrystallized quartz, and a lack of idioblastic texture. The mafic gneisses and amphibolites show some

relict, primarily igneous mafic minerals, such as Qtz + Plag ± Kfs + Hbl ± Opx, but a lack of idioblastic texture combined with presence of quartz ribbons, recrystallized quartz, and GSPO in amphiboles indicates that this group of rocks experienced a thorough metamorphic overprint. The schists display quartzofeldspathic mineralogy and compositional layering that are probably primary, with evidence of later recrystallization marked by development of a calcite cement. In a majority of samples from all rock types, metamorphic mineral assemblages and textural relationships indicate that regional metamorphism thoroughly overprinted primary rock characteristics.

4.1.1 Felsic gneisses

4.1.1.1 Quartzofeldspathic gneisses

Lonewolf Nunataks felsic gneisses include twenty-six garnet-free samples (Table 3). The mineralogy of a typical garnet-free felsic gneiss includes: quartz + plagioclase feldspar ± potassium feldspar + biotite ± muscovite ± chlorite. Accessory minerals typically consist of an opaque phase + apatite ± zircon. Individual samples also contain augite (LWA-1.2), magnesian-tourmaline (LWA-1.6), epidote (LWA10.1, LWB-2.7, LWB-4.7, LWB-5.1), or pumpellyite (LWA-10.1) (Table 3). The non-garnet-bearing felsic gneisses vary from very fine-grained to coarse-grained, but are typically medium- to coarse-grained. These rocks range from massive to well-foliated, but moderately to well-foliated rocks are characteristic. Planar preferred orientation is commonly shown in biotite, and quartz ribbons (LWB-2.7, LWB-4.4, LWB-4.8, LWB-5.1, LWB-5.2) indicate strong penetrative deformation by dynamic recrystallization. Common microtextures in the felsic gneisses are myrmekite and deformation twins in plagioclase feldspar.

Complete mineralogy of each sample is listed in Table 3 and described in detail with accompanying pictures in Appendix A.

Table 3. Mineralogy of 52 metamorphic glacial clasts from Lonewolf Nunataks A and B.

Sample No.	Rock Name	Quartz	Plagioclase feldspar	Potassium feldspar	Biotite	Muscovite	Chlorite	Garnet	Kyanite	Hornblende (Incl. tsch)	Other Amphiboles	Orthopyroxene	Clinopyroxene	Scapolite	Zircon	Apatite	Fe-Ti oxide	Epidote	Pumpellyite	Sphene	Mg-tourmaline	Calcite
LWA-1.1	Grt-Bt gneiss	x	x				x	x					x			x	x	x		x		
LWA-1.2	Bt gneiss	x	x		x	x	x						x		x	x	x					
LWA-1.3	Grt-Bt gneiss	x	x	x	x	x		x								x	x					
LWA-1.4	Bt gneiss	x	x	x	x	x									x	x						
LWA-1.5	Bt gneiss	x	x	x	x	x									x		x					
LWA-1.6	Bt gneiss	x	x	x	x	x									x		x				x	
LWA-1.7	Bt gneiss	x	x	x	x										x		x					
LWA-10.1	Hbl orthogneiss	x	x				x			x					x	x	x	x	x			
LWA-2.1	Bt-Ms orthogneiss	x	x	x	x	x										x	x					
LWA-2.2	Grt-Bt gneiss	x	x		x			x						x	x	x	x					
LWA-2.3	Grt-Hbl-Bt gneiss	x	x		x	x	x	x		x						x	x					
LWA-3.1	Bt-Ms schist	x	x		x	x									x	x	x					x
LWA-3.2	Ms-Bt schist	x	x		x	x									x		x					x
LWA-4.1	Bt gneiss	x	x	x	x	x									x	x	x					

Notes: Rt = rutile, Rb = Riebeckite, Act = actinolite

Table 3. Mineralogy of 52 metamorphic glacial clasts from Lonewolf Nunataks A and B.

Sample No.	Rock Name	Quartz	Plagioclase feldspar	Potassium feldspar	Biotite	Muscovite	Chlorite	Garnet	Kyanite	Hornblende (Incl. tsch)	Other Amphiboles	Orthopyroxene	Clinopyroxene	Scapolite	Zircon	Apatite	Fe-Ti oxide	Epidote	Pumpellyite	Sphene	Mg-tourmaline	Calcite
LWA-5.1	Hypersthene-Grt-Hbl gneiss	x	x					x		x		x				x	x					
LWA-6.1	Bt-Ms orthogneiss	x	x	x	x	x	x								x	x	Rt					
LWA-6.2	Bt-Ms gneiss	x	x		x	x									x		x					
LWA-6.3	Bt gneiss	x	x		x	x									x	x	x					
LWA-6.7	Bt-Ms gneiss	x	x		x	x	x								x		Rt					
LWB-1.1	Grt-Tsch-Bt gneiss	x	x		x		x	x		tsch						x	x					
LWB-1.2	Grt-Bt-ky gneiss	x	x		x			x	x								x			x		
LWB-1.3	Grt-Bt gneiss	x	x		x	x		x							x	x	x					
LWB-1.4	Grt-Bt-Hbl gneiss	x	x		x			x		x				x	x	x	x					
LWB-1.5	Grt-Bt orthogneiss	x	x		x	x		x							x		x					
LWB-1.6	Grt-Bt gneiss	x	x		x			x							x	x	x	x				
LWB-1.7	Grt-Ms leucogneiss	x	x	x	x	x		x								x						
LWB-2.2	Hbl-Bt gneiss	x	x	x	x	x				x					x	x	x					
LWB-2.3	Grt gneiss	x	?					x							x		x	x				
LWB-2.4	Hbl-hypersthene Grt gneiss	x	x		x			x		x		x					x					

Notes: Rt = rutile, Rb = Riebeckite, Act = actinolite

Table 3. Mineralogy of 52 metamorphic glacial clasts from Lonewolf Nunataks A and B.

Sample No.	Rock Name	Quartz	Plagioclase feldspar	Potassium feldspar	Biotite	Muscovite	Chlorite	Garnet	Kyanite	Hornblende (Incl. tsch)	Other Amphiboles	Orthopyroxene	Clinopyroxene	Scapolite	Zircon	Apatite	Fe-Ti oxide	Epidote	Pumpellyite	Sphene	Mg-tourmaline	Calcite
LWB-2.5	Hbl amphibolite	x	x		x					x						x	x	x				
LWB-2.6	Tsch-Bt-Grt gneiss	x	x		x		Fe-	x		tsch				x	x	x	x					
LWB-2.7	Bt gneiss	x	x		x	x	x								x	x	x	x		x		
LWB-2.8	Grt gneiss	x	x	x				x							x	x	x					
LWB-4.1	Hbl-Bt orthogneiss	x	x	x	x	x	x			x					x	x	x	x				x
LWB-4.3	Grt-Bt orthogneiss	x	x	x	x		x	x		x					x		x					
LWB-4.4	Bt-Ms orthogneiss	x	x	x	x	x	x								x		x					
LWB-4.5	Bt orthogneiss / deformed granodiorite	x	x		x	x	x								x	x	x					
LWB-4.6	Bt orthogneiss / deformed diorite (?)	x	x	x	x										x	x	x					
LWB-4.7	Bt-Ms orthogneiss	x	x	x	x	x	x								x	x	x	x				
LWB-4.8	Ms-Bt orthogneiss	x	x	x	x	x	x								x		x					
LWB-5.1	Bt-Ms gneiss	x	x	x	x	x	x								x	x	x	x				
LWB-5.2	Ms gneiss	x	x	x	x	x										x	x					
LWB-5.3	Bt gneiss	x	x		x		x								x	x	x					

Notes: Rt = rutile, Rb = Riebeckite, Act = actinolite

Table 3. Mineralogy of 52 metamorphic glacial clasts from Lonewolf Nunataks A and B.

Sample No.	Rock Name	Quartz	Plagioclase feldspar	Potassium feldspar	Biotite	Muscovite	Chlorite	Garnet	Kyanite	Hornblende (Incl. tsch)	Other Amphiboles	Orthopyroxene	Clinopyroxene	Scapolite	Zircon	Apatite	Fe-Ti oxide	Epidote	Pumpellyite	Sphene	Mg-tourmaline	Calcite
LWB-5.4	Bt-Ms orthogneiss	x	x	x	x	x									x							
LWB-5.5	Bt-Ms gneiss	x	x	x	x	x									x							
LWB-5.6	Ms-Bt gneiss	x	x	x	x	x									x	x						
LWB-5.7	Bt orthogneiss	x	x	x	x						act?				x	x	x			x		
LWB-5.8	Bt orthogneiss	x	x	x	x	x	x								x	x	x	x				
LWB-6.1	Grt-Tsch-scapolite gneiss	x	x		x			x		tsch	Rb			x								
LWB-6.2	Grt-Tsch amphibolite	x	x		x			x		tsch							x					
LWB-6.3	Grt-Tsch gneiss	x	x		x		x	x		tsch					x		x	x				
LWB-6.4	Grt-Bt gneiss	x	x		x			x							x		x					

Notes: Rt = rutile, Rb = Riebeckite, Act = actinolite

4.1.1.2 Garnetiferous quartzofeldspathic gneisses

Lonewolf Nunataks felsic gneisses include 13 garnetiferous samples (Table 3). The mineralogy of a typical garnetiferous quartzofeldspathic gneiss includes: quartz + plagioclase feldspar ± potassium feldspar + garnet + biotite ± muscovite ± chlorite. Typical accessory minerals are an opaque phase + apatite ± zircon. With only one exception (kyanite in LWB-1.2), these samples lack aluminosilicate minerals. Other notable occurrences include scapolite (LWA-2.2) and hypersthene (LWA-5.1). The garnetiferous quartzofeldspathic gneisses range from very fine-grained to coarse-grained, but are typically fine-grained to medium-grained. These rocks range from poorly-foliated to well-foliated. Foliation is expressed by the alignment, or grain-shape preferred-orientation (GSPO), of minerals, as well as by compositional layering and occasionally the presence of quartz ribbons (LWA-1.3, LWB-1.2, LWB-1.5, LWB-6.4). Linear feldspar boudins/augen (LWB-1.5, LWB-4.3) are also present. Common microtextures in the felsic gneisses are myrmekite and deformation twins in plagioclase feldspar.

Notably, LWA-5.1, a hypersthene-garnet-hornblende gneiss, exhibits hypersthene phenocrysts which are granular and don't possess a well-defined crystal shape, which indicates that they are relict igneous minerals which have been altered by metamorphism. There are also pyroxene reaction rims around opaques, though this pyroxene cannot optically be identified as hypersthene. The presence of a reaction rim suggests that as metamorphism progressed, the opaques were in disequilibrium with the P-T conditions, causing the pyroxene in the reaction rims to form in a rock with a previous mafic component (i.e. hypersthene). Sample LWA-2.3 shows fibrous unidentified mineral

coronae around garnet, as well as the presence of epidote, possibly indicating hydrothermal alteration during metamorphism and/or metasomatism.

4.1.2 Mafic gneisses and amphibolites

4.1.2.1 Mafic gneisses and amphibolites

Lonewolf Nunataks amphibolites and mafic gneisses include three non-garnet-bearing samples (Table 3). The mineralogy of a typical non-garnet-bearing amphibolite/mafic gneiss includes: quartz + plagioclase feldspar ± potassium feldspar + hornblende ± biotite. Common accessory minerals are an opaque phase + apatite ± zircon ± muscovite ± epidote ± calcite. These samples are characteristically medium- to coarse-grained and moderately-foliated to well-foliated. Foliation is expressed by the presence of quartz ribbons (LWB-2.5, LWB-4.1) as well as layering. Common microtextures are myrmekite and deformation twins in plagioclase feldspar.

4.1.2.2 Garnetiferous mafic gneisses and amphibolites

Lonewolf Nunataks mafic gneisses and amphibolites include nine garnetiferous samples (Table 3). Mineralogically, a typical garnetiferous mafic gneiss or amphibolite includes: quartz + plagioclase feldspar ± potassium feldspar + tschermakitic amphibole + garnet ± biotite ± chlorite. Some samples also contain scapolite (LWB-1.4, LWB-2.6) or hypersthene (LWB-2.4). Typical accessory minerals include an opaque phase + apatite ± zircon. These samples vary from very fine-grained to coarse-grained, but are primarily medium-grained. Samples range from non-foliated to well-foliated, but they are typically one type or the other: poorly-foliated or well-foliated. Foliation is most commonly expressed by quartz ribbons (LWB-2.6, LWB-6.2) and compositional layering. GSPO in

amphiboles shows a linear fabric. Common microtextures include myrmekite and deformation twins in plagioclase feldspar.

4.1.3 Schists

Lonewolf Nunataks metamorphic clasts include two schist samples (Table 3). The mineralogy of the schists is: quartz + plagioclase feldspar + calcite + biotite + muscovite. Accessory minerals are apatite and zircon. These samples are fine- to medium-grained and well foliated, formed by a GSPO of muscovite and some biotite. Microstructures include quartz ribbons and crenulation cleavage.

4.2 Metamorphic mineral compositions

4.2.1 Mineral compositions

For this study, I analyzed mineral compositions in 16 samples from the Lonewolf Nunataks via energy dispersive spectroscopy (EDS). Mineral compositions were quantitatively determined for garnet, biotite, amphibole, and pyroxene. Compositional results for each mineral phase are presented below.

4.2.1.1 Garnet compositions

Garnet compositions were determined by EDS analysis for two or three porphyroblasts in each of 16 samples of the 21 garnet-bearing samples from the Lonewolf Nunataks. Garnet composition is controlled by variations in the number of cations of Fe, Mg, Ca, and Mn in the M site. Many garnets analyzed in this study have compositions that are reasonably well represented by a combination of the Fe (almandine, $Fe_3Al_2Si_3O_{12}$) and Mg (pyrope, $Mg_3Al_2Si_3O_{12}$) end-member compositions. In regional metamorphic rocks, the almandine and pyrope end-members dominate, and garnets are typically low in Ca and Mn. However, some garnets from the Lonewolf samples have significant amounts of Ca and/or Mn; these garnets therefore cannot be modeled as simple Fe-Mg garnet solid solutions. As a result, subsequent geothermobarometry calculations must be corrected for elevated Ca or Mn contents in these garnets (as discussed below).

Representative analyses of garnets are included in Table A in Appendix B. The values listed are calculated as averages of three individual spot analyses, omitting any outliers, as described in the methods section. Cation proportions for garnet were

recalculated on the basis of 12 oxygens, and all Fe was assumed to be FeO. A typical garnet formula is $X_3Y_2Z_3O_{12}$, where X is the metal site, or M site. Following convention, one unit cell of garnet contains eight cations, including three M-site metals.

For all garnets analyzed, Fe is the most abundant cation, indicating that these garnets are predominantly almandine in composition. Fe is typically followed in abundance by Mg, Ca, and Mn, respectively, with some exceptions. In samples LWB-1.1 and LWB-6.2, Ca is the second most abundant metal cation after Fe. Sample LWB-1.7 has Mn as its second most abundant metal and contains almost no Ca and no Mg. The proportion of Ca and Mn is commonly quite similar in Lonewolf garnets, and in all but one sample, the amount of Mn is less than or equal to the amount of Ca. However, in LWA-1.3, the garnets analyzed have slightly greater Mn than Ca.

Fourteen of the 16 samples analyzed have at least one garnet that shows evidence of slight to moderate compositional zoning (prograde and/or retrograde) from core to rim. Compositional growth zoning is shown in a garnet profile by increases or decreases in abundance of the M-site metals Fe, Mg, Ca, and Mn from a garnet's core to its rim. Garnet has sluggish internal solid-state diffusion during metamorphic growth (Winter, 2010), so instead of re-equilibrating with changing rock composition or P-T conditions, garnet grows incrementally by stabilizing a new composition at its rim that is in chemical equilibrium with the new conditions. Thus, each growth stage preserves a different garnet composition, such that the compositions vary from the core to the rim.

Compositional growth zoning in garnet is not always preserved. For example, retrograde metamorphism may obscure or overprint a garnet's original compositional

zoning at garnet rims (Winter, 2010). Such overprinting occurs as the garnet has time to compositionally re-equilibrate with surrounding minerals after the rock has reached peak metamorphic conditions and begins to cool and/or decompress. The result may be garnet rims that no longer reflect peak metamorphic conditions. Additionally, compositional zoning may be erased completely if garnet reaches a high enough temperature at peak metamorphism.

Garnet zoning is well-displayed by the abundance of Fe and Mg. These divalent cations substitute easily for one another in a metal site because they are the same valence. Typical Fe-Mg zonation patterns in garnets show higher Mg content at the core than at the rim, and consequently a higher Fe content at the rim than the core. This phenomenon is only minimally attributable to the size of the cations: the ionic radius of Mg^{2+} is smaller than that of Fe^{2+}. Mineral structures can accommodate larger cations at higher temperatures, so as temperature increases (common with prograde metamorphism), the larger Fe^{2+} is theoretically more readily accepted by the garnet M-sites. This theory is applicable to garnets forming in isolation from other phases; however such a scenario rarely occurs. In fact, the composition of garnet, like many Fe-Mg phases, becomes more Mg rich with higher T, as a result of the partitioning of Fe-Mg in a coupled way between garnet and other phases like biotite (Fig. 14). The compositional changes of garnet during growth, therefore, are not as simple as just due to size of cations alone. Consequently, the chemical zonation of garnets in this study is highly dependent upon the mineral assemblage of the rock in question.

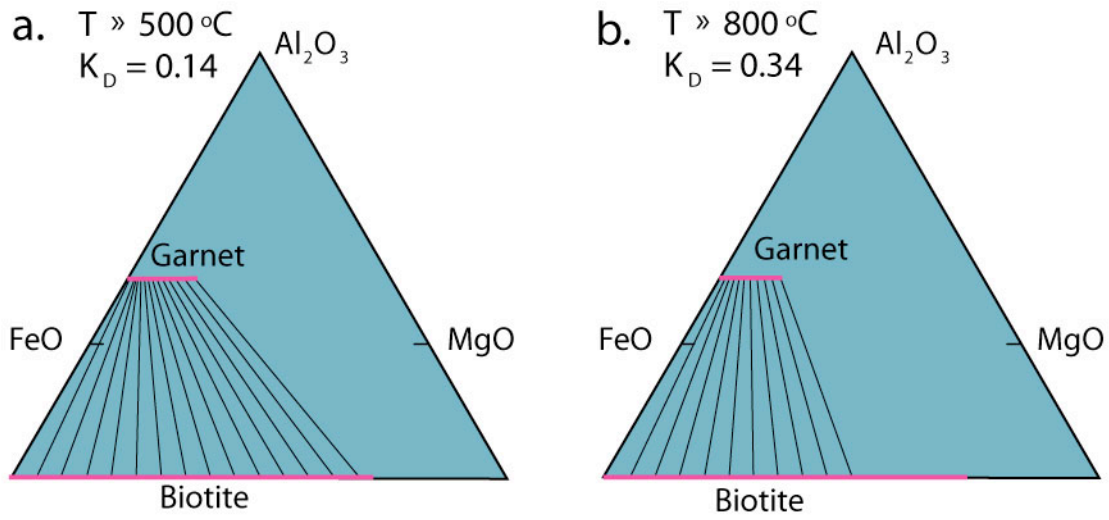

Figure 14. AFM projections showing the relative distribution of Fe and Mg in garnet vs. biotite at approximately 500 °C (a) and 800 °C (b). From Spear (1993), reproduced in Winter (2010).

Most zoned garnets in this study (Fig. 15) show a decrease in Mg from the core to the rim, and an increase in Fe from the core to the rim, with exceptions of garnets from samples LWA-1.3, LWB-1.1, LWB-1.3, LWB-1.7, and LWB-6.2. One garnet in LWA-1.3 does show an increase in Fe and a decrease in Mg toward the rim but also a sharp increase in Fe and decrease in Mg at the center of the garnet coinciding with a crack. This anomaly along the crack was probably caused by alteration along the crack and is not representative of the original garnet zoning.

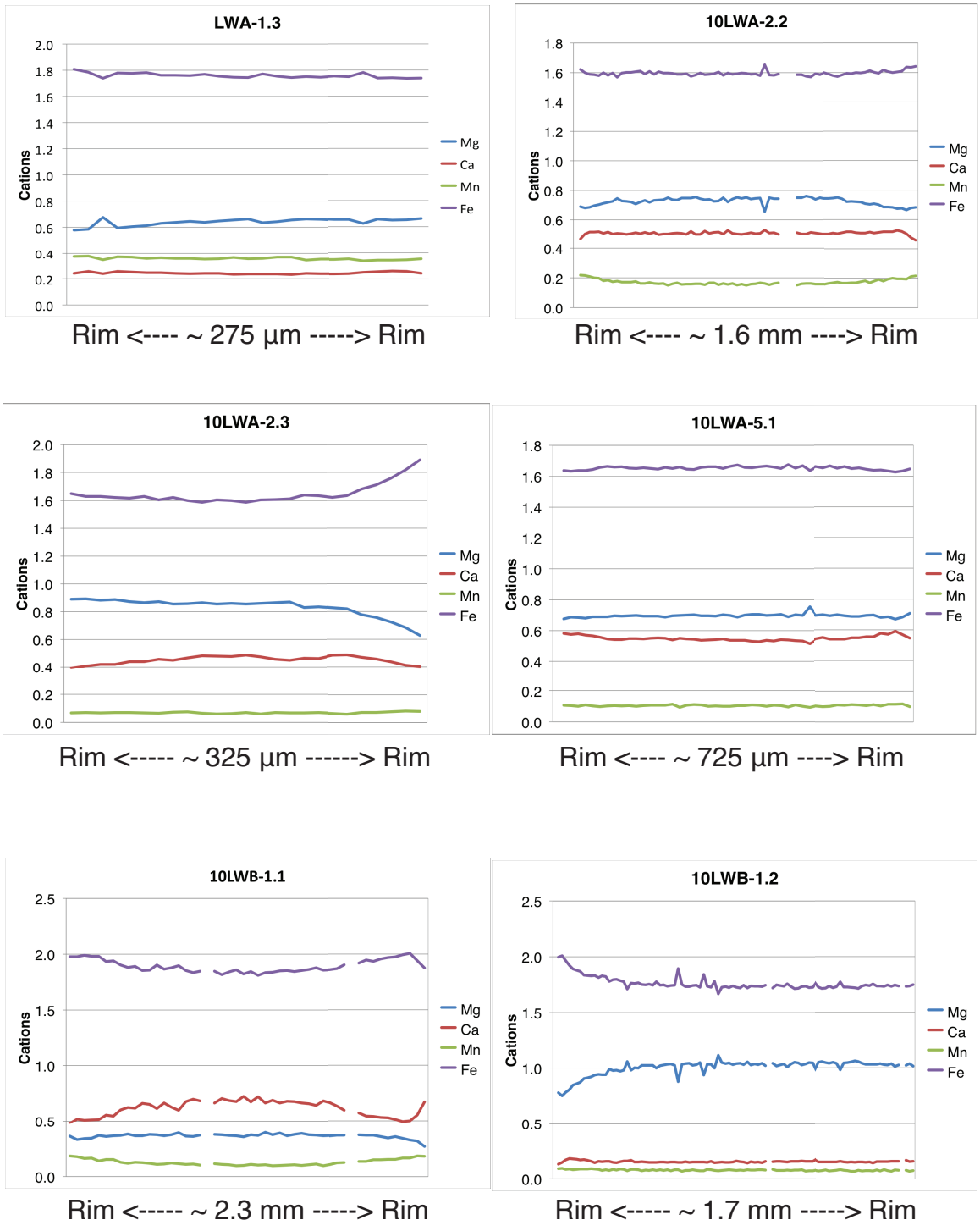

Figure 15. Garnet profiles from rim to rim, showing Fe, Mg, Ca, and Mn cations per formula unit. Each profile shown is the most representative profile from each sample, or a particularly informative profile as explained in the text.

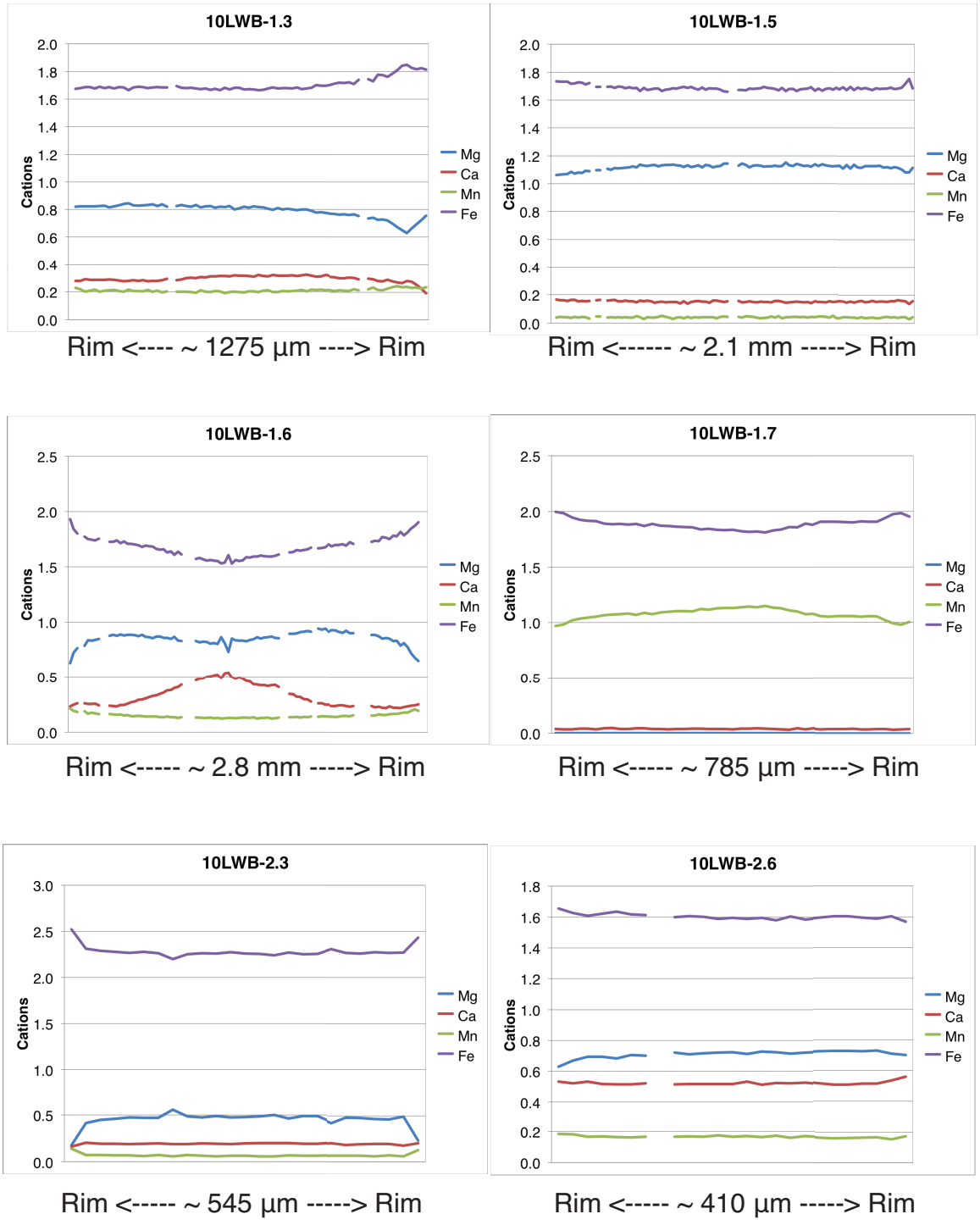

Figure 15 (continued). Garnet profiles from rim to rim, showing Fe, Mg, Ca, and Mn cations per formula unit. Each profile shown is the most representative profile from each sample, or a particularly informative profile as explained in the text.

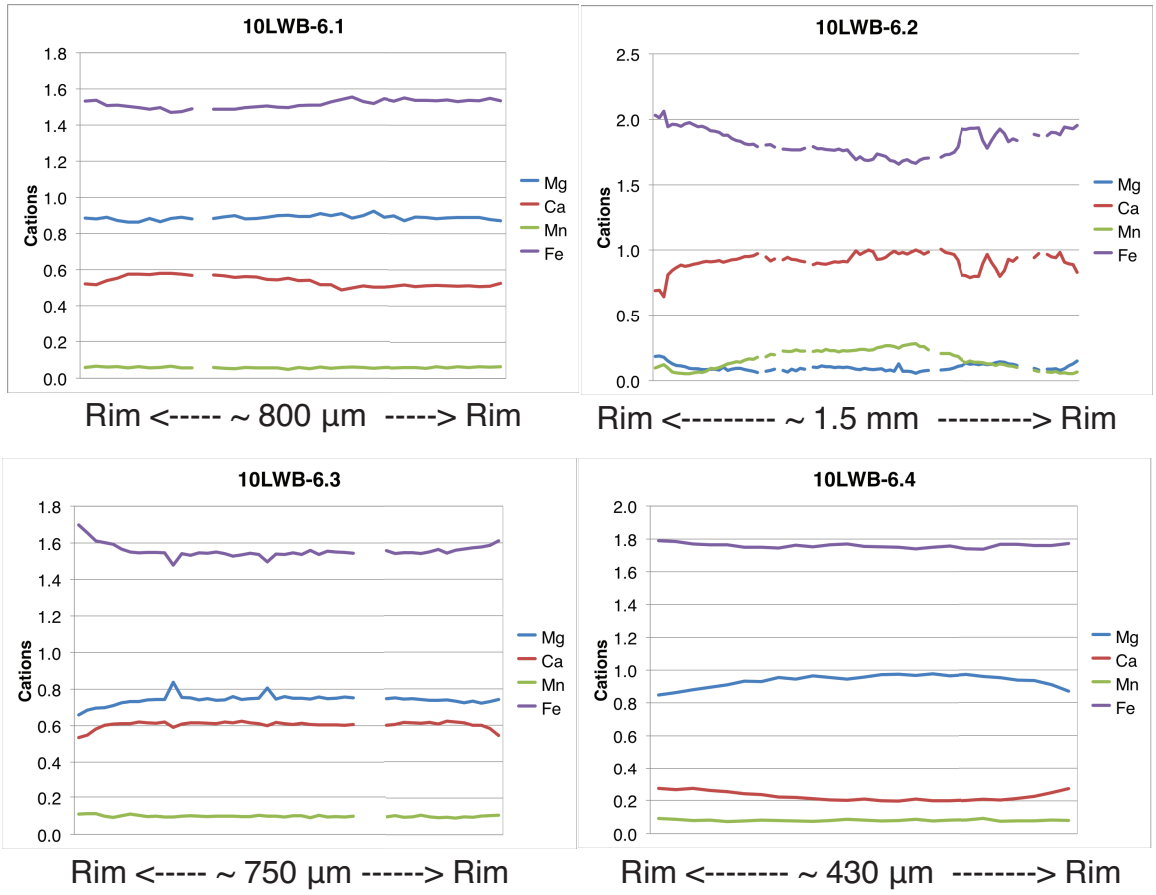

Figure 15 (continued). Garnet profiles from rim to rim, showing Fe, Mg, Ca, and Mn cations per formula unit. Each profile shown is the most representative profile from each sample, or a particularly informative profile as explained in the text.

In LWB-1.1 and LWB-6.2, Fe and Ca are the two most abundant metal cations. As a result, the amount of Ca decreases (just as Mg typically does) from the core to the rim while the amount of Fe increases from the core to the rim. This abundance of Ca as opposed to Mg in the garnets of these samples is possibly related to a protolith rock composition low in Mg.

In one garnet from LWB-1.3, Mg abundance decreases and Fe abundance increases from the core to the rim until a point very near one rim, at which the Mg

sharply increases and Fe decreases again. This sharp decrease occurs only on one side of one garnet profile in this sample. This sharp shift could be the result of a preservation problem. Garnet might have developed a growth pattern that is only partly preserved due to differential re-equilibration or dissolution along one side.

The profile from garnet 1 in LWB-1.6 shows increased Fe and decreased Mg content at both rims as well as a notable increase in Fe content and a notable dip in Mg content toward the center of the profile. This profile gives the appearance that two zoned garnets have grown together. If this is the case, it appears that the pattern of Mg-depletion and Fe-enrichment from core to rim is also true for this sample. Garnets in LWB-1.7 have no detectable Mg and very little Ca, but they show a zonation relationship between Fe and Mn in which Mn decreases (just as Mg typically does) and Fe increases from core to rim. The absence of Mg in garnet from this sample may reflect a protolith rock composition with little Mg and abundant Fe, such as an iron formation. This lack of Mg and Ca is probably responsible for a zoning pattern dominated by Mn and Fe.

In some samples with zoned garnet, not every garnet profile shows zoning. Several explanations might explain this lack of zoning in some garnet profiles. First, there might be different generations of garnet growth; if a later phase of growth did not re-equilibrate the older phase, the two might show compositional differences. Second, within a given rock sample consisting of different compositional layers, local equilibrium might result in different compositions and zoning patterns. Third, and probably most likely, the profiles I obtained may have transected different cross-section planes among the different garnets analyzed; sections penetrating near the center of a crystal might

show more complete zoning profiles than sections crossing only outer growth domains (Fig. 16). Some garnet profiles display zoning on only one side of the profile, which may indicate that the garnet crystals were deformed or underwent chemical dissolution such that that the profile obtained is not representative of the original garnet. Whatever the cause, for the purposes of this project I focus to the extent possible on those crystals showing evidence of compositional zoning, which afford the best opportunity to evaluate progressive changes in *P-T* conditions.

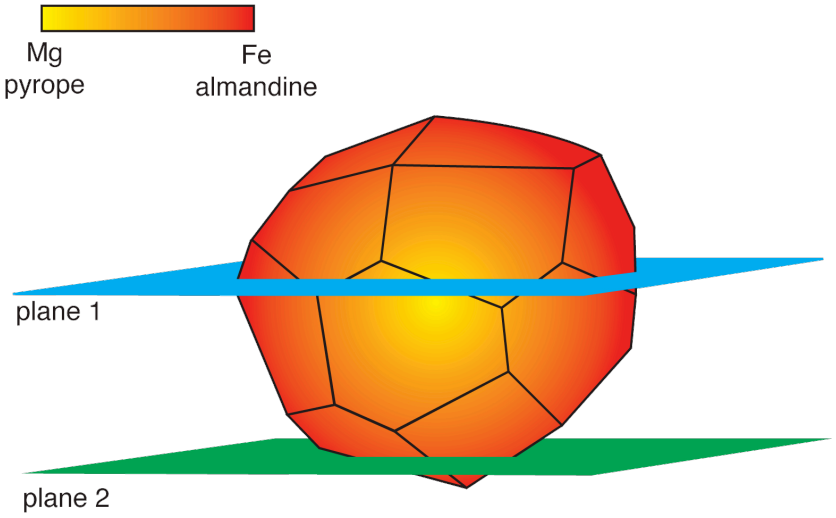

Figure 16. Illustration of garnet crystal cut by two planes representing thin sections. The garnet is compositionally zoned from the core to the rim; yellow represents Mg-rich garnet (pyrope) at the core and red represents Fe-rich garnet (almandine) at the rims. If the thin section cuts the garnet along plane 1, the garnet will show a compositional profile with Mg-Fe zoning from the core to the rims. However, if the thin section cuts the garnet along plane 2, the garnet will present a very Fe-rich composition and will display little compositional zoning.

Given all of the above complications and considerations, I have selected one 'representative' garnet profile from each of the 16 samples to display in Figure 15. Samples LWA-2.2, LWB-1.1, LWB-1.3, LWB-1.5, LWB-1.6, LWB-1.7, LWB-6.2 and

LWB-6.4 show evidence of prograde zoning in at least one garnet, and samples LWA-1.3, LWA-2.2, LWA-2.3, LWB-1.1, LWB-1.2, LWB-1.3, LWB-1.7, LWB-2.3, LWB-2.6, LWB-6.2, LWB-6.3, and LWB-6.4 appear to have been affected by retrograde metamorphism. Samples LWA-5.1 and LWB-6.1 showed no discernable zoning at all. Note that some samples exhibited both prograde and retrograde metamorphism. A detailed summary is provided in Table 4.

Table 4. Summary of the garnet zonation profiles for each sample analyzed from the Lonewolf Nunataks A and B.

Sample	Garnet zonation pattern
LWA-1.3	Two profiles flat and one with possible retrogression at the rims.
LWA-2.2	Slight prograde zoning and minor retrograde overprint
LWA-2.3	Extensive retrograde on one side of one garnet, otherwise flat
LWA-5.1	Flat – no evidence of zoning
LWB-1.1	One garnet shows prograde zoning, another is flat, and both show retrogressive zoning. Another garnet provides no useful information.
LWB-1.2	All with flat profiles except for one garnet with a retrogressive rim on one side.
LWB-1.3	Slight prograde zoning, and retrogressive zoning on one side of one garnet.
LWB-1.5	Prograde zoning
LWB-1.6	Prograde zoning
LWB-1.7	Prograde zoning with slight retrogressive zoning
LWB-2.3	Flat profiles with retrogressive zoning on one garnet
LWB-2.6	Minor retrograde zoning, otherwise flat
LWB-6.1	Flat – no evidence of zoning
LWB-6.2	Prograde zoning with retrograde zoning in all but one garnet
LWB-6.3	Retrograde in two of the three garnets, otherwise flat
LWB-6.4	One garnet shows prograde zoning, while the others are flat. One of the flat profiles has retrogressive zoning.

4.2.1.2 Biotite compositions

Biotite compositions were analyzed in nine samples. Annite ($K_2Fe_6[Si_6Al_2O_{20}](OH)_4$) and phlogopite ($K_2Mg_6[Si_6Al_2O_{20}](OH)_4$) are the ideal Fe and Mg end-members, respectively, of the tri-octahedral sheet silicates known as biotites (Deer et. al, 1992). Most biotites in Lonewolf Nunataks samples contain more Mg than Fe (X_{Mg} = 0.56-0.60), making their compositions phlogopite-rich. The only exception is LWB-1.1, in which biotite is more Fe-rich (X_{Mg} = 0.36). Average compositions of biotite are listed in Table B of Appendix B.

4.2.1.3 Amphibole compositions

Amphibole compositions were analyzed in six samples. Amphiboles are double-chain silicates commonly found in metamorphic rocks. Amphiboles have a very broad range of compositions and numerous cations can be accepted to fill sites of a general formula $A_{0\text{-}1}B_2C_5T_8O_{22}(OH,F)_2$. The four generally-accepted groups of amphiboles (Leake et al., 1978; Deer et al., 1992, and refined by Leake et al., 1997) are defined by the cations that are dominant in the B site: calcic amphiboles (Ca), sodic amphiboles (Na), sodic-calcic amphiboles (both Ca and Na), and magnesium-iron-manganese-lithium amphiboles (mainly Fe, Mg and Mn). The amphiboles analyzed in this study were generally very Ca-rich and fall into the calcic amphibole type defined as tschermakite. Tschermakite — $Ca_2(Mg,Fe)_3Al_2Si_6Al_2O_{22}](OH)_2$ — forms when the coupled Al^{3+} replacement of Si^{4+} and $(Mg,Fe)^{2+}$ continues to occur beyond the formation of a general hornblende composition. Presence of tschermakite indicates high-grade metamorphism, such as in rocks of the upper amphibolite facies or in altered eclogites (Deer et al., 1992). Given the absence of eclogitic mineralogy in Lonewolf clasts, it is likely that the tschermakitic composition of the amphiboles is the result of high-T metamorphism stabilization. This is consistent with temperature estimates discussed below. Average compositions of amphiboles are listed in Table C of Appendix B.

4.2.1.4 Pyroxene compositions

Pyroxene compositions were determined in one sample. Pyroxenes are ferromagnesian single-chain silicates that are generally divided into several categories:

magnesium-iron pyroxenes, calcic pyroxenes, and sodium pyroxenes, as well as two minor sub-categories (calcium-sodium pyroxenes and lithium pyroxenes). Pyroxenes analyzed in Lonewolf samples are hypersthene, part of the enstatite-ferrosilite series in magnesium-iron orthopyroxene. In one additional Lonewolf sample not analyzed by EDS, hypersthene was identified optically by a strong pink-green pleochroism. Hypersthenes are typically associated in metamorphic rocks with high-grade metamorphism of the granulite facies. Rocks with significant hypersthene content are considered charnockites (Deer et al., 1992). Average pyroxene compositions are listed in Table D of Appendix B.

4.2.2 Other notable minerals

In support of optical petrography, identification of other phases was conducted by a combination of back-scattered electron imaging and EDS analysis. Spot analyses revealed the presence of several notable minerals.

4.2.2.1 Ilmenite

Opaque phases are common in Lonewolf samples and in all cases identified by EDS as ilmenite. Ilmenite is an iron-titanium oxide of general composition (Fe, Mg, Mn)TiO_3. Ilmenite is a typical accessory mineral in metamorphic and igneous rocks, including orthogneisses.

4.2.2.2 Scapolite

Scapolite is a framework silicate that forms in metamorphic rocks from greenschist to granulite facies. End-members of the scapolite series are $Na_4[Al_3Si_9O_{24}]Cl$ (marialite) and $Ca_4[Al_6Si_6O_{24}]CO_3$ (meionite), in which meionite (Ca) content increases

with metamorphic grade. Scapolite occurs in three Lonewolf metamorphic samples: LWA-2.2, LWB-1.4, and LWB-2.6, all of which also contain garnet. Lonewolf scapolites are calcic (meionitic) in composition as identified by element peaks recorded by EDS (Reed, 2005). Presence of Ca-scapolite is significant because it indicates that rocks in which it is found experienced high-grade metamorphism (Deer et. al., 1992).

4.3 Geothermobarometry analysis

4.3.1 Theory of geothermobarometry

Knowledge of the pressure and temperature conditions experienced by rocks constrains their past position in the crust and is essential for the reconstruction of metamorphic setting. Optical petrography of metamorphic clasts from Lonewolf Nunataks sites A and B allowed for determination of general metamorphic facies and an estimate of temperature conditions based on mineral assemblage and textural relationships. However, these approaches give only a qualitative idea of the physical conditions. To help quantitatively constrain metamorphic conditions, mineral composition data (discussed in section 4.2) were applied to thermodynamically-based geothermobarometers.

Geothermobarometers are derived on a theoretical or experimental basis to determine the mineral compositional dependence on temperature and/or pressure. Once a relationship is established between mineral composition and physical conditions, a rock's *P-T* history can be reconstructed inversely by applying mineral compositions to that relationship in order to calculate past conditions during which the minerals achieved chemical equilibrium (see Winter, 2010). Thus, geothermobarometry works by determining the compositions of certain mineral phases (garnet, biotite, amphibole, etc.) and applying these to calibrated relationships between composition, temperature and pressure. A good geothermometer will have a steep slope on a *P-T* diagram, indicating that mineral composition is mostly dependent on temperature and pressure has little to no effect (Fig. 17). Conversely, a good geobarometer will have a shallow slope on a *P-T*

diagram because compositions of the phases will vary most strongly with a change in pressure but negligibly with a change in temperature (Fig. 17).

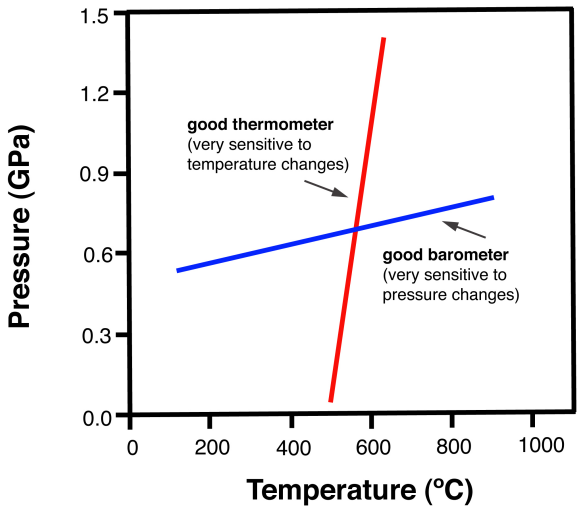

Figure 17. Schematic *P-T* plot showing slopes of isopleths (lines of constant K_D) in ideal geothermometers and geobarometers. After Whitney (accessed 2011).

Elemental compositions of coexisting phases in a rock vary with temperature and pressure principally by ion-exchange or net-transfer reactions between metamorphic minerals (Winter, 2010). An ion-exchange reaction involves the reciprocal exchange of components (such as Fe and Mg) between two or more minerals or phases by cation diffusion. Garnet-biotite thermometry, for example, is based on the chemical exchange of Fe and Mg between garnet and biotite in a metamorphic system. Exchange reactions are different from net-transfer reactions in that the modal amounts of the phases in the system remain constant and only the compositions of these phases change (both of these factors vary in a net-transfer reaction). In petrologic applications, ion-exchange reactions involve cation substitutions within minerals exhibiting solid solution. Balanced ion-exchange reactions can be written with end-member varieties of specific minerals on opposite sides

of the equation as either reactant or product phases (e.g., Fe-garnet and Mg-biotite as reactants, and Mg-garnet and Fe-biotite as products). For example, an Fe-Mg exchange reaction will take the general form (Winter, 2010):

$$A_{Fe} + B_{Mg} = A_{Mg} + B_{Fe} \quad (1)$$

where A and B are different mineral phases. For the garnet-biotite geothermometer, the end-member Fe-Mg exchange reaction is:

$$Fe_3Al_2Si_3O_{12} + KMg_3AlSi_3O_{10}(OH)_2 = Mg_3Al_2SiO_{12} + KFe_3AlSi_3O_{10}(OH)_2 \quad (2)$$

almandine + *phlogopite* = *pyrope* + *annite*

Because such a basic geothermometer expression accounts only for pure end-member phase compositions, and because such pure end-member compositions are rarely found in natural systems, adjustments need to be made to the geothermometers to allow them to be applied more broadly to natural mineral compositions. Refinements to these geothermometers to account for compositions that deviate from pure end-member compositions result in different calibrations, as discussed below.

4.3.1.1 Methods

This study used garnet-biotite (GB) and garnet-hornblende (GH) geothermometers, and aluminum-in-amphibole and garnet-aluminosilicate-silica-plagioclase (GASP) geobarometers. Mineral compositions in thirteen metamorphic glacial clasts from the Lonewolf Nunataks (Table 5) were analyzed in order to be used in geothermobarometry. These samples include nine felsic garnet gneisses and five garnet-bearing amphibolites/mafic gneisses.

Table 5. Metamorphic glacial clasts analyzed for mineral composition for use in geothermobarometry

10LWA-1.3
10LWA-2.2
10LWA-2.3
10LWB-1.1
10LWB-1.2
10LWB-1.3
10LWB-1.5
10LWB-1.6
10LWB-2.6
10LWB-6.1
10LWB-6.2
10LWB-6.3
10LWB-6.4

Mineral compositions were determined by energy dispersive spectroscopy (EDS) on a scanning electron microscope (SEM) and applied to geothermobarometers from the literature. Compositional data – reported in oxide form for garnet, biotite, amphibole, and pyroxene – were then normalized to cation proportions (Appendix B). The cation values given for minerals listed in Appendix B are typically a simple mean of three spot analyses in one area (omitting obvious outliers and anomalous results). Spot analysis (typically exciting x-rays from a 2-3 μm-diameter sample volume) allows for determination of unique mineral compositions in different parts of compositionally zoned mineral grains. Locations for compositional analysis were chosen with great care based on the following criteria:

(1) When present, inclusions of biotite or amphibole in garnet were analyzed. The composition of such inclusions near the crystal core was coupled with garnet core compositions to give a best estimate of the *P*-*T* conditions at the time of growth of the garnet core.

(2) In cases where inclusions of biotite and hornblende were not available to compare to a garnet's core composition, compositions of biotite, amphibole, and orthopyroxene from the rock matrix were used to assess temperature. This was done in two different ways, depending on the relative amount of matrix biotite, amphibole, or orthopyroxene present in the sample:

(a) In rocks with abundant matrix biotite or amphibole, especially with sparse garnet, compositions of matrix biotite and amphibole were used with garnet core compositions to estimate prograde conditions. This approach is considered valid because the modal abundances of either biotite or hornblende are so high that their compositions control the exchange reactions and probably did not change much during prograde and peak metamorphism. In the upper amphibolite to granulite facies, retrograde Fe-Mg exchange takes place during cooling. In rocks with abundant biotite and amphibole in the matrix (Tracy et al., 1976), retrogression will likely not greatly change the composition of any given biotite or amphibole. However, garnet rims are much more susceptible to retrogressive change in samples where biotite or amphibole are more abundant (Tracey et al., 1976). As a result, combining the composition of a garnet rim with the composition of a biotite or amphibole touching that rim can be inaccurate because the composition of the garnet might have changed much more than the composition of the biotite or amphibole during retrogression (Bucher and Frey, 2002). In these types of rocks, it is better to compare

the garnet core (which presumably was not affected by preferential retrograde exchange) with rim biotite or amphibole. In fact, the garnet core is more likely to represent a record of T_{max} as opposed to a garnet rim because the garnet core is less likely to have been affected by retrogression. For rocks rich in matrix biotite or amphibole, and which show evidence of retrograde metamorphism, garnet core compositions can be used with matrix biotite or amphibole compositions to estimate T_{max} conditions.

(b) In rocks with abundant garnet, particularly if the modal biotite or hornblende is low, compositions of garnet rims were used in conjunction with compositions of biotites or hornblendes touching the rim of the garnet in order to estimate T_{max}. This approach can be used for rocks containing garnets with visible zonation attributed to prograde growth, but not where late retrogression is suspected (see below).

4.3.1.2 Assumptions

Iron in minerals may be either divalent (Fe^{2+}) or trivalent (Fe^{3+}). To simplify mineral formula calculations, it was assumed that all iron in garnet and amphibole is ferrous (Fe^{2+}). However, biotite calculations here include both ferric and ferrous iron based on Guidotti and Dyar's (1991) findings that 10-13% of iron in biotite is ferric (Fe^{3+}) in magnetite-bearing assemblages, and 4% of Fe is ferric in graphite-bearing assemblages. Because Lonewolf clasts contain mainly ilmenite, it is reasonable to conclude that these rocks have an oxidation state similar to those containing magnetite as

opposed to graphite. Therefore, in biotite cation calculations made in this study, a value of 12% Fe_{total} was used for Fe^{3+}.

Ion-exchange expressions such as Eq. (1) account for near pure end-member Fe-Mg phase compositions, and such pure end-member compositions are rarely found in natural systems. Many geothermobarometers have been recalibrated to account for compositions less similar to end-member compositions. Thermometers used in this study include classical calibrations for near end-member mineral compositions as well as re-calibrated thermobarometers which account for the unique non-ideality in my sample compositions, particularly the Ca and Mn components in garnet, the Al and Ti content in biotite, and the Ca content in amphibole.

4.3.2 Calibrations

All geothermobarometers applied in this study include different calibrations that account for varying ranges of phase composition and unique assumptions of cation site assignment. Based on the compositional data obtained by EDS, particular calibrations of the geothermobarometers were chosen for this study. Calculations and graphs for GB (garnet-biotite), GH (garnet-hornblende), and GASP (garnet-aluminosilicate-silica-plagioclase) geothermobarometers were produced using the GTB software program (Spear and Kohn, 2006). Calibrations of each of the thermobarometers used are listed in Table 6.

Table 6. Calibrations of geothermobarometers used on Lonewolf Nunataks clasts.

Geothermobarometer	Calibration
GB (garnet-biotite)	Ferry & Spear (1978) Hodges & Spear (1982) Ferry & Spear with Berman (1990) garnet model Kleeman & Reinhardt (1994)
GH (garnet-hornblende)	Graham & Powell (1984) Perchuk et al (1985)
GASP (garnet-aluminosilicate-silica-plagioclase	Koziol (1989)
Al in amphibole	Ernst & Liu (1998)

4.3.2.1 Garnet-biotite calibrations

Nine samples were analyzed for GB thermometry (LWA-1.3, LWA-2.2, LWA-2.3, LWB-1.1, LWB-1.2, LWB-1.3, LWB-1.5, LWB-1.6, LWB-6.4). The following four garnet-biotite calibrations were applied to these samples using the GTB software (Spear and Kohn, 2006).

Ferry and Spear (1978)

Ferry and Spear's (1978) thermometer is one of two experimental determinations of the Fe-Mg exchange upon which all other subsequent calibrations are based. Although the near-end member compositions used in the original experiments are not necessarily good approximations of natural minerals, I chose to include results from Ferry and Spear's original thermometer as a reference. This thermometer works well on samples with nearly pure almandine-pyrope garnets and annite-phlogopite biotites. The thermometer assumes ideal Fe-Mg mixing in garnet and ideal Al-Ti mixing in biotite. The authors suggest that this thermometer is not reliable for garnets with $X_{Ca+Mn} > 0.2$ or

biotites with $X_{Al+Ti} > 0.15$. This calibration has an uncertainty range of approximately ±50 °C. The expression derived by Ferry and Spear for the GB thermometer is:

$$\ln K = -2019/T + 0.782 \quad (3)$$

where $K = (Mg/Fe)_{garnet}/(Mg/Fe)_{biotite}$ and temperature is in degrees K.

Hodges and Spear (1982)

Since the original GB calibration was established, it has been shown that Fe and Mg in garnet do not mix ideally, as Ferry and Spear had assumed. Their original thermometer, and other subsequent GB thermometers which assume Fe-Mg ideality (e.g., Thompson, 1976; Goldman and Albee, 1977), give wide data scatter when used on rocks with non-Fe-Mg garnet and biotite compositions, and their results do not always correlate well with independent thermometry results (for example, garnet-clinopyroxene; Dasgupta, 1991). Hodges and Spear (1982) developed a thermometer that assumes non-ideal solution behavior for garnet. This thermometer is an improvement over Ferry and Spear's (1978) calibration, but it still assumes ideality of Fe-Mg mixing in biotite. The authors suggest using caution when applying this calibration to granulite facies rocks, to rocks with spessartine-rich garnets ($X_{sps} >> 0.2$, where spessartine is the Mn-rich variety), and to biotites where Ti is a 'major component'.

Ferry and Spear with Berman (1990) garnet solution model

Berman (1990) developed a comprehensive mixing model for Ca-Mg-Fe-Mn garnets. This mixing model is used with Ferry and Spear's (1978) calibration to give a thermometer that is applicable to a wider variety of garnet compositions (including non-ideal Fe-Mg mixtures).

Kleeman and Reinhardt (1994)

Kleeman and Reinhardt's (1994) thermometer is perhaps the most applicable to the widest range of both garnets and biotites. Before developing a new thermometer, Kleeman and Reinhardt tested eleven different garnet-biotite thermometers by using experimental data from Ferry and Spear (1978), as well as Perchuk and Lavrent'eva (1983), and determined that the majority of these calibrations did not provide significant accuracy. Kleeman and Reinhardt developed their own thermometer that uses Berman's (1990) garnet mixing model to account for larger variations in garnet composition. They developed a new activity model for biotite that accounts for Mg-Fe-Al non-ideal mixing and Mg-Fe-Ti mixing, which they found to be strongly temperature dependent. The amount of Al^{vi} in biotite was found to affect temperature much more strongly than the amount of Ti. Their model did not assume non-ideality in Fe-Mg mixing. Their new thermometer showed better accuracy than the other 11 calibrations they tested.

4.3.2.2 Garnet-hornblende calibrations

Garnet-hornblende (GH) thermometry was used to determine temperatures in six Lonewolf Nunataks samples (LWA-2.3, LWB-1.1, LWB-2.6, LWB-6.1, LWB-6.2, and LWB-6.3). Two GH calibrations are incorporated in the GTB software (Spear and Kohn, 2006) to obtain temperature results, summarized here.

Graham and Powell (1984)

Graham and Powell (1984) developed a GH thermometer by calibrating it against a garnet-clinopyroxene (Grt-Cpx) thermometer of Ellis and Green (1979). Graham and Powell experimented on Grt + Hbl + Cpx samples from both Barrovian-type Dalradian

garnet amphibolites as well as the Pelona Schist in California. The authors found that their calibration of Fe-Mg partitioning between garnet and hornblende agreed well with the results of Ellis and Green's (1979) Grt-Cpx thermometer on the same rocks. The authors note that their thermometer is primarily applicable below 850 °C and using Mn-poor garnets with a wide variety of hornblende compositions. Furthermore, it is highly applicable to mafic gneisses where thermometry with aluminous pelitic assemblages is not possible, as in the Pelona Schist. The expression for this thermometer is:

$$T(K) = \frac{2880 + 3280 X_{Ca,g}}{\ln K_D + 2.426} \quad (4)$$

where $K_D = \frac{X_{Fe,Grt} / X_{Mg,Grt}}{X_{Fe,Hbl} / X_{Mg,Hbl}}$

Perchuk et al. (1985)

Perchuk et al.'s (1985) garnet-hornblende calibration produced the following thermometer:

$$T(K) = \frac{3300}{\ln K_D + 2.333} \quad (5)$$

4.3.3 Metamorphic temperature results

Geothermometry results for Lonewolf Nunataks clast samples are listed below in Table 7. Multiple geothermometric calculations were completed for each sample, and the table below summarizes the most reasonable results of those calculations. All results in Table 7 are simple averages of results of all calibrations for that particular pair. A complete list of all geothermometry calculations is given in Appendix C. Temperature

results for all samples are plotted in Figure 18. All temperatures were generated based on an input pressure of 5 kbar in Spear and Kohn's (2006) GTB program. Temperature results would not change appreciably (within the thermometers' margins of error) for higher pressure inputs.

Table 7. Geothermometry results for moraine samples collected from Lonewolf Nunataks A and B.

Sample	T (°C) Garnet core	T (°C) Garnet rim
10LWA-1.3	480 (GB)	595 (GB)
10LWA-2.2	**575** (GB) 530 (GB)	**650** / 625 / 670 (GB) 575 (GB)
10LWA-2.3	**805** (GB) 795 (GH)	**785** (GB) 780 (GH)
10LWB-1.1	**700** (GB) 675 (GH)	**745** (GH) / **740** (GB) 595 (GH)
10LWB-1.2	**725** / 600 (GB)	**575** / 730 (GB)
10LWB-1.3	660 / 645 / 675 (GB) **735** / 730 / 735 (GB)	560 / 575 (GB) 610 / **535** / 645 (GB)
10LWB-1.5	**615** / 600 (GB) 580 / 555 (GB)	795 (GB) 625 / **595** (GB)
10LWB-1.6	730 / 780 **/ 760** / **760** (GB)	530 / 595 / 565 / **570** (GB) 725 / 725 / 700
10LWB-2.6	**715** (GH) 725 / 715 (GH)	650 (GH) 690 / **715** (GH)
10LWB-6.1	745 (GH) 655 **/ 595** / 705 (GH)	740 / 730 (GH) **660** / 690 / 695 (GH)
10LWB-6.2	525 / 530 / **525** (GH) 610 / 600 / 520 (GH)	580 / 580 / 595 (GH) **585** / 570 / 585 (GH)
10LWB-6.3	625 /650 / 610 / **630** (GH) 655 (GH)	640 / 595 / **615**/ 660 (GH) 605 / 620 (GH)
10LWB-6.4	**570** / 670 (GB) 705/ **710*** (GB)	670 (GB) 645 / 650 / 675 (GB)

Notes: All temperatures are rounded to the nearest 5 °C. In general, uncertainty associated with the GB thermometer is ± 50°C. Data are from GB and GH geothermometers. Each line of numerical data represents measurements associated with one individual garnet within a sample, except for sample 10LWB-1.6, where the second line of temperatures in the rim column actually indicate temperatures partway between the core and rim of the garnet, representing prograde metamorphism. Temperatures are averages of four calibrations for GB thermometry and two calibrations for GH thermometry, calculated at an assumed pressure of 5 kbar. Temperatures shown in bold font were determined to be the most reliable where more than one choice was geologically reasonable. A complete list of all temperature calculations, even those values not considered valid for thermometry analysis, is included in Appendix C. *garnet core and biotite rim best represent T_{max}.

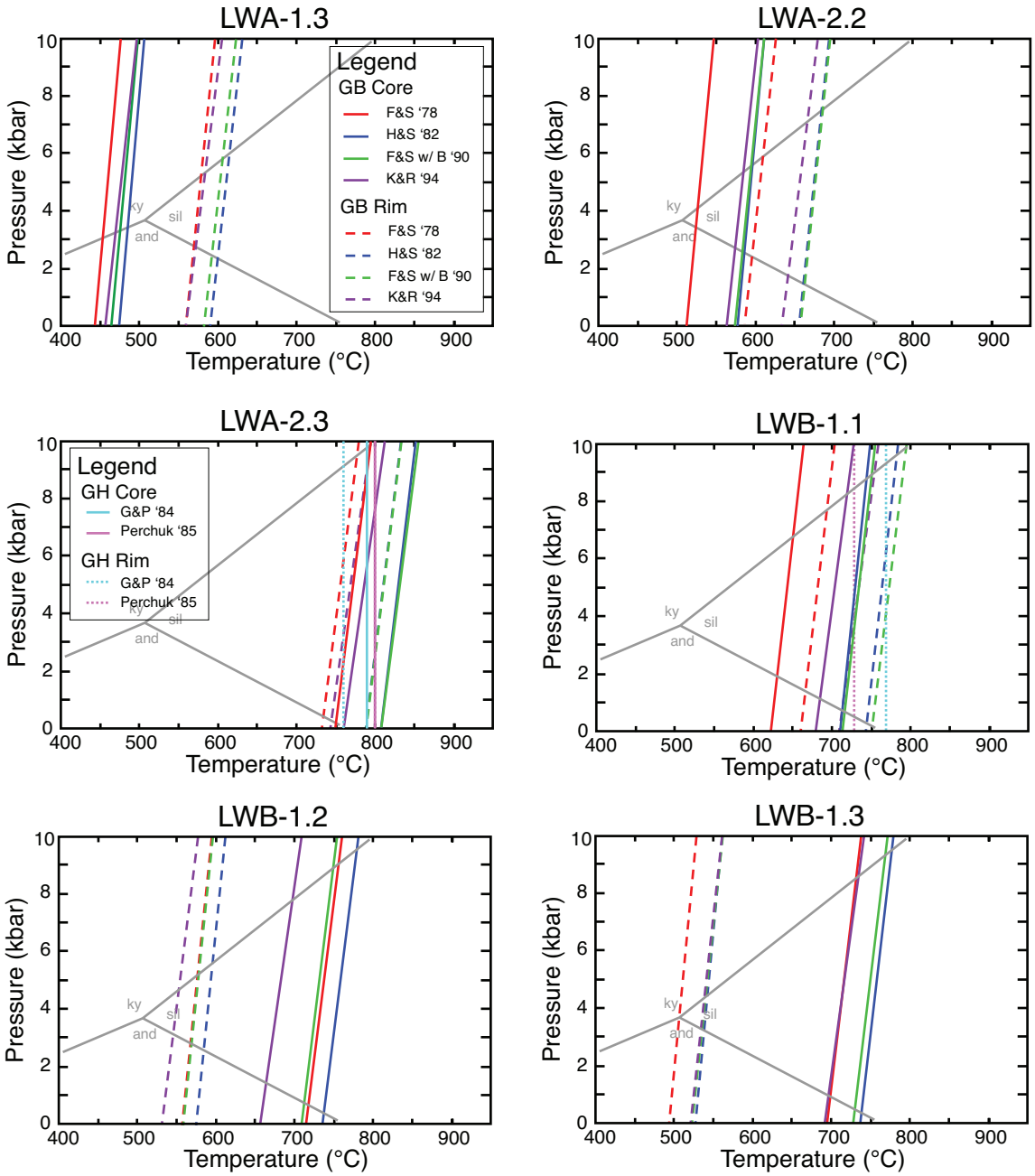

Figure 18. *P-T* diagrams of temperatures obtained by GB and GH thermometry using core and rim compositions of garnet in different samples. For GB thermometry, F&S '78 = Ferry and Spear (1978); H&S '82 = Hodges and Spear (1982); F&S w/ B '90 = Ferry and Spear with Berman (1990) garnet model; K&R '94 = Kleeman and Reinhardt (1994). For GH thermometry, G&P '84 = Graham and Powell (1984); Perchuk '85 = Perchuk et al. (1985).

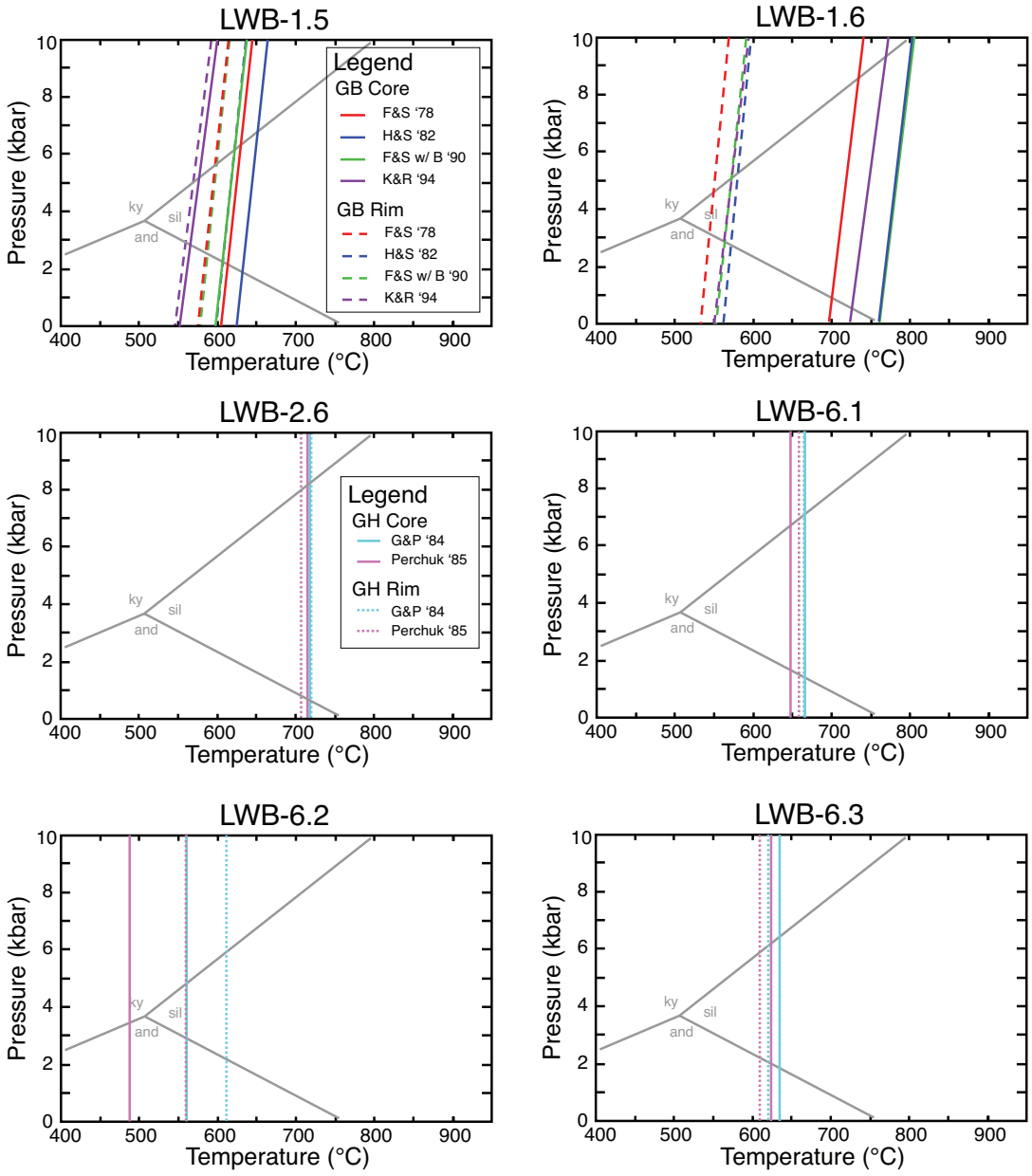

Figure 18 (continued). *P-T* diagrams of temperatures obtained by GB and GH thermometry using core and rim compositions of garnet in different samples. For GB thermometry, F&S '78 = Ferry and Spear (1978); H&S '82 = Hodges and Spear (1982); F&S w/ B '90 = Ferry and Spear with Berman (1990) garnet model; K&R '94 = Kleeman and Reinhardt (1994). For GH thermometry, G&P '84 = Graham and Powell (1984); Perchuk '85 = Perchuk et al. (1985).

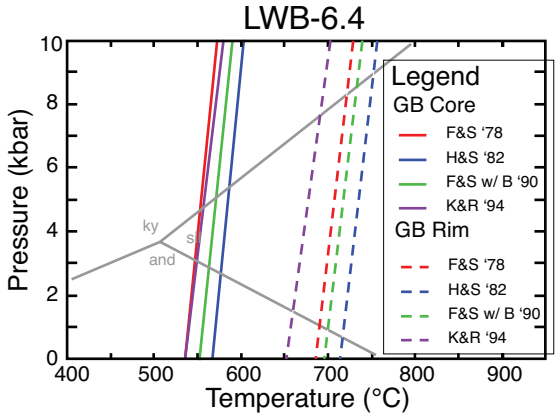

Figure 18 (continued). *P-T* diagrams of temperatures obtained by GB and GH thermometry using core and rim compositions of garnet in different samples. For GB thermometry, F&S '78 = Ferry and Spear (1978); H&S '82 = Hodges and Spear (1982); F&S w/ B '90 = Ferry and Spear with Berman (1990) garnet model; K&R '94 = Kleeman and Reinhardt (1994). For GH thermometry, G&P '84 = Graham and Powell (1984); Perchuk '85 = Perchuk et al. (1985).

Care was taken in analysis of geothermometry data discussed below to choose appropriate sites for temperature measurement based on the abundance of biotite or amphibole in comparison to garnet in each sample (as discussed in section 4.3.2.1). Results for each sample are discussed below. For clarification, the term 'adjacent' is used to refer to a grain (biotite or amphibole) that touches the rim of the garnet close to where the garnet rim measurement was taken.

In LWA-1.3, a garnet core composition and a biotite inclusion composition (Pair 1, see Appendix C) yield a temperature of ~ 480 °C. Based on the textural context, these compositions are associated with an early stage of growth, which I interpret as reflecting prograde conditions. Compositions from a garnet rim and an adjacent biotite (Pair 3) yield a temperature of ~595 °C. This sample has sparse biotite, meaning the biotite could have been preferentially affected by retrograde metamorphism. Thus, an adjacent biotite (one in contact with the garnet) was chosen to get a better representation of biotite

composition at the end of garnet growth. The close proximity of Pair 3 measurements and the general absence of evidence of retrogression in this sample make it reasonable to assume that the ~595 °C temperature is a good estimate for the end of garnet growth, or T_{max}. Thus, this sample shows an increase in temperature from the garnet core to the garnet rim, consistent with a record of prograde metamorphism.

Two different garnets within sample LWA-2.2 yield temperature results that are different from one another, but which exhibit the same trend during growth. Temperatures derived from analyses of a garnet core and a biotite inclusion are ~575 °C (pair 1) and ~530 °C (pair 5); these indicate an early stage of growth, and thus approximate a core growth temperature. Compositions of garnet rims and adjacent biotites give temperatures of ~650 °C (pair 2) and ~575 °C (pair 6), respectively. Based on textural evidence, these temperatures are taken to represent temperatures near the end of garnet growth. Pair 1 and pair 2 are from the same garnet, and pair 5 and pair 6 are from a different garnet in the same sample. Pair 1 and 2 data seem more reliable because the original crystal shape of the garnet remains intact, while the garnet associated with the pair 5 and pair 6 data has ragged edges and no idiomorphic crystal shape, meaning that the 'rim' of the garnet from which the measurement was taken is probably not the original growth rim of the garnet but rather the rim left after some dissolution occurred. Even the final temperature for pair 6 may not be representative of the true closure temperature, as the profile of the garnet does indicate some minor retrogression in that area. The two core temperatures are within the margin of error (±50 °C for GB thermometry) of one another, and both garnets record a prograde temperature increase

from the garnet core to the rim. This indicates that the difference in temperature between the two garnets may be insignificant, and that both garnets record a prograde metamorphic history reflecting a temperature increase of about ~50-70 °C.

In sample LWA-2.3, garnet core and a matrix biotite composition yield a temperature of ~805 °C (pair 2), which can be interpreted to represent the conditions at the beginning of garnet growth. When the composition of this garnet's rim is compared with the same matrix biotite, it yields a temperature of ~785 °C (pair 1). For a second garnet, a core composition paired with a matrix hornblende composition gives a temperature of 795 °C (pair 5), while a rim composition from the garnet paired with the same matrix hornblende yields temperatures of 780 °C (pair 3) and 640 °C (pair 4). Based on textural evidence, the temperatures obtained by using garnet core measurements with matrix minerals can be taken to represent the conditions at the beginning of garnet growth. Likewise, the temperatures produced from compositions of garnet rims and matrix minerals represent the temperature near the end garnet growth. The anomalously low 640 °C rim temperature corresponds with the end of the garnet profile that shows retrograde metamorphism, so it is not considered to be a reliable indicator of T_{max}. Excluding pair 4, the remaining GB temperatures are within error of each other and give an average of about 790 °C; I consider this to be the best estimate of peak metamorphic temperature in this sample as recorded by Grt-Bt thermometry. Both GB and GH data indicate high temperatures of up to ~800 °C using the compositions of garnet cores. Rim temperatures are slightly lower than core temperatures; however, because they are still within the margin of error of the core temperatures, no significant conclusions can be

drawn. Most likely, the garnets were re-homogenized at such high temperatures that the profiles are relatively flat. Interestingly, the temperature results from two different garnets are remarkably consistent, even though one garnet was analyzed with GB thermometry and the other with GH thermometry. This provides a measure of confidence that the thermometry results obtained from these samples are meaningful.

In LWB-1.1, the temperatures which best approximate conditions at the beginning of garnet growth are determined from compositions of two different garnet cores, one compared with matrix biotite and another with matrix amphibole (neither garnet contained useful inclusions, so matrix biotite and amphibole were used). The garnet-biotite pair yielded a temperature of ~ 700 °C (pair 4) and the garnet-hornblende pair gave a temperature of ~675 °C (pair 7), both of which are within the margin of error for GB thermometry. Plausible rim temperatures (based on garnet profiles that do not show obvious retrogression) use both GB and GH thermometry. Rim compositions from two different garnets are compared with both matrix and adjacent biotite and hornblende to obtain temperatures. Resultant temperatures range from ~595 °C (pair 8, garnet rim/adjacent hornblende) in one garnet to ~745 °C and ~740 °C (pair 1 – garnet rim, adjacent hornblende, and pair 3 - garnet rim/matrix biotite). The temperatures of ~740-745 °C give the better estimate of T_{max} because other garnet rim locations with evidence of retrogression in their compositional profiles give lower temperatures similar to ~595 °C, such that the pair 8 temperature of 595 °C appears suspect. This sample indicates a possible ~40-70 °C prograde temperature increase during metamorphism from core to

rim, although the lower end of this range is within the margins of error of the thermometers, so that conclusion is not firm.

LWB-1.2 temperatures representing early stage garnet growth vary widely (~725 °C from pair 1, where a garnet core composition was used with an adjacent biotite vs. ~600 °C from pair 2, where the same garnet core composition was used with a different adjacent biotite), depending on which biotite is selected. In all cases, matrix biotites from adjacent to the garnet rims were used because there are no visible inclusions within garnet. The ~725 °C temperature seems more reasonable because the flat garnet profile indicates that this is a high-T garnet. Two different garnet rim compositions used with an adjacent biotite composition produce temperatures of ~575°C (pair 3) and ~730 °C (pair 6). The composition of the garnet rim used in pair 6 has effectively the same composition and gives a very similar temperature (~730 °C) to that produced by the garnet's core composition. Thus, pair 6 essentially duplicates a T_{max} measurement, so pair 3 is a better representation of the conditions at the close of garnet growth. However, garnet profiles indicate extensive retrogression for the composition used in pair 3, which gives a temperature of ~575 °C. While this temperature does not represent the temperature when the garnet stopped growing, it does represent the temperature experienced by this sample during the period of retrogressive exchange.

The two garnets analyzed in LWB-1.3 both show flat compositional profiles but have significant temperature discrepancies. In one garnet, compositions of the garnet core compared with matrix biotites consistently give core temperatures (texturally indicative of time of garnet growth initiation) of ~645-670 °C (pairs 3-5). Garnet rims and adjacent

biotites from the same garnet produce reasonable estimates of temperature at the final stages of garnet growth of ~560-575 °C (pairs 1 and 2). The compositions of garnet cores used with compositions of adjacent biotites in a second garnet give temperatures of ~735 °C (pairs 6-8), which reasonably represent conditions at the time of initial garnet growth. Compositions of garnet rims compared with adjacent biotites in this same second garnet give temperatures of between 535 °C and 645 °C (pairs 9-11), which again can be taken to reasonably approximate conditions at the close of garnet growth. Thus both garnets show histories of cooling during garnet growth, but the discrepancy in core temperatures in the two garnets is at least ~90 °C and at the rims is up to ~70 °C. Core temperatures from the second garnet seem to be more reliable because the profile from that garnet is much more uniform throughout and the core compositions were measured very close to the center of the garnet, as opposed to the first garnet in which data from the core were collected about halfway between the core and the rim due to inclusions of quartz at the core. Thus, a core temperature of ~735 °C is reasonable for this sample. Based on the quality of garnet-biotite pairs in the same garnet, a rim temperature of ~535 °C is the most reasonable. This rim temperature also agrees within a margin of error with rim temperatures obtained from the first garnet of ~560 °C and ~575 °C. It is likely that this sample reached temperatures as high as ~735 °C, which caused re-homogenization of garnets that resulted in their flat profiles. The sample then likely underwent substantial retrograde metamorphism of as much as ~200 °C lower temperature.

Garnet profiles in LWB-1.5 are almost entirely flat, with indications of minimal retrogression at the rims on one profile. Temperatures obtained from garnet cores coupled

with biotite inclusions vary from ~555 °C (pair 10) to ~615 °C (pair 1). Despite the fact that these core/inclusion pairs are not at the center of the garnet, they are more reliable indicators of temperature at the beginning of garnet formation than garnet core compositions compared to matrix biotite (pairs 3-4, 11-13) because there is so little biotite in this sample that the matrix biotite might reflect a composition that has been altered by retrograde metamorphism or has recorded later stage prograde metamorphism rather than representing a true composition at the time of early garnet growth. However, neither of these 'core' temperatures may be a true representation of the conditions when the garnet began forming, because these pairs are not directly in the center of the current remnant garnets, and it is not possible to determine whether they were near the core of the original garnet as it was forming. Comparing the temperature of a garnet rim with a matrix biotite in a garnet-dominant rock may not be as reliable for determining temperature during the last stage of garnet growth, so the rim temperature used comes from data collected where garnet and biotite are in direct contact with one another (pair 16), giving a temperature of ~595 °C. No prograde or retrograde history is really resolvable in this sample because the uncertainties associated with this thermometer are more than twice the difference in temperatures calculated, and because the two differing 'core' temperatures bracket the rim temperature either higher or lower. The best estimate for this sample is to say that at some point it likely reached a temperature of ~595 °C.

In LWB-1.6, temperatures representative of conditions at the time of garnet formation (calculated from garnet core and biotites at the garnet rim) are ~730 °C, ~780 °C, and 760 °C (pairs 1, 2, and 6), and (from a garnet core with a matrix biotite) ~760

°C. Rim temperatures, or those assumed to be near the end of garnet growth, are calculated from garnet compositions at the rim and adjacent or matrix biotite. These temperatures are ~ 530 °C, ~595 °C, ~565 °C, and ~570 °C (pairs 3, 4, 5, and 8, respectively), depending upon which biotite is used. Temperatures that record prograde growth are calculated from garnet compositions between the core and rim of the garnet and various biotites. These prograde temperatures are ~725 °C, ~ 725 °C, and ~700 °C (pairs 9-11). These temperatures show a clear decrease from the core to the rim. This cooling is interpreted to have occurred during garnet growth because the garnet profile has a rounded shape from core to rim which indicates prograde growth, as opposed to a flat profile with curved 'tails' at the ends that are more consistent with retrogressive re-equilibration at the rim.

In LWB-2.6, all core temperatures from two garnets (determined from garnet core and matrix amphibole compositions) cluster between ~715 °C (pairs 1 and 4) and 725 °C (pair 3). Temperatures approximating final stages of garnet growth in one garnet are as low as ~650 °C (pair 2, from a garnet rim composition and an adjacent hornblende) but final temperatures from the other garnet (as measured from garnet rim compositions and matrix hornblendes) are ~690 °C (pair 5) and ~715 °C (pair 6). The ~650 °C rim data may not be representative of T_{max} because there appears to be some retrograde effect at that end of the garnet profile. The other two rim temperatures are approximately the same as the core temperatures (although the ~690 °C rim may have been affected slightly by retrograde metamorphism). The fact that the core and rim temperatures are very similar

indicates that these garnets were likely re-homogenized at high temperatures, resulting in flat garnet profiles.

Two garnets analyzed in LWB-6.1 record similar temperature trends but calculated temperatures that differ by ~ 50-75 °C from one another. The garnet with a very well preserved crystal shape and amphibole inclusions was chosen as the more reliable of the two garnets. One temperature estimate approximating conditions at the beginning of garnet formation is the ~ 655 °C temperature obtained from a garnet composition and an immediately adjacent amphibole inclusion (pair 4); however, this pair was far from the core. Another garnet core measurement and hornblende inclusion closer to the actual core of the garnet gave a temperature of ~ 595 °C (pair 5). A garnet rim and an adjacent hornblende gave a temperature of ~660 °C (pair 7). Garnet rims and a matrix hornblende gave temperatures of ~685 °C (pair 8) to ~695 °C (pair 9). The most reliable representation of temperature at the end of garnet growth is pair 7, a garnet rim and a hornblende touching that rim, which gave a temperature of ~660 °C (pair 7). This sample does exhibit a ~60 °C temperature increase from core to rim, indicating prograde growth.

Core temperatures in LWB-6.2 are almost all between ~520 °C and ~530 °C (including pairs 1-3, garnet core and hornblende touching the rim; pair 9, garnet core and matrix hornblende), with the exception of two garnet compositions and adjacent hornblende inclusions that record a temperature of ~600 °C (pairs 7 and 8). This higher temperature could be because this inclusion and its corresponding garnet measurement were actually about halfway between the true core of the garnet and its rim, so this pair may have recorded higher-T prograde conditions. Temperatures representative of final

garnet growth yielded temperatures that all fall between ~570 °C and ~595 °C (pairs 4-6, garnet rims and adjacent hornblendes; 10-12, garnet rims and adjacent or matrix hornblendes), demonstrating that temperature increased as the garnets grew. The rim temperatures probably do not represent peak temperatures because remnant rims of all garnets in the sample appear to have been replaced by quartz and plagioclase, likely erasing the garnets' initial rims. It is possible that the garnet actually reached higher temperatures that are no longer recorded by the existing rims. This possibility is supported by the temperatures of ~600 °C (pairs 7 and 8) given by an inclusion between the garnet rim and the garnet core, where retrograde metamorphism and dissolution may not have had an effect.

LWB-6.3 underwent significant retrogression, as shown by chlorite and epidote that partially replace garnets in one layer. Garnet profiles are very flat but also show retrogressive tails at the edges. Temperatures representative of conditions at the time of initiation of garnet growth were all determined from the compositions of garnet cores and amphiboles at garnet rims. Scatter among core temperatures ranges from ~610 °C to ~655 °C (pairs 1-4, 10), depending upon which amphibole is used, and after omitting an anomalously high outlier temperature (pair 9). A simple average of the remaining core temperatures is ~634 °C. Rim temperatures were all calculated from garnet rims and adjacent amphibole compositions. Again, depending upon the amphibole used, temperatures vary from 595 °C to 655 °C (pair 5-8, 11), omitting the amphibole that produced the anomalously high temperature in the core calculations. A simple average of these temperatures is ~625 °C. Thus, this rock likely reached a peak temperature of at

least ~635 °C. We know it experienced retrograde metamorphism because of the mineralogy, but temperatures can't resolve this because of the large errors associated with this type of thermometry. Plotted temperatures shown in Figure 18 are from garnet-amphibole pairs that most closely matched the calculated average temperatures (pair 4 and 12).

In LWB-6.4, three garnet core compositions from two different garnets together with the compositions of biotites analyzed near garnet rims (pairs 2, 4, and 5) gave temperatures of ~670 °C to ~710 °C. However, a garnet core composition and a biotite inclusion (which is more reliable as an indicator of temperature at the beginning of garnet growth) had a significantly lower temperature of ~570 °C (pair 1). Temperatures at garnet rims determined by garnet rim compositions and biotites touching the rim from both garnets ranged from ~645 °C to ~675 °C (pair 3, pair 6-8), however garnet profiles indicate possible retrograde metamorphism affecting the areas of the garnet rims involved in these calculations, and the effect may be even more intense given the higher relative abundance of biotite as compared to garnet. T_{max} is actually better represented by the garnet core/biotite rim pairings, which give temperatures as high as ~710 °C (pair 5). This shows that the garnets recorded an increase in temperature of as much as ~140 °C during growth, and then were later affected by retrograde metamorphism.

To summarize, 13 garnet-bearing samples from Lonewolf Nunataks had mineralogy suitable for geothermometry. Temperatures varied significantly from sample to sample, though the entire rock suite is interpreted to represent high-temperature metamorphism. Six samples record a prograde metamorphic history in the form of an

increase in temperature from the beginning to the end of garnet growth. Four samples appear to have been re-homogenized at a very high temperature, so show no temperature variation in their composition from garnet cores to rims. Many samples showed textural and/or mineralogical indications of retrogression, but two recorded this retrogression and/or cooling in their compositions.

4.3.4 Metamorphic pressure results

The lack of pelitic metamorphic assemblages in Lonewolf Nunataks clasts hindered the opportunity for application of the well-calibrated GASP barometer. The GASP barometer was used on only one garnet-bearing sample (LWB-1.2), which contained kyanite. The GASP barometer is based on the pressure-dependent breakdown of anorthite to grossular-rich garnet, aluminum-silicate (kyanite, sillimanite, or andalusite), and quartz, by the reaction:

$$Ca_3Al_2Si_3O_{12} + 2\ Al_2SiO_5 + SiO_2 = 3\ CaAl_2Si_2O_8 \qquad (6)$$

garnet + Al-silicate + quartz = plagioclase

The GASP pressure was calculated here with Spear and Kohn's (2006) GTB program. Of the five calibrations incorporated in GTB (Newton & Haselton, 1981; Hodges & Spear, 1982; Ganguly & Saxena, 1984; Hodges & Crowley, 1985; and Koziol, 1989), only one (Koziol, 1989) produced plausible results. When combined with the independently determined temperature data for this sample, only the pressures given by Koziol's (1989) calibration plotted in the kyanite stability field; the others plotted in the sillimanite field. Given the presence of kyanite in this sample, Koziol's calibration is the best fit.

Table 8. Pressure results from GASP barometry calculated by GTB.

		N&H '81	***H&S '82***	***G&S '84***	***H&C '85***	***K '89***
	Temp °C	Pressure (kbar)				
Pair 1	700 °C	7.0	6.3	7.5	7.2	8.1
	750 °C	7.9	6.9	8.2	8.0	9.1
Pair 2	700 °C	7.0	6.2	7.5	7.2	8.1
	750 °C	7.9	6.9	8.2	8.0	9.1
Pair 3	700 °C	7.0	6.2	7.5	7.2	8.1
	750 °C	7.9	6.9	8.1	8.0	9.0
Pair 4	700 °C	7.0	6.2	7.4	7.2	8.1
	750 °C	7.9	6.9	8.1	8.0	9.0
Pair 5	700 °C	7.1	6.4	7.6	7.3	8.3
	750 °C	8.1	7.1	8.3	8.1	9.2

*N&H '81 = Newton & Haselton, 1981. H&S '82 = Hodges & Spear, 1982. G&S '84 = Ganguly and Saxena, 1984. H&C, 85 = Hodges and Crowley, 1985. K' 89 = Koziol, 1989.

The pressure results from all five calibrations are listed in Table 8. The Koziol (1989) barometer produced results of ~8-9 kbar pressure for this sample. It is important to note that Pair 5 was calculated from the core composition of both a garnet and plagioclase, while pairs 1-4 were calculated from rim compositions. Calculated pressures for the core compositions seem to be ~150-200 bars higher than pressures indicated by the rim compositions. This may suggest that the rock underwent partial decompression as the crystals grew. The ~8-9 kbar pressure calculated for this sample is reflected in Figure 20, which shows a *P-T* path reconstruction of all Lonewolf samples.

Semi-quantitative pressure calculations were also made using the Al content in amphibole (Ernst & Liu, 1998). Ernst and Liu synthesized new calcic amphiboles from a natural MORB (mid-ocean ridge basalt) starting material over a temperature range of 650 °C to 950 °C at 0.8 to 2.2 GPa (8-22 kbar). Their results are of particular interest for this study because of the highly calcic nature of the amphiboles, as well as the temperature

range over which their experiments were conducted, which were similar to the metamorphic conditions found for these samples from geothermometry. Ernst and Liu found that in the presence of Al and Ti-rich phases, Ca-amphibole changes from sodic-calcic to calcic composition with increasing temperature. Of particular interest here, Al_2O_3 content increases with both *P* and *T*. Thus, I was able to use the Al_2O_3 content of several samples to reasonably approximate pressures. Figure 19 shows the estimated pressure of six Lonewolf samples based on Ernst and Liu's determination of the Al dependence on pressure. Approximate values of pressure are listed in Table 9. These semi-quantitative pressures are reflected in the *P-T* paths shown in Figure 20.

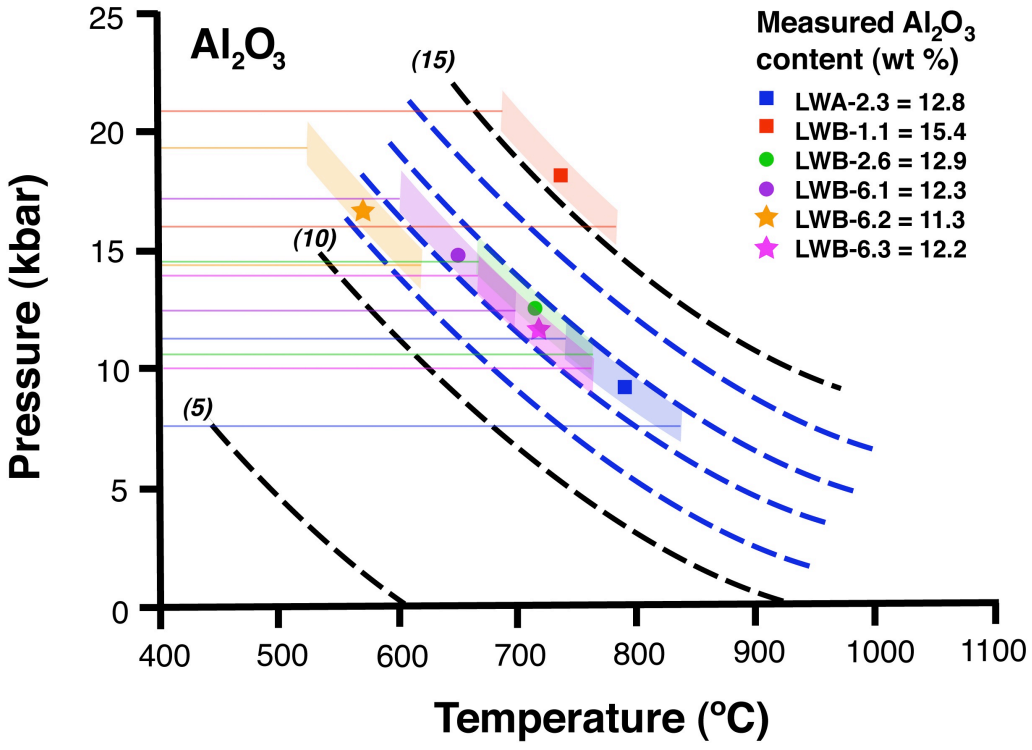

Figure 19. Isopleths of Al_2O_3 in calcic amphibole as a function of pressure and temperature (from Ernst & Liu, 1998), with samples from Lonewolf Nunataks plotted on the basis of GH thermometry and Al_2O_3 content. Shaded boxes represent potential error margin for pressure as a function of input temperature. Error associated with this barometry method was not stated in the original source.

Table 9. Estimated metamorphic pressure based on Al_2O_3 content in calcic amphibole combined with temperatures derived from GH thermometry.

Sample No.	Estimated metamorphic pressure (kbar)
LWA-2.3	~10
LWB-1.1	~19
LWB-2.6	~12.5
LWB-6.1	~15
LWB-6.2	~17.5
LWB-6.3	~12

Semi-quantitative metamorphic pressures obtained for each moraine sample from Lonewolf Nunataks sites A and B are listed in Table 9.

4.3.5 *P-T* paths

Figure 20 shows estimated prograde and retrograde *P-T* paths for all analyzed rocks in this study based on metamorphic temperature and pressure estimates presented above. To summarize, the LWA and LWB metamorphic rocks show indications of consistently high pressure, on the order of 8-19 kbar, in cases for which pressure could be estimated. High pressures documented by geothermobarometry are consistent with the presence of tschermakite in mafic samples (LWA-2.3, LWB-1.1, LWB-2.6, LWB-6.1, LWB-6.2, and LWB-6.3), as well as meionitic scapolites (LWA-2.2, LWB-1.4, and LWB-2.6) and kyanite (LWB-1.2). For the seven evaluated samples, high- to very-high pressure/medium-high temperature results are consistent with conditions that might be expected in plate-convergent tectonic regimes. Only one sample, LWB-6.2, has a geothermal gradient of ~10 °C/km consistent with that of a subduction zone where

pressures are very high but temperatures are suppressed due to subduction of a cold slab. In the absence of other evidence of subduction in this suite (for example, lithologies such as blueschists and eclogites), inferring a subduction zone setting is poorly founded. A collisional belt setting is much more compatible with *P-T* conditions in the remainder of samples, and is a better place to find such highly metamorphosed rocks as the Lonewolf clasts. Additionally, most subduction zone rocks are oceanic, and as a whole the Lonewolf suite is volumetrically felsic. LWB-1.1, LWB-2.6, LWB-6.2, and LWB-6.3 all have geothermal gradients of ~13-20 °C/km and LWA-2.3 and LWB-1.2 have geothermal gradients of ~ 25 °C/km – typical of stable continental crust and certainly of Barrovian orogenic belts. Evidence of metamorphism at great depth combined with geothermal gradients consistent with orogenic belts indicate that it is possible most of the samples are indicative of deep to very deep crust associated with various depths achieved during collision/orogenesis. A tectonic setting cannot be reliably inferred for the remaining rocks for which there are no independent pressure estimates.

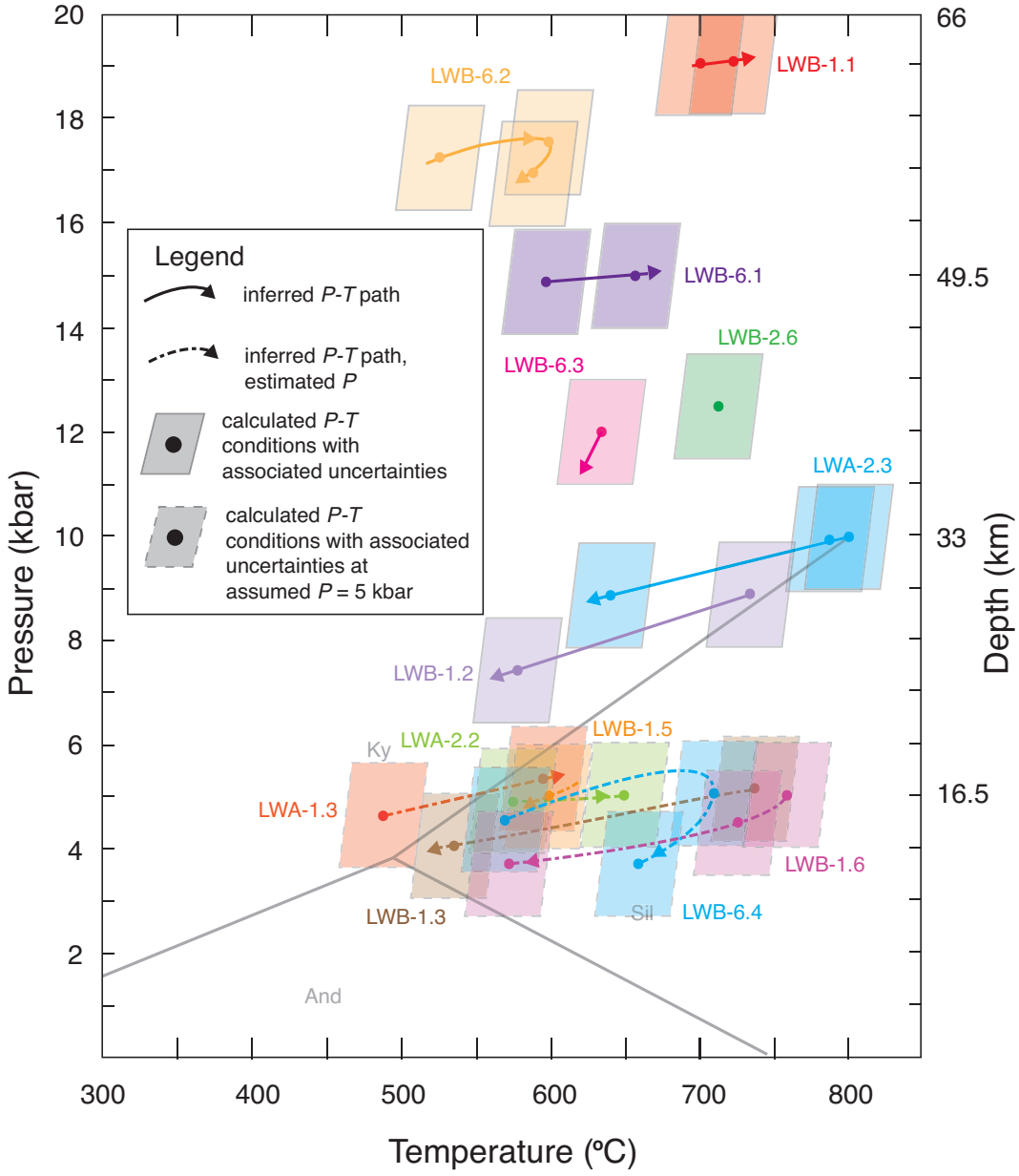

Figure 20. Inferred pressure-temperature paths of garnet-bearing metamorphic samples from Lonewolf Nunataks, interpreted from thermobarometric constraints, mineral compositional zoning, and petrographic evidence. All temperatures reflected in these paths were calculated assuming a pressure of 5 kbar, as described above. Paths with solid lines indicate samples where pressure was calculated either with GASP barometry or semi-quantitatively with the Al-in-Hbl method, as described above. Pressures for paths with dashed lines were not calculated due to lack of appropriate mineralogy. Instead, all samples with no pressure calculations are shown at a pressure of about 5 kbar, which was assumed as a default value. Approximate depth given based on ~1 kbar = 3.3 km.

5. DISCUSSION

Glacially transported metamorphic clasts from the Byrd Glacier drainage collected at Lonewolf Nunataks provide samples of basement material eroded from rocks of the East Antarctic shield (EAS). Fifty-two metamorphic samples were analyzed via optical petrography and were classified as either: (a) felsic gneiss (both garnetiferous and garnet-free types); (b) mafic gneiss and amphibolite (both garnetiferous and garnet-free types); or (c) schist. Among garnetiferous samples, 13 were suitable for subsequent geochemical study and application of geothermobarometers, as described in the Results section above. Important implications of these findings are discussed below.

5.1. Lonewolf clasts as samples of the Mawson Continent

As discussed earlier, East Antarctica and southern Australia have a well-established paleogeographic connection across the southern ocean that dates to the Paleoproterozoic, long prior to assembly of Rodinia. The two cratons once formed the so-called Mawson Continent, which primarily includes the Gawler craton (Australia), Terre Adélie craton (Wilkes Land, Antarctica), and Miller Range area (Antarctica) (Fig. 20), which amalgamated at ~1.7 Ga (Boger, 2011). Smaller entities, such as the Coompana Block and Curnumona Province, were added later between ~1.6-1.55 Ga (Payne et al., 2009). Bedrock correlations between the Nimrod Group in the TAM and rocks from the Terre Adélie and Gawler cratons, suggest that much of the bedrock underlying the Byrd Glacier drainage correlates with bedrock in southern Australia (see Fig. 2) as a part of the Mawson Continent. Results from the present study are compared with previous work to

evaluate the connection of Lonewolf Nunataks samples to those from the Mawson Continent.

5.1.1 Correlation with southern Australia geology

Substantial evidence indicates that the Gawler craton in southern Australia was contiguous with the Terre Adélie region of East Antarctica during the Proterozoic, similar to the reconstruction shown in Figure 21. If this reconstruction is a plausible representation of the Proterozoic paleogeographic fit of East Antarctica and Australia, and assuming that these Proterozoic crustal provinces extend well into East Antarctica, rocks from a large portion of the source area underlying the Byrd Glacier drainage should be similar to what are found in the Gawler and Terre Adélie cratons.

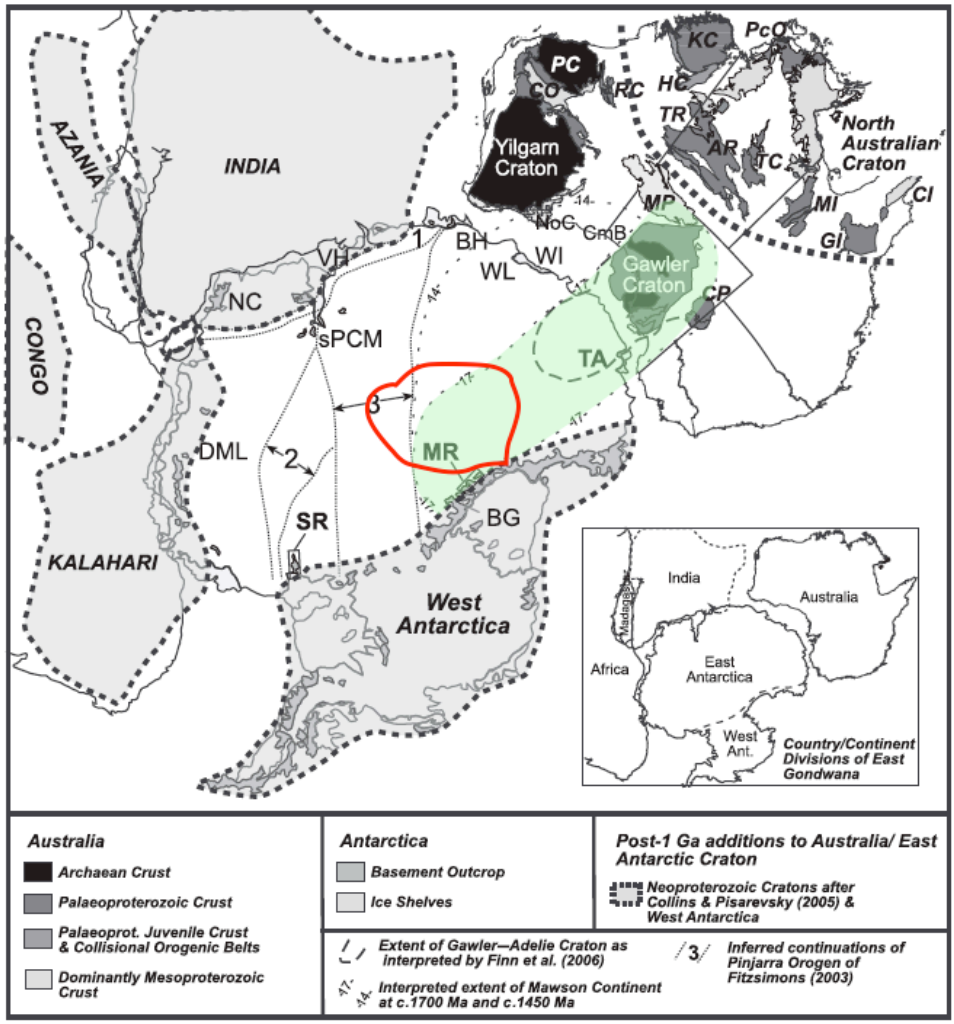

Figure 21. Reconstruction summarizing paleogeographic linkages between East Antarctica, Australia, India, and southern Africa in the Proterozoic. Modified from Payne et al. (2009). The green shaded area is the proposed Mawson Continent containing the combined Terre-Adélie/Gawler cratons (after Fanning et al., 1995). The red line outlines the boundary of the Byrd Glacier drainage (Rignot &Thomas, 2002). Note that the Byrd Glacier drainage overlaps with much of what is thought to be the Mawson Continent as it continues into Antarctica. East Antarctica terranes are: BG, Beardmore Glacier; BH, Bunger Hills; DML, Dronning Maud Land; NC, Napier Complex; sPCM, southern Prince Charles Mountains; VH, Vestfold Hills; WI, Windmill Islands; WL, Wilkes Land. Bold abbreviations are MR, Miller Range; SR, Shackleton Range; and TA, Terre Adélie Craton. Australian terrains are: AR, Arunta Region; CI, Coen Inlier; CmB, Coompana Block; CO, Capricorn Orogen; CP, Curnamona Province; GI, Georgetown Inlier; HC, Halls Creek Orogen; KC, Kimberly Craton; MI, Mt. Isa Inlier; MP, Musgrave Province; NoC, Nornalup Complex; PC, Pilbara Craton; PcO, Pink Creek Orogen; RC, Rudall Complex; TC, Tennant Creek Region; and TR, Tanami Region.

The Gawler craton is dominated by late Archean to early Paleoproterozoic supracrustal and magmatic rocks that contain Paleo- and Mesoproterozoic intrusives (Daly et al., 1998; Fanning et al., 2007). Of particular relevance here is the pervasive metamorphic event of ~1730-1690 Ma that strongly affected the Gawler craton. Various studies have estimated the *P-T* conditions of the Kimban Orogeny as 625-650 °C/5.5-6.5 kbar to 700-750 °C/8-9 kbar in the western Gawler craton (Teasdale, 1997), to 600-675 °C/5-7 kbar to 800-850 °C/7-9 kbar in the southern Gawler craton (Parker, 1993; Ton et al., 2004). These *P-T* results for the Kimban Orogeny are somewhat consistent with *P-T* results from Lonewolf Nunataks determined in this study. All samples estimated for *P-T* show peak metamorphic temperatures greater than ~600 °C, matching minimum temperature conditions from the Gawler craton (Fig. 22). Where pressure could be estimated, two samples (LWA-2.3 and LWB-1.2) yielded pressures consistent with the estimates of Kimban metamorphism in the Gawler craton. However, pressures estimated in five samples (LWB-1.1, LWB-2.6, LWB-6.1, LWB-6.2, and LWB-6.3) are considerably higher pressure than estimates given for the Gawler craton. Lack of pressure estimates prevents correlation with any of the felsic gneisses from Lonewolf Nunataks.

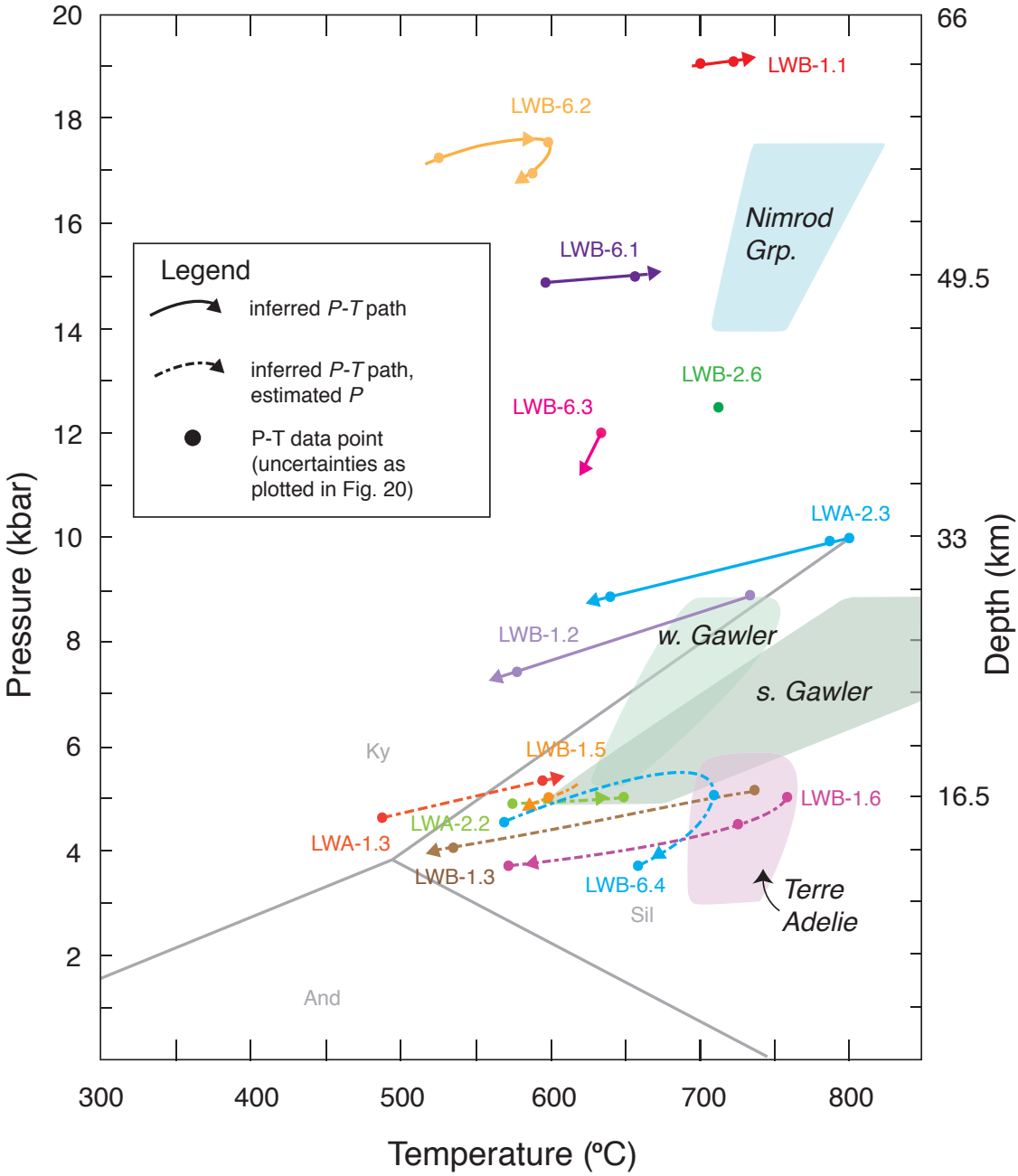

Figure 22. Inferred pressure-temperature paths of garnet-bearing metamorphic samples from Lonewolf Nunataks, interpreted from thermobarometric constraints, mineral compositional zoning, and petrographic evidence. All temperatures reflected in these paths were calculated assuming a pressure of 5 kbar, as described above. Paths with solid lines indicate samples where pressure was calculated either with GASP barometry or semi-quantitatively with the Al-in-Hbl method, as described above. Pressures for paths with dashed lines were not calculated due to lack of appropriate mineralogy. Instead, all samples with no pressure calculations are shown at a pressure of about 5 kbar, which was assumed as a default value. Uncertainties for *P-T* conditions are not displayed here but

Figure 22 caption (continued). are the same as shown in Fig. 20. Shaded polygons represent metamorphic conditions experienced by other metamorphic rock suites, included for comparison. Light green, western (Teasdale, 1997) and southern (Parker, 1993; Ton et al., 2004) Gawler craton; pink, Terre Adélie craton peak metamorphic conditions (Monnier, 1995; Monnier et al, 1995); light blue, Nimrod Group (Peacock and Goodge, 1995). Approximate depth given based on ~1 kbar = 3.3 km.

5.1.2 Comparison with Terre Adélie geology

Basement of Terre Adélie and George V Land is exposed on the coast of East Antarctica from ~140 °E to 144 °E (see Figure 3). The Terre Adélie basement is heterogeneous, with two major unrelated geologic units consisting of the Port Martin granodioritic orthogneiss and the Point Geologié aluminous metapelites (Peucat et al., 1999). The Point Geologié rocks are primarily a migmatitic and diatexitic assemblage of aluminous metapelites with minor metagreywacke, plus amphibolitized dolerites and gabbros thought to represent relict dikes and sills (Ménot, 1991; Monnier, 1995). Metamorphism of these rocks occurred during a single metamorphic episode under uniform HT-LP metamorphism, with peak conditions of 750-700 °C and 4-6 kbar (Fig. 22). No evidence of other metamorphism is recorded in these metapelites (Monnier, 1995; Monnier et al., 1995). These conditions are typical of mid-crustal levels, but elevated temperature gradient (about twice the stable continental geotherm), similar to a magmatic province or arc setting. Inherited zircon ages of 1.72-1.76 Ga, reflecting protolith modification, and geochronological evidence of metamorphism and anatexis at 1.69 Ga in sedimentary rocks from Point Geologié, leave a small ~ 40.0-70.0 Ma time interval for sediment deposition. Such a short time interval suggests a source of sediment in a subsiding volcano-sedimentary basin (Peucat et al., 1999), similar to those known in

the Gawler craton in South Australia (Daly et al., 1998). These age constraints thus indicate that metamorphism in the Terre Adélie craton was associated temporally with the Kimban Orogeny at ~1.7 Ga. The Kimban Orogeny in Australia is generally coeval with the Nimrod Orogeny discussed below, supporting a broad tectonic linkage between widely-separated cratonic units exposed on different continents.

There are both similarities and differences between the rocks from Point Geologié in Terre Adélie and the rocks collected from Lonewolf Nunataks. The pelitic compositions observed at Point Geologié are not common in the suite of metamorphic samples collected from Lonewolf Nunataks. However, with the exception of true pelitic mineralogy (i.e., Al-silicates), the similar Qtz + Pl + Kfs + Grt + Bt + Ms mineralogy is consistent with Lonewolf clast mineralogy. Other characteristics of the rocks from Point Geologié, such as heterogeneous grain sizes and foliations, are also similar to the Lonewolf clasts. Metamorphic conditions (at ~1.69 Ga) of 700-750 °C are consistent with those seen for seven Lonewolf samples (LWA-2.3, LWB-1.1, LWB-1.2, LWB-1.3, LWB-1.6, LWB-2.6, and LWB-6.4). The lack of pelitic assemblages in Lonewolf gneisses hinders reliable pressure estimations for three of these seven samples (LWB-1.3, LWB-1.6, and LWB-6.4). The remaining four samples with similar peak temperatures to those in the Terre Adélie (which are all mafic gneiss) have considerably higher pressures (8-19 kbar) than those calculated for the Terre Adélie. Thus, though some Lonewolf clasts experienced similar temperatures to those in the Terre Adélie craton, calculated pressures are different enough to rule out a definitive correlation.

To summarize this comparison of Lonewolf clasts with Terre Adélie and Gawler craton geology, the rocks of the EAS collected at Lonewolf Nunataks have some similar mineralogical and textural characteristics to those from the Terre Adélie and Gawler cratons, and some samples also experienced similar peak metamorphic temperatures. Metamorphic pressures are a more tenuous connection; several Lonewolf samples experienced pressures similar to those of the Gawler craton, but none correlate with pressures for Terre Adélie rocks. This difference in pressure might reflect different crustal levels of formation (for the same tectonic event) for the Point Geologié rocks and clasts collected at Lonewolf Nunataks. The differences between these areas could also reflect their formation in different tectonic environments, though they may still be associated with the same overall set of tectonic events.

5.2 Relationship to Nimrod Group events

Another important consideration in this study is the relationship of samples from Lonewolf Nunataks to patterns and events known from the Nimrod Group. To review from earlier discussion, the Nimrod Group experienced a significant magmatic event at ~3000 Ma followed by crustal metamorphism at 2955-2900, anatectic magmatism at ~2500 Ma, and a period of magmatism, metamorphism, and eclogite formation at 1730-1700 Ma. The Nimrod Group was then overprinted by a medium-P/T Ross-age magmatic and metamorphic event. Of particular interest here, the 1730-1720 Ma metamorphic event known as the Nimrod Orogeny in East Antarctica (coeval with the Kimban Orogeny in southern Australia) is a high-P/high-T event that formed at pressures ≥14

kbar and temperatures ≥710-760 °C (Peacock and Goodge, 1995). This pressure range is consistent with pressures obtained from samples LWB-1.1, LWB-2.6, LWB-6.1, LWB-6.2, and LWB-6.3, which all yielded pressure estimates of >12 kbar. Other samples may also record such high pressures, but mineralogy was insufficient for barometry. Furthermore, the temperature range given for the Nimrod Orogeny is similar to the ≥700 °C peak temperatures recorded in samples LWA-2.3, LWB-1.2, LWB-1.3, and LWB-1.6. Any of these samples could conceivably represent a metamorphic overprint similar to that of the Nimrod-Kimban Orogenies. However, metamorphism associated with the Ross Orogen at ~540 Ma produced upper amphibolite to lower granulite facies metamorphism at slightly lower, though still high, pressure of between 8-12 kbar. This is consistent with pressure estimates for LWB-1.2 and LWA-2.3. Finally, plagioclase rims around garnet, a textural artifact of ~1.7 Ga metamorphism in the Nimrod Group, is also present in some Lonewolf metamorphic samples.

5.3 Summary

The suite of metamorphic glacial clasts from Lonewolf Nunataks reflects the heterogeneous nature of EAS basement rocks in the Byrd Glacier drainage. High-grade gneisses found in the Lonewolf suite are lithologically similar to rock types found in the Terre Adélie craton (with the exception of pelitic metasedimentary rocks), gneisses from the Gawler Craton, and layered gneisses of the Nimrod Group. High-pressure rocks (>12 kbar) may be representative of Nimrod metamorphism that is suggestive of Paleoproterozoic crustal collision (Goodge et al., 2001). Yet other clasts exhibiting

somewhat lower pressures (8-12 kbar) may represent moderate-P amphibolite-facies metamorphism associated with either the Ross Orogeny, or with an orogenic event of older age such as the Nimrod or Kimban orogenies. Other samples for which pressure is unconstrained are of ambiguous relationship to the metamorphic terrains known elsewhere. All of the Lonewolf Nunatak samples reached peak metamorphic temperatures of at least 600 °C, consistent with both the Nimrod-Kimban orogeny and also the Ross Orogeny. It is important to note that while *P-T* results presented in this study are consistent with Nimrod-Kimban metamorphism, and while there are other strong lines of evidence supporting the presence of Mawson Continent rocks beneath the Byrd Glacier drainage (as discussed above), these results are not exclusive of connections with other cratons and metamorphic events. For example, another possibility is that the high-grade metamorphic rocks of the Lonewolf suites could be associated with Grenville-age metamorphic belts known from other parts of East Antarctica, as well as Australia and Laurentia.

Ultimately, the geochronologic and *P-T* correlation between the Gawler craton, Terre Adélie craton, and Nimrod Group suggests there is a poorly-defined but possibly continuous strip of crust underlying the central EAS (Fig. 21) that may be sampled by glacial erosion and deposition at Lonewolf Nunataks. If it is true that at least some of the metamorphic clasts from Lonewolf Nunataks are representative of ice-covered geology affiliated with the Mawson Continent, then these samples can be used as the basis for further depiction of the character of this distinctive crustal province. However, if the LW clasts do not represent conditions similar to the geology of the TAC, it may indicate that

the geology of the latter does not extend into the interior of the EAS. The *P-T* and petrologic evidence presented here indicates that some Lonewolf clasts may have similar affinities with Gawler craton, Terre Adélie craton, and Nimrod Group rocks. These results are possibly consistent with continuation of the Proterozoic Mawson Continent into the vast area of East Antarctica underlying the Byrd Glacier drainage.

5.4 Further work and geochronology

The conclusions drawn and predictions made in this study can be tested directly by geochronologic study of Lonewolf Nunataks clast samples in order to determine the ages of metamorphism. Radiometric mineral ages could help to compare clast samples with specific metamorphic events known elsewhere, in order to test petrologic correlations proposed here. Specifically, U-Pb zircon or monazite dating on these metamorphic clasts might reveal Paleoproterozoic ages that affirm a linkage with Nimrod-Kimban events known from other parts of the Mawson Continent. Such ages might reflect relicts of igneous crystallization preserved by inheritance, or metamorphic growth and/or overprinting of new zircon or monazite. The presence of Paleoproterozoic ages might indicate a relatively distal, upstream source for the clasts. In this case, the clasts might provide potentially valuable and unique information about the geology of the Gamburtsev Subglacial Mountains near the Byrd Glacier drainage divide, which to this day remain elusive and enigmatic. Alternatively, either of these minerals might yield Ross-age crystallization or overgrowth ages that indicate the clasts have a relatively proximal source near the Transantarctic Mountains. In this case, they offer the chance to compare Ross overprint events on older Proterozoic basement.

For this study I chose to study a suite of metamorphic clasts from Lonewolf Nunataks with the goal that they may reflect crustal conditions associated with metamorphism in the greater EAS. In contrast, igneous rocks are commonly advantageous in such a paleogeographic framework, because the chemical composition, isotopic composition, and crystallization ages are commonly useful tracers of magmatic affinity. Many samples in the Lonewolf metamorphic suite of this study retain a strong indication of igneous protolith sufficient to refer to them as 'orthogneiss'. However, in the absence of whole-rock geochemical data and geochronologic constraints, it is not possible as of yet to definitively associate any rocks from the Lonewolf Nunataks suite with magmatic events known from the Nimrod Group, much less with possibly coeval rocks in Laurentia. Nonetheless, the following samples clearly have igneous protoliths and may be useful for further future study (Table 10).

Table 10. Rock types among metamorphic glacial clasts at sites LWA and LWB with igneous protoliths.

Group		Sample No.	Rock name [a]
1	Felsic gneisses	LWA-2.1	Biotite-muscovite orthogneiss
		LWA-6.1	Biotite-muscovite orthogneiss
		LWA-10.1	Hornblende orthogneiss
		LWB-4.4	Biotite-muscovite orthogneiss
		LWB-4.5	Biotite orthogneiss/deformed granodiorite
		LWB-4.6	Biotite orthogneiss/deformed diorite(?)
		LWB-4.7	Biotite-muscovite orthogneiss
		LWB-4.8	Muscovite-biotite orthogneiss
		LWB-5.4	Biotite-muscovite orthogneiss
		LWB-5.7	Biotite orthogneiss
		LWB-5.8	Biotite orthogneiss
	Felsic garnet gneisses	LWB-1.5	Garnet-biotite orthogneiss
		LWB-4.3	Garnet-biotite orthogneiss
2	Amphibolites and mafic gneisses	LWB-4.1	Hornblende-biotite orthogneiss

Notes: [a] full descriptions given in Appendix A.

LWA-10.1, LWB-4.3, and LWB-4.5 have already been dated (Goodge et al., 2012) and confirm their igneous origin. LWA-10.1 yielded a zircon weighted-mean $^{207}Pb/^{206}Pb$ age of 2010 ± 3 Ma, LWB-4.3 yielded a zircon Concordia age of 1444 ± 3 Ma, and LWB-4.5 yielded an inner igneous domain of ~2020 Ma and magmatic overgrowths at ~1848 ± 13 Ma. These ages show that the crust of the EAS in the Byrd Glacier drainage is definitively underlain by Proterozoic igneous crust of ~2.0 Ga, 1.85 and 1.45 Ga age. Neither the ~2.0 Ga nor the ~1.45 Ga ages is known from basement exposure, thus providing important information about the otherwise inaccessible ice-covered geology. Dating of additional orthogneisses in this suite will also likely show Proterozoic igneous inheritance of various age populations, despite possible Ross-age igneous zircon growth.

In addition to ages from Lonewolf clasts mentioned above, other igneous clasts from the Byrd Glacier drainage which were not analyzed in this study independently reveal ~1.58, ~1.88, and ~2.0 Ga ages (Goodge et al., 2010), confirming that the Byrd Glacier drainage samples a heterogeneous Proterozoic basement. A clast from the nearby Nimrod Glacier catchment yields a ~1.06 Ga age, which is consistent with ages of the Grenville Province in Laurentia, and is indicative that Grenville-age crust is a major component of the EAS near the Ross Sea margin (Goodge et al., 2010). The Grenville-age ties to Laurentia allow for the interpretation that the older ~1.58, ~1.88, and ~2.0 Ga clasts are coeval with Yavapai-Mazatzal rocks in Laurentia, and their ~1.4 Ga intrusives. These findings are significant in their confirmation of heterogeneous Proterozoic crust beneath the Byrd Glacier drainage near the Ross Sea margin. Furthermore, these results

strengthen arguments for potential Rodinia reconstructions favoring a Laurentia-East Antarctica connection. A combination of ongoing geochronologic work with petrologic investigations on glacially transported clasts from the East Antarctic shield can help shed even more light on East Antarctica's distant past.

6. CONCLUSIONS

Ice-covered East Antarctica contains a Precambrian craton roughly the size of the conterminous U.S. and Mexico. The geology of the interior of the East Antarctic shield remains enigmatic but holds valuable information about one of Earth's major Precambrian continents. The complex assembly of the East Antarctic shield spans the Precambrian and is intricately involved in multiple formations and breakups of supercontinents. Geologic correlation between East Antarctica's geology and other Precambrian terranes is useful for understanding supercontinent reconstructions. East Antarctica's assembly also likely played a major role in the development of the East Antarctic ice sheet which currently contains 61% of the world's fresh water. A petrologic study of glacial clasts sourced from the interior EAS provides specific information about the geological past of East Antarctica.

Three lithologic groups identified from metamorphic rocks collected at the Lonewolf Nunataks include: (a) felsic gneisses, (b) mafic gneisses and amphibolites, and (c) schists. Both felsic gneisses and mafic gneisses and amphibolites include garnet-bearing and garnet-free samples. Felsic gneisses typically consist of quartz + plagioclase ± microcline + biotite ± muscovite ± garnet ± scapolite, while mafic gneiss and amphibolite assemblages are commonly quartz + plagioclase ± microcline + biotite ± muscovite ± garnet ± tschermakite ± hypersthene ± scapolite. Rocks experienced amphibolite- to granulite-facies metamorphism as shown by petrologic evidence such as the presence of garnet, Ca-amphibole, scapolite, and hypersthene in otherwise anhydrous rocks. Compositionally zoned garnets record prograde metamorphism in eight samples

and retrograde metamorphism in 12 samples; garnets in two samples record no compositional change with growth. Geothermobarometry reflects temperatures ranging from ~500 to ~800 °C, and peak temperatures of ≥ 600 °C in all samples. Lack of pelitic mineralogy hinders a pressure determination, although GASP barometry in one sample indicates pressures of 8-9 kbar. High aluminum content in tschermakites from five mafic gneisses/amphibolites yields pressures of ~10-20 kbar. Overall, the rocks record high- to very-high P/high-T conditions consistent with metamorphism at varying depths in a Barrovian metamorphic environment.

The petrology and metamorphic history of the Lonewolf metamorphic clasts are broadly similar to rocks from the Terre Adélie craton in East Antarctica, the Gawler craton in southern Australia, and the Nimrod Group in the Transantarctic Mountains. These findings, combined with U-Pb zircon dating, indicate that rock clasts of the Byrd Glacier drainage and bedrock from the Terre Adélie craton, Gawler craton, and Nimrod Group all underwent a coeval metamorphic event that could possibly, though not definitively, be associated with the ~1.7 Ga Nimrod-Kimban Orogeny. This implies that the Mawson Continent likely extends into the EAS and underlies at least part of the Byrd Glacier drainage. Differences in *P-T* conditions in rocks from all four sites can be attributed to different crustal depths and/or tectonic environments, even if associated with the same tectonic event. Igneous crystallization ages of ~1.4, ~1.58, ~1.88, and ~2.0 Ga from clasts in the same area as the clasts in this study confirm the existence of heterogeneous Proterozoic crust underlying the Byrd Glacier drainage and strengthen possible paleogeographic correlations between East Antarctica and Laurentia as part of

Rodinia. The general patterns of metamorphism observed in glacial clasts from Lonewolf Nunataks therefore may reflect a key episode in the Proterozoic crustal growth of East Antarctic and its role in assembly of the Mawson Continent.

REFERENCES

Anderson, J.L., and Cullers, R.L., 1999. Paleo- and Mesoproterozoic granite plutonism of Colorado and Wyoming. Rocky Mountain Geology, vol. 34, no.2, pp. 149-164.

Anderson, J.L., and Morrison, J, 2005. Ilmenite, magnetite, and peraluminous Mesoproterozoic anorogenic granites of Laurentia and Baltica. Lithos, vol. 80, pp. 45-60.

Bamber, J.L., Baughan, D.G., and Joughin, I., 2000. Widespread Complex Flow in the Interior of the Antarctic Ice Sheet. Science, vol. 287, no. 5456, pp. 1248-1250.

Berman, R.G., 1990. Mixing properties of Ca-Mg-Fe-Mn garnets. American Mineralogist, vol. 75, pp. 328-344.

Bennett V.C., and DePaolo, D.J., 1987. Proterozoic crustal history of the western United States as determined by neodymium isotopic mapping. Geological Society of America Bulletin, v. 99, p. 674-685

Berry, R.F., Holm, O.H., and Steele, D.A., 2005. Chemical U-Th-Pb monazite dating and the Proterozoic history of King Island, southeast Australia. Australian Journal of Earth Sciences, vol. 52, pp. 461-471.

Borg, S.G., DePaolo, D.J., Smith, B.M., 1990. Isotopic Structure and Tectonics of the Central Transantarctic Mountains. Journal of Geophysical Research, vol. 95, no. B5, pp. 6647-6667.

Borg, S.G., and DePaolo, D.J., 1994. Laurentia, Australia, and Antarctica as a Late Proterozoic supercontinent: Constraints from isotopic mapping. Geology, vol. 22, pp. 307-310.

Boger, S.D., 2011. Antarctica – Before and after Gondwana. Gondwana Research, vol. 19, pp. 335-371.

Bucher, K. and Frey, M., 2002. Petrogenesis of metamorphic rocks. 7th Ed. Federal Republic of Germany: Springer-Verlag: Heidelberg, Federal Republic of Germany, 2002. Print.

Brecke, D.M., 2007. Provenance of glacially transported material near Nimrod Glacier, East Antarctica: Evidence of the ice-covered East Antarctic shield. Master's thesis, University of Minnesota, Duluth.

Burrett, C., and Berry, R., 2000. Proterozoic Australia-Western United States (AUSWUS) fit between Laurentia and Australia. Geology: February 2000; vol. 28, no. 2, pp. 103-106.

Cande, S.C., Stock, J.M., Deitmar Muller, R., and Ishihara, T., 2000. Nature, vol. 404, pp. 145-150.

Cooper, A.F., Maas, R., Scott, J.M., Barber, A.J.W., 2011. Dating of volcanism and sedimentation in the Skelton Group, Transantarctic Mountains: Implications for the Rodinia-Gondwana transition in southern Victoria Land, Antarctica. GSA Bulletin; March/April 2011; vol. 123, no. 3/4, pp. 681-702.

Damaske, D., Ferraccioli, F., and Bozzo, E., 2003. Aeromagnetic anomaly investigations along the Antarctic coast between Yule Bay and Mertz Glacier. Terra Antarctica 10 (3), pp. 85-96.

Dasgupta, S., Sengupta, P., Guha, D. and Fukoka, M., 1991. A refined garnet-biotite Fe-Mg exchange geothermometer and its application in amphibolites and granulites. Contributions to Mineralogy and Petrology, 109, pp. 130-137.

Deer, W.A., Howie, R., and Zussman, J., 1992. An introduction to the Rock-Forming Minerals, 2nd ed. Longma, England.

Ellis, D.J., and Green, D.H., 1979. An experimental study of the effect of Ca upon garnet-clinopyroxene Fe-Mg exchange equilibria. Contributions to Mineralogy and Petrology, 71, pp. 13-22.

Ernst, W.G., and Liu, J., 1998. Experimental phase-equilibrium study of Al- and Ti-contents of calcic amphibole in MORB – a semiquantitative thermobarometer. American Mineralogist, vol. 83, pp. 952-969.

Fanning, C.M., Daly, S.J., Bennett, V.C., Ménot, R.P., Peucat, J.J., Oliver, R.L., and Monnier, O., 1995. The "Mawson block': Once contiguous Archaean to Proterozoic crust in the East Antarctic Shield and Gawler craton, *in* VII International Symposium on Antarctic Earth Sciences: Siena, Italy, p. 124.

Fanning, C.M., Reid, A.J., and Teale, G.S., 2007. A geochronological framework for the Gawler Craton, South Australia. South Australian Geological Survey. Bulletin 55, 258 pp.

Ferraccioli, F., Armadillo, E., Jordan, T., Bozzo, E. and Corr, H., 2009. Aeromagnetic exploration over the East Antarctic Ice Sheet: A new view of the Wilkes Subglacial Basin. Tectonophysics, 478, pp. 62-77.

Ferry, J.M., and Spear, F.S., 1978. Experimental calibration of the partitioning of Fe and Mg between biotite and garnet. Contributions to Mineralogy and Petrology, Vol. 66, pp. 113-117.

Fioretti A.M., Black, L.P., Foden, J., and Visona, D., 2005. Grenville-age magmatism at the South Tasman Rise (Australia): A new piercing point for the reconstruction of Rodinia. Geology: October 2005, vol. 33, no. 10, pp. 769-772.

Fitzsimons, I.C.W., 2000. A review of tectonic events in the East Antarctic Shield and their implications for Gondwana and earlier supercontinents. Journal of African Earth Sciences, vol. 31, No. 1, pp. 3-23.

Gapais, D., Pelletier, A., Ménot, R-P, and Peucat, J-J, 2008. Paleoproterozoic tectonics in the Terre Adélie Craton (East Antarctica). Precambrian Research, 162, pp. 531-539.

Ganguly, J., and Saxena, S.K., 1984. Mixing properties of aluminosoilicate garnets: constraints from natural and experimental data, and applications to geothermo-barometry. American Mineralogist, 69, pp. 88-97.

Gleason, J.D., Miller, C.F., Wooden, J.L., and Bennett, V.C., 1994. Petrogenesis of the highly potassic 1.42 Ga Barrel Spring pluton, southeastern California, with implications for mid-Proterozoic magma genesis in the southwestern USA. Contrib. Mineral Petrol, 118, pp. 182-197.

Goldman, D.S. and Albee, A.L., 1977. Correlation of Mg/Fe partitioning between garnet and biotite with 18O/16O partitioning between quartz and magnetite. American Journal of Science, vol. 277, June, pp. 750-767.

Golynsky, A., Bell, R., Blankenship, D., Damaske, D., Ferraccioli, F., Finn, C., Golynsky, D., Ivanov, S., Jokat, W., Masolov, V., Riedel, S., von Frese, R., Young, D., and ADMAP Working Group, 2012. Air and shipborne magnetic surveys of the Antarctic into the 21st century. Tectonophysics, in press, 10 pages.

Goodge, J.W.; Hansen, V.L.; Peacock, S.M.; Smith, B.K.; Walker, N.W., 1993a: Kinematic evolution of the Miller Range shear zone central Transantarctic Mountains, Antarctica, and implications for Neoproterozoic to early Paleozoic tectonics of the East Antarctic margin of Gondwana. Tectonics 12 (6): 1460-1478.

Goodge, J.W., Walker, N.W., and Hansen, V.L., 1993b. Neoproterozoic-Cambrian basement-involved orogenesis within the Antarctic margin of Gondwana. Geology, 21 (1), pp. 37-40.

Goodge, J.W., and Dallmeyer, R.D., 1996. Contrasting thermal evolution within the Ross Orogen, Antarctica: Evidence from mineral $^{40}Ar/^{39}Ar$ ages. Journal of Geology, vol. 104, pp. 435-458.

Goodge, J.W., and Fanning, C. M., 1999. 2.5 b.y. of punctuated Earth history as recorded in a single rock. Geology, vol. 27, no. 11, pp. 1007-1010.

Goodge, J.W., Fanning, C.M., and Bennett, V.C., 2001. U-Pb evidence of ~1.7 Ga crustal tectonism during the Nimrod Orogeny in the Transantarctic Mountains, Antarctica: implications for Proterozoic plate reconstructions. Precambrian Research, 112, pp. 261-288.

Goodge, J.W., and Fanning, C.M., 2002. Precambrian crustal history of the Nimrod Group, central Transantarctic Mountains: *In* Gamble, J., and Skinner, D.A., eds. *Antarctica at the Close of a Millennium,* Wellington, Royal Society of New Zealand Bulletin 35, Proceedings of the 8th International Symposium on Antarctic Earth Science, pp. 43-50.

Goodge, J.W., Myrow, P., Williams, I.S., and Bowring, S.A., 2002. Age and Provenance of the Beardmore Group, Antarctica: Constrains on Rodinia supercontinent breakup. The Journal of Geology, vol. 119, pp. 393-406.

Goodge, J.W., Williams, I.S., and Myrow, P., 2004. Provenance of Neoproterozoic and lower Paleozoic siliciclastic rocks of the central Ross orogen, Antarctica: Detrital record of rift-, passive-, and active-margin sedimentation. GSA Bulletin; September/October 2004, vol. 116, no. 9/10, pp. 1253-1279.

Goodge, J.W., and Vervoort, J.D., 2006. Origin of Mesoproterozoic A-type granites in Laurentia: Hf isotope evidence. Earth and Planetary Science Letters, 243, pp. 711-731.

Goodge, J.W., 2007. Metamorphism in the Ross orogen and its bearing on Gondwana margin tectonics, in Cloos, M., Carlson, W.D., Gilbert, M.C., Liou, J.G., and Sorensen, S.S., eds., Convergent Margin Terranes and Associated Regions: A Tribute to W.G. Ernst: Geological Society of America Special Paper 419, pp. 185-203.

Goodge, J. W., Vervoort, J. D., Fanning, C. M., Brecke, D. M. Farmer, G. L., Williams, I. S., Myrow, P. M., DePaolo, D. J., 2008, A positive test of East Antarctica-Laurentia juxtaposition within the Rodinia supercontinent: Science, vol. 321, pp. 235-240.

Goodge, J.W. and Fanning, M., 2010. Composition and age of the East Antarctic Shield in eastern Wilkes Land determined by proxy from Oligocene-Pleistocene

glaciomarine sediment and Beacon Supergroup sandstones, Antarctica. GSA Bulletin: July/August 2010, vol. 122, no. 7/8, pp. 1135-1159.

Goodge, J. W., Fanning, C. M., Brecke, D. M., Licht, K. J., & Emerson, F. P., 2010. Continuation of the Laurentian Grenville Province across the Ross Sea Margin of East Antarctica. The Journal of Geology, 118, pp. 601-619.

Goodge, J.W. and Finn, C.A., 2010. Glimpses of East Antarctica: Aeromagnetic and satellite magnetic view from the central Transantarctic Mountains of East Antarctica. Journal of Geophysical Research, vol. 115, 22p.

Goodge, J.W., Fanning, C.M., Norman, M.D., and Bennett, V.C., 2012. Temporal, isotopic and spatial relations of early Paleozoic Gondwana-margin arc magmatism, Central Transantarctic Mountains, Antarctica. pp. 1-39.

Graham, C.M., and Powell, R., 1984. A garnet-hornblende geothermometer: calibration, testing, and application to the Pelona Schist, Southern California. Journal of Metamorphic Geology, vol. 2, issue 1, pp. 13-31.

Grindley, G.W., McGregor, V.R., & Walcott, R.I., 1964. Outline of the geology of the Nimrod-Beardmore-Axel Heiberg Glaciers region, Ross Dependency. In: Adie, R.J. (ed.) *Antarctic Geology*. North Holland Publishing Company, Amsterdam, pp. 206-219.

Grindley, G.W., 1972, Polyphase deformation of the Precambrian Nimrod Group, central Transantarctic Mountains, *in* Adie, R.J., ed., Antarctic geology and geophysics: Oslo, Universitetsforlaget, pp. 313-318.

Guidotti, C.VOL. and Dyar, M.D., 1991. Ferric iron in metamorphic biotite and its petrologic and crystallochemical implications. American Mineralogist, vol. 76, pp. 161-175.

Hambrey, M.J., and Alean, J., 2004. Glaciers. 2nd Edition. Cambridge University Press. 376 pages.

Hand, M., Reid, A., and Jagodzinski, L., 2007. Tectonic framework and evolution of the Gawler craton, southern Australia. Economic Geology vol. 102, pp. 1377-1395.

Harley, S.L., 2003. Archaean-Cambrian crustal development of East Antarctica: metamorphic characteristics and tectonic implications. In Yoshida, M., Windley, B.F., & Dasgupta, S. (eds.) 2003. *Proterozoic East Gondwana: Supercontinent Assembly and Breakup*. Geological Society, London, Special Publications, 206, 203-230 The Geological Society of London.

Hodges, K.V., and Crowley, P.D., 1985. Error estimation and empirical geothermobarometry for pelitic systems. American Mineralogist, vol. 70, pp. 702-709.

Hodges, K.V., and Spear, F.S., 1982. Geothermometry, geobarometry and the Al2SiO5 triple point at Mt. Moosilauke, New Hampshire. American Mineralogist, vol. 67, pp. 1118-1134.

Hoffman, P.F., 1991. Did the breakout of Laurentia turn Gondwanaland inside-out? Science, New Series. vol. 252, no. 5011, pp. 1409-1412.

Karlstrom, K.E., Williams, M.L., McLelland, J., Geissman, J.W., and Ahall, K-I, 1999. Refining Rodinia: Geologic Evidence for the Australia-Western U.S. connection in the Proterozoic. GSA Today, vol. 9, no. 10, pp. 1-7.

Kleeman, U. and Reinhardt, J., 1994. Garnet-biotite thermometry revisited: the effect of Al^{VI} and Ti in biotite. European Journal of Mineralogy, 6, pp. 925-941.

Kozoil, A.M., 1989. Recalibration of the garnet-plagioclase-Al2SiO5-quartz (GASP) geobarometer and applications to natural parageneses. EOS, 70, 493.

Leake, B.E, 1978. Nomenclature of amphiboles. Mineralogical Magazine, 42, pp. 533-563.

Leake, B.E., Woolley, A.R., Arps, C.E.S., Birch, W.D., Gilbert, M.C., Grice, J.D., Hawthorne, F.C., Kato, A., Kisch, H.J., Krivovichev, V.G., Linthout, K., Laird, J., Mandarino, J.A., Maresch, W.V., Nickel, E.H., Rock, N.M.S., Schumacher, J.C., Smith, D.C., Stephenson, N.C.N., Ungaretti, L., Whittaker, E.J.W., and Youzhi, G., 1997. Nomenclature of amphiboles: report of the subcommittee on amphiboles of the International Mineralogical Association, Commission on New Mineral and Mineral Names. The Canadian Mineralogist, vol. 35, pp. 219-246.

Li, Z-X, Zhang, L., Powell, C.McA., 1995. South China in Rodinia: Part of the missing link between Australia-East Antarctica and Laurentia? Geology; May 1995, vol. 23, no. 5, pp. 407-410.

Li, Z.X., Bogdanova, S.V., Collins, A.S., Davidson, A., De Waele, B., Ernst, R.E., Fitzsimons, I.C.W., Fuck, R.A., Gladkochub, D.P., Jacobs, J., Krlstrom, K.E., Lu, S., Natapov, L.M., Pease, V., Pisarevsky, S.A., Thrane, K. and Vernikovsky, V., 2008. Assembly, configuration, and break-up history of Rodinia: A synthesis. Precambrian Research, 160, pp. 179-210.

Landsat Image Mosaic of Antarctica (LIMA) Project. (Artist). (2012). *Map of Antarctica and southern ocean*. [Web Map]. Retrieved from http://geology.com/world/antarctica-satellite-image.shtml

Ménot, R-P, Pêcher, A., Rolland, Y., Peucat, J-J, Pelletier, A., Duclaux, G. and Guillot, S., 2005. Structural setting of the Neoarchean terrains in the Commonwealth Bay Area (143-145°E), Terre Adélie Craton, East Antarctica. Gondwana Research, vol. 8, no. 1, pp. 1-9.

Moores, E.M., 1991. Southwest U.S.-East Antarctic (SWEAT) connection: A hypothesis. Geology, 19, pp. 425-428.

Newton, R.C, and Haselton, H.T., 1981. Thermodynamics of the garnet-plagioclase=Al2SiO5-quartz geobarometer. In R.C. Newton, et. al, Eds., Thermodynamics of Minerals and Melts, pp. 131-147, Springer-Verlag, New York.

Oliver, R.L., and Fanning, C.M., 1997. Australia and Antarctica: Precise correlation of Palaeoproterozoic terrains *in* Ricci, C.A., ed., Antarctic Region: Geological Evolution and Processes: Siena, Terra Antarctica Publishers, p. 163-172.

Oliver, R.L., and Fanning, C.M., 2002. Proterozoic geology east and southeast of Commonwealth Bay, George V Land, Antarctica, and its relationship to that of adjacent Gondwana terranes, *in* Gamble, J.A., Skinner, D.N.B., and Henrys, S., (eds.), Antarctica at the Close of the Millennium: Wellington, New Zealand, Royal Society of New Zealand Bulletin 35, p. 51-58.

Payne, J.L., Hand, M., Barovich, K.M., Reid, A., and Evans, D.A.D., 2009. Correlations and reconstruction models for the 2500-1500 Ma evolution of the Mawson Continent. From: Reddy, S.M., Mazumder, R., Evans, D.A.D., and Collins, A.S. (eds.) *Palaeoproterozoic Supercontinents and Global Evolution*. Geological Society, London, Special Publications, vol. 323, pp. 319-355.

Peacock, S.M., and Goodge, J.W., 1995. Eclogite-facies metamorphism preserved in tectonic blocks from a lower crustal shear zone, central Transantarctic Mountains, Antarctica. Lithos 36, pp. 1-13.

Perchuk, L.L., Aranovich, L.Y., Podlesskii, K.K., Lavrent'eva, IlV., Gerasimov, V.Y., Fed'kin, V.V., Kitsul, V.I., Karasakov, L.P., and Berdnikov, N.V., 1985. Precambrian granulites of the Aldan Shield, eastern Siberia, USSR. Journal of Metamorphic Geology, vol. 3, pp. 265-310.

Perchuk, L.L. & Lavrent'eva, I.V., 1983. Experimental investigation of exchange equilibria in the system cordierite-garnet-biotite. In: Saxena (Ed) "Kinetics and

Equilibrium in Mineral Reactions". Advances in Physical Geochemistry, 3, pp. 199-239. Springer-Verlag, New York.

Peucat, J.J., Ménot, R.P., Monnier, O., and Fanning, C.M., 1999. The Terre Adélie basement in the East Antarctica Shield: geological and isotopic evidence for a major 1.7 Ga thermal event; comparison with the Gawler Craton in South Australia. Precambrian Research 94, pp. 205-224.

Peucat, J.J., Capdevila, R., Fanning, C.M., Menot, R.P., Pecora, L., Testut, L., 2002. 1.60 Ga felsic volcanic blocks in the moraines of the Terre Adélie Craton, Antarctica: comparisons with the Gawler Range Volcanics, South Australia. Australian Journal of Earth Sciences, Vol. 49, Issue 5, pp. 831-845.

Pisarevsky S.A., Natapov, L.M., Donskaya, T.V., Gladkochub, D.P., and Vernikovsky, V.A, 2008. Proterozoic Siberia: A promontory of Rodinia. Precambrian Research 160, pp. 66-76.

Reed, S.J.B., 2005. Electron microprobe analysis and scanning electron microscopy in geology. 2nd ed. New York, NY: Cambridge University Press. DOI: www.cambridge.org/9780521848756

Reeves, C., and de Wit, M., 2000. Making ends meet in Gondwana: retracing the transforms of the Indian Ocean and reconnecting continental shear zones. Terra Nova, vol. 12, no. 6, pp. 272-280.

Rignot, E., Mouginot, J., & Scheuchl, B. (2011). Ice flow of the Antarctic Ice Sheet. Science, 333, pp. 1427-1430.

Rignot, E., and Thomas, R.H., 2002. Mass Balance of Polar Ice Sheets. Science, 297(30 August 2002) pp. 1502 - 1506.

Spear, F.S., 1993. Metamorphic phase equilibria and pressure-temperature-time paths. Mineral. Soc. Amer. Monograph 1. MSA.

Spear, F.S., and Kohn, M.H., 2006. Program GTB: GeoThermoBarometry. http://ees2.geo.rpi.edu/MetaPetaRen/Software/GTB_Prog/GTB.html

Stearns, L., and Hamilton, G., 2005. A new velocity map for Byrd Glacier, East Antarctica, from Sequential Aster Satellite Imagery. Annals of Glaciology, pp. 71-76.

Stearns, L.A., Smith, B.E., and Hamilton, G.S., 2008. Increased flow speed on a large East Antarctic outlet glacier caused by subglacial floods. Nature Geoscience, vol. 1, pp. 827-831.

Studinger, M., Bell, R.E., Buck, W.R., Karner, G.D., Blankenship, D.D., 2004. Sub-ice geology inland of the Transantarctic Mountains in light of new aerogeophysical data. Earth and Planetary Science Letters, vol. 220, pp. 391-408.

Torsvik, T.H., 2003. The Rodinia jigsaw puzzle. Science, vol. 33, pp. 1379-1381.

Thompson, A.B. 1976. Mineral reactions in pelitic rocks: I. Prediction of P-T-X (Fe-Mg) phase relations. American Journal of Science, vol. 276, pp. 401-424.

Tracy, R.J., Robinson, P., and Thompson, A.B., 1976.Garnet composition and zoning in the determination of temperature and pressure of metamorphism, central Massachusetts. American Mineralogist, vol. 61, pp. 762-775.

van Heeswijk, M., 1984. Meteorite concentration by ice flow. Institute of Polar Studies at the Ohio State University, Department of Geology and Mineralogy, Report no. 83, 67 p.

Whillans, I.M., and Cassidy, W.A., 1983. Catch a falling star: Meteorites and old ice. Science, vol. 222, no. 4619, pp. 55-57.

Whitney, D.L., and Evans, B.W., 2010. Abbreviations for names of rock-forming minerals. American Mineralogist, vol. 95, pp. 185-187.

Whitney, D. Teaching Phase Equilibria: "Classical" Thermobarometry. Accessed November 2011. SERC Carleton website: http://serc.carleton.edu/research_education/equilibria/PTtPaths.html

Will, T.M., Frimmel, H.E., Zeh, A., Le Roux, P., and Schmädicke, E., 2010. Geochemical and isotopic constraints on the tectonic and crustal evolution of the Shackleton Range, East Antarctica, and correlation with other Gondwana crustal segments. Precambrian Research, vol. 180, pp. 85-112.

Winter, J. D. (2010). *Principles of igneous and metamorphic petrology*. 2nd ed., pp. 579-606. Upper Saddle River, New Jersey: Pearson Prentice Hall.

Wysoczanski, R.J., and Allibone, A.H., 2004. Age, correlation, and provenance of the Neoproterozoic Skelton Group, Antarctica: Grenville age detritus on the Margin of East Antarctica. The Journal of Geology, vol. 112, pp. 401-416.

Appendix A

Petrographic Sample Descriptions[1]

Lonewolf A, Lonewolf Nunataks, Antarctica

Felsic Gneisses

Gneisses

10LWA-1.2 *Biotite gneiss* is a moderately foliated, fine-grained grey rock. The gneiss is composed of plagioclase feldspar, quartz, biotite, and chlorite with accessory augite, muscovite, zircon, opaque, and apatite. Biotite is commonly interfingered with chlorite. Plagioclase displays extensive tapered/ghost/deformation twinning and alteration by fine-grained white mica. Plagioclase and quartz both display minor myrmekite on edges. Zircon can be up to 0.3 mm and visibly zoned in thin section.

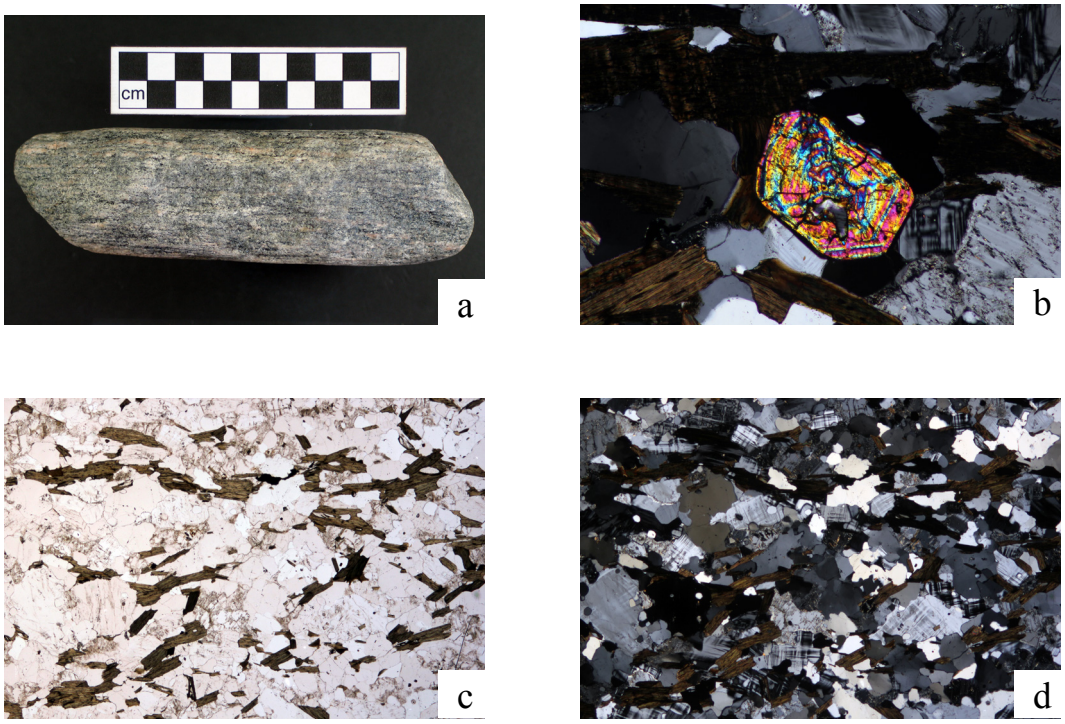

Fig 1. (a) Clast photo. (b) XPL thin section photo of large zircon. FOV ~1 mm. (c) PPL thin section photo. FOV ~6 mm. (d) XPL thin section photo. FOV ~6 mm.

[1] PPL, plane-polarized light; XPL, crossed-polarized light; FOV, field of view.

Felsic Gneisses

Gneisses

10LWA-1.4 *Biotite gneiss* is a both fine and coarse-grained, well-foliated, layered grey rock. The gneiss is composed of plagioclase feldspar, quartz, potassium feldspar, biotite, and muscovite, with accessory apatite and zircon. Millimeter scale layers of fine-grained biotite, plagioclase, and quartz alternate with millimeter scale layers of coarse-grained plagioclase and quartz. Plagioclase feldspar exhibits tapered and deformation twins and is commonly altered to fine-grained mica. Microcline is considerably less altered than plagioclase. Microtextures include myrmekite.

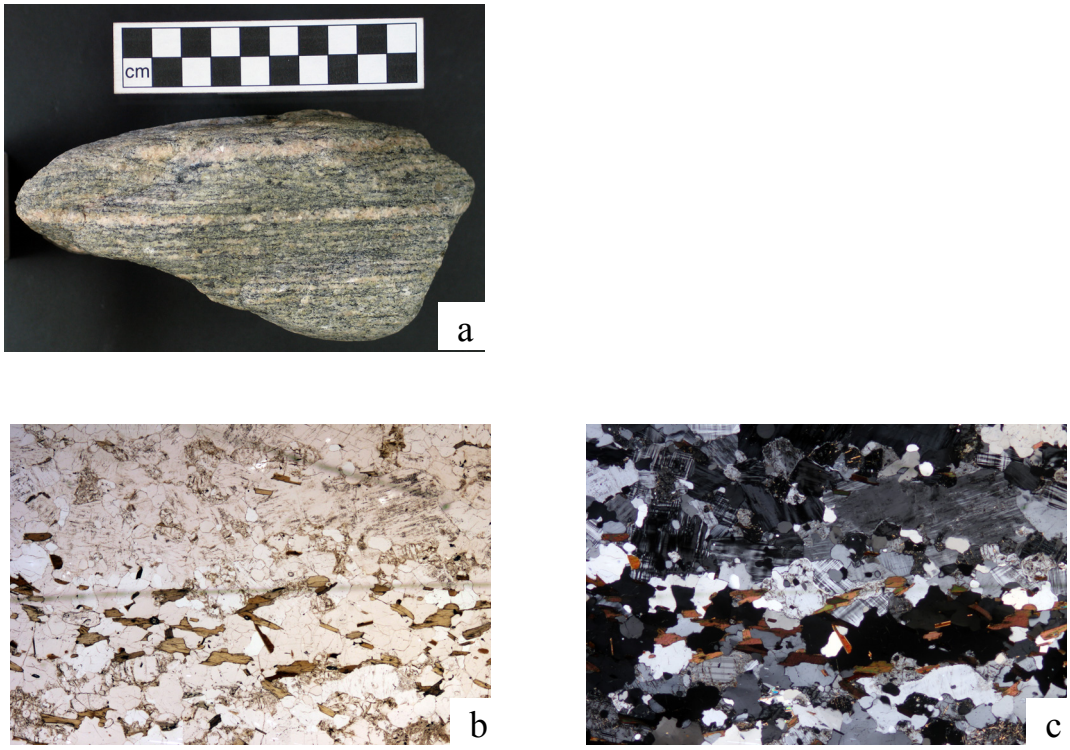

Fig 2. (a) Clast photo. (b) PPL thin section photo. FOV ~6 mm. (c) XPL thin section photo. FOV ~6 mm.

Felsic Gneisses

Gneisses

10LWA-1.5 *Biotite gneiss* is a medium-grained, moderately foliated, cream to dark-grey, thinly-layered rock. The gneiss is composed of plagioclase feldspar, quartz, potassium feldspar, biotite, and minor muscovite, with accessory zircon and opaque. Biotite forms foliation between layers of sausseritized plagioclase and quartz. Muscovite overgrows biotite. Plagioclase is altered to sausserite and shows deformation twinning. Grain boundaries of quartz and plagioclase are ragged, and myrmekite is common.

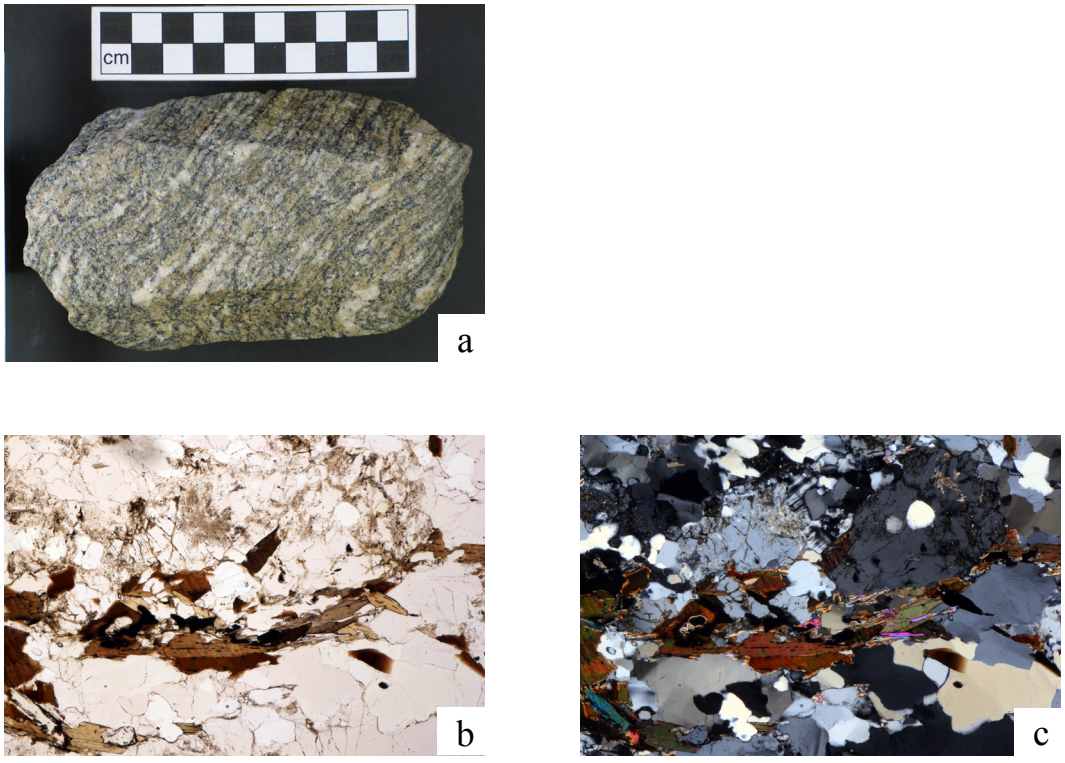

Fig 3. (a) Clast photo. (b) PPL thin section photo. FOV ~3 mm. (c) XPL thin section photo. FOV ~3 mm.

Felsic Gneisses

Gneisses

10LWA-1.6 *Biotite gneiss* is a very fine-grained, weakly foliated, homogeneous grey rock. The gneiss is composed of plagioclase feldspar, potassium feldspar, quartz, biotite, and muscovite, with accessory magnesium-tourmaline, zircon, and opaque. The rock is almost entirely quartzofeldspathic; biotite and muscovite are equal in proportion and are minor components. Plagioclase displays deformation and tapered twins. Magnesian-tourmaline with sieve texture and quartz inclusions is visible in several locations.

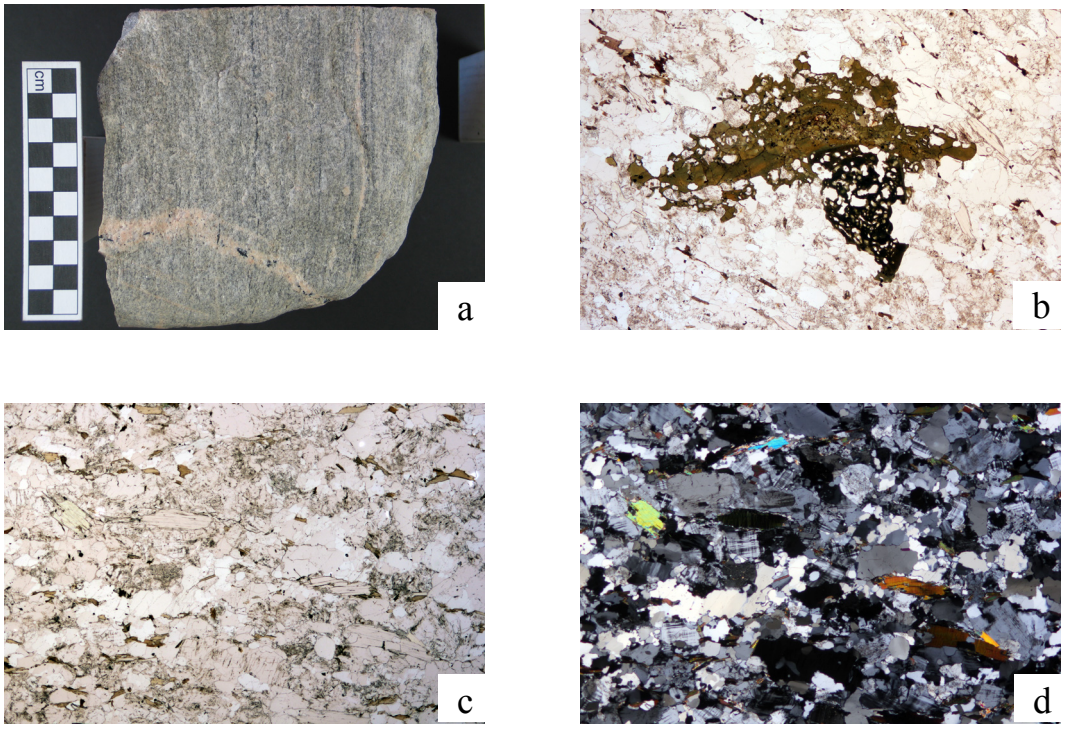

Fig 4. (a) Clast photo. (b) PPL thin section photo of mg-tourmaline with sieve texture. FOV ~6 mm. (c) PPL thin section photo. FOV ~6 mm. (d) XPL thin section photo. FOV ~6 mm.

Felsic Gneisses

Gneisses

10LWA-1.7 *Biotite gneiss* is a fine-grained, moderately-well foliated, light grey rock. The gneiss is composed of quartz, plagioclase feldspar, potassium feldspar, and minor biotite, with accessory zircon and opaques. Minor myrmekite is present.

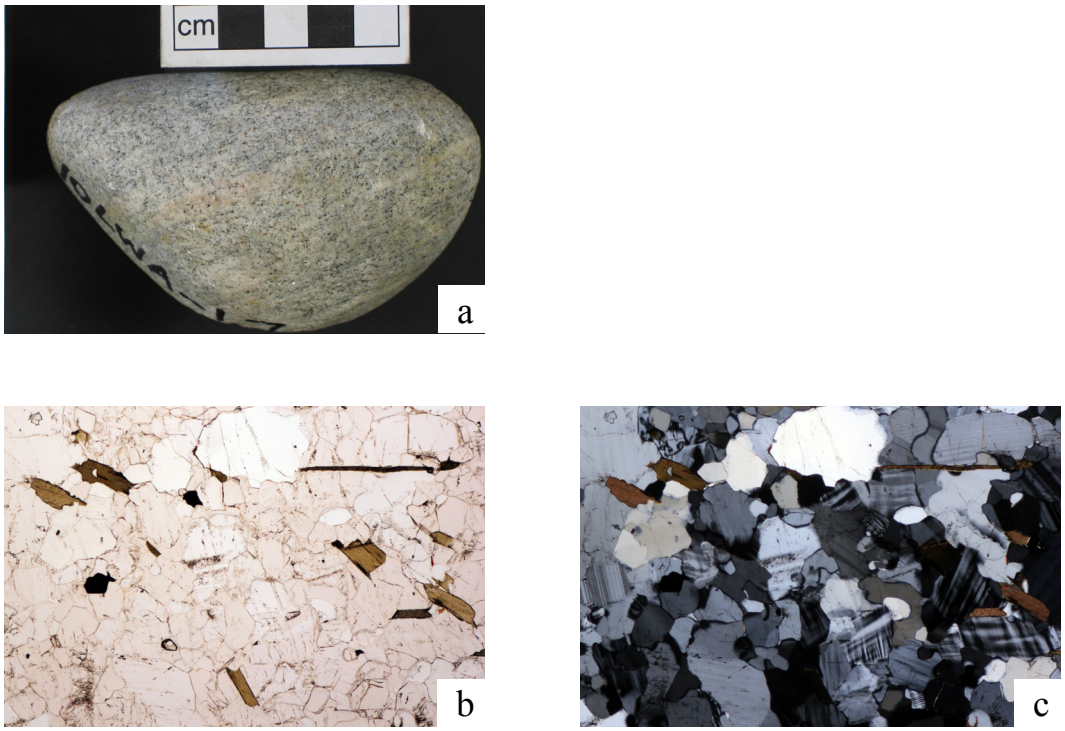

Fig 5. (a) Clast photo. (b) PPL thin section photo. FOV ~3 mm. (c) XPL thin section photo. FOV ~3 mm.

Felsic Gneisses

Gneisses

10LWA-2.1 *Biotite-muscovite orthogneiss* is a medium-grained, well foliated dark-grey to white layered rock with feldspar augen visible in hand sample. The gneiss is composed of quartz, plagioclase feldspar, potassium feldspar, biotite, and muscovite, with accessory opaques and apatite. Plagioclase is altered to sausserite and exhibits deformation and tapered twins. Microtextures include biotite strain tails on a deformed plagioclase porphyroblast, ragged edges on several large muscovite grains, and myrmekite.

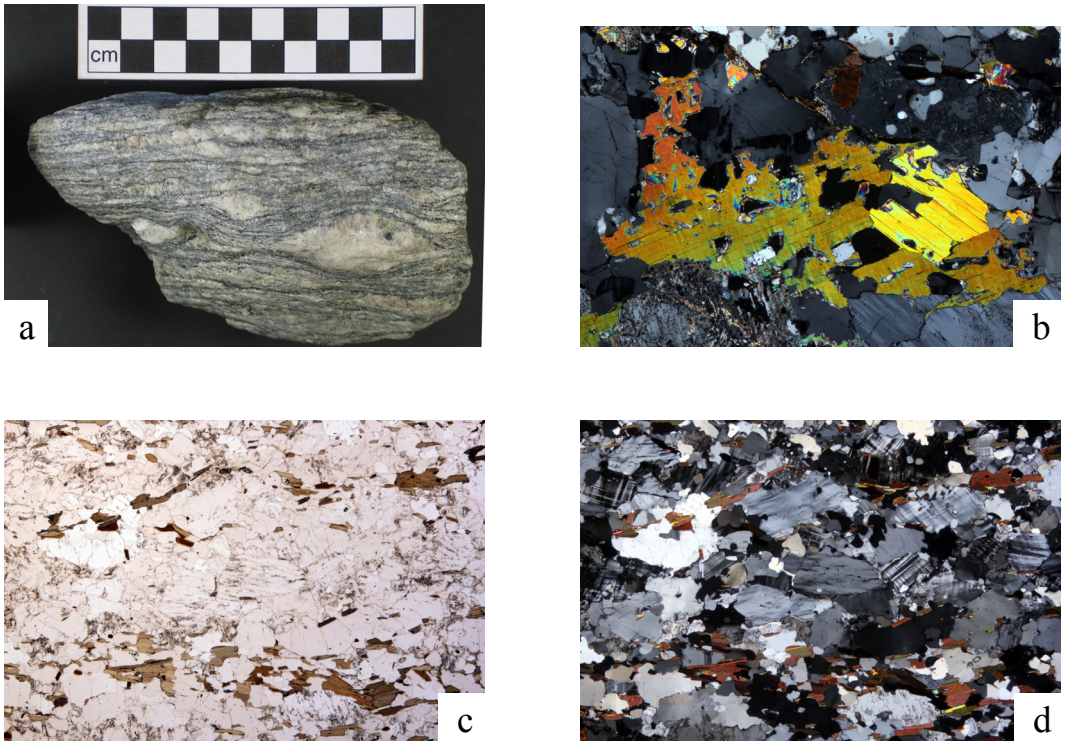

Fig 6. (a) Clast photo. (b) XPL thin section photo of muscovite with ragged edges. FOV ~3 mm. (c) PPL thin section photo. FOV ~6 mm. (d) XPL thin section photo. FOV ~6 mm.

Felsic Gneisses

Gneisses

10LWA-4.1 *Biotite gneiss* is a medium to coarse-grained, moderately foliated, grey rock. The gneiss is composed of plagioclase feldspar, quartz, potassium feldspar, biotite, and minor muscovite, with accessory zircon, opaques, and apatite. Plagioclase exhibits deformation and tapered twins, quartz forms ribbons, and myrmekite is present on quartz grain edges.

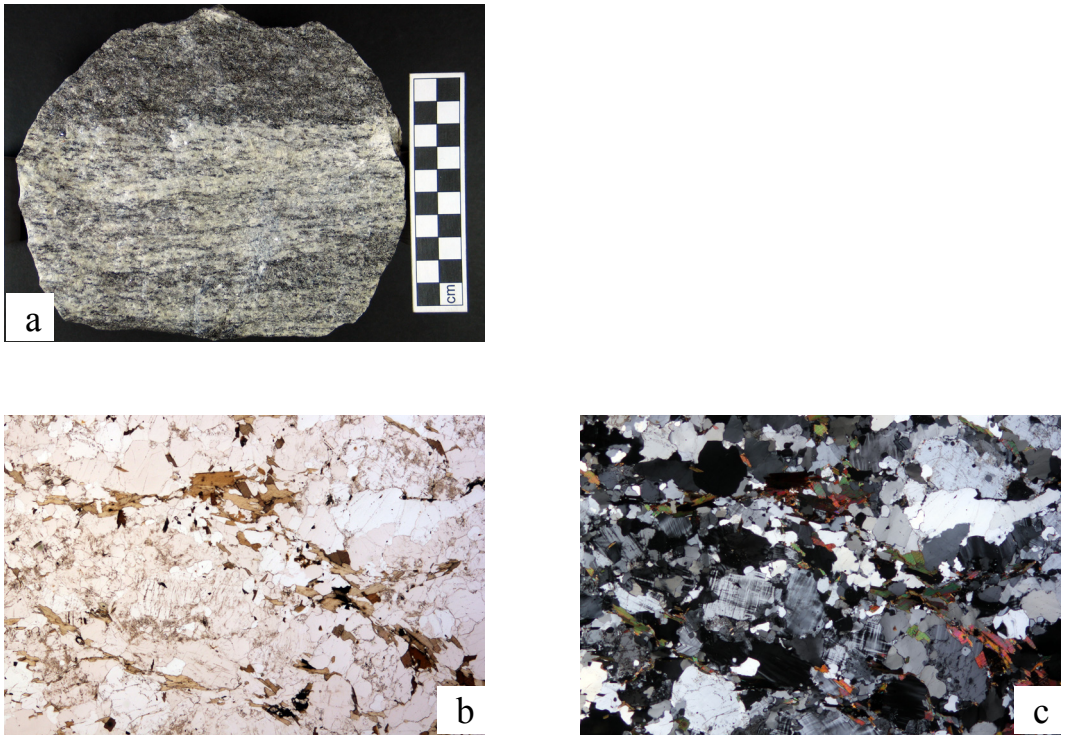

Fig 7. (a) Clast photo. (b) PPL thin section photo. FOV ~6 mm. (c) XPL thin section photo. FOV ~6 mm.

Felsic Gneisses

Gneisses

10LWA-6.1 *Biotite-muscovite orthogneiss* is a medium to coarse-grained, moderately-foliated, megacrystic rock with alternating white, pink, and black layers and slight folding. The gneiss is composed of plagioclase feldspar, quartz, potassium feldspar, biotite, muscovite, and chlorite with accessory apatite, opaque, and zircon. Plagioclase is commonly megacrystic, is altered to sausserite, exhibits deformation twins, and contains many quartz, opaque, and muscovite inclusions. Some chlorite has fine-grained inclusions that are likely rutile. Microtextures include myrmekite, intergrowth of chlorite and biotite, and overgrowth of muscovite on other minerals.

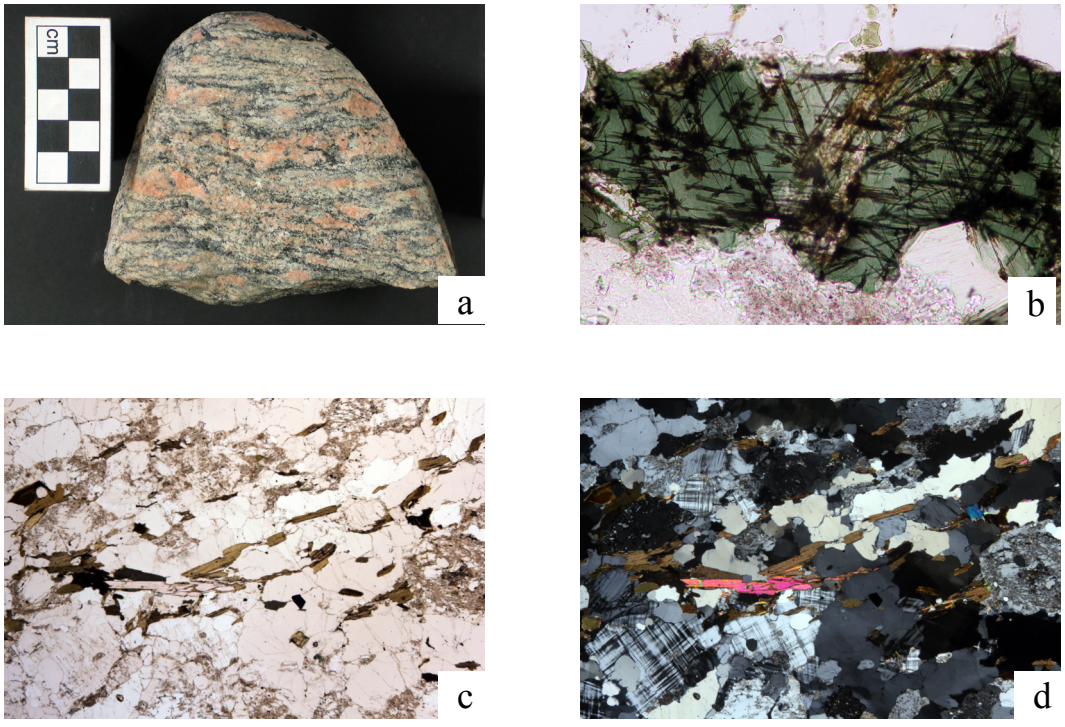

Fig 8. (a) Clast photo. (b) PPL thin section photo of chlorite with rutile inclusions. FOV ~0.75 mm. (c) PPL thin section photo. FOV ~6 mm. (d) XPL thin section photo. FOV ~6 mm.

Felsic Gneisses

Gneisses

10LWA-6.2 Biotite-muscovite gneiss is a well-foliated, fine-grained, pink to black, thinly layered rock. The gneiss is composed of plagioclase feldspar, quartz, biotite, muscovite, and accessory zircon and opaques. Biotite and muscovite overgrow one another, but muscovite primarily overgrows biotite. Quartz overgrows biotite in some locations. Microtextures include myrmekite.

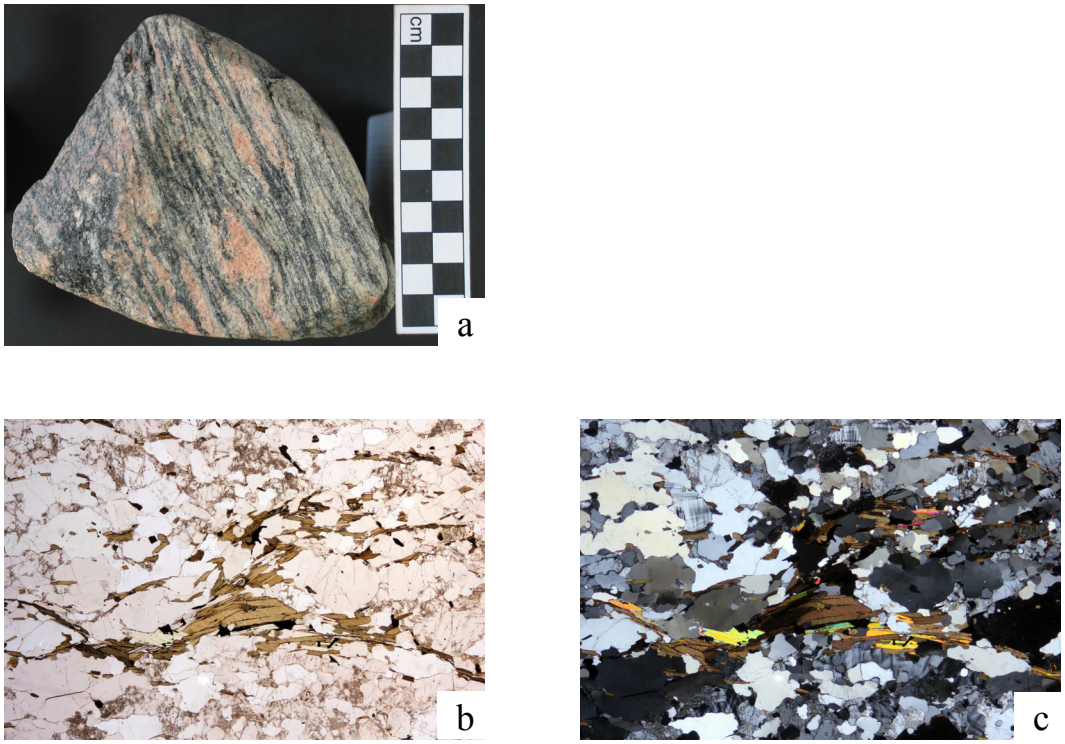

Fig 9. (a) Clast photo. (b) PPL thin section photo. FOV ~6 mm. (c) XPL thin section photo. FOV ~6 mm.

Felsic Gneisses

Gneisses

10LWA-6.3 *Biotite gneiss* is a medium-grained, poorly-foliated, light grey rock. The gneiss is composed of quartz, plagioclase feldspar, biotite, and minor muscovite, with accessory apatite, opaque, and zircons. Quartz is much more abundant than plagioclase, and varies from coarse grains to a very-fine-grained quartz matrix surrounding the larger grains. Microtextures include extensive myrmekite on plagioclase feldspar grain boundaries and occasionally bent biotite.

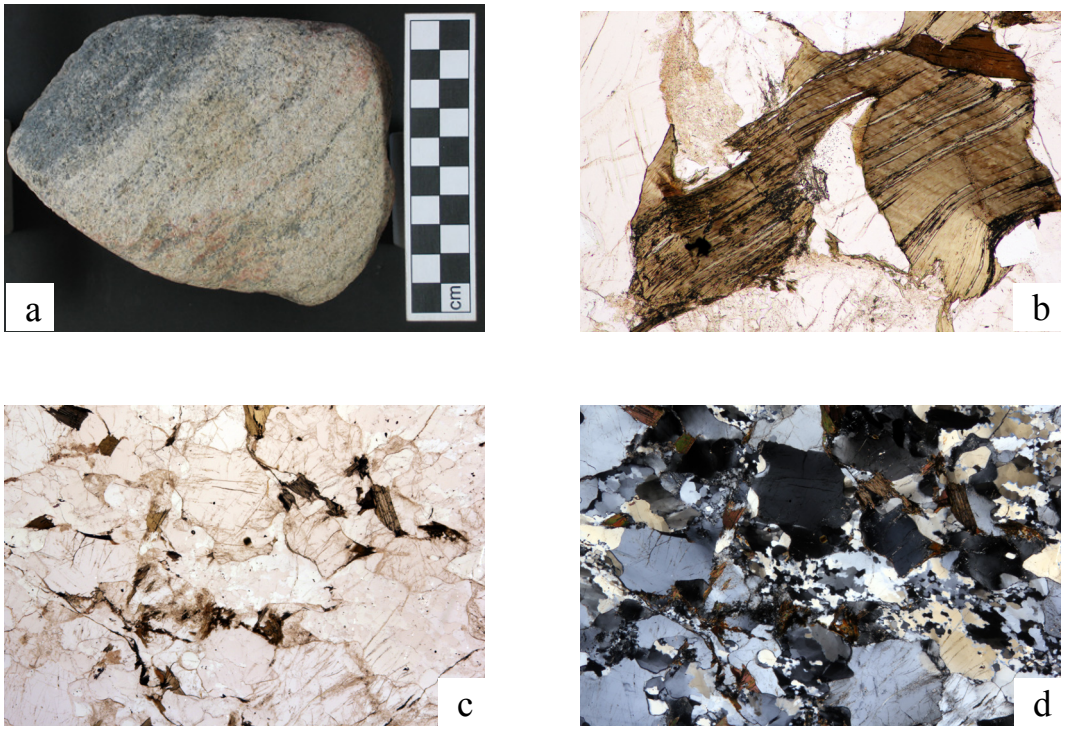

Fig 10. (a) Clast photo. (b) PPL thin section photo of bent biotite. FOV ~1 mm. (c) PPL thin section photo. FOV ~6 mm. (d) XPL thin section photo. FOV ~6 mm.

Felsic Gneisses

Gneisses

10LWA-6.7 *Biotite-muscovite gneiss* is a medium-grained, well-foliated, light grey to pink rock. The gneiss is composed of quartz, plagioclase feldspar, biotite, muscovite, and chlorite, with accessory zircon, opaque, and probable rutile. Plagioclase exhibits quartz inclusions, tapered and deformation twinning, and altered to sausserite with small muscovite overgrowths. Quartz and feldspar grain boundaries are ragged, but no other significant microtextures were observed.

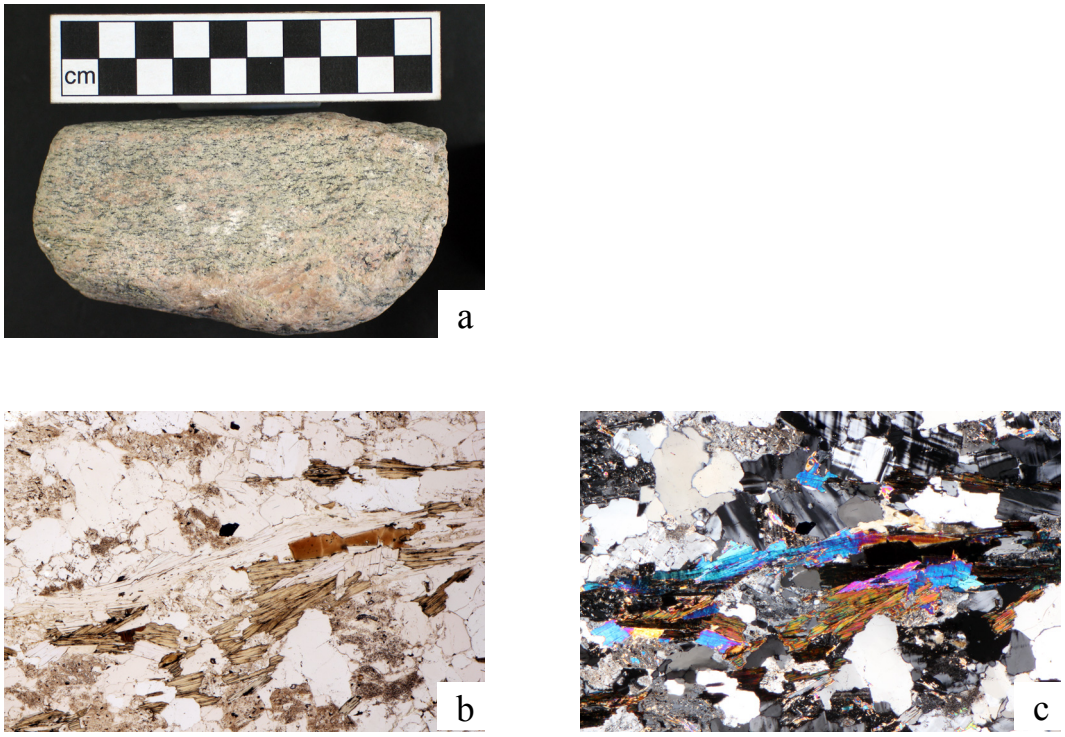

Fig 11. (a) Clast photo. (b) PPL thin section photo. FOV ~3 mm. (c) XPL thin section photo. FOV ~3 mm.

Felsic Gneisses

Gneisses

10LWA-10.1 *Hornblende orthogneiss* is a coarse-grained, weakly foliated, cream-colored rock with black flecks of hornblende. The orthogneiss is composed of quartz, plagioclase feldspar, amphibole, and chlorite, with minor epidote (?), and pumpellyite (?), and accessory zircon, apatite, and opaque. Plagioclase is altered to sausserite. Plagioclase has quartz and muscovite inclusions and exhibits ghost and tapered twins that are occasionally bent. Twins in some plagioclase have been replaced by chlorite. One fracture is filled with pumpellyite.

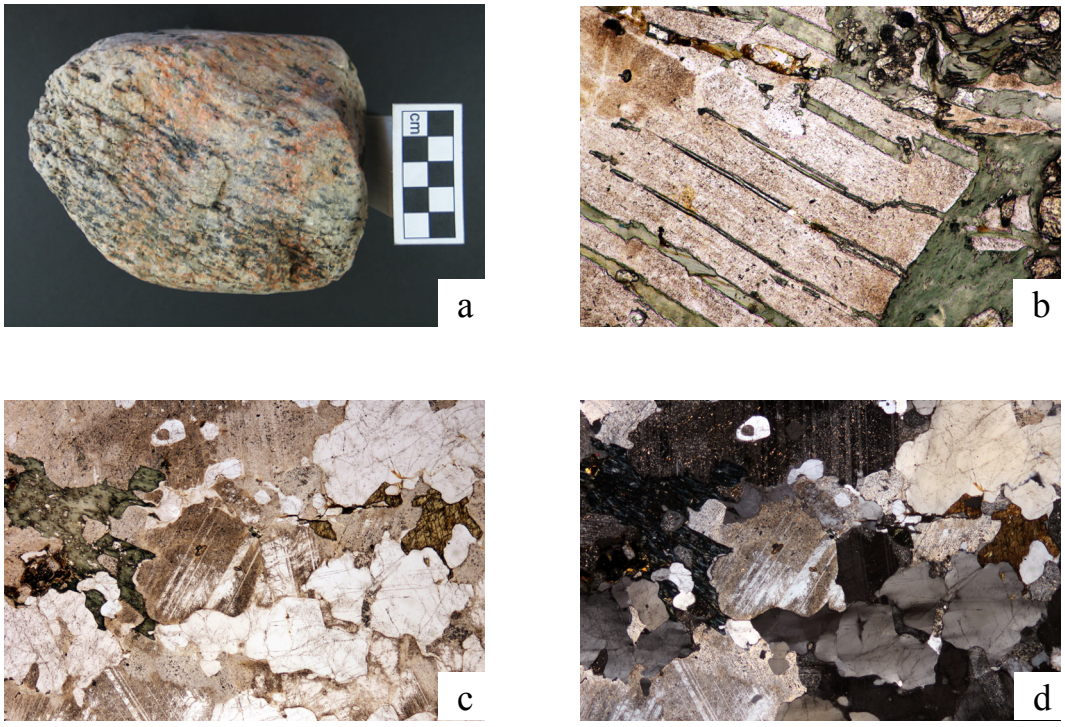

Fig 12. (a) Clast photo. (b) PPL thin section photo of chlorite in plagioclase twins. FOV ~1 mm. (c) PPL thin section photo. FOV ~6 mm. (d) XPL thin section photo. FOV ~6 mm.

Felsic Gneisses

Garnet Gneisses

10LWA-1.1 *Garnet-biotite gneiss* is a medium-grained, weakly-foliated, diffusely banded grey gneiss with pink and green veins visible in hand sample. The gneiss is composed of quartz, plagioclase feldspar, augite, and garnet, with accessory chlorite, epidote, sphene, apatite, and abundant opaques. Plagioclase and quartz are occasionally coarse-grained. Plagioclase commonly contains quartz inclusions, exhibits minor tapered and ghost twins, and is altered to sausserite. Garnets are small and have many quartz and opaque inclusions.

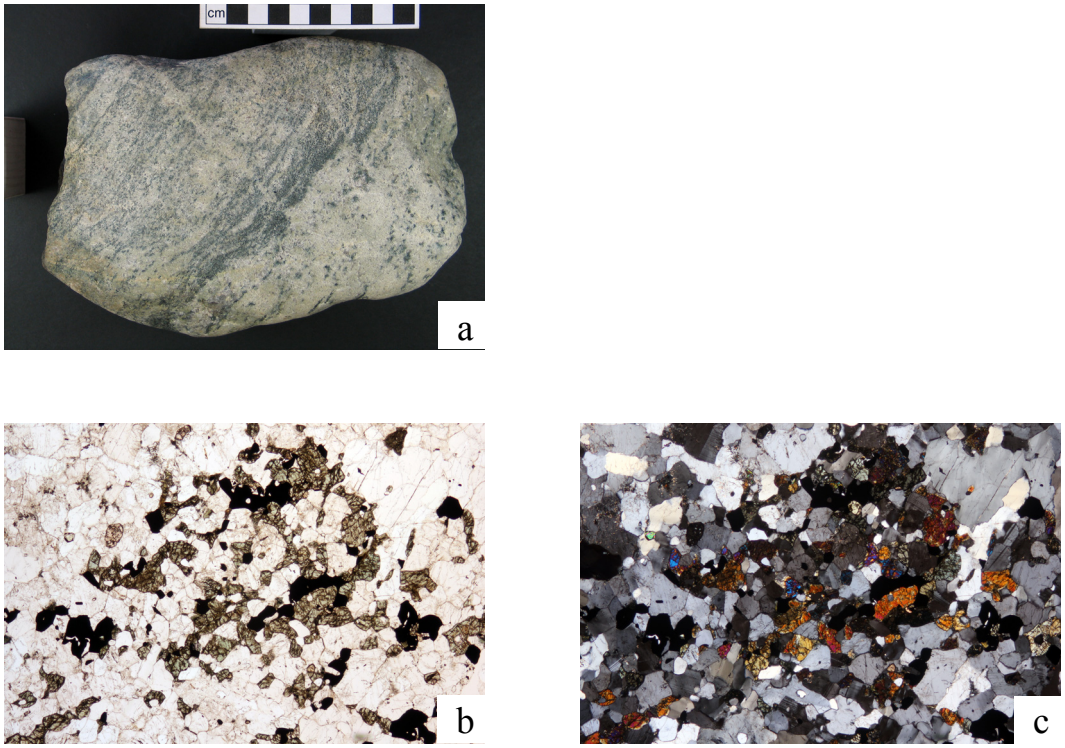

Fig 13. (a) Clast photo. (b) PPL thin section photo. FOV ~6 mm. (c) XPL thin section photo. FOV ~6 mm.

Felsic Gneisses

Garnet Gneisses

10LWA-1.3 *Garnet-biotite gneiss* is a very fine-grained, well foliated, dark-grey to pink rock. The gneiss is composed of quartz, plagioclase feldspar, potassium feldspar, garnet, and biotite with accessory muscovite, opaque, and apatite. Millimeter-scale biotite-oxide rich layers alternate with millimeter-scale quartzofeldspathic layers. Plagioclase shows twins, tapered twins, and deformation twins. Quartz forms small discontinuous ribbons. Garnets are small and not abundant; most are granular or stretched out and contain biotite, quartz, and opaque inclusions. Additional microtextures include minor myrmekite.

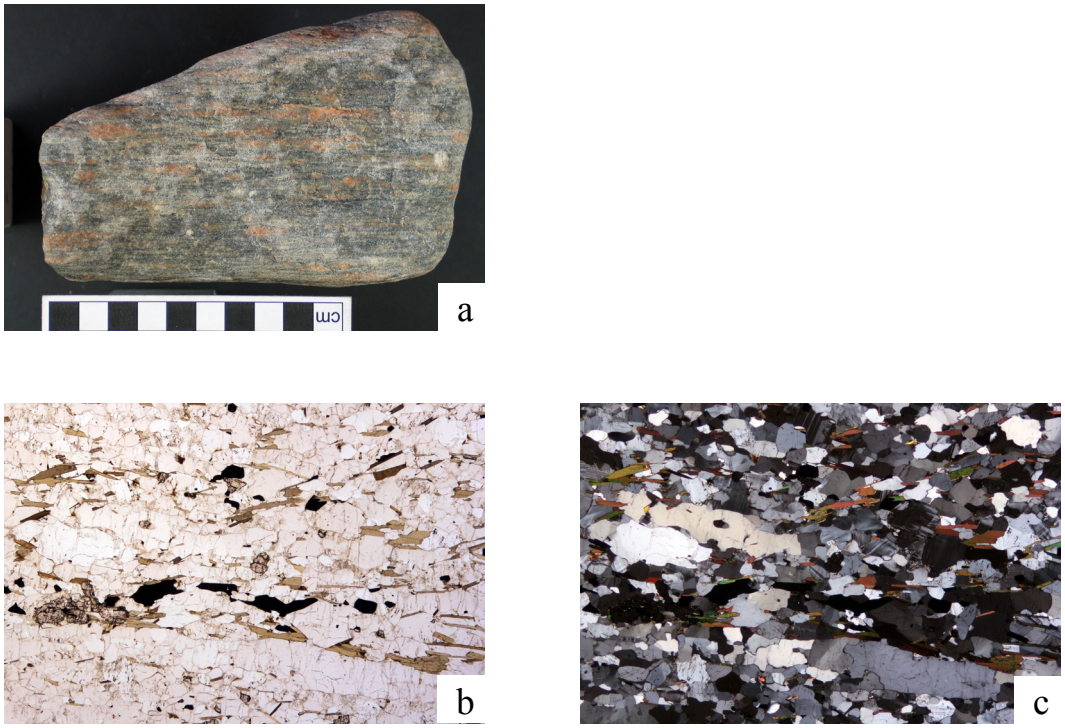

Fig 14. (a) Clast photo. (b) PPL thin section photo. FOV ~6 mm. (c) XPL thin section photo. FOV ~6 mm.

Felsic Gneisses

Garnet Gneisses

10LWA-2.2 *Garnet-biotite gneiss* is a medium-grained, moderately foliated grey rock. The gneiss is composed of quartz, plagioclase feldspar, garnet, biotite, scapolite, and accessory apatite, zircon, and opaque. Plagioclase is twinned and taper-twinned and is relatively unaltered. Biotite is coarse and robust. Garnet is commonly irregular with jagged edges and has biotite and quartz inclusions.

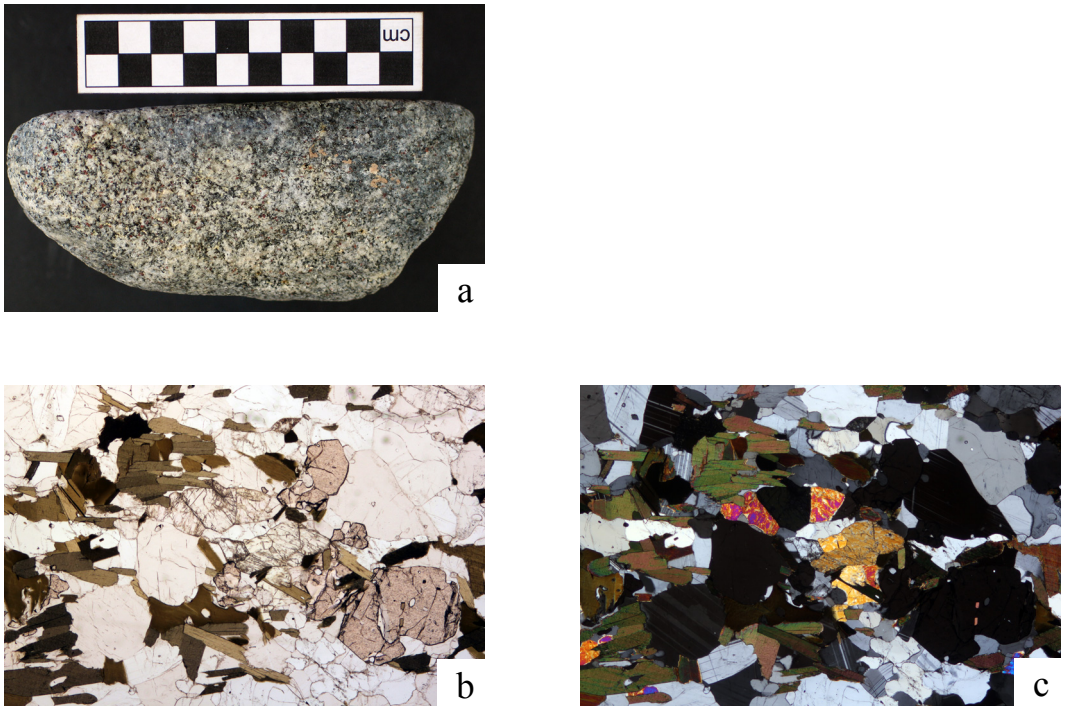

Fig 15. (a) Clast photo. (b) PPL thin section photo. FOV ~6 mm. (c) XPL thin section photo. FOV ~6 mm.

Felsic Gneisses

Garnet Gneisses

10LWA-2.3 – *Garnet-hornblende-biotite gneiss* is a medium-grained, moderately foliated, light grey rock. The gneiss is composed of plagioclase, quartz, garnet, biotite, and amphibole, with minor muscovite, apatite, chlorite, and opaque. Plagioclase is mostly unaltered. The rock is almost entirely quartzofeldspathic; amphibole and biotite are generally fine-grained, not abundant, and are commonly broken up and altered. Garnets are small and not abundant; they commonly occur in granular aggregates, are broken up with ragged edges, and have quartz and opaque inclusions. Locally, numerous very fine-grained garnets are grouped together in an elongated shape. Some biotite intergrows with chlorite.

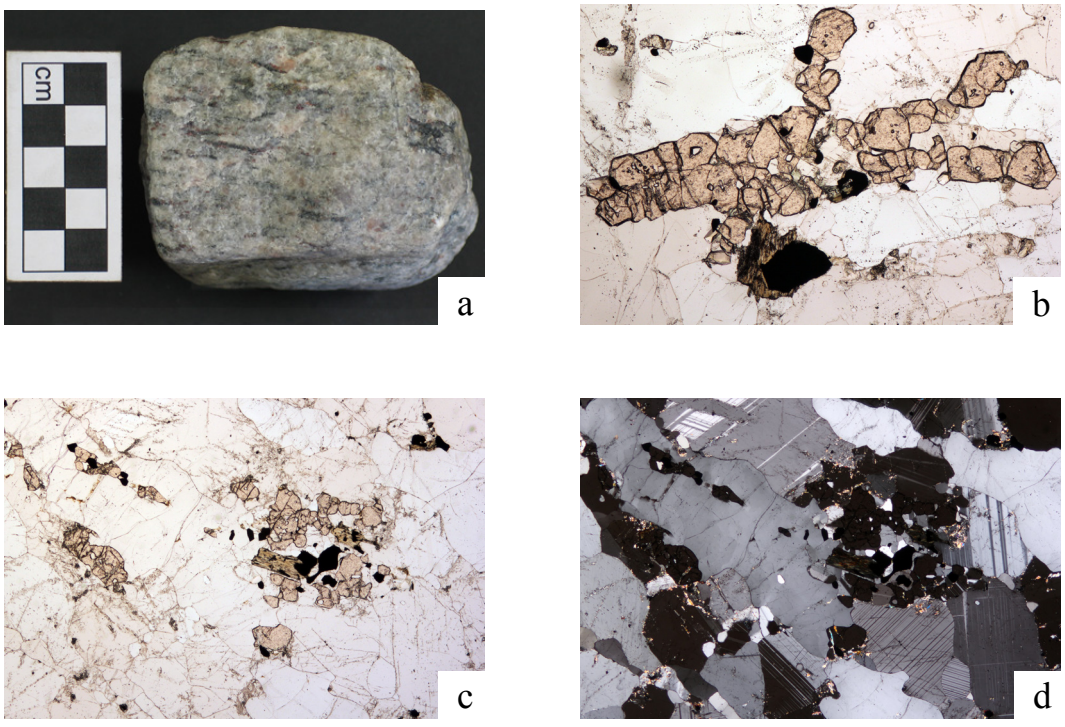

Fig 16. (a) Clast photo. (b) PPL thin section photo of string of granular garnets. FOV ~3 mm. (c) PPL thin section photo. FOV ~6 mm. (d) XPL thin section photo. FOV ~6 mm.

Felsic Gneisses

Garnet Gneisses

10LWA-5.1 *Hypersthene-garnet-hornblende gneiss* is a fine-to medium-grained, poorly to moderately foliated charnockitic dark grey rock. The gneiss is composed of quartz, plagioclase feldspar, hypersthene, garnet and minor amphibole, with accessory apatite and opaque. Plagioclase commonly exhibits well-developed bent and tapered twins. Plagioclase and quartz have a bimodal grain-size distribution: some medium-grained quartz and plagioclase alternates with very-fine-grained clumps of quartz and plagioclase. Hypersthene is typically coarse and displays very-fine-grained brown alteration along some cracks. Hornblende is small and ragged. Garnet is generally round to blocky and mostly intact, with some quartz inclusions. Additional microtextures include myrmekite-like reaction rims surrounding some opaques.

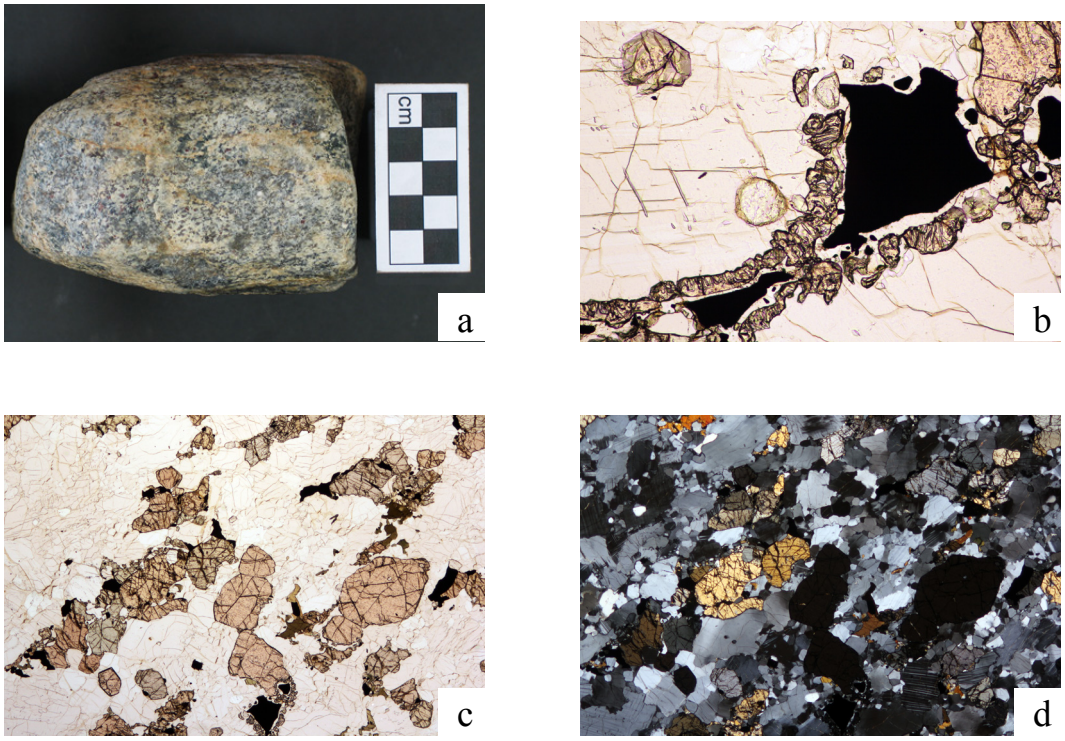

Fig 17. (a) Clast photo. (b) PPL thin section photo of reaction rim around opaque. FOV ~1 mm. (c) PPL thin section photo. FOV ~6 mm. (d) XPL thin section photo. FOV ~6 mm.

Schists

10LWA-3.1 *Biotite-muscovite-calcite schist* is a fine-to medium grained, exceptionally well foliated rock with alternating dark grey and white layers. The schist is composed of quartz, calcite, plagioclase feldspar, biotite, muscovite, and accessory apatite, zircon, and opaque. Sub-mm to mm-scale quartz ribbons and veins throughout the rock alternate with sub-mm to mm-scale layers of muscovite and biotite. Quartz veins contain significant calcite – mostly with ragged grain edges that have been overgrown by quartz, but some larger subhedral grains in coarse quartz ribbons. Muscovite displays crenulation cleavage.

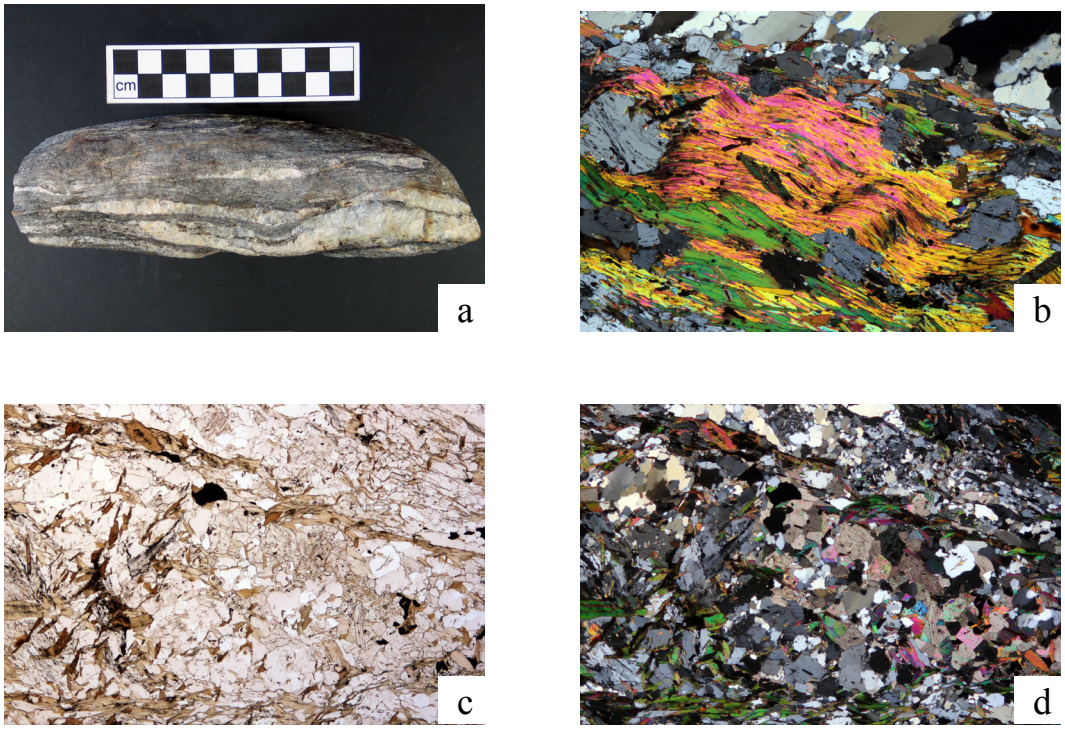

Fig 18. (a) Clast photo. (b) XPL thin section photo of crenulation cleavage in muscovite. FOV ~3 mm. (c) PPL thin section photo. FOV ~6 mm. (d) XPL thin section photo. FOV ~6 mm.

Schists

10LWA-3.2 *Calcite-muscovite-biotite schist* is a fine to medium-grained, exceptionally well-foliated dark grey rock. The schist is composed of quartz, calcite, plagioclase feldspar, biotite, and muscovite, with accessory zircon and foliation-parallel opaque. Sub-mm to mm-scale veins and ribbons of quartz, calcite, and plagioclase alternate with sub-mm to mm-scale layers of muscovite and biotite. Quartz ranges from very-fine grained patches to large recrystallized grains; calcite is almost always coarser than quartz.

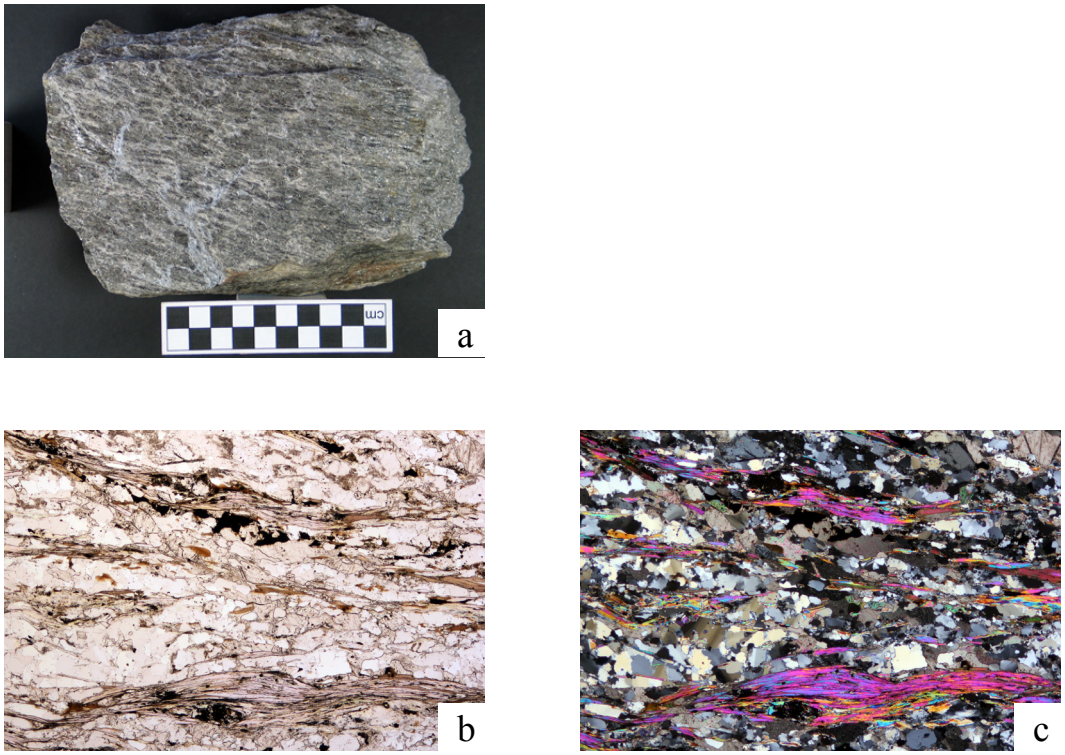

Fig 19. (a) Clast photo. (b) PPL thin section photo. FOV ~6 mm. (c) XPL thin section photo. FOV ~6 mm.

Lonewolf B (LW-4b), Lonewolf Nunataks

Felsic Gneisses

Gneisses

10LWB-2.7 *Biotite gneiss* is a medium-grained, well-foliated rock with alternating white and dark grey layers. The gneiss is composed of quartz, plagioclase, biotite, chlorite, and minor muscovite with accessory zircon, apatite, epidote, opaques, and sphene. Plagioclase exhibits bent, tapered, and ghost twins, and is commonly nearly obscured by fine-grained muscovite. Quartz is deformed and forms ribbons. Some mm-scale layers are significantly more biotite-rich than others, producing banding. Chlorite occurs only where it intergrows with biotite. Opaques are occasionally cracked and contain quartz inclusions.

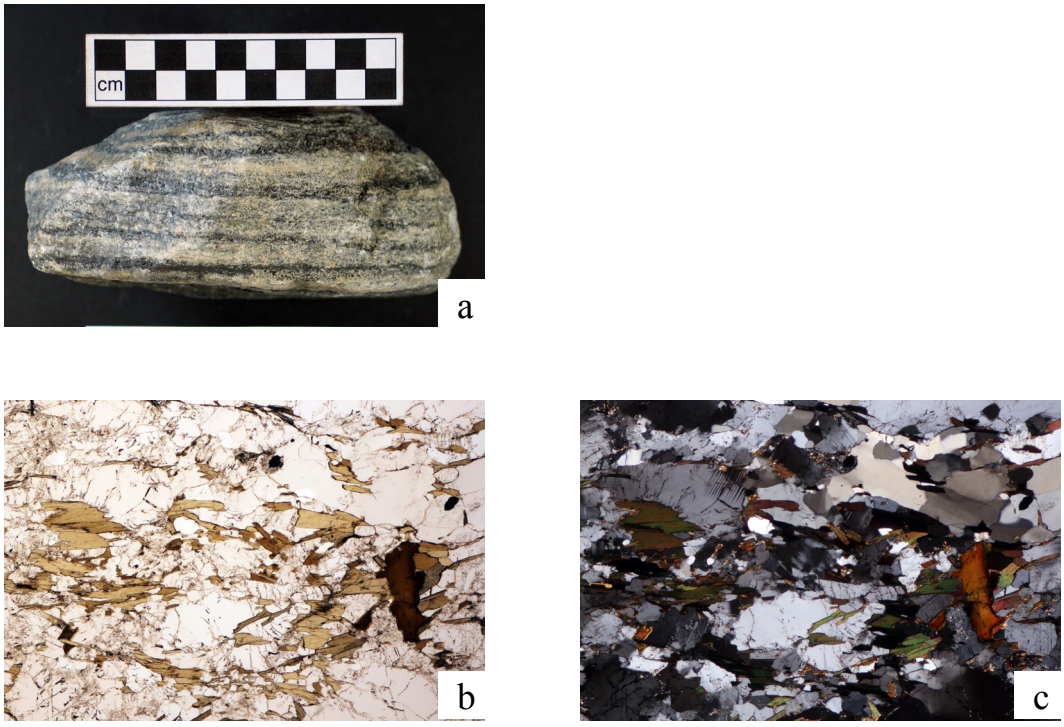

Fig 20. (a) Clast photo. (b) PPL thin section photo. FOV ~3 mm. (c) XPL thin section photo. FOV ~3 mm.

Felsic Gneisses

Gneisses

10LWB-4.4 *Biotite-muscovite orthogneiss* is a medium-grained, moderately to well-foliated grey augen gneiss with sparse pink potassium feldspar porphyroblasts visible in hand sample. The gneiss is composed of quartz, plagioclase feldspar, potassium feldspar, biotite, and muscovite, with accessory zircon and opaque. Quartz is commonly recrystallized and forms discontinuous ribbons. Plagioclase is altered to sausserite, exhibits deformation, tapered, and ghost twins. Chlorite occurs individually as well as intergrown with biotite. Additional microtextures include muscovite occasionally overgrowing biotite and well-developed myrmekite.

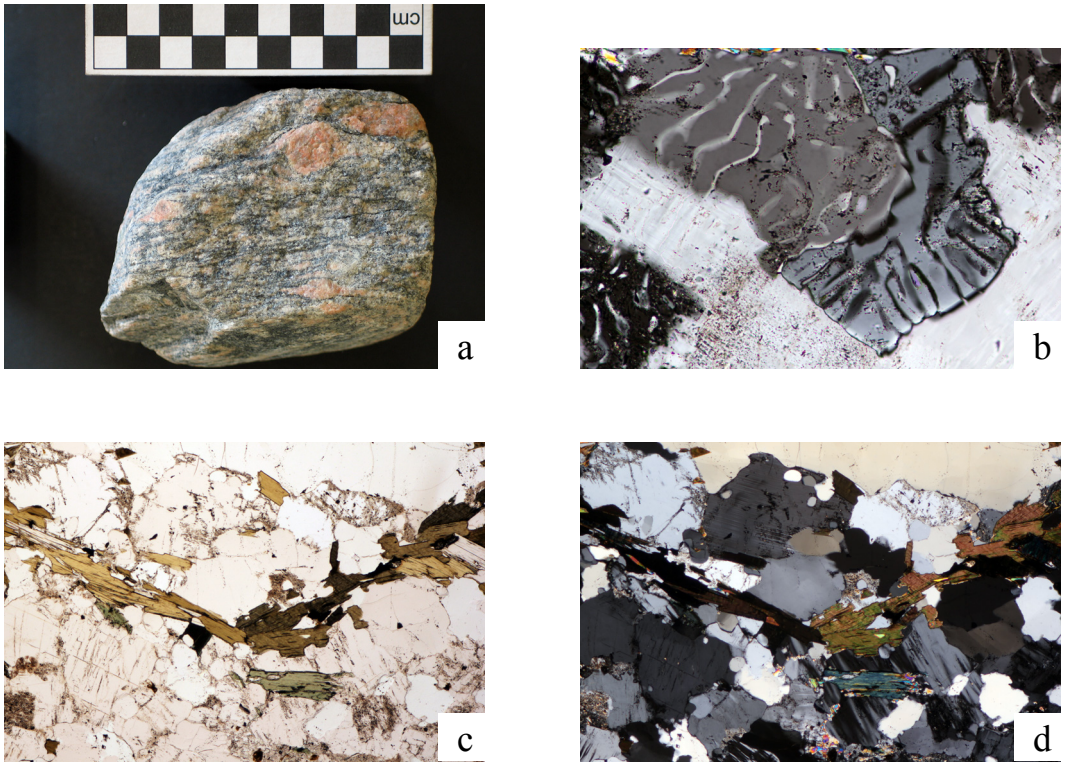

Fig 21. (a) Clast photo. (b) XPL thin section photo of myrmekite. FOV ~0.75 mm. (c) PPL thin section photo. FOV ~3 mm. (d) XPL thin section photo. FOV ~3 mm.

Felsic Gneisses

Gneisses

10LWB-4.5 *Biotite orthogneiss/deformed granodiorite* is a medium to coarse-grained, weakly foliated, dark-grey to pink granodioritic rock. The rock is composed of quartz, plagioclase feldspar, biotite, muscovite, and minor chlorite, with accessory apatite, zircon, and opaques. Plagioclase is commonly riddled with very fine-grained white mica and quartz inclusions and exhibits twins that are occasionally bent. Microtextures include heavily deformed quartz, bent biotite, and fine-grained muscovite rimming almost all plagioclase and biotite grains and even some oxides.

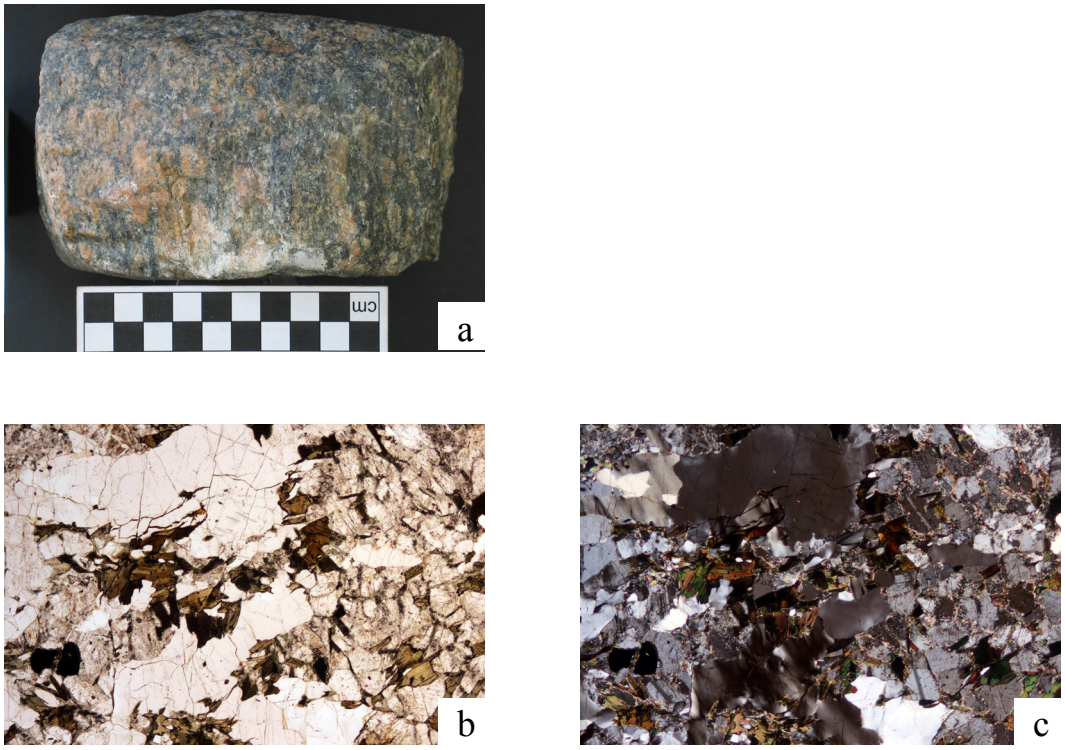

Fig 22. (a) Clast photo. (b) PPL thin section photo. FOV ~6 mm. (c) XPL thin section photo. FOV ~6 mm.

Felsic Gneisses

Gneisses

10LWB-4.6 *Biotite orthogneiss/deformed diorite(?)* is a medium-grained, equigranular, weakly foliated grey rock. The rock is composed of quartz, plagioclase feldspar, biotite and minor potassium feldspar, with accessory apatite, zircon, and opaque. Plagioclase exhibits relict, ghost and deformation twins, some of which are partially replaced by fine-grained mica. Quartz varies from fine to medium-grained. Microtextures include well-developed myrmekite.

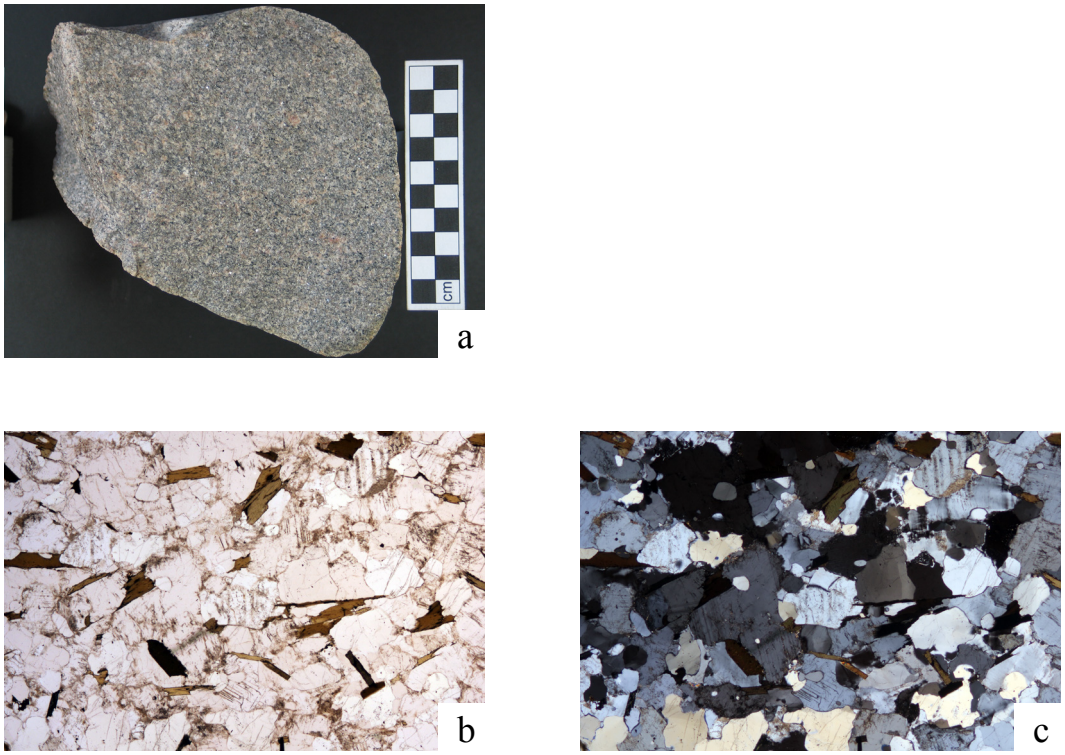

Fig 23. (a) Clast photo. (b) PPL thin section photo. FOV ~6 mm. (c) XPL thin section photo. FOV ~6 mm.

Felsic Gneisses

Gneisses

10LWB-4.7 *Biotite-muscovite orthogneiss* is a fine to coarse-grained, moderately-foliated grey and pink-banded rock. The gneiss is composed of quartz, plagioclase feldspar, biotite, potassium feldspar, and muscovite, with accessory chlorite, opaque, apatite, zircon, and epidote. Quartz varies in size from fine to coarse-grained, is commonly recrystallized, and has jagged grain boundaries. Plagioclase exhibits ghost and tapered twins. Microtextures include intergrowth of chlorite and biotite, muscovite commonly following biotite foliation, muscovite occasionally overgrowing biotite, and minor myrmekite.

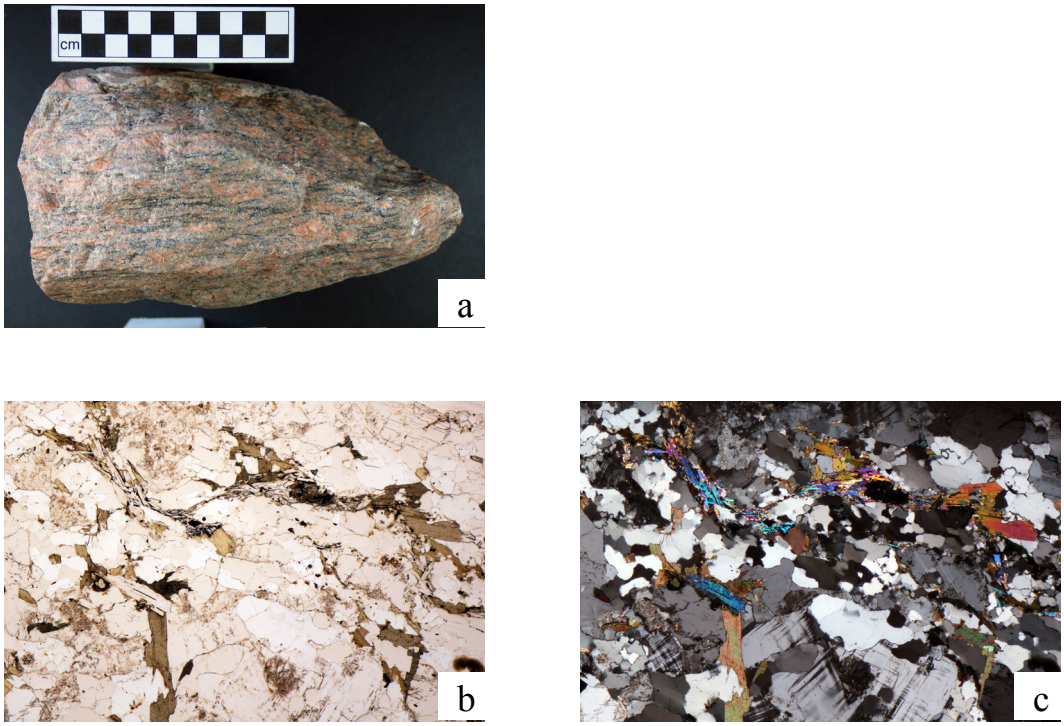

Fig 24. (a) Clast photo. (b) PPL thin section photo. FOV ~3 mm. (c) XPL thin section photo. FOV ~3 mm.

Felsic Gneisses

Gneisses

10LWB-4.8 *Muscovite-biotite orthogneiss* is a fine to medium-grained, well foliated, grey and salmon-colored layered rock. The gneiss is composed of quartz, plagioclase feldspar, potassium feldspar, biotite, muscovite, and chlorite, with accessory opaques and zircon. Quartz is occasionally very fine-grained along grain boundaries of other minerals, but is typically medium-grained, recrystallized, and forms discontinuous ribbons. Plagioclase exhibits ghost and tapered twins. Microtextures include foliation-parallel muscovite and biotite, and muscovite occasionally bent around large potassium feldspar porphyroblasts.

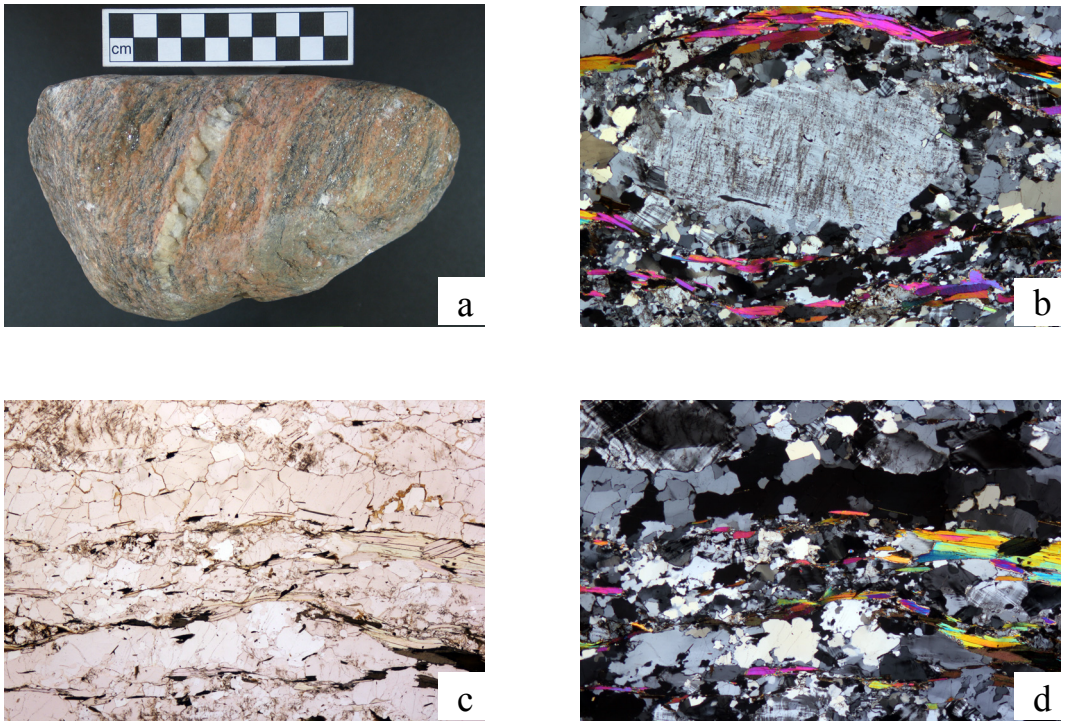

Fig 25. (a) Clast photo. (b) XPL thin section photo of muscovite bending around a feldspar porphyroblast. FOV ~6 mm. (c) PPL thin section photo. FOV ~3 mm. (d) XPL thin section photo. FOV ~3 mm.

Felsic Gneisses

Gneisses

10LWB-5.1 *Biotite-muscovite gneiss* is a medium to coarse-grained, moderately to well-foliated light grey rock. The gneiss is composed of quartz, plagioclase feldspar, potassium feldspar, biotite, muscovite, and chlorite, with accessory zircon, apatite, opaque, and epidote. Quartz has jagged grain boundaries and forms discontinuous coarse-grained ribbons. Plagioclase exhibits tapered and ghost twins, and has very fine-grained muscovite inclusions and quartz inclusions.

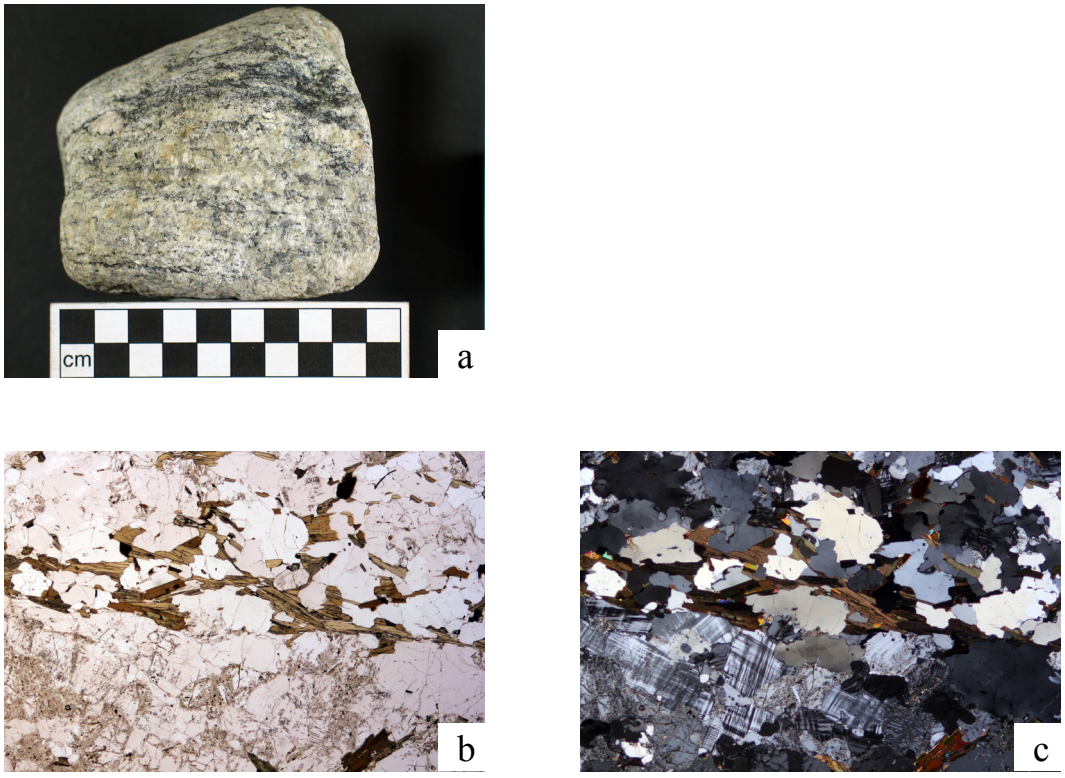

Fig 26. (a) Clast photo. (b) PPL thin section photo. FOV ~6 mm. (c) XPL thin section photo. FOV ~6 mm.

Felsic Gneisses

Gneisses

10LWB-5.2 *Muscovite-gneiss* is a fine-grained, well-foliated, light grey rock. The gneiss is composed of quartz, plagioclase feldspar, potassium feldspar, muscovite, and minor biotite, with accessory apatite and opaque. Plagioclase exhibits ghost and tapered twins and commonly has quartz and muscovite inclusions. Most plagioclase altered to sausserite making the grains recognizable only by relict twinning. Rarely, sausserite has a quartz rim around it. Quartz has jagged grain boundaries and is recrystallized into ribbons. Muscovite generally forms a foliation aligned parallel to quartz ribbons and quartzofeldspathic layers.

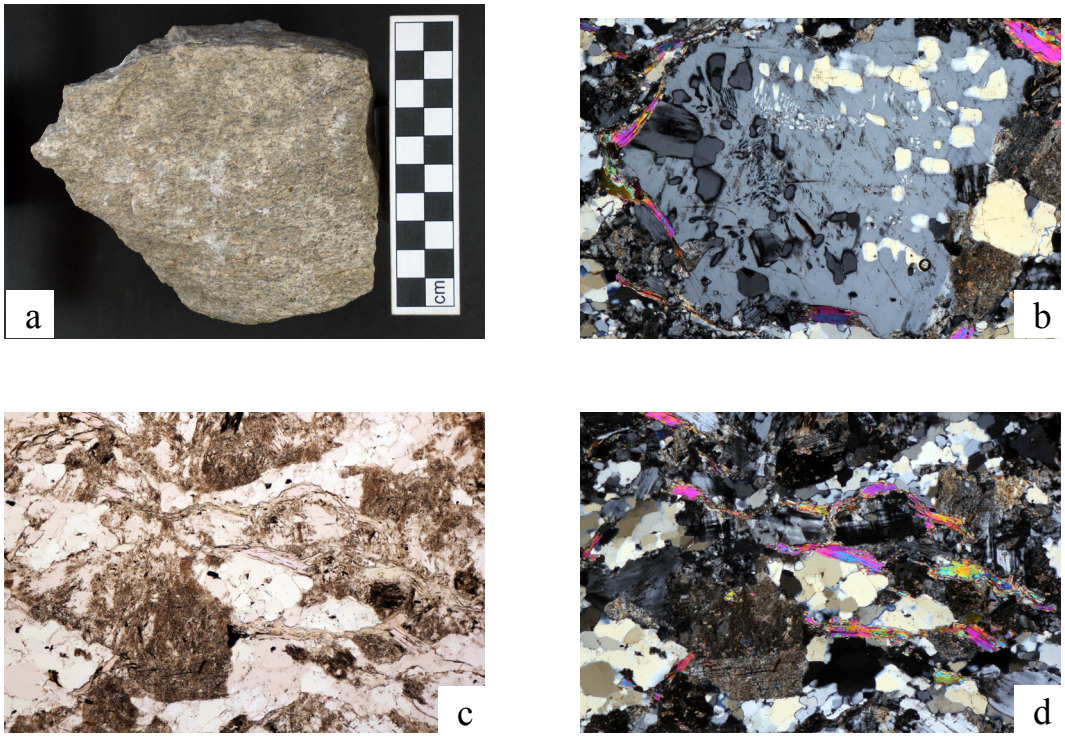

Fig 27. (a) Clast photo. (b) XPL thin section photo of plagioclase feldspar with extensive quartz inclusions. FOV ~3 mm. (c) PPL thin section photo. FOV ~3 mm. (d) XPL thin section photo. FOV ~3 mm.

Felsic Gneisses

Gneisses

10LWB-5.3 *Biotite-gneiss* is a medium-grained, well-foliated, thinly layered, light grey rock. The rock is composed of quartz, plagioclase feldspar, biotite, and chlorite, with accessory apatite, opaques, and zircons. Plagioclase exhibits twins and ghost twins and commonly has small quartz inclusions. Minor alteration to fine-grained brown mica is visible on some plagioclase twins, but overall the rock is relatively fresh. Biotite is robust and intact. Microtextures include distinct and commonly ragged grain boundaries on quartz, as well as myrmekite.

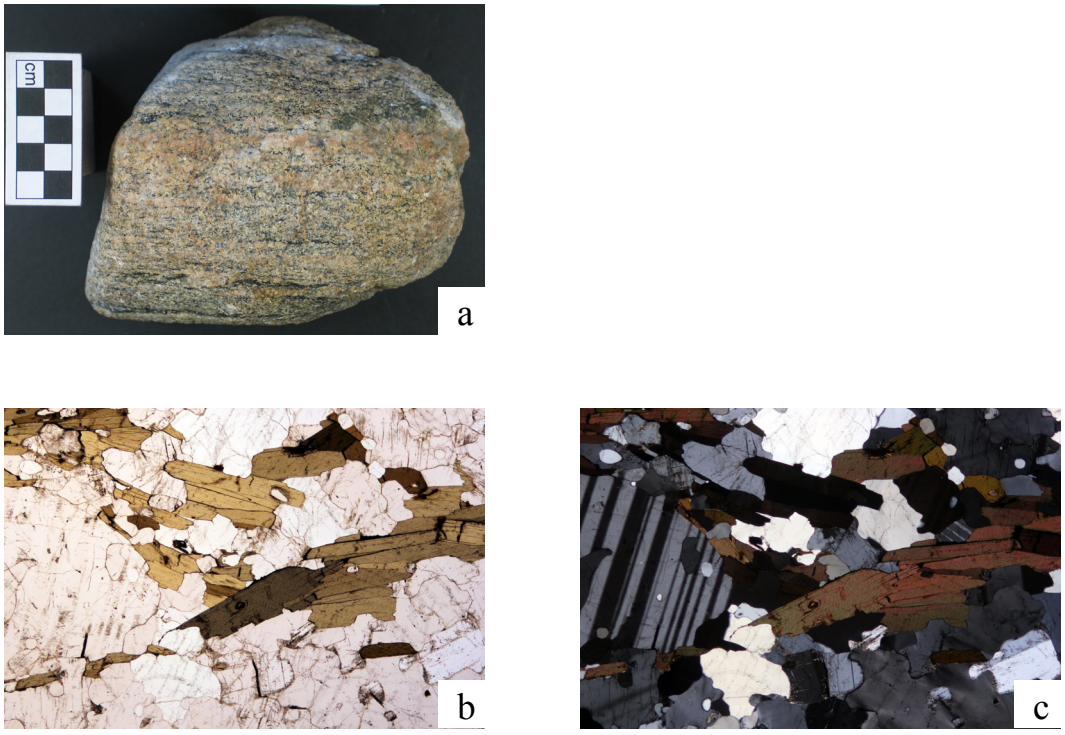

Fig 28. (a) Clast photo. (b) PPL thin section photo. FOV ~6 mm. (c) XPL thin section photo. FOV ~6 mm.

Felsic Gneisses

Gneisses

10LWB-5.4 *Biotite-muscovite gneiss* is a fine- to medium-grained, well-foliated, thinly banded light grey rock with feldspar augen visible in hand sample. The gneiss is composed of quartz, plagioclase feldspar, potassium feldspar, biotite, and muscovite, with accessory zircon. Biotite is more abundant than muscovite, but muscovite is larger and more robust than muscovite. Plagioclase exhibits ghost and tapered twins as well as muscovite inclusions. Plagioclase is commonly almost completely altered to sausserite so that it is identifiable only by relict twinning. Microtextures include muscovite overgrowth of biotite, as well as minor myrmekite.

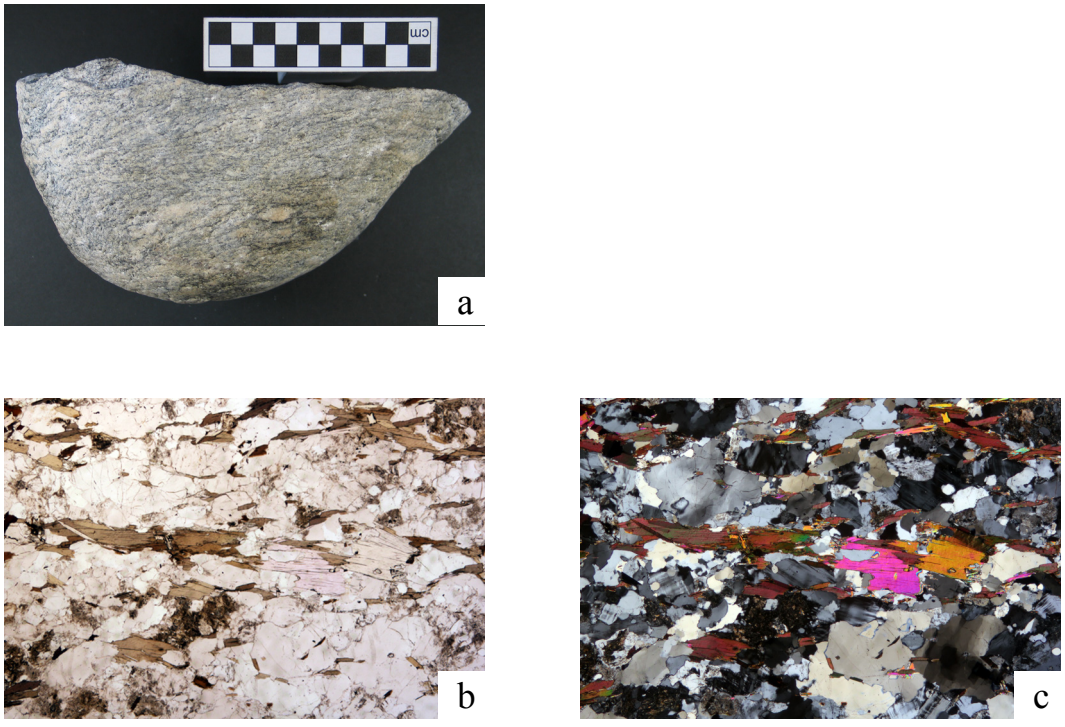

Fig 29. (a) Clast photo. (b) PPL thin section photo. FOV ~6 mm. (c) XPL thin section photo. FOV ~6 mm.

Felsic gneisses

Gneisses

10LWB-5.5 *Biotite-muscovite gneiss* is a fine-grained, well-foliated, thinly banded, slightly folded grey rock. The gneiss is composed of quartz, plagioclase feldspar, potassium feldspar, biotite, and muscovite, with accessory zircon. Plagioclase exhibits deformation, tapered, and ghost twins, frequently has quartz inclusions, and locally is altered to sausserite. Quartz forms large grains as well as small grains that occur together in patches. Biotite is more abundant than muscovite, but muscovite is coarser and more robust than biotite. Microtextures include myrmekite.

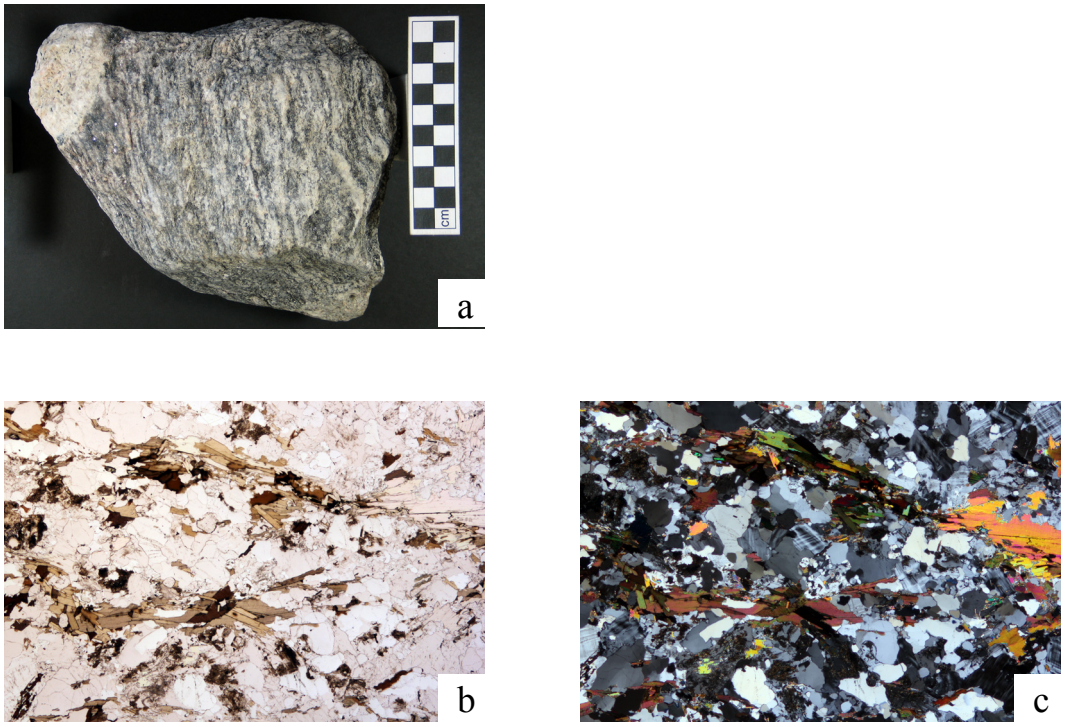

Fig 30. (a) Clast photo. (b) PPL thin section photo. FOV ~6 mm. (c) XPL thin section photo. FOV ~6 mm.

Felsic Gneisses

Gneisses

10LWB-5.6 *Muscovite-biotite gneiss* is a fine to medium-grained, well-foliated, finely banded, light grey rock. The gneiss is composed of quartz, plagioclase feldspar, potassium feldspar, muscovite, and biotite, with accessory apatite and zircon. Plagioclase displays twins and tapered twins and has quartz inclusions. Quartz occurs as large recrystallized grains as well as small grains in a matrix with feldspar. Biotite has a myrmekite-like reaction rim in one location surrounding a minor unknown mineral. Few small opaques are present.

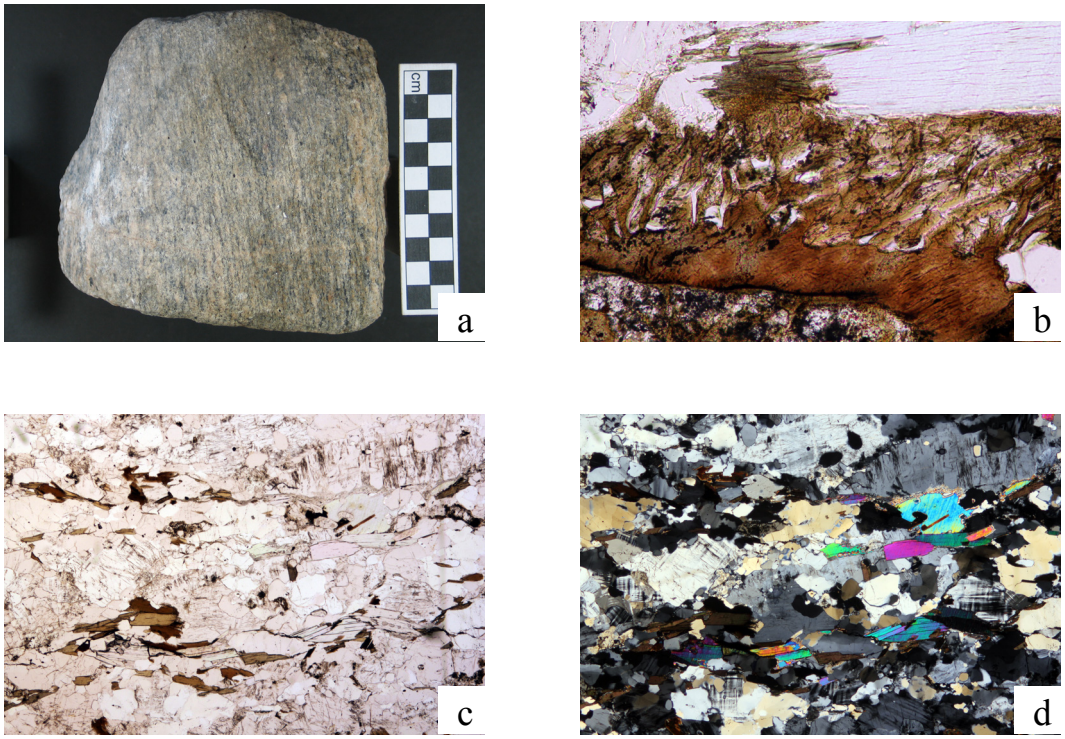

Fig 31. (a) Clast photo. (b) PPL thin section photo of myrmekite-like reaction rim around biotite. FOV ~ 0.75 mm. (c) PPL thin section photo. FOV ~6 mm. (d) XPL thin section photo. FOV ~6 mm.

Felsic Gneisses

Gneisses

10LWB-5.7 *Biotite orthogneiss* is a medium- to coarse-grained, well-foliated, thinly layered, grey rock with feldspar augen visible in hand sample. The gneiss is composed of quartz, plagioclase feldspar, potassium feldspar (?), and biotite, with accessory apatite, zircon (abundant and coarse), possible sphene, opaques, and an unknown fibrous mineral (actinolite?) surrounding opaques. Mm-scale quartzofeldspathic layers alternate with mm-scale quartzofeldspathic layers that include abundant biotite. Microtextures include myrmekite, as well as fibrous growths around two coarse opaques, and the presence of coarse-grained feldspar porphyroblasts.

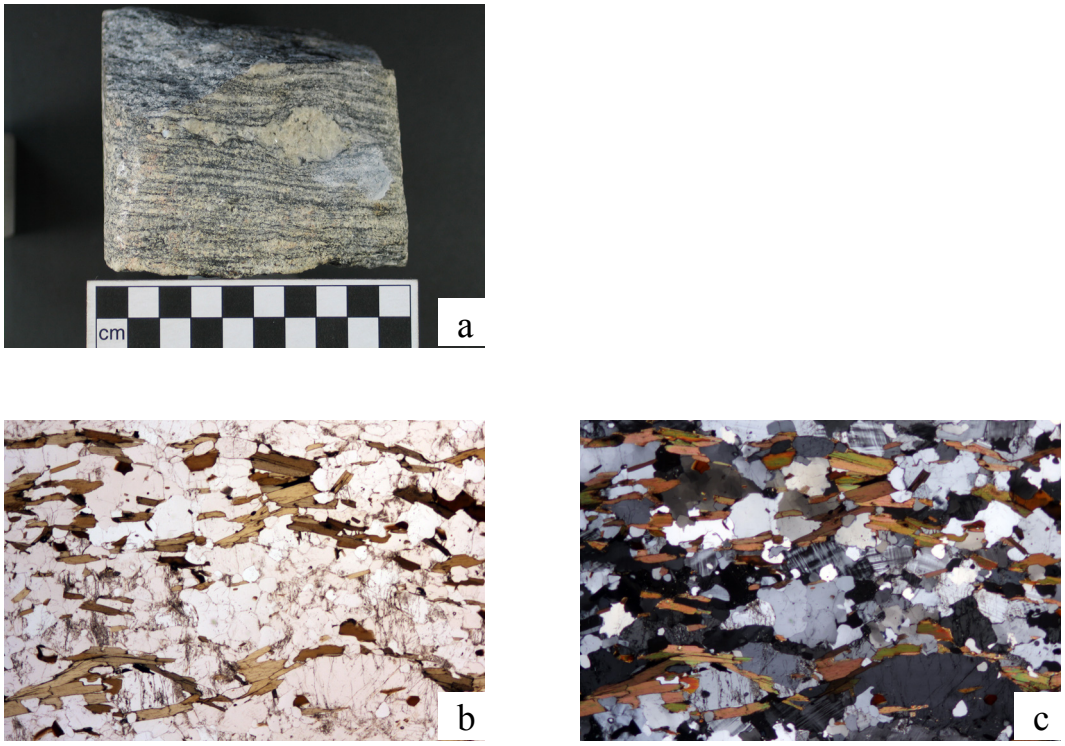

Fig 32. (a) Clast photo. (b) PPL thin section photo. FOV ~6 mm. (c) XPL thin section photo. FOV ~6 mm.

Felsic Gneisses

Gneisses

10LWB-5.8 *Biotite gneiss* is a medium to coarse-grained, well-foliated, thinly layered, slightly folded, grey-black rock with coarse augen feldspar visible in hand sample. The gneiss is composed of quartz, plagioclase feldspar, potassium feldspar, and biotite, with minor muscovite and chlorite, and accessory apatite, epidote, zircon, and opaque. Quartz can be coarse-grained or fine-grained and occurs in a matrix with feldspar. Plagioclase feldspar exhibits tapered and ghost twins, contains quartz and muscovite inclusions, and is altered to sausserite. Muscovite occurs as inclusions in both plagioclase and potassium feldspar. Microtextures include myrmekite and occasional chlorite and biotite intergrowth.

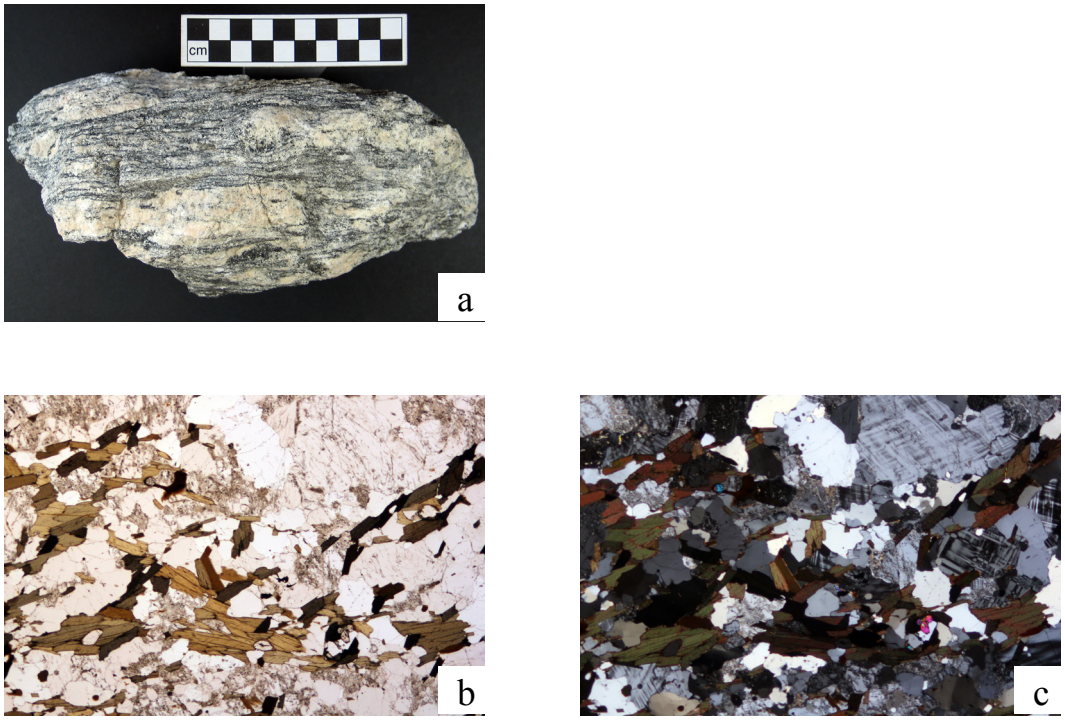

Fig 33. (a) Clast photo. (b) PPL thin section photo. FOV ~6 mm. (c) XPL thin section photo. FOV ~6 mm.

Felsic Gneisses

Garnet Gneisses

10LWB-1.2 *Garnet-biotite-kyanite gneiss* is a coarse-grained, well-foliated, banded, light grey rock with 1-4 cm layers. The gneiss is composed of quartz, plagioclase feldspar, garnet, biotite, and kyanite with accessory opaques and sphene. Garnet and biotite-bearing cm-scale layers alternate with cm-scale quartzofeldspathic layers. Kyanite occurs in only one layer with biotite and garnet and has quartz inclusions. Abundant garnet is typically large and robust and generally round or elongate in shape. Garnet exhibits many cracks as well as quartz and biotite inclusions, but remain largely intact. Quartz can be very fine-grained in a matrix with feldspar, or large recrystallized grains forming ribbons. Plagioclase exhibits twinning, tapered twinning, and occasionally shows bent twins. Opaques occasionally fill fractures in minerals.

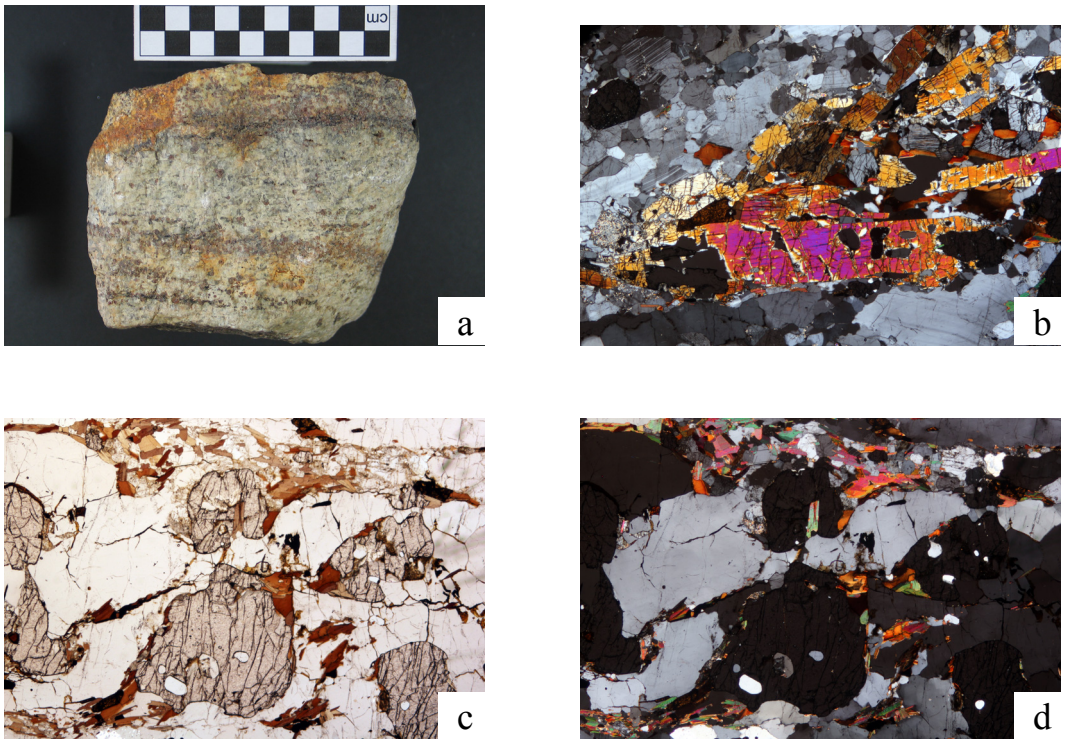

Fig 34. (a) Clast photo. (b) XPL thin section photo of kyanite. FOV ~ 6 mm. (c) PPL thin section photo. FOV ~6 mm. (d) XPL thin section photo. FOV ~6 mm.

Felsic Gneisses

Garnet Gneisses

10LWB-1.3 *Garnet-biotite gneiss* is a medium-grained, moderately foliated, poorly layered grey rock. The gneiss is composed of quartz, plagioclase feldspar, garnet, and biotite, with minor muscovite and accessory apatite, opaque, and few zircons. Plagioclase exhibits twins, tapered twins, and ghost twins, and has quartz and occasional muscovite and/or biotite inclusions. Plagioclase and quartz range from fine-grained matrix components to coarse individual grains. Garnets are round to mostly elongate, and some are broken up by biotite. Many garnets have inclusions of quartz and/or biotite.

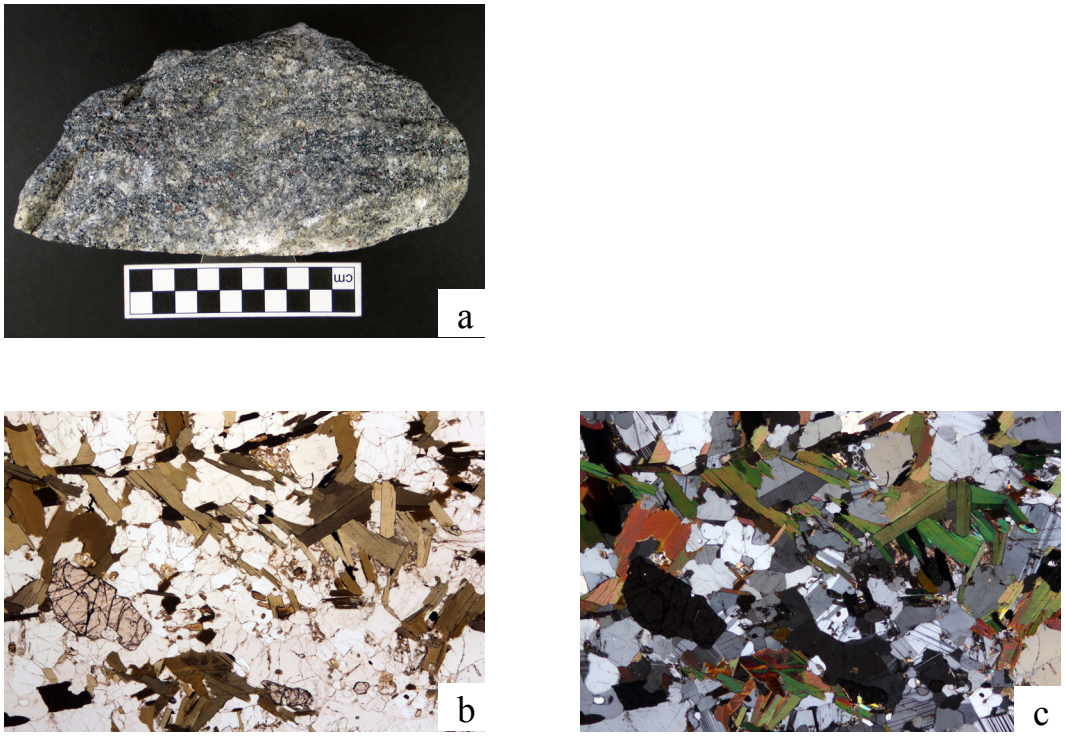

Fig 35. (a) Clast photo. (b) PPL thin section photo. FOV ~6 mm. (c) XPL thin section photo. FOV ~6 mm.

Felsic Gneisses

Garnet Gneisses

10LWB-1.5 *Garnet-biotite gneiss* is a fine- to medium-grained, well foliated, pink to grey rock with feldspar porphyroclasts visible in hand sample. The gneiss is composed of quartz, plagioclase feldspar, garnet, and biotite, with accessory opaque and zircon. Continuous recrystallized quartz ribbons with exceptionally strong LPO alternate with layers of a garnet-rich, fine-grained quartzofeldspathic matrix. Most plagioclase is fine to medium-grained and occurs in matrix with quartz, exhibits twins or ghost twins; in some layers, plagioclase is altered to sausserite and contains many small muscovite inclusions. Garnets are coarse and elongated with many quartz, opaque, and biotite inclusions, and are mostly intact.

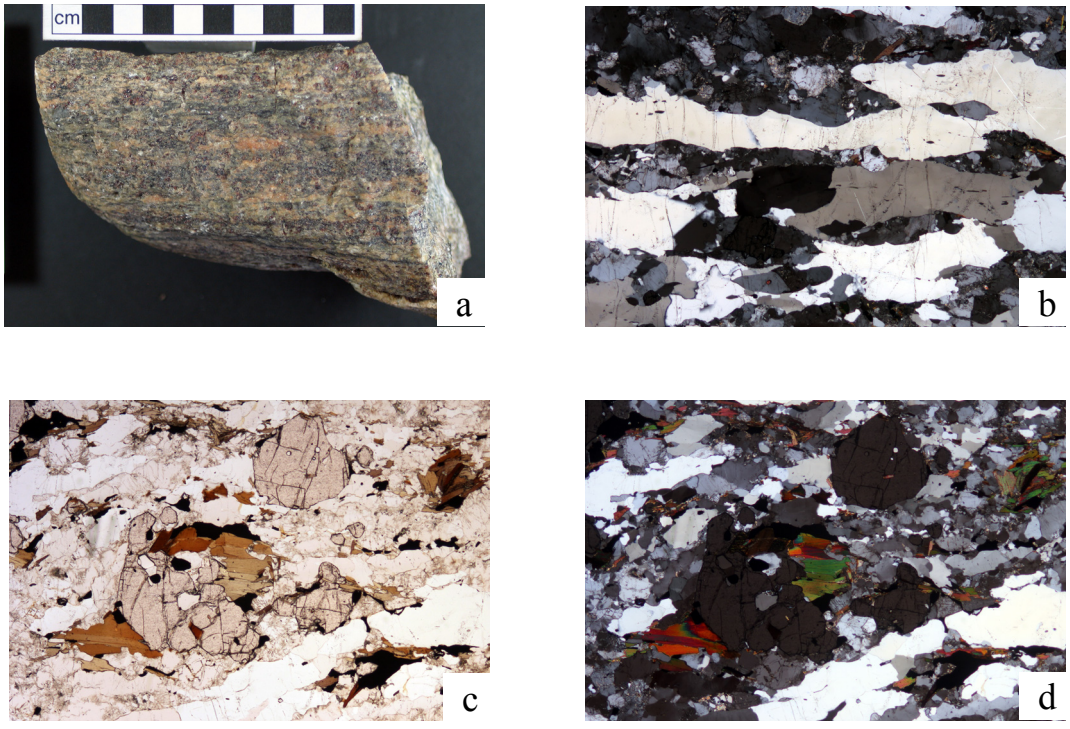

Fig 36. (a) Clast photo. (b) XPL thin section photo of quartz ribbons. FOV ~ 6 mm. (c) PPL thin section photo. FOV ~6 mm. (d) XPL thin section photo. FOV ~6 mm.

Felsic Gneisses

Garnet Gneisses

10LWB-1.6 *Garnet-biotite gneiss* is a medium to coarse-grained, well-foliated, banded, grey to white rock. The gneiss is composed of quartz, plagioclase feldspar, garnet, and biotite, with accessory apatite, opaques, epidote, and zircon. Plagioclase exhibits twins, ghost twins, and tapered twins. Biotite is robust and abundant. Garnets are coarse (up to .75 cm), have ragged edges, contain quartz and biotite inclusions, and are generally intact.

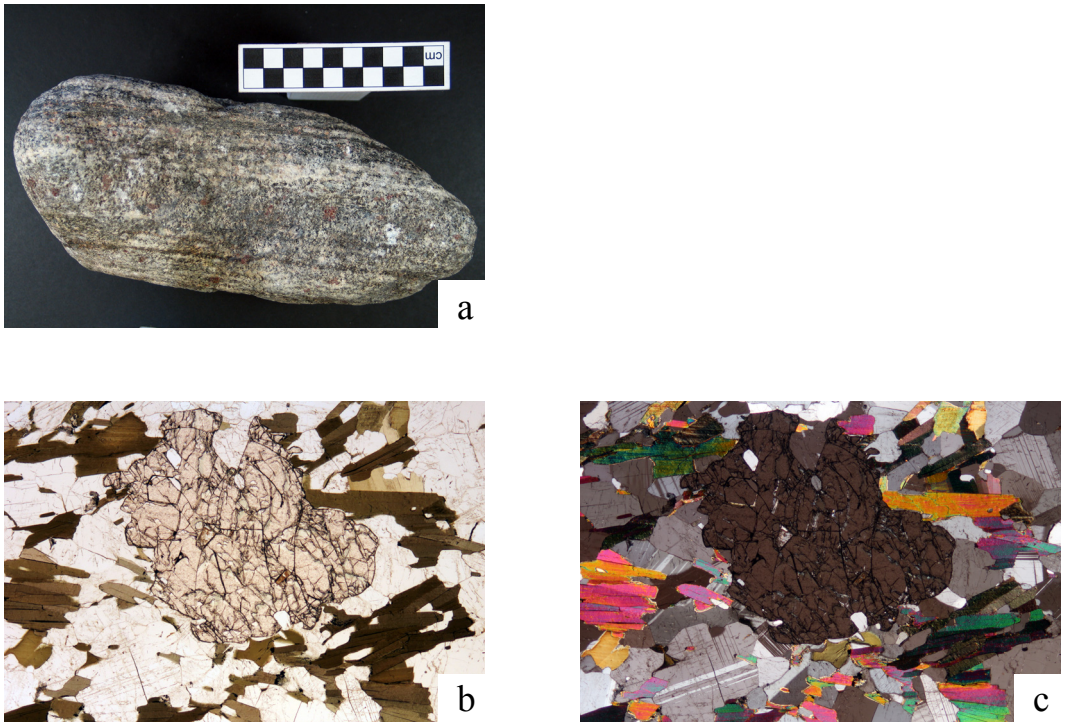

Fig 37. (a) Clast photo. (b) PPL thin section photo. FOV ~6 mm. (c) XPL thin section photo. FOV ~6 mm.

Felsic Gneisses

Garnet Gneisses

10LWB-1.7 *Garnet-muscovite-leucogneiss* is a fine to medium-grained, poorly foliated, light grey rock. The rock is composed of quartz, plagioclase feldspar, potassium feldspar, muscovite, biotite, and garnet, with accessory apatite. Plagioclase is altered to sausserite, exhibits ghost and tapered twins, and has quartz and muscovite inclusions. Quartz is either fine-grained and in the matrix with plagioclase, or as medium- to coarse-grained recrystallized grains. Garnets are small (<1 mm), sparse, and have quartz and rarely apatite inclusions. Microtextures include myrmekite.

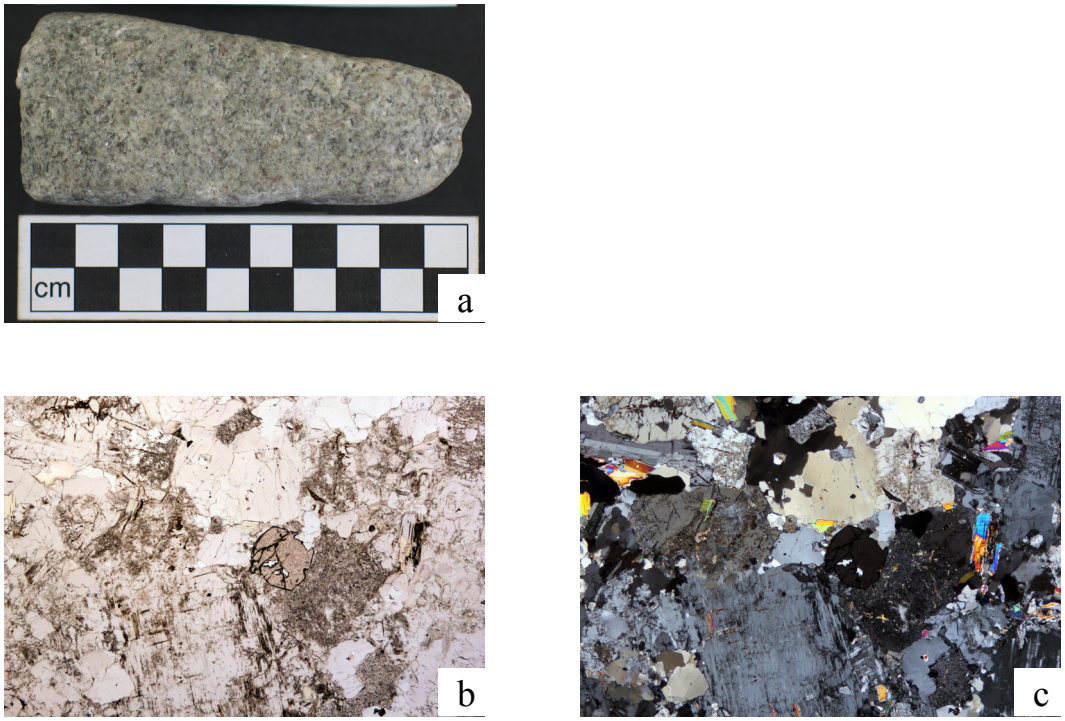

Fig 38. (a) Clast photo. (b) PPL thin section photo. FOV ~6 mm. (c) XPL thin section photo. FOV ~6 mm.

Felsic Gneisses

Garnet Gneisses

10LWB-2.3 *Garnet gneiss* is a fine-grained, poorly foliated, thinly banded, dark grey rock. The gneiss is composed of quartz, garnet, an unknown fibrous mineral forming coronas around garnets, and possible plagioclase feldspar (obscured), with accessory zircon, opaques, and epidote or piemontite. Alternating mm-scale layers have significantly more opaques, garnets, and are more deteriorated than other layers. Garnets are very small (< 0.25 mm), exhibit cracks but are intact, and are all surrounded by a corona of very-fine-grained fibrous minerals. It appears that the fibrous material is replacing the garnet from the outside in (in some places the fibrous corona has retained fractures shown by garnet) and locally the fibrous mineral has completely replaced some garnets. Rims of opaque occasionally surround these fine-grained coronas. A significant fine-grained matrix of possible micas and oxides separates grains so that most do not touch.

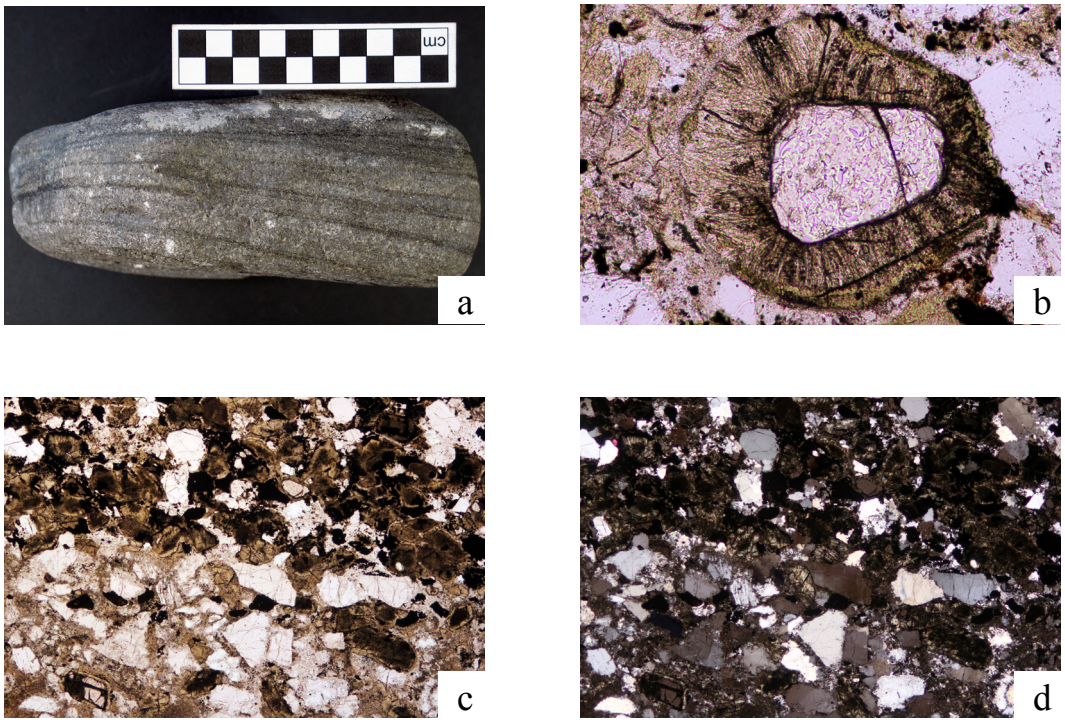

Fig 39. (a) Clast photo. (b) PPL thin section photo of garnet with corona. FOV ~ 0.75 mm. (c) PPL thin section photo. FOV ~6 mm. (d) XPL thin section photo. FOV ~6 mm.

Felsic Gneisses

Garnet Gneisses

10LWB-4.3 *Garnet-biotite orthogneiss* is a coarse-grained, poorly foliated, pink rock with dark grey veins and feldspar augen visible in hand sample. The gneiss is composed of quartz, plagioclase feldspar, potassium feldspar, garnet, biotite, and chlorite, with accessory zircon and opaques. Coarse grains of plagioclase and/or microcline show relict ghost and deformation twins, have quartz, opaque and occasional muscovite inclusions, and are heavily altered to sausserite. Quartz is mostly fine-grained and arranged in clumps between grains of feldspars. Garnets are extremely fine-grained (<< 0.25 mm) and were not suitable for further analysis. Microtextures include minor myrmekite, as well as the intergrowth of biotite with chlorite, opaque, amphibole, and zircon in veins separating feldspars.

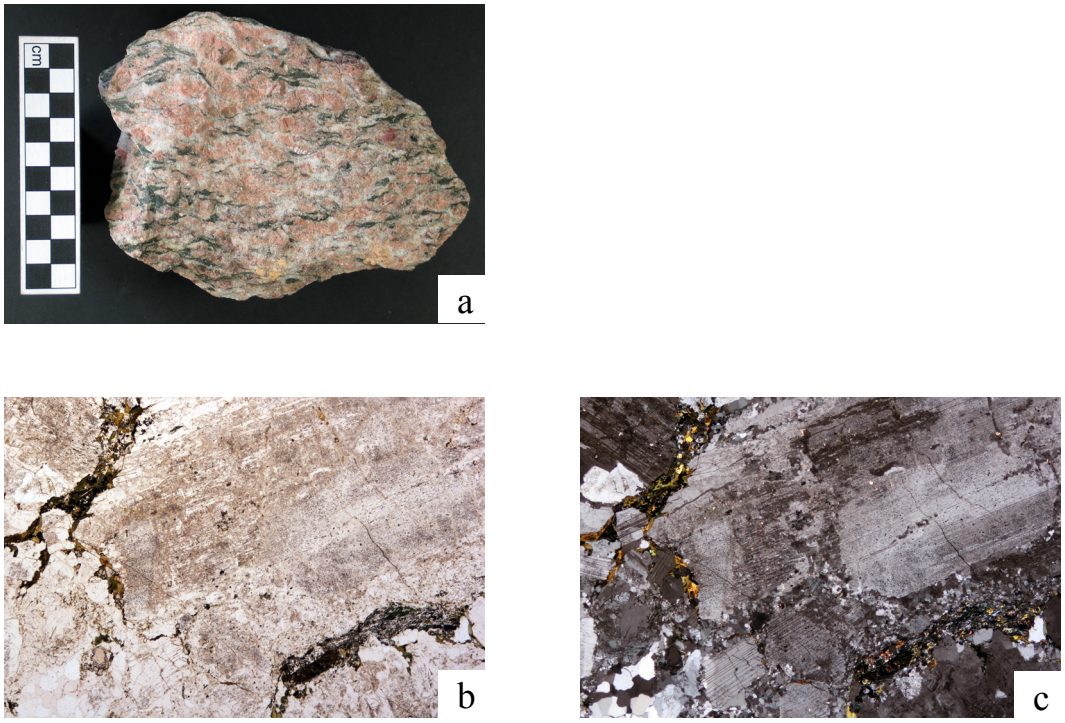

Fig 40. (a) Clast photo. (b) PPL thin section photo. FOV ~6 mm. (c) XPL thin section photo. FOV ~6 mm.

Felsic Gneisses

Garnet Gneisses

10LWB-6.4 *Garnet biotite gneiss* is a fine-grained, well-foliated grey rock with garnets up to 2 cm visible in hand sample. The gneiss is composed of quartz, plagioclase feldspar, garnet, and biotite, with accessory opaques and zircon. Plagioclase feldspar is fresh and exhibits twins, tapered twins, and bent twins. Recrystallized quartz occasionally forms discontinuous mm-length ribbons. Mm-scale quartzofeldspathic layers alternate with mm-scale layers that are more biotite-rich. Garnets are generally <5mm in thin section, have ragged edges and are disarticulated, and have quartz, biotite, and opaque inclusions. Many garnets are << 1 mm.

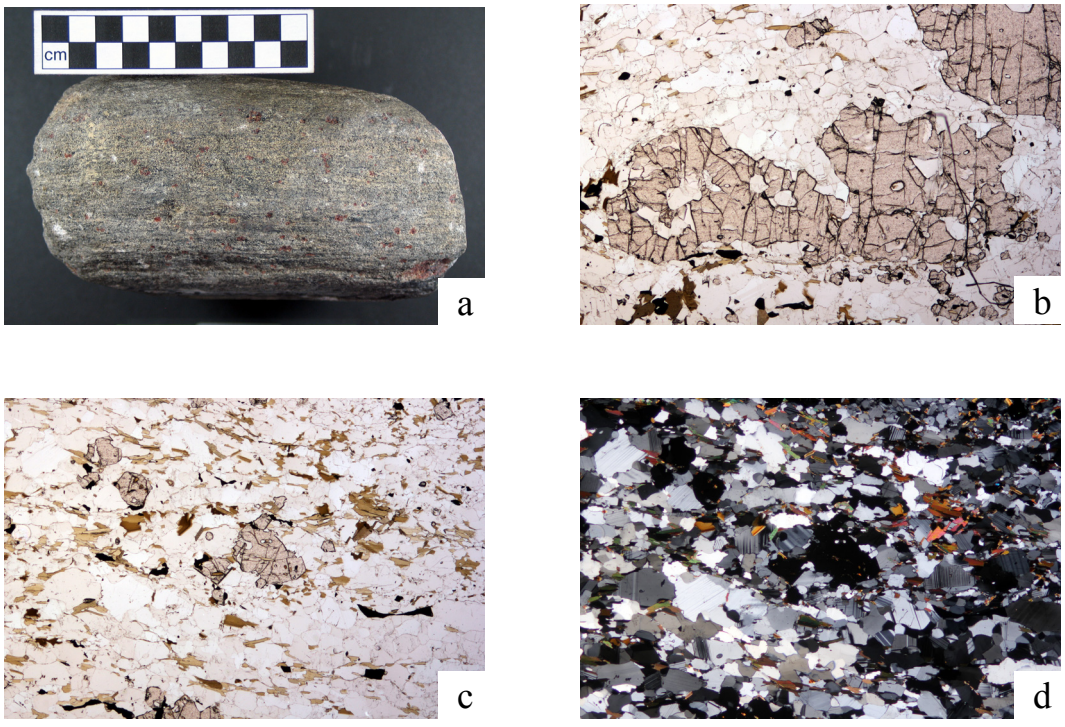

Fig 41. (a) Clast photo. (b) PPL thin section photo of ragged garnet. FOV ~ 6 mm. (c) PPL thin section photo. FOV ~6 mm. (d) XPL thin section photo. FOV ~6 mm.

Amphibolites and Mafic Gneisses

Amphibolites and Mafic Gneisses

10LWB-2.2 *Hornblende-biotite gneiss* is a coarse-grained, well-foliated, grey rock with amphibole clearly visible in hand sample. The amphibolite is composed of quartz, plagioclase feldspar, hornblende, biotite, and potassium feldspar, with accessory opaques, apatite, muscovite and zircon. Plagioclase exhibits twinning and tapered twinning and has quartz inclusions. Amphibole has abundant quartz inclusions.

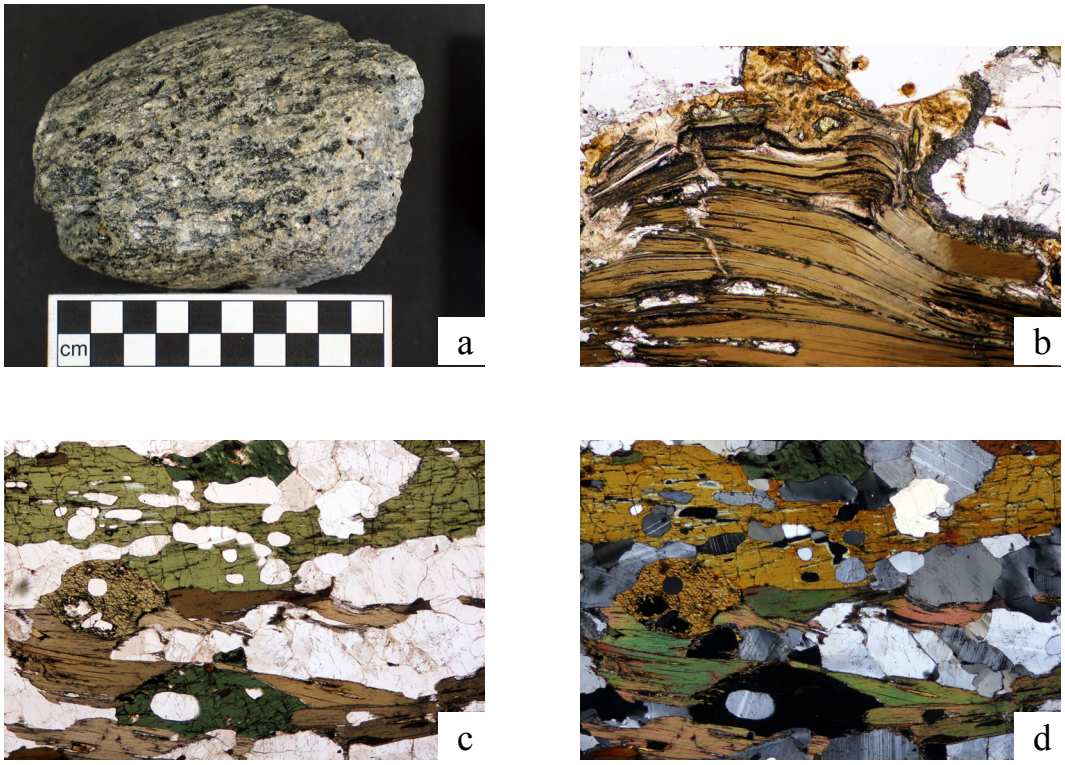

Fig 42. (a) Clast photo. (b) PPL thin section photo of bent biotite. FOV ~ 1 mm. (c) PPL thin section photo. FOV ~6 mm. (d) XPL thin section photo. FOV ~6 mm.

Amphibolites and Mafic Gneisses

Amphibolites and Mafic Gneisses

10LWB-2.5 *Hornblende amphibolite* is a medium-grained, well-foliated, dark grey, layered amphibolite. The amphibolite is composed of plagioclase feldspar, quartz, and amphibole, with minor biotite and accessory opaque, apatite, epidote. Plagioclase exhibits tapered, ghost and bent twins and is altered to sausserite. Quartz mostly occurs as individual grains but also forms discontinuous ribbons. Biotite is a minor component of the rock, and occasionally overgrows amphibole. Opaques are large and blocky as well as small and disseminated throughout amphiboles. A vein in the rock is filled with epidote.

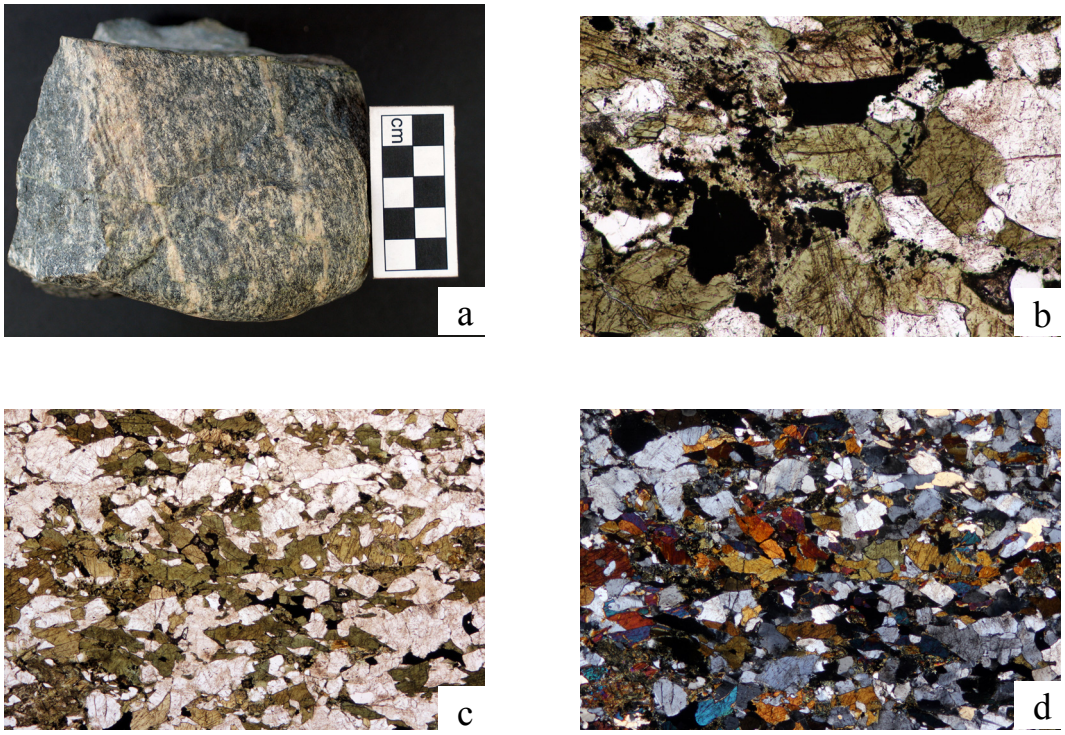

Fig 43. (a) Clast photo. (b) PPL thin section photo of both blocky and disseminated opaques. FOV ~ 1 mm. (c) PPL thin section photo. FOV ~6 mm. (d) XPL thin section photo. FOV ~6 mm.

Amphibolites and Mafic Gneisses

Amphibolites and Mafic Gneisses

10LWB-4.1 *Hornblende-biotite orthogneiss* is a medium to coarse-grained, moderately foliated, slightly folded grey rock with white and salmon-colored lenticular feldspar augen visible in hand sample. Composed of quartz, plagioclase feldspar, potassium feldspar, biotite, and hornblende with accessory calcite, epidote, chlorite, apatite, muscovite, zircon, and opaque. Large feldspar augen are not single crystals but aggregates of smaller grains. Plagioclase displays twins and tapered twins. Potassium feldspar is much more fresh and unaltered than plagioclase feldspar; plagioclase feldspar is commonly riddled with muscovite inclusions, especially along twins and grain boundaries. Quartz is commonly extremely deformed and recrystallized into ribbons. Amphibole is fine-grained. Calcite and epidote fill cracks and inter-grain spaces. Epidote is especially prevalent in fine-grained areas between augen. Opaques are abundant and ragged.

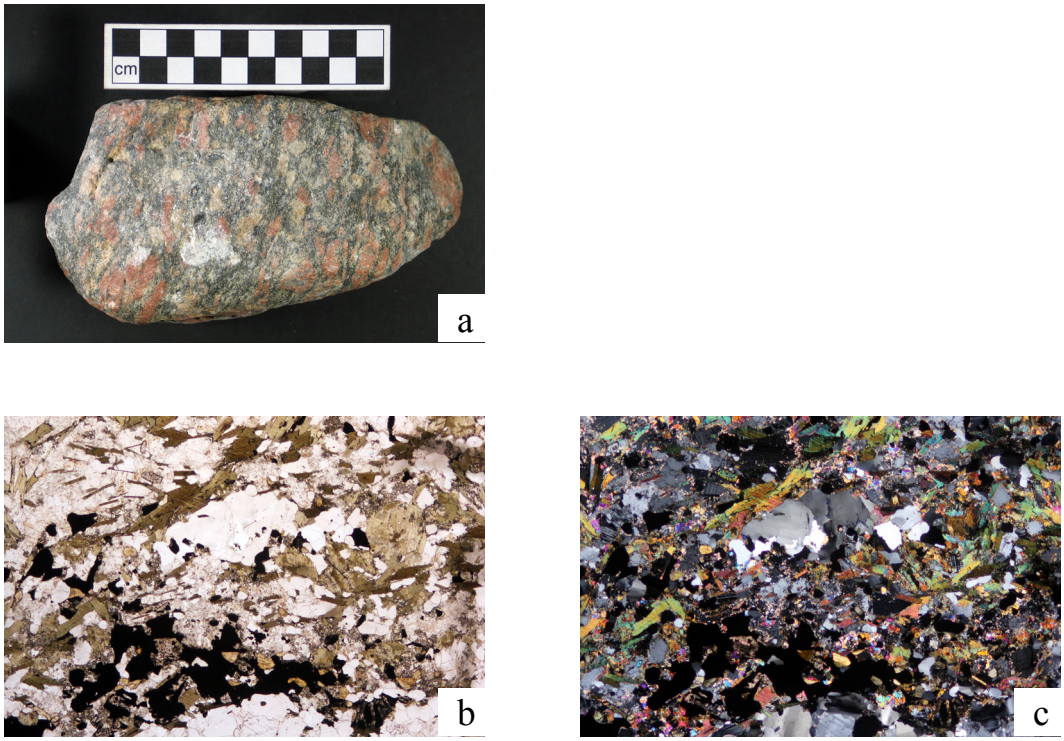

Fig 44. (a) Clast photo. (b) PPL thin section photo. FOV ~6 mm. (c) XPL thin section photo. FOV ~6 mm.

Amphibolites and Mafic Gneisses

Garnet-Amphibolites / Garnet-Mafic Gneisses

10LWB-1.1 *Garnet-tschermakite-biotite gneiss* is a medium-grained, moderately-foliated, layered, cream and black rock. The gneiss is composed of quartz, plagioclase feldspar, hornblende, garnet, biotite, and chlorite, with accessory apatite and opaque. Garnets are large (up to 2 mm) and mostly round/blocky to slightly elongate. Garnets are heavily cracked and contain quartz and oxide inclusions, but are commonly intact with few exceptions. Plagioclase feldspar is fresh and exhibits twins, tapered twins, and bent twins. An unknown blue mineral, possibly riebeckite, grows in cracks and along amphibole grain boundaries. Biotite grains have a rim of a very-fine-grained unknown mineral around them.

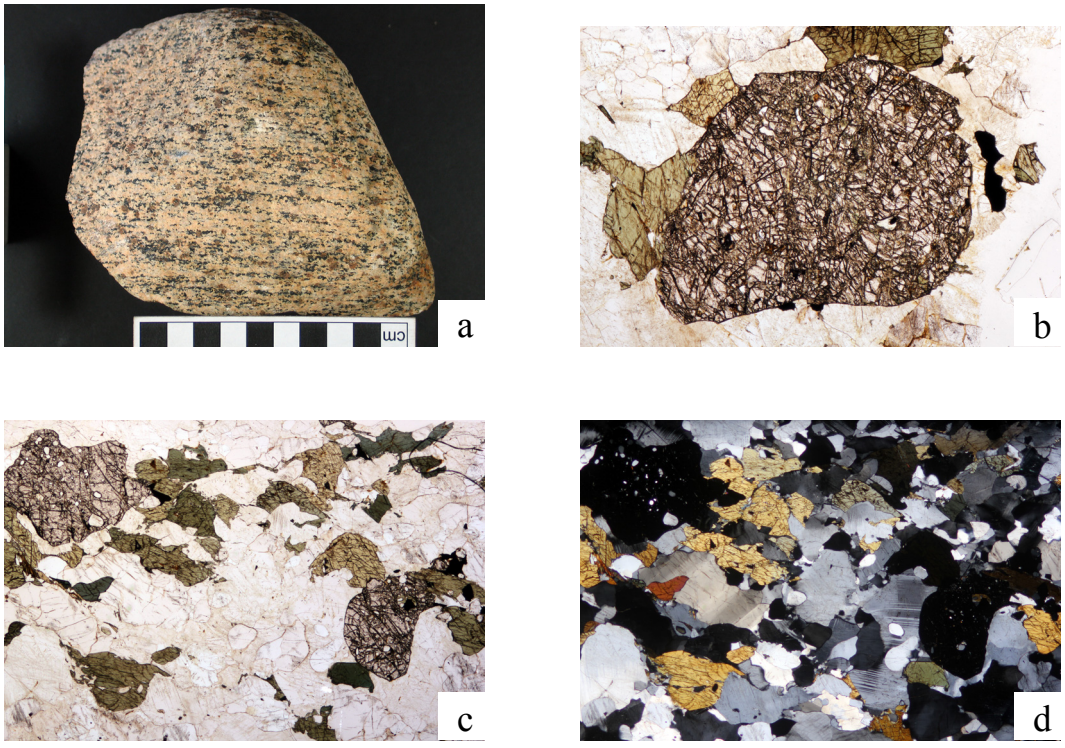

Fig 45. (a) Clast photo. (b) PPL thin section photo of highly cracked garnet. FOV ~ 3 mm. (c) PPL thin section photo. FOV ~6 mm. (d) XPL thin section photo. FOV ~6 mm.

Amphibolites and Mafic Gneisses

Garnet-Amphibolites / Garnet-Mafic Gneisses

10LWB-1.4 *Garnet-biotite-hornblende gneiss* is a medium to coarse-grained, poorly foliated, poorly-layered to massive grey rock. The gneiss is composed of quartz, plagioclase feldspar, garnet, biotite, hornblende, and scapolite, with accessory apatite, opaques, and zircon. Plagioclase exhibits twins and tapered twins and has abundant quartz inclusions that vary from round to elongate in shape. Hornblende and biotite are not coarse but are intact. Garnets are disarticulated and broken up and have abundant quartz, opaque and biotite inclusions.

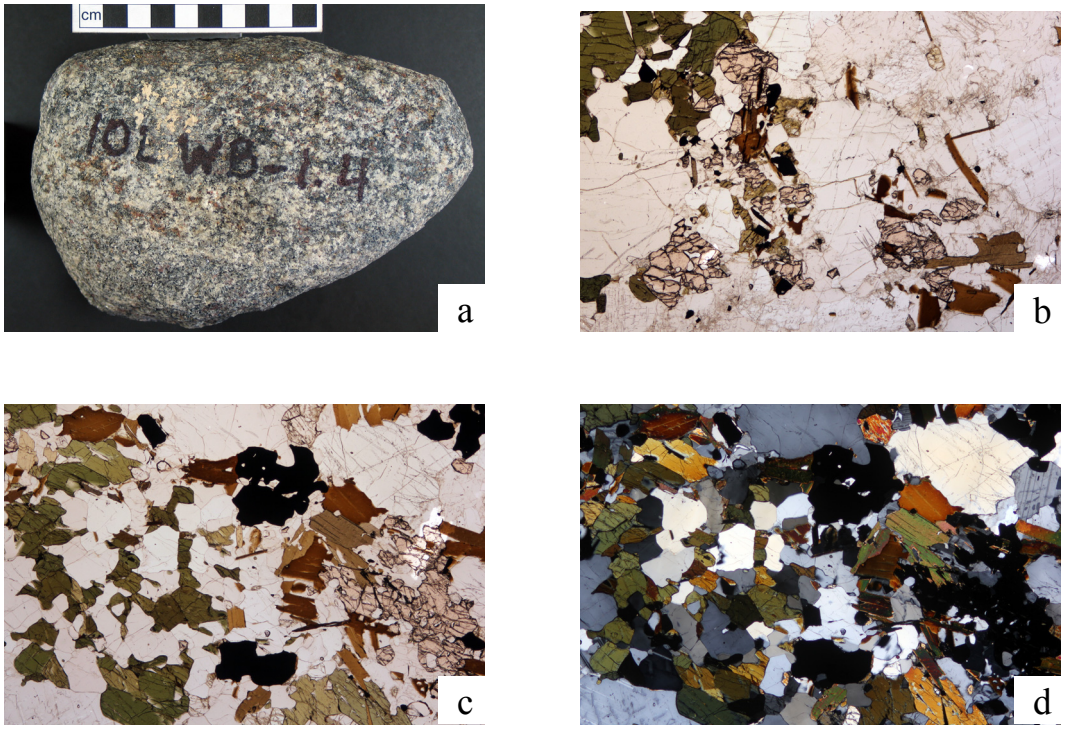

Fig 46. (a) Clast photo. (b) PPL thin section photo of disarticulated garnet. FOV ~ 3 mm. (c) PPL thin section photo. FOV ~6 mm. (d) XPL thin section photo. FOV ~6 mm.

Amphibolites and Mafic Gneisses

Garnet-Amphibolites / Garnet-Mafic Gneisses

10LWB-2.4 *Hornblende-hypersthene-garnet gneiss* is a very fine to fine-grained, poorly foliated, thinly-layered rock. The amphibolite is composed of quartz, plagioclase feldspar, hypersthene, and hornblende, with minor garnet and biotite and abundant accessory opaque. Plagioclase is fresh and exhibits twins and tapered twins. Discontinuous, very thin (<< 1 mm) layers of amphibole and orthopyroxene alternate with quartzofeldspathic layers. There are very few garnets and they are very small (<< 1 mm), boxy, and have some opaque inclusions.

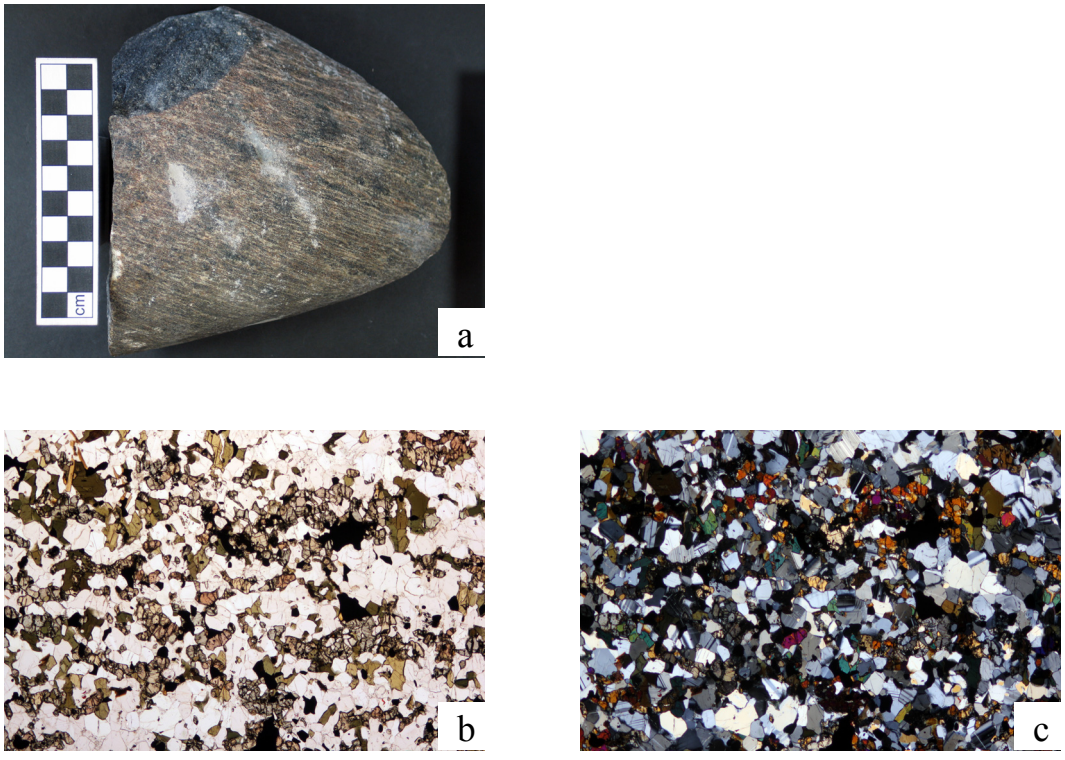

Fig 47. (a) Clast photo. (b) PPL thin section photo. FOV ~6 mm. (c) XPL thin section photo. FOV ~6 mm.

Amphibolites and Mafic Gneisses

Garnet-Amphibolites / Garnet-Mafic Gneisses

10LWB-2.6 *Tschermakite-biotite-garnet gneiss* is a medium-grained, well- (though discontinuously) foliated, crudely-layered, cream colored rock with dark splotches. The amphibolite is composed of quartz, plagioclase feldspar, hornblende, garnet, scapolite, and biotite, with accessory zircon, opaques, apatite, and iron chlorite. Plagioclase is fresh and exhibits twins, ghost twins, and tapered twins. Quartz is mostly small individual grains, but rarely forms discontinuous ribbons. Tschermakite has quartz and opaque inclusions. Garnets are fine-grained (<1 mm), rounded to elongate, typically intact, and have quartz inclusions. Garnets occur mostly in the quartzofeldspathic layers, and where they do occur in amphibole-rich layers, they are heavily cracked and irregularly shaped.

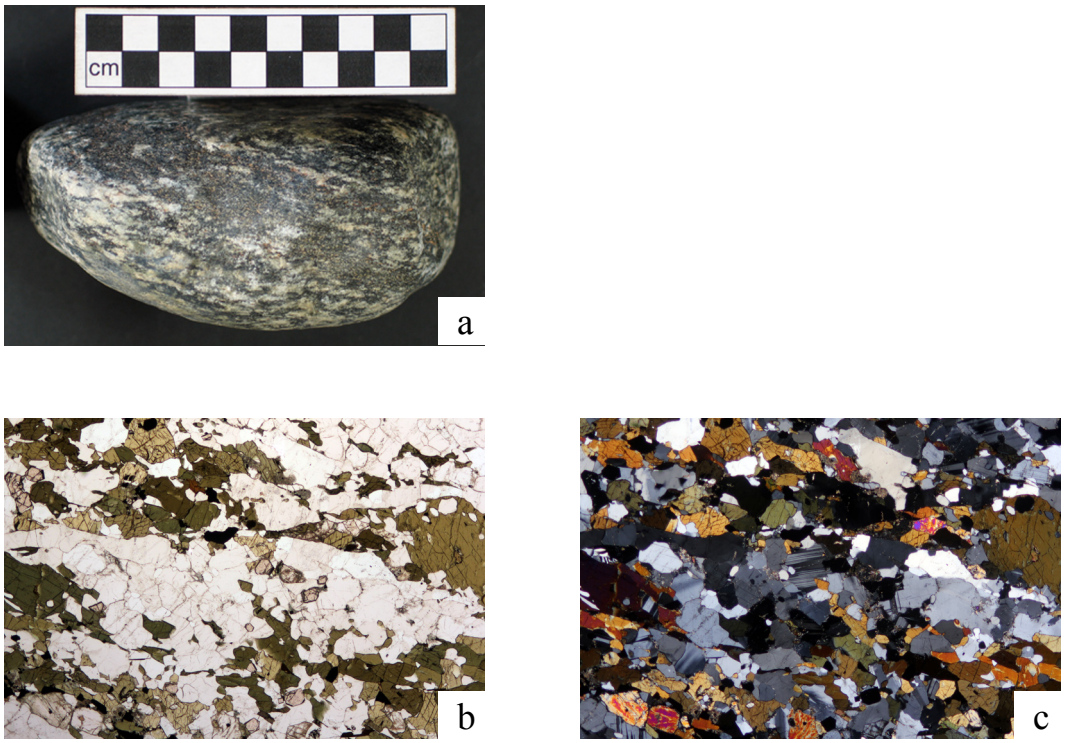

Fig 48. (a) Clast photo. (b) PPL thin section photo. FOV ~6 mm. (c) XPL thin section photo. FOV ~6 mm.

Amphibolites and Mafic Gneisses

Garnet-Amphibolites / Garnet-Mafic Gneisses

10LWB-2.8 *Garnet gneiss* is a medium-grained, non-foliated, light grey thinly-banded rock. The gneiss is composed of quartz, plagioclase feldspar, and microcline and relict unknown yellow mineral (possibly pyroxene) with minor garnet, and accessory opaques, zircon, and late-stage apatite. This rock is extremely altered, possibly by very fine-grained micaceous minerals. Some layer differentiation is visible with less-altered quartzofeldspathic layers alternating with more highly-altered layers. The exceptionally highly altered layers probably contained a mafic mineral like pyroxene but the relict mineral is now too deteriorated to be identified. Garnets are very small (<< 1 mm) and not common. Apatite is notably fresh and appears to have grown much later than deformation and alteration. All opaques have a distinctive rim of fine-grained minerals surrounding them, which may be the remnants of pyroxene.

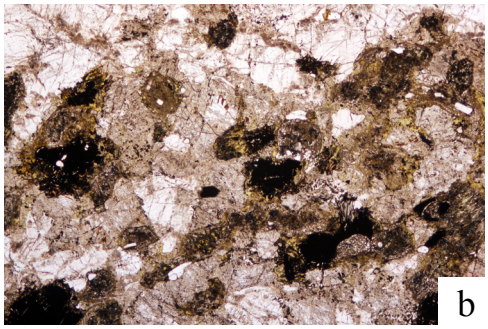

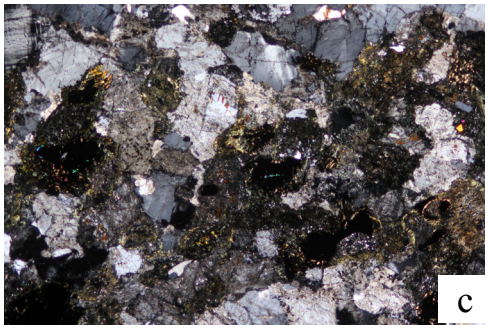

Fig 49. (a) Clast photo. (b) PPL thin section photo. FOV ~6 mm. (c) XPL thin section photo. FOV ~6 mm.

Amphibolites and Mafic Gneisses

Garnet-Amphibolites / Garnet-Mafic Gneisses

10LWB-6.1 *Garnet-tschermakite-scapolite gneiss* is a medium-grained, moderately-foliated discontinuously layered black rock. The amphibolite is composed of quartz, plagioclase feldspar, garnet, tschermakite, and scapolite with minor biotite and riebekite. Discontinuous quartzofeldspathic layers alternate with amphibole-rich layers. Plagioclase exhibits twins, tapered twins, and some bent twins. Amphibole commonly has quartz inclusions. Garnets are small (<1 mm) and blocky to elongate; several are commonly clumped together in a long 'chain' of garnets. Garnet has quartz and amphibole inclusions.

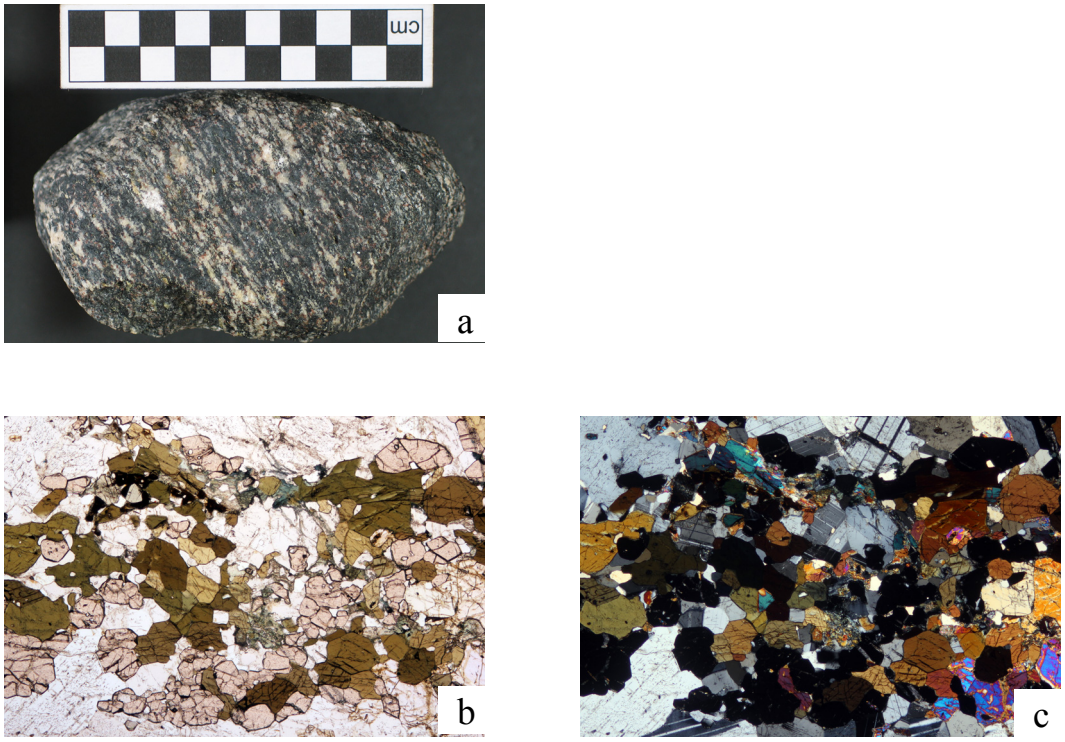

Fig 50. (a) Clast photo. (b) PPL thin section photo. FOV ~6 mm. (c) XPL thin section photo. FOV ~6 mm.

Amphibolites and Mafic Gneisses

Garnet-Amphibolites / Garnet-Mafic Gneisses

10LWB-6.2 *Garnet-tschermakite amphibolite* is a very fine-grained, well-foliated platy black rock. The amphibolite is composed of tschermakite, quartz, plagioclase feldspar, garnet, and biotite, with accessory opaque. The rock is almost entirely composed of amphibole; extremely small grains of plagioclase feldspar and quartz form a matrix between amphibole folia, and there are several thin continuous quartz ribbons. Garnets are large (0.5 mm – 2 mm), round, and have few cracks. Garnets have quartz, hornblende, and occasional biotite inclusions. Some garnets are relatively intact, some are riddled with inclusions, and others have almost completely deteriorated. Deteriorated garnet rims have been replaced by feldspar, quartz, and amphibole.

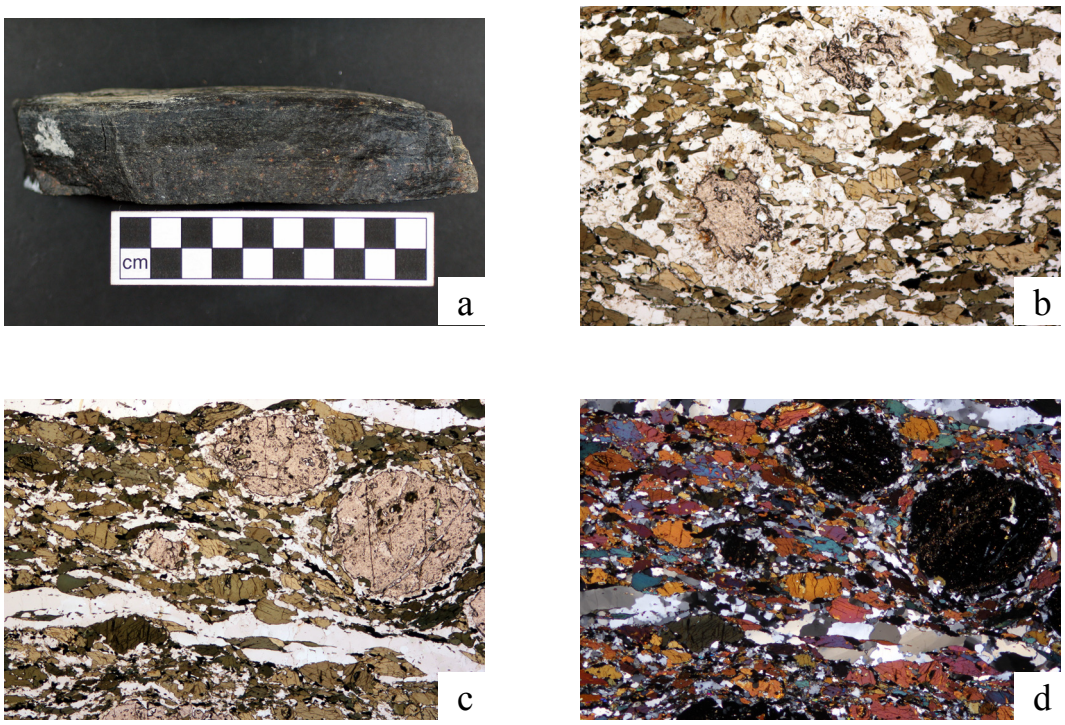

Fig 51. (a) Clast photo. (b) PPL thin section photo of deteriorated garnets. FOV ~ 3 mm. (c) PPL thin section photo. FOV ~6 mm. (d) XPL thin section photo. FOV ~6 mm.

Amphibolites and Mafic Gneisses

Garnet-Amphibolites / Garnet-Mafic Gneisses

10LWB-6.3 *Garnet-tschermakite gneiss* is a medium-grained, poorly foliated, spotted, cream to black rock. The amphibolite is composed of quartz, plagioclase feldspar, garnet, tschermakite, and biotite, with accessory epidote, chlorite, zircon, and opaque. Plagioclase feldspar is fresh and exhibits twins and tapered twins. Garnets can be up to 1 mm wide and blocky, but most are smaller, disarticulated, and broken up. Some garnets are even broken up and replaced by chlorite/epidote. Garnets have abundant quartz inclusions, as well as amphibole and some opaque inclusions. Small garnets commonly occur in clumps. Biotite is robust and overgrows amphibole. Epidote and chlorite occurs with fine-grained quartz and feldspar in only one layer.

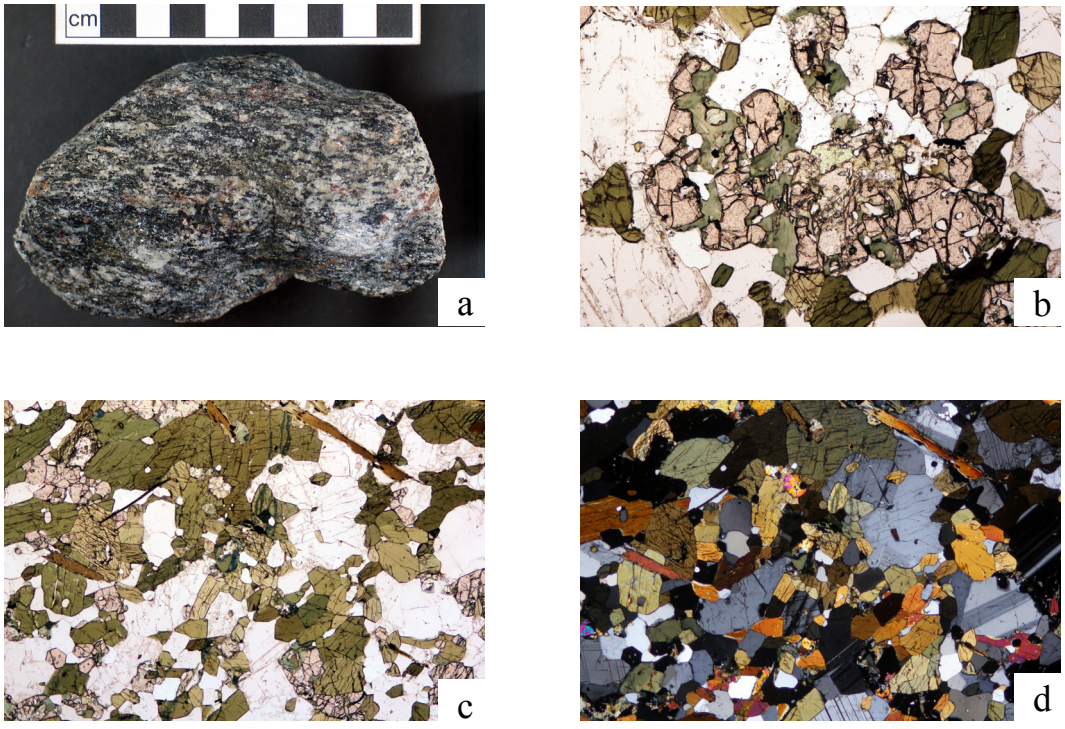

Fig 52. (a) Clast photo. (b) PPL thin section photo of garnet with chlorite and epidote. FOV ~ 3 mm. (c) PPL thin section photo. FOV ~6 mm. (d) XPL thin section photo. FOV ~6 mm.

Appendix B
Mineral Composition Data

Table A. Representative analyses of garnet.

Sample	10LWA-1.3			10LWA-2.2				10LWA-2.2						10LWA-2.2			
	Garnet 3			Garnet 1				Garnet 1b						Garnet 2			
	Core	Rim 1	Rim 2	Core	Rim 1	Rim 2	Rim 3	Rim 4	Rim 5	Rim 6	Rim 7	Rim 8	Rim 9	Core	Rim 1	Rim 2	Rim 3
SiO_2	38.24	37.88	38.29	39.25	39.43	38.76	39.44	38.38	38.90	38.88	38.75	38.73	38.81	39.04	39.00	38.88	38.57
Al_2O_3	21.73	21.51	21.71	22.15	22.13	21.82	22.10	21.69	21.87	21.80	21.93	21.73	21.85	21.95	21.92	22.00	21.83
FeO	27.57	27.70	27.12	25.89	26.40	26.23	26.58	26.01	25.83	25.82	25.77	27.06	26.65	25.75	25.92	25.76	26.72
MgO	5.29	4.71	5.48	6.27	5.76	5.75	5.40	5.19	6.05	5.87	5.69	4.93	5.21	6.05	5.84	5.64	4.57
MnO	5.32	5.79	5.20	2.53	3.61	3.45	3.68	3.71	3.11	2.94	3.20	3.83	3.87	2.92	3.41	3.80	4.68
CaO	3.02	2.93	3.00	6.27	5.59	5.73	6.70	5.85	5.49	6.26	6.21	6.18	6.48	6.15	5.83	5.82	6.02
Total	101.17	100.53	100.79	102.37	102.92	101.74	103.90	100.82	101.26	101.56	101.54	102.46	102.88	101.86	101.91	101.91	102.41
	Cations (calculated on the basis of 12 oxygens assuming all Fe as FeO)																
Si	2.99	2.99	3.00	2.99	3.00	2.99	2.99	2.99	3.00	2.99	2.99	2.98	2.98	2.99	3.00	2.99	2.98
Al	2.00	2.00	2.00	1.99	1.98	1.98	1.97	1.99	1.99	1.98	1.99	1.97	1.97	1.98	1.98	1.99	1.99
Fe	1.80	1.83	1.77	1.65	1.68	1.69	1.68	1.69	1.67	1.66	1.66	1.74	1.71	1.65	1.66	1.66	1.73
Mg	0.62	0.55	0.64	0.71	0.65	0.66	0.61	0.60	0.70	0.67	0.65	0.57	0.60	0.69	0.67	0.65	0.53
Mn	0.35	0.39	0.34	0.16	0.23	0.23	0.24	0.24	0.20	0.19	0.21	0.25	0.25	0.19	0.22	0.25	0.31
Ca	0.25	0.25	0.25	0.51	0.46	0.47	0.54	0.49	0.45	0.52	0.51	0.51	0.53	0.51	0.48	0.48	0.50
Total	8.01	8.01	8.00	8.02	8.01	8.02	8.03	8.01	8.01	8.02	8.02	8.03	8.04	8.01	8.01	8.01	8.03
Mol%Fe (Alm)	0.60	0.61	0.59	0.54	0.56	0.55	0.55	0.56	0.55	0.55	0.55	0.57	0.55	0.54	0.55	0.55	0.56
Mol%Mg (Pyr)	0.20	0.18	0.21	0.23	0.22	0.22	0.20	0.20	0.23	0.22	0.22	0.18	0.19	0.23	0.22	0.21	0.17
Mol% Mn (Sps)	0.12	0.13	0.11	0.05	0.08	0.07	0.08	0.08	0.07	0.06	0.07	0.08	0.08	0.06	0.07	0.08	0.10
Mol%Ca (Grs)	0.08	0.08	0.08	0.17	0.15	0.16	0.18	0.16	0.15	0.17	0.17	0.17	0.17	0.17	0.16	0.16	0.16
Total	1.00	1.00	1.00	1.00	1.00	1.00	1.00	1.00	1.00	1.00	1.00	1.00	1.00	1.00	1.00	1.00	1.00
Mg/(Mg+Fe)	0.25	0.23	0.26	0.30	0.28	0.28	0.27	0.26	0.29	0.29	0.28	0.25	0.26	0.30	0.29	0.28	0.23

Table A (continued). Representative analyses of garnet.

Sample	10LWA-2.3							10LWA-5.1						10LWB-1.1			
	Garnet 1			Garnet 2				Garnet 1			Garnet 2			Garnet 1		Garnet 1b	
	Core	Rim 1	Rim 2	Core	Rim 1	Rim 2	Rim 3	Core	Rim 1	Rim 2	Core	Rim 1	Rim 2	Rim 1	Rim 2	Core	Rim 3
SiO_2	38.74	38.63	39.29	38.87	37.90	38.71	39.44	37.99	38.17	38.01	37.88	37.90	37.82	38.04	38.09	37.90	37.96
Al_2O_3	22.11	22.05	22.40	22.05	21.42	22.09	22.51	21.28	21.42	21.50	21.34	21.55	21.35	21.50	21.72	21.58	21.34
FeO	26.56	26.87	26.99	26.32	30.24	27.17	27.28	26.92	26.31	26.15	26.69	26.10	25.92	31.10	29.71	28.56	31.39
MgO	7.28	7.14	7.02	7.27	5.14	6.81	7.52	5.78	5.64	5.61	5.74	5.58	5.63	2.36	3.02	2.64	2.83
MnO	1.20	1.43	1.65	1.07	1.42	1.14	1.08	1.70	1.66	1.82	1.64	1.78	1.67	3.06	1.71	2.65	2.65
CaO	5.37	5.01	5.11	5.90	4.92	5.72	4.84	6.48	7.06	6.99	6.44	6.64	6.85	5.94	7.56	8.04	5.77
Total	101.27	101.14	102.47	101.47	101.04	101.64	102.67	100.16	100.26	100.08	99.73	99.55	99.24	101.99	101.82	101.38	101.94
	Cations (calculated on the basis of 12 oxygens assuming all Fe as FeO)																
Si	2.97	2.97	2.98	2.97	2.97	2.97	2.98	2.98	2.98	2.98	2.98	2.98	2.98	2.99	2.98	2.98	2.99
Al	2.00	2.00	2.00	1.99	1.98	2.00	2.00	1.97	1.97	1.98	1.98	2.00	1.98	1.99	2.00	2.00	1.98
Fe	1.70	1.73	1.71	1.68	1.98	1.74	1.72	1.76	1.72	1.71	1.75	1.72	1.71	2.05	1.94	1.88	2.07
Mg	0.83	0.82	0.79	0.83	0.60	0.78	0.85	0.68	0.66	0.65	0.67	0.65	0.66	0.28	0.35	0.31	0.33
Mn	0.08	0.09	0.11	0.07	0.09	0.07	0.07	0.11	0.11	0.12	0.11	0.12	0.11	0.20	0.11	0.18	0.18
Ca	0.44	0.41	0.42	0.48	0.41	0.47	0.39	0.54	0.59	0.59	0.54	0.56	0.58	0.50	0.63	0.68	0.49
Total	8.03	8.03	8.02	8.03	8.04	8.03	8.02	8.04	8.03	8.03	8.03	8.02	8.03	8.01	8.02	8.02	8.02
Mol%Fe (Alm)	0.56	0.57	0.57	0.55	0.64	0.57	0.57	0.57	0.56	0.56	0.57	0.56	0.56	0.68	0.64	0.62	0.67
Mol%Mg (Pyr)	0.27	0.27	0.26	0.27	0.19	0.25	0.28	0.22	0.21	0.21	0.22	0.21	0.22	0.09	0.12	0.10	0.11
Mol% Mn (Sps)	0.03	0.03	0.04	0.02	0.03	0.02	0.02	0.04	0.04	0.04	0.04	0.04	0.04	0.07	0.04	0.06	0.06
Mol%Ca (Grs)	0.14	0.14	0.14	0.16	0.13	0.15	0.13	0.18	0.19	0.19	0.18	0.18	0.19	0.17	0.21	0.22	0.16
Total	1.00	1.00	1.00	1.00	1.00	1.00	1.00	1.00	1.00	1.00	1.00	1.00	1.00	1.00	1.00	1.00	1.00
Mg/(Mg+Fe)	0.33	0.32	0.32	0.33	0.23	0.31	0.33	0.28	0.28	0.28	0.28	0.28	0.28	0.12	0.15	0.14	0.14

Table A (continued). Representative analyses of garnet.

Sample	10LWB-1.1 (continued)						10LWB-1.2					10LWB-1.3					
	Garnet 1b (continued)			Garnet 2			Garnet 2b					Garnet 1					Garnet 2
	Rim 4	Rim 5	Rim 6	Core	Rim 1	Rim 2	Core	Rim 1	Rim 2	Rim 3	Rim 4	Core	Rim 1	Rim 2	Rim 3	Rim 4	Core
SiO_2	38.02	38.31	38.19	38.04	37.58	37.85	38.69	38.72	39.09	38.82	38.98	38.38	38.12	38.13	37.61	37.63	38.40
Al_2O_3	21.54	21.80	21.73	21.72	21.54	21.44	22.02	21.89	22.20	22.02	22.01	22.08	21.84	22.00	21.32	21.19	22.02
FeO	31.00	28.80	29.06	28.26	29.11	30.45	27.45	27.35	30.71	29.11	28.03	28.71	29.57	28.46	28.40	28.74	27.34
MgO	2.77	3.03	3.13	3.04	2.37	2.63	8.71	8.71	6.51	7.48	8.22	6.12	5.34	5.89	5.53	5.30	6.86
MnO	2.67	1.73	1.61	1.59	2.63	2.82	1.24	1.24	1.42	1.34	1.30	4.08	4.72	4.14	4.69	4.46	3.24
CaO	5.67	8.15	7.83	8.39	7.17	5.90	1.79	1.93	1.58	1.95	1.91	3.26	2.43	3.04	2.60	2.69	3.78
Total	101.66	101.82	101.55	101.04	100.40	101.09	99.91	99.85	101.51	100.73	100.45	102.64	102.03	101.65	100.15	100.01	101.63
Cations (calculated on the basis of 12 oxygens assuming all Fe as FeO)																	
Si	2.99	2.99	2.99	2.98	2.99	2.99	2.99	3.00	3.01	3.00	3.00	2.95	2.97	2.96	2.98	2.98	2.96
Al	2.00	2.00	2.00	2.01	2.02	2.00	2.01	2.00	2.02	2.01	2.00	2.00	2.00	2.01	1.99	1.98	2.00
Fe	2.04	1.88	1.90	1.85	1.93	2.01	1.77	1.77	1.98	1.88	1.81	1.85	1.92	1.85	1.88	1.91	1.76
Mg	0.32	0.35	0.36	0.36	0.28	0.31	1.00	1.00	0.75	0.86	0.94	0.70	0.62	0.68	0.65	0.63	0.79
Mn	0.18	0.11	0.11	0.11	0.18	0.19	0.08	0.08	0.09	0.09	0.09	0.27	0.31	0.27	0.31	0.30	0.21
Ca	0.48	0.68	0.66	0.70	0.61	0.50	0.15	0.16	0.13	0.16	0.16	0.27	0.20	0.25	0.22	0.23	0.31
Total	8.01	8.01	8.01	8.01	8.01	8.01	8.01	8.01	7.98	8.00	8.00	8.04	8.03	8.03	8.03	8.03	8.04
Mol%Fe (Alm)	0.68	0.62	0.63	0.61	0.64	0.67	0.59	0.59	0.67	0.63	0.60	0.60	0.63	0.60	0.61	0.62	0.57
Mol%Mg (Pyr)	0.11	0.12	0.12	0.12	0.09	0.10	0.33	0.33	0.25	0.29	0.32	0.23	0.20	0.22	0.21	0.20	0.26
Mol% Mn (Sps)	0.06	0.04	0.04	0.03	0.06	0.06	0.03	0.03	0.03	0.03	0.03	0.09	0.10	0.09	0.10	0.10	0.07
Mol%Ca (Grs)	0.16	0.23	0.22	0.23	0.20	0.17	0.05	0.05	0.04	0.05	0.05	0.09	0.07	0.08	0.07	0.07	0.10
Total	1.00	1.00	1.00	1.00	1.00	1.00	1.00	1.00	1.00	1.00	1.00	1.00	1.00	1.00	1.00	1.00	1.00
Mg/(Mg+Fe)	0.14	0.16	0.16	0.16	0.13	0.13	0.36	0.36	0.27	0.31	0.34	0.28	0.24	0.27	0.26	0.25	0.31

Table A (continued). Representative analyses of garnet.

Sample	10LWB-1.3 (continued)								10LWB-1.5									
	Garnet 2 (continued)					Garnet 2b			Garnet 1					Garnet 2b				
	Rim 1	Rim 2	Rim 3	Rim 4	Rim 5	Core	Rim 6	Rim 7	Core	Rim 1	Rim 2	Incl	Rim 3	Core	Rim 1	Rim 2	Incl	Rim 3
SiO_2	38.33	38.14	37.99	37.06	37.81	38.49	38.58	38.30	39.29	39.20	39.22	38.67	38.92	39.69	39.85	39.85	39.38	39.04
Al_2O_3	22.07	21.97	21.76	20.92	21.48	22.08	22.13	22.08	22.44	22.35	22.37	22.03	22.15	22.59	22.74	22.62	22.27	22.10
FeO	27.40	28.92	29.47	30.16	29.13	27.45	28.14	27.71	27.31	28.39	27.02	27.05	27.41	27.43	27.34	27.29	26.80	28.18
MgO	6.88	6.03	5.37	4.30	5.39	6.76	6.82	7.27	9.42	8.56	9.29	9.84	9.85	9.45	9.54	9.63	10.09	9.11
MnO	3.44	3.70	3.78	3.82	3.80	3.28	3.49	3.26	0.67	0.65	0.62	0.67	0.63	0.66	0.58	0.69	0.60	0.69
CaO	3.12	2.40	3.25	3.21	2.83	3.82	2.72	2.26	1.88	1.82	1.96	1.80	1.95	2.37	2.25	2.19	2.07	2.11
Total	101.24	101.16	101.61	99.47	100.43	101.89	101.88	100.88	101.01	100.98	100.49	100.05	100.91	102.19	102.29	102.27	101.21	101.23
	Cations (calculated on the basis of 12 oxygens assuming all Fe as FeO)																	
Si	2.97	2.97	2.96	2.98	2.98	2.96	2.97	2.97	2.99	3.00	3.00	2.97	2.97	2.99	2.99	2.99	2.98	2.98
Al	2.01	2.02	2.00	1.98	2.00	2.00	2.01	2.02	2.01	2.01	2.01	2.00	1.99	2.00	2.01	2.00	1.99	1.99
Fe	1.77	1.88	1.92	2.03	1.92	1.77	1.81	1.80	1.74	1.82	1.73	1.74	1.75	1.73	1.72	1.71	1.70	1.80
Mg	0.79	0.70	0.63	0.51	0.63	0.78	0.78	0.84	1.07	0.98	1.06	1.13	1.12	1.06	1.07	1.08	1.14	1.04
Mn	0.23	0.24	0.25	0.26	0.25	0.21	0.23	0.21	0.04	0.04	0.04	0.04	0.04	0.04	0.04	0.04	0.04	0.04
Ca	0.26	0.20	0.27	0.28	0.24	0.31	0.22	0.19	0.15	0.15	0.16	0.15	0.16	0.19	0.18	0.18	0.17	0.17
Total	8.03	8.02	8.03	8.03	8.02	8.04	8.03	8.02	8.00	8.00	8.00	8.03	8.03	8.01	8.00	8.01	8.02	8.02
Mol%Fe (Alm)	0.58	0.62	0.63	0.66	0.63	0.58	0.59	0.59	0.58	0.61	0.58	0.57	0.57	0.57	0.57	0.57	0.56	0.59
Mol%Mg (Pyr)	0.26	0.23	0.20	0.17	0.21	0.25	0.26	0.28	0.36	0.33	0.35	0.37	0.37	0.35	0.36	0.36	0.37	0.34
Mol% Mn (Sps)	0.07	0.08	0.08	0.08	0.08	0.07	0.07	0.07	0.01	0.01	0.01	0.01	0.01	0.01	0.01	0.01	0.01	0.01
Mol%Ca (Grs)	0.08	0.07	0.09	0.09	0.08	0.10	0.07	0.06	0.05	0.05	0.05	0.05	0.05	0.06	0.06	0.06	0.06	0.06
Total	1.00	1.00	1.00	1.00	1.00	1.00	1.00	1.00	1.00	1.00	1.00	1.00	1.00	1.00	1.00	1.00	1.00	1.00
Mg/(Mg+Fe)	0.31	0.27	0.25	0.20	0.25	0.31	0.30	0.32	0.38	0.35	0.38	0.39	0.39	0.38	0.38	0.39	0.40	0.37

Table A (continued). Representative analyses of garnet.

Sample	10LWB-1.6							10LWB-1.7									
	Garnet 2							Garnet 1					Garnet 2				
	Core	Rim 1	Rim 2	Rim 3	Rim 4	Rim 5	Rim 6	Core	Rim 1	Rim 2	Rim 3	Rim 4	Core	Rim 1	Rim 2	Rim 3	Rim 4
SiO_2	38.42	37.48	38.04	37.57	37.88	37.89	38.51	35.97	35.73	35.99	36.31	36.24	35.56	35.48	35.75	35.66	35.82
Al_2O_3	21.96	21.63	22.02	21.67	22.01	21.90	22.26	20.93	20.79	21.01	21.17	21.19	20.73	20.63	20.74	20.95	20.85
FeO	25.14	30.00	27.87	29.27	28.19	30.72	28.19	26.74	28.84	29.16	28.98	28.81	26.54	28.21	28.23	27.63	28.48
MgO	6.91	4.86	6.75	5.30	6.58	5.39	7.68	0.00	0.00	0.00	0.00	0.00	0.00	0.00	0.00	0.00	0.00
MnO	2.04	3.33	2.61	3.12	2.79	3.32	2.48	16.61	14.14	14.27	14.38	14.49	16.68	14.72	14.86	15.29	14.83
CaO	5.79	2.75	3.06	2.99	2.73	2.79	2.79	0.40	0.38	0.35	0.39	0.41	0.40	0.37	0.42	0.39	0.40
Total	100.26	100.06	100.35	99.91	100.17	102.02	101.91	100.65	99.87	100.78	101.23	101.14	99.92	99.41	99.99	99.91	100.38
	Cations (calculated on the basis of 12 oxygens assuming all Fe as FeO)																
Si	2.98	2.97	2.97	2.97	2.96	2.95	2.95	2.96	2.96	2.96	2.97	2.96	2.95	2.96	2.96	2.95	2.96
Al	2.00	2.02	2.02	2.02	2.03	2.01	2.01	2.03	2.03	2.04	2.04	2.04	2.03	2.03	2.03	2.05	2.03
Fe	1.63	1.99	1.82	1.94	1.84	2.00	1.81	1.84	2.00	2.00	1.98	1.97	1.84	1.97	1.96	1.91	1.97
Mg	0.80	0.58	0.79	0.63	0.77	0.63	0.88	0.00	0.00	0.00	0.00	0.00	0.00	0.00	0.00	0.00	0.00
Mn	0.13	0.22	0.17	0.21	0.19	0.22	0.16	1.16	0.99	0.99	0.99	1.00	1.17	1.04	1.04	1.07	1.04
Ca	0.48	0.23	0.26	0.25	0.23	0.23	0.23	0.03	0.03	0.03	0.03	0.04	0.04	0.03	0.04	0.03	0.04
Total	8.02	8.02	8.02	8.02	8.02	8.04	8.04	8.02	8.02	8.02	8.01	8.02	8.03	8.03	8.02	8.02	8.03
Mol%Fe (Alm)	0.54	0.66	0.60	0.64	0.61	0.65	0.59	0.61	0.66	0.66	0.66	0.65	0.60	0.65	0.64	0.63	0.65
Mol%Mg (Pyr)	0.26	0.19	0.26	0.21	0.25	0.20	0.29	0.00	0.00	0.00	0.00	0.00	0.00	0.00	0.00	0.00	0.00
Mol% Mn (Sps)	0.04	0.07	0.06	0.07	0.06	0.07	0.05	0.38	0.33	0.33	0.33	0.33	0.38	0.34	0.34	0.36	0.34
Mol%Ca (Grs)	0.16	0.08	0.08	0.08	0.08	0.08	0.07	0.01	0.01	0.01	0.01	0.01	0.01	0.01	0.01	0.01	0.01
Total	1.00	1.00	1.00	1.00	1.00	1.00	1.00	1.00	1.00	1.00	1.00	1.00	1.00	1.00	1.00	1.00	1.00
Mg/(Mg+Fe)	0.33	0.22	0.30	0.24	0.29	0.24	0.33	0.00	0.00	0.00	0.00	0.00	0.00	0.00	0.00	0.00	0.00

Table A (continued). Representative analyses of garnet.

Sample	10LWB-2.6								10LWB-6.1								
	Garnet 1				Garnet 2				Garnet 1			Garnet 2					
	Core	Rim 1	Rim 2	Rim 3	Core	Rim 1	Rim 2	Rim 3	Core	Rim 1	Rim 2	Core	Incl 1	Incl 2	Rim 1	Rim 2	Rim 3
SiO_2	38.71	38.92	38.66	38.83	39.31	39.22	39.03	39.07	39.06	39.44	38.16	38.41	37.95	38.38	38.09	38.28	38.47
Al_2O_3	21.61	21.77	21.69	21.88	21.92	21.91	21.84	22.03	22.13	22.21	21.57	21.80	21.52	21.81	21.51	21.72	21.84
FeO	25.67	25.59	27.15	26.49	25.85	25.43	26.15	26.14	23.93	24.35	23.92	24.42	24.99	24.90	24.70	25.97	24.95
MgO	5.99	5.84	4.90	5.68	6.15	5.98	5.41	5.82	8.19	8.17	7.71	7.54	7.00	7.74	7.41	6.70	7.26
MnO	2.61	2.62	3.05	2.74	2.62	2.64	2.85	2.76	0.92	0.94	0.96	0.97	0.94	0.94	1.01	1.05	1.02
CaO	6.21	6.51	6.35	6.24	6.35	6.59	6.48	6.42	6.32	6.25	6.11	6.54	6.75	6.16	6.30	6.31	6.39
Total	100.79	101.25	101.80	101.86	####	101.76	101.77	102.25	100.55	101.36	98.41	99.68	99.15	99.94	99.02	100.03	99.92
	Cations (calculated on the basis of 12 oxygens assuming all Fe as FeO)																
Si	3.00	3.00	2.99	2.99	3.00	3.00	3.00	2.99	2.99	2.99	2.99	2.98	2.97	2.97	2.98	2.98	2.98
Al	1.97	1.98	1.98	1.98	1.97	1.98	1.98	1.99	1.99	1.99	1.99	1.99	1.99	1.99	1.98	1.99	1.99
Fe	1.66	1.65	1.76	1.70	1.65	1.63	1.68	1.67	1.53	1.54	1.57	1.58	1.64	1.61	1.61	1.69	1.62
Mg	0.69	0.67	0.57	0.65	0.70	0.68	0.62	0.66	0.93	0.92	0.90	0.87	0.82	0.89	0.86	0.78	0.84
Mn	0.17	0.17	0.20	0.18	0.17	0.17	0.19	0.18	0.06	0.06	0.06	0.06	0.06	0.06	0.07	0.07	0.07
Ca	0.52	0.54	0.53	0.51	0.52	0.54	0.53	0.53	0.52	0.51	0.51	0.54	0.57	0.51	0.53	0.53	0.53
Total	8.01	8.01	8.02	8.02	8.01	8.01	8.01	8.02	8.02	8.02	8.02	8.03	8.04	8.04	8.03	8.03	8.02
Mol%Fe (Alm)	0.55	0.54	0.58	0.56	0.54	0.54	0.56	0.55	0.50	0.51	0.51	0.52	0.53	0.52	0.53	0.55	0.53
Mol%Mg (Pyr)	0.23	0.22	0.19	0.21	0.23	0.23	0.21	0.22	0.31	0.30	0.30	0.28	0.27	0.29	0.28	0.25	0.27
Mol% Mn (Sps)	0.06	0.06	0.07	0.06	0.06	0.06	0.06	0.06	0.02	0.02	0.02	0.02	0.02	0.02	0.02	0.02	0.02
Mol%Ca (Grs)	0.17	0.18	0.17	0.17	0.17	0.18	0.18	0.17	0.17	0.17	0.17	0.18	0.18	0.17	0.17	0.17	0.17
Total	1.00	1.00	1.00	1.00	1.00	1.00	1.00	1.00	1.00	1.00	1.00	1.00	1.00	1.00	1.00	1.00	1.00
Mg/(Mg+Fe)	0.29	0.29	0.24	0.28	0.30	0.30	0.27	0.28	0.38	0.37	0.36	0.36	0.33	0.36	0.35	0.32	0.34

Table A (continued). Representative analyses of garnet.

Sample	10LWB-6.2														10LWB-6.3		
	Garnet 1							Garnet 2							Garnet 2		
	Core	Rim 1	Rim 2	Rim 3	Rim 4	Rim 5	Rim 6	Core	Rim 1	Rim 2	Rim 3	Incl	Rim 4	Rim 5	Core	Rim 1	Rim 2
SiO_2	37.37	37.01	37.20	37.48	37.34	36.96	37.19	37.45	37.01	37.07	37.01	37.19	37.22	37.01	38.56	38.44	38.42
Al_2O_3	20.96	21.02	20.90	21.29	21.01	20.91	21.12	21.02	20.92	20.83	20.96	20.85	20.91	20.75	21.61	21.50	21.50
FeO	30.49	32.50	30.92	32.80	30.43	31.40	32.29	26.68	30.48	28.97	31.08	28.34	31.09	30.07	24.83	26.97	25.33
MgO	0.96	1.50	1.25	1.54	1.34	1.49	1.55	0.75	1.26	0.71	1.47	0.78	1.42	1.15	6.31	5.49	5.94
MnO	2.00	2.24	1.09	2.24	1.65	2.06	2.15	3.90	1.48	0.96	1.54	2.77	1.80	1.18	1.60	1.69	1.63
CaO	9.34	6.31	9.33	6.38	9.20	7.63	6.75	10.98	8.56	11.04	7.71	10.40	8.06	9.55	7.47	6.41	7.47
Total	101.12	100.58	100.68	101.72	100.96	100.44	101.05	100.78	99.71	99.58	99.76	100.33	100.50	99.70	100.37	100.49	100.29
	Cations (calculated on the basis of 12 oxygens assuming all Fe as FeO)																
Si	2.98	2.98	2.98	2.98	2.98	2.97	2.97	2.98	2.98	2.99	2.98	2.98	2.98	2.98	2.99	3.00	2.99
Al	1.97	1.99	1.97	1.99	1.97	1.98	1.99	1.97	1.99	1.98	1.99	1.97	1.98	1.97	1.97	1.98	1.97
Fe	2.03	2.19	2.07	2.18	2.03	2.11	2.16	1.78	2.06	1.95	2.10	1.90	2.08	2.03	1.61	1.76	1.65
Mg	0.11	0.18	0.15	0.18	0.16	0.18	0.18	0.09	0.15	0.09	0.18	0.09	0.17	0.14	0.73	0.64	0.69
Mn	0.14	0.15	0.07	0.15	0.11	0.14	0.15	0.26	0.10	0.07	0.11	0.19	0.12	0.08	0.11	0.11	0.11
Ca	0.80	0.54	0.80	0.54	0.79	0.66	0.58	0.94	0.74	0.95	0.67	0.89	0.69	0.83	0.62	0.54	0.62
Total	8.03	8.03	8.04	8.03	8.04	8.04	8.03	8.03	8.02	8.02	8.02	8.03	8.03	8.03	8.03	8.02	8.03
Mol%Fe (Alm)	0.66	0.71	0.67	0.71	0.66	0.68	0.70	0.58	0.67	0.64	0.69	0.62	0.68	0.66	0.53	0.58	0.54
Mol%Mg (Pyr)	0.04	0.06	0.05	0.06	0.05	0.06	0.06	0.03	0.05	0.03	0.06	0.03	0.06	0.04	0.24	0.21	0.22
Mol% Mn (Sps)	0.04	0.05	0.02	0.05	0.04	0.05	0.05	0.09	0.03	0.02	0.03	0.06	0.04	0.03	0.03	0.04	0.04
Mol%Ca (Grs)	0.26	0.18	0.26	0.18	0.25	0.21	0.19	0.31	0.24	0.31	0.22	0.29	0.23	0.27	0.20	0.18	0.20
Total	1.00	1.00	1.00	1.00	1.00	1.00	1.00	1.00	1.00	1.00	1.00	1.00	1.00	1.00	1.00	1.00	1.00
Mg/(Mg+Fe)	0.05	0.08	0.07	0.08	0.07	0.08	0.08	0.05	0.07	0.04	0.08	0.05	0.08	0.06	0.31	0.27	0.29

Table A (continued). Representative analyses of garnet.

Sample	10LWB-6.3 (continued)											LWB-6.4						
	Garnet 2 (continued)						Garnet 3					Garnet 2				Garnet 3		
	Rim 3	Rim 4	Rim 5	Rim 6	Rim 7	Rim 8	Core	Rim 1	Rim 2	Rim 3	Rim 4	Core	Rim 1	Rim 2	Rim 3	Core	Rim 1	Rim 2
SiO_2	38.31	38.33	37.96	37.97	37.96	37.97	38.45	38.61	37.68	37.65	38.64	38.64	38.59	39.03	38.79	39.21	38.92	40.14
Al_2O_3	21.47	21.62	21.42	21.36	21.39	21.48	21.66	21.63	21.18	21.25	21.65	22.00	21.79	22.41	22.24	22.24	22.17	22.46
FeO	25.61	25.25	27.44	26.89	26.97	27.52	26.10	25.93	27.19	27.08	26.10	27.52	27.14	28.24	27.92	28.30	28.83	28.44
MgO	6.20	6.10	5.38	5.67	5.86	5.35	6.32	6.16	5.48	5.43	6.14	8.18	8.10	7.25	7.84	8.27	7.06	7.51
MnO	1.71	1.67	1.74	1.77	1.66	1.78	1.77	1.76	1.77	1.70	1.77	1.36	1.27	1.59	1.33	1.33	1.44	1.35
CaO	6.57	7.32	6.45	6.33	6.20	6.13	6.45	6.40	6.11	6.25	6.47	2.86	2.89	3.04	2.92	2.53	3.30	3.21
Total	99.86	100.28	100.39	100.00	100.03	100.23	100.76	100.49	99.41	99.37	100.77	100.56	99.78	101.55	101.05	101.89	101.72	103.11
	Cations (calculated on the basis of 12 oxygens assuming all Fe as FeO)																	
Si	2.99	2.98	2.97	2.98	2.98	2.98	2.98	3.00	2.98	2.98	2.99	2.99	2.99	2.99	2.99	2.99	2.99	2.99
Al	1.98	1.98	1.98	1.98	1.98	1.99	1.98	1.98	1.97	1.98	1.98	1.98	1.98	1.98	1.98	1.98	1.98	1.98
Fe	1.67	1.64	1.80	1.76	1.77	1.80	1.69	1.68	1.80	1.79	1.69	1.69	1.69	1.69	1.69	1.69	1.69	1.69
Mg	0.72	0.71	0.63	0.66	0.68	0.63	0.73	0.71	0.65	0.64	0.71	0.71	0.71	0.71	0.71	0.71	0.71	0.71
Mn	0.11	0.11	0.12	0.12	0.11	0.12	0.12	0.12	0.12	0.11	0.12	0.12	0.12	0.12	0.12	0.12	0.12	0.12
Ca	0.55	0.61	0.54	0.53	0.52	0.52	0.54	0.53	0.52	0.53	0.54	0.54	0.54	0.54	0.54	0.54	0.54	0.54
Total	8.02	8.03	8.04	8.03	8.04	8.03	8.03	8.02	8.03	8.03	8.02	8.02	8.02	8.02	8.02	8.02	8.02	8.02
Mol%Fe (Alm)	0.55	0.54	0.58	0.57	0.57	0.59	0.55	0.55	0.58	0.58	0.55	0.55	0.55	0.55	0.55	0.55	0.55	0.55
Mol%Mg (Pyr)	0.24	0.23	0.20	0.22	0.22	0.20	0.24	0.23	0.21	0.21	0.23	0.23	0.23	0.23	0.23	0.23	0.23	0.23
Mol% Mn (Sps)	0.04	0.04	0.04	0.04	0.04	0.04	0.04	0.04	0.04	0.04	0.04	0.04	0.04	0.04	0.04	0.04	0.04	0.04
Mol%Ca (Grs)	0.18	0.20	0.18	0.17	0.17	0.17	0.17	0.17	0.17	0.17	0.18	0.18	0.18	0.18	0.18	0.18	0.18	0.18
Total	1.00	1.00	1.00	1.00	1.00	1.00	1.00	1.00	1.00	1.00	1.00	1.00	1.00	1.00	1.00	1.00	1.00	1.00
Mg/(Mg+Fe)	0.30	0.30	0.26	0.27	0.28	0.26	0.30	0.30	0.26	0.26	0.30	0.30	0.30	0.30	0.30	0.30	0.30	0.30

Table B. Representative analyses of biotite.

Sample	10LWA-1.3		10LWA-2.2										10LWA-2.3	10LWB-1.1	10LWB-1.2	
	Garnet 3		Garnet 1				Garnet 1b			Garnet 2			Garnet 1	Garnet 1b	Garnet 2b	
	Bt Incl	Bt 1	Bt Incl	Bt 1	Bt 2	Bt 3	Bt 4	Bt 5	Bt 6	Bt Incl	Bt 1	Bt 2	Bt 1	Bt 1	Bt 1	Bt 2
SiO_2	38.17	36.82	37.86	36.73	38.14	37.11	34.70	37.13	36.85	37.06	36.57	36.79	35.74	34.45	37.48	36.63
TiO_2	4.44	4.43	2.96	2.31	2.59	2.46	2.34	2.44	2.52	2.73	1.99	2.56	2.04	2.84	5.06	4.93
Al_2O_3	15.89	15.44	16.93	16.93	17.44	16.72	16.87	16.92	16.40	15.64	16.70	16.40	17.40	16.63	17.03	16.68
Fe_2O_3																
FeO	11.98	16.39	12.61	17.07	16.79	17.19	17.67	16.82	17.49	11.45	15.76	16.98	16.74	23.30	11.35	13.80
MnO	0.00	0.00	0.00	0.00	0.00	0.00	0.00	0.00	0.00	0.00	0.00	0.00	0.00	0.00	0.00	0.00
MgO	15.70	12.40	15.95	12.92	14.23	13.67	13.60	13.68	13.40	16.64	14.01	12.88	13.00	8.12	15.05	13.29
CaO	0.00	0.00	0.00	0.00	0.00		0.00	0.00	0.00	0.00	0.00	0.00	0.00	0.00	0.00	0.00
Li_2O																
Na_2O	0.00	0.00	0.29	0.00										0.00		
K_2O	9.68	9.97	9.78	9.73	9.98	9.94	7.37	9.98	9.85	8.66	8.51	9.39	7.23	9.42	10.29	10.33
Cr_2O_3																
Total	95.87	95.46	96.39	95.69	99.16	97.08	92.56	96.97	96.51	92.19	93.54	94.99	92.15	94.75	96.25	95.65
Cations (calculated on the basis of 11 oxygens and corrected for Fe3+)																
Si	2.79	2.77	2.76	2.76	2.75	2.75	2.68	2.75	2.75	2.80	2.77	2.78	2.74	2.70	2.73	2.72
Fe3+ (iv)	0.06	0.08	0.06	0.09	0.08	0.09	0.09	0.08	0.09	0.06	0.08	0.09	0.09	0.12	0.06	0.07
Al(iv)	1.16	1.15	1.18	1.16	1.17	1.17	1.23	1.17	1.16	1.15	1.15	1.14	1.17	1.17	1.22	1.21
Al(vi)	0.06	0.08	0.06	0.09	0.08	0.09	0.09	0.08	0.09	0.06	0.08	0.09	0.09	0.12	0.06	0.07
Ti	0.24	0.25	0.16	0.13	0.14	0.14	0.14	0.14	0.14	0.15	0.11	0.15	0.12	0.17	0.28	0.28
Fe3+(vi)	0.09	0.12	0.09	0.13	0.12	0.13	0.14	0.12	0.13	0.09	0.12	0.13	0.13	0.18	0.08	0.10
Fe2+(vi)	0.59	0.82	0.61	0.86	0.81	0.85	0.91	0.83	0.87	0.58	0.80	0.86	0.86	1.22	0.55	0.69
Mg	1.71	1.39	1.73	1.45	1.53	1.51	1.57	1.51	1.49	1.87	1.58	1.45	1.49	0.95	1.63	1.47
Mn	0.00	0.00	0.00	0.00	0.00	0.00	0.00	0.00	0.00	0.00	0.00	0.00	0.00	0.00	0.00	0.00
Cr	0.00	0.00	0.00	0.00	0.00	0.00	0.00	0.00	0.00	0.00	0.00	0.00	0.00	0.00	0.00	0.00
Ca	0.00	0.00	0.00	0.00	0.00	0.00	0.00	0.00	0.00	0.00	0.00	0.00	0.00	0.00	0.00	0.00
Na	0.00	0.00	0.04	0.00	0.00	0.00	0.00	0.00	0.00	0.00	0.00	0.00	0.00	0.00	0.00	0.00
K	0.90	0.96	0.91	0.93	0.92	0.94	0.73	0.94	0.94	0.83	0.82	0.90	0.71	0.94	0.96	0.98
Total	7.59	7.63	7.61	7.58	7.60	7.65	7.57	7.63	7.66	7.58	7.52	7.57	7.39	7.59	7.56	7.58
Mg/(Mg+Fe)	0.74	0.63	0.74	0.63	0.65	0.64	0.63	0.64	0.63	0.76	0.66	0.63	0.63	0.44	0.75	0.68

Table B (continued). Representative analyses of biotite.

Sample	10LWB-1.3								10LWB-1.5							10LWB-1.6			
	Garnet 1					Garnet 2			Garnet 1			Garnet 2b				Garnet 2			
	Bt 1	Bt 2	Bt 3	Bt 4	Bt 5	Bt 1	Bt 2	Bt 3	Bt Incl	Bt 1	Bt 2	Bt Incl	Bt 1	Bt 2	Bt 3	Bt 1	Bt 2	Bt 3	Bt 4
SiO_2	35.01	36.01	35.34	35.01	35.46	34.78	35.64	36.12	37.53	36.76	37.25	38.73	37.86	37.22	36.78	35.99	35.72	35.80	36.02
TiO_2	2.81	2.61	2.88	2.86	2.84	2.33	2.43	2.50	6.71	5.96	5.24	5.67	5.33	5.68	5.02	1.80	1.71	1.87	1.95
Al_2O_3	18.03	18.43	18.64	18.00	18.42	18.18	18.26	18.57	15.98	15.96	16.07	18.41	16.37	15.58	15.90	18.25	17.80	18.15	18.03
Fe_2O_3																			
FeO	16.29	15.33	14.25	15.37	15.29	15.47	15.54	14.84	10.53	13.77	12.77	9.04	10.97	14.03	12.96	14.58	15.75	15.62	15.79
MnO	0.00	0.00	0.00	0.00	0.00	0.00	0.00	0.00	0.00	0.00	0.00	0.00	0.00	0.00	0.00	0.00	0.00	0.00	
MgO	11.33	12.80	13.20	11.93	12.21	12.29	12.47	12.85	15.13	13.03	14.13	15.11	15.23	13.46	14.51	13.44	13.02	13.54	13.61
CaO	0.00	0.00	0.00	0.00	0.00	0.00	0.00	0.00	0.00	0.00	0.00	0.00	0.00	0.00	0.00	0.00	0.00	0.00	
Li_2O																			
Na_2O								0.00	0.36	0.00	0.00								
K_2O	8.79	8.76	9.62	9.59	9.86	8.45	8.83	9.84	9.82	9.99	9.93	9.70	10.05	10.11	10.18	9.89	9.85	9.74	10.21
Cr_2O_3										0.25	0.11				0.00				
Total	92.26	93.95	93.92	92.76	94.09	91.50	93.17	94.73	96.05	95.71	95.49	96.65	95.81	96.07	95.36	93.95	93.85	94.72	95.60
Cations (calculated on the basis of 11 oxygens and corrected for Fe3+)																			
Si	2.71	2.71	2.67	2.70	2.69	2.70	2.71	2.71	2.73	2.73	2.75	2.75	2.76	2.75	2.73	2.72	2.72	2.70	2.70
Fe3+ (iv)	0.08	0.08	0.07	0.08	0.08	0.08	0.08	0.07	0.05	0.07	0.06	0.04	0.05	0.07	0.06	0.07	0.08	0.08	0.08
Al(iv)	1.21	1.21	1.26	1.23	1.23	1.22	1.21	1.22	1.22	1.20	1.18	1.20	1.19	1.18	1.21	1.20	1.20	1.22	1.22
Al(vi)	0.08	0.08	0.07	0.08	0.08	0.08	0.08	0.07	0.05	0.07	0.06	0.04	0.05	0.07	0.06	0.07	0.08	0.08	0.08
Ti	0.16	0.15	0.16	0.17	0.16	0.14	0.14	0.14	0.37	0.33	0.29	0.30	0.29	0.32	0.28	0.10	0.10	0.11	0.11
Fe3+(vi)	0.13	0.12	0.11	0.12	0.12	0.12	0.12	0.11	0.08	0.10	0.09	0.06	0.08	0.10	0.10	0.11	0.12	0.12	0.12
Fe2+(vi)	0.84	0.77	0.72	0.79	0.78	0.80	0.79	0.74	0.51	0.68	0.63	0.43	0.53	0.69	0.64	0.74	0.80	0.79	0.79
Mg	1.31	1.44	1.49	1.37	1.38	1.42	1.42	1.44	1.64	1.44	1.56	1.60	1.65	1.48	1.61	1.51	1.48	1.52	1.52
Mn	0.00	0.00	0.00	0.00	0.00	0.00	0.00	0.00	0.00	0.00	0.00	0.00	0.00	0.00	0.00	0.00	0.00	0.00	0.00
Cr	0.00	0.00	0.00	0.00	0.00	0.00	0.00	0.00	0.00	0.01	0.00	0.00	0.00	0.00	0.00	0.00	0.00	0.00	0.00
Ca	0.00	0.00	0.00	0.00	0.00	0.00	0.00	0.00	0.00	0.00	0.00	0.00	0.00	0.00	0.00	0.00	0.00	0.00	0.00
Na	0.00	0.00	0.00	0.00	0.00	0.00	0.00	0.00	0.05	0.00	0.00	0.00	0.00	0.00	0.00	0.00	0.00	0.00	0.00
K	0.87	0.84	0.93	0.94	0.95	0.84	0.86	0.94	0.91	0.95	0.94	0.88	0.93	0.95	0.96	0.95	0.96	0.94	0.98
Total	7.39	7.39	7.48	7.47	7.47	7.40	7.40	7.45	7.61	7.59	7.58	7.32	7.55	7.62	7.66	7.49	7.54	7.55	7.59
Mg/(Mg+Fe)	0.61	0.65	0.67	0.63	0.64	0.64	0.64	0.66	0.76	0.68	0.71	0.79	0.76	0.68	0.71	0.67	0.65	0.66	0.66

Table B (con't). Representative analyses of biotite.

Sample	**10LWB-6.4**			
	Garnet 2		Garnet 3	
	Bt Incl	Bt 1	Bt 1	Bt 2
SiO_2	36.97	36.55	37.05	36.71
TiO_2	3.82	4.00	3.92	4.17
Al_2O_3	17.01	16.78	17.31	17.37
Fe_2O_3				
FeO	11.16	13.24	14.47	14.34
MnO	0.00	0.00	0.00	0.00
MgO	15.99	14.25	13.86	13.62
CaO	0.00	0.00	0.00	0.00
Li_2O				
Na_2O				
K_2O	10.26	10.21	10.34	10.10
Cr_2O_3				
Total	95.21	95.03	96.96	96.30
Cations (as above)				
Si	2.72	2.72	2.72	2.71
Fe3+ (iv)	0.05	0.07	0.07	0.07
Al(iv)	1.22	1.21	1.21	1.22
Al(vi)	0.05	0.07	0.07	0.07
Ti	0.21	0.22	0.22	0.23
Fe3+(vi)	0.08	0.10	0.11	0.11
Fe2+(vi)	0.55	0.66	0.71	0.71
Mg	1.75	1.58	1.52	1.50
Mn	0.00	0.00	0.00	0.00
Cr	0.00	0.00	0.00	0.00
Ca	0.00	0.00	0.00	0.00
Na	0.00	0.00	0.00	0.00
K	0.96	0.97	0.97	0.95
Total	7.62	7.60	7.59	7.56
Mg/(Mg+Fe)	0.76	0.71	0.68	0.68

Table C. Representative analyses of amphibole.

Sample	10LWA-2.3	10LWB-1.1			10LWB-2.6			10LWB-6.1					10LWB-6.2	
	Garnet 2	Garnet 1b		Garnet 2	Garnet 1	Garnet 2		Garnet 1	Garnet 2				Garnet 1	
	Hbl 1	Hbl 1	Hbl 2	Hbl 1	Hbl 1	Hbl 1	Hbl 2	Hbl 1	Incl 1	Incl 2	Hbl 1	Hbl 2	Hbl 1	Hbl 2
SiO_2	42.47	39.56	40.28	41.25	41.72	42.02	42.53	41.81	41.71	42.74	42.16	42.58	42.57	42.49
TiO_2	1.44	0.32	0.62	0.95	2.39	1.96	2.15	2.04	2.36	2.08	2.01	1.87	1.21	1.17
Al_2O_3	12.81	16.54	14.92	14.81	13.28	12.99	12.49	12.21	12.62	12.28	12.44	12.10	11.75	11.46
FeO	16.86	21.21	20.88	19.46	15.67	15.84	15.55	13.12	12.03	10.49	13.00	13.26	24.03	24.04
MnO	0.00	0.00	0.00	0.00	0.00	0.00	0.00	0.00	0.00	0.00	0.00	0.00	0.00	0.00
MgO	10.08	5.84	6.49	7.62	10.35	10.33	10.63	11.50	12.24	13.80	11.93	11.85	5.55	5.68
CaO	11.36	11.48	11.36	11.29	11.46	11.63	11.52	11.40	11.52	11.53	11.58	11.53	10.63	10.59
Na2O	1.24	1.24	1.28	1.38	1.58	1.44	1.48	1.57	1.75	1.93	1.66	1.65	1.44	1.50
K2O	1.24	1.10	0.95	0.87	1.82	1.88	1.77	1.58	1.47	1.32	1.80	1.44	0.61	0.63
Total	97.51	97.30	96.79	97.62	98.27	98.10	98.12	95.24	95.69	96.16	96.57	96.27	97.79	97.56
	Cations (Calculated on the basis of 23 oxygens assuming all Fe as FeO)													
Si	6.38	6.09	6.22	6.25	6.23	6.29	6.35	6.36	6.29	6.35	6.33	6.40	6.56	6.57
Al(iv)	1.62	1.91	1.78	1.75	1.77	1.71	1.65	1.64	1.71	1.65	1.67	1.60	1.44	1.43
Al(vi)	0.65	1.09	0.93	0.90	0.57	0.58	0.54	0.55	0.53	0.50	0.53	0.55	0.69	0.66
Cr	0.00	0.00	0.00	0.00	0.00	0.00	0.00	0.00	0.00	0.00	0.00	0.00	0.00	0.00
Fe	2.12	2.73	2.70	2.47	1.96	1.98	1.94	1.67	1.52	1.30	1.63	1.67	3.10	3.11
Ti	0.16	0.04	0.07	0.11	0.27	0.22	0.24	0.23	0.27	0.23	0.23	0.21	0.14	0.14
Mg	2.26	1.34	1.49	1.72	2.30	2.31	2.36	2.61	2.75	3.06	2.67	2.66	1.28	1.31
Mn	0.00	0.00	0.00	0.00	0.00	0.00	0.00	0.00	0.00	0.00	0.00	0.00	0.00	0.00
Ca	1.83	1.89	1.88	1.83	1.83	1.86	1.84	1.86	1.86	1.84	1.86	1.86	1.75	1.75
Na	0.36	0.37	0.38	0.41	0.46	0.42	0.43	0.46	0.51	0.56	0.48	0.48	0.43	0.45
K	0.24	0.22	0.19	0.17	0.35	0.36	0.34	0.31	0.28	0.25	0.34	0.28	0.12	0.12
Total	15.62	15.67	15.64	15.60	15.73	15.73	15.70	15.69	15.72	15.74	15.75	15.69	15.51	15.54
Mg/(Mg+Fe)	0.52	0.33	0.36	0.41	0.54	0.54	0.55	0.61	0.64	0.70	0.62	0.61	0.29	0.30

Table C (continued). Representative analyses of amphibole.

Sample	10LWB-6.2 (continued)						10LWB-6.3							
	Garnet 1 (con't)		Garnet 2				Garnet 2					Garnet 3		
	Hbl 3	Hbl 4	Hbl 1	Hbl Incl	Hbl 2	Hbl 3	Hbl 1	Hbl 2	Hbl 3	Hbl 4	Hbl 5	Hbl 1	Hbl 2	Hbl 3
SiO_2	42.91	42.09	42.53	41.22	42.05	43.03	41.96	42.72	41.94	41.65	43.13	42.30	41.72	41.88
TiO_2	1.21	1.19	1.03	1.47	1.21	1.30	1.66	1.48	1.39	1.71	1.47	1.73	1.65	1.81
Al_2O_3	11.36	11.42	10.51	11.21	11.22	11.62	12.38	11.83	12.46	12.53	11.06	12.40	12.36	12.30
FeO	24.07	23.95	23.83	26.34	24.49	22.52	14.89	14.26	13.94	14.01	13.80	14.95	13.45	14.01
MnO	0.00	0.00	0.00	0.00	0.00		0.00	0.00	0.00	0.00	0.00	0.00	0.00	0.00
MgO	5.84	5.78	5.77	4.04	5.95	5.61	11.11	11.73	11.40	11.34	12.12	11.07	11.70	11.43
CaO	10.51	10.43	10.66	10.77	10.08	10.86	11.51	11.63	11.50	11.38	11.56	11.62	11.51	11.46
Na2O	1.58	1.60	1.14	1.71	1.58	1.06	1.39	1.38	1.41	1.52	1.34	1.41	1.42	1.46
K2O	0.61	0.64	0.53	0.23	0.53	0.62	1.86	1.78	1.82	1.83	1.68	1.88	1.86	1.87
Total	98.10	97.09	95.99	96.98	97.10	96.62	96.75	96.81	95.86	95.97	96.16	97.35	95.66	96.21
	Cations (Calculated on the basis of 23 oxygens assuming all Fe as FeO)													
Si	6.59	6.54	6.67	6.50	6.55	6.65	6.34	6.43	6.37	6.32	6.51	6.35	6.34	6.34
Al(iv)	1.41	1.46	1.33	1.50	1.45	1.35	1.66	1.57	1.63	1.68	1.49	1.65	1.66	1.66
Al(vi)	0.65	0.64	0.62	0.58	0.60	0.77	0.55	0.52	0.60	0.57	0.48	0.55	0.55	0.54
Cr	0.00	0.00	0.00	0.00	0.00	0.00	0.00	0.00	0.00	0.00	0.00	0.00	0.00	0.00
Fe	3.09	3.11	3.13	3.47	3.19	2.91	1.88	1.79	1.77	1.78	1.74	1.88	1.71	1.77
Ti	0.14	0.14	0.12	0.17	0.14	0.15	0.19	0.17	0.16	0.20	0.17	0.20	0.19	0.21
Mg	1.34	1.34	1.35	0.95	1.38	1.29	2.50	2.63	2.58	2.57	2.73	2.48	2.65	2.58
Mn	0.00	0.00	0.00	0.00	0.00	0.00	0.00	0.00	0.00	0.00	0.00	0.00	0.00	0.00
Ca	1.73	1.74	1.79	1.82	1.68	1.80	1.86	1.87	1.87	1.85	1.87	1.87	1.87	1.86
Na	0.47	0.48	0.35	0.52	0.48	0.32	0.41	0.40	0.41	0.45	0.39	0.41	0.42	0.43
K	0.12	0.13	0.11	0.05	0.10	0.12	0.36	0.34	0.35	0.35	0.32	0.36	0.36	0.36
Total	15.54	15.58	15.46	15.57	15.57	15.36	15.75	15.73	15.74	15.76	15.70	15.74	15.75	15.75
Mg/(Mg+Fe)	0.30	0.30	0.30	0.21	0.30	0.31	0.57	0.59	0.59	0.59	0.61	0.57	0.61	0.59

Table D. Representative Analyses of Pyroxene

Sample	**10LWA-5.1** Garnet 1 Pyx 1	Pyx 2	Garnet 2 Pyx 1
SiO_2	51.13	51.09	50.34
Al_2O_3	1.30	1.48	2.84
FeO	26.28	26.33	10.15
MnO	0.60	0.57	0.00
MgO	19.37	19.28	12.09
CaO	0.43	0.47	21.45
Na_2O	-	-	0.62
Total	99.11	99.23	97.48
Cations (calculated on the basis of 6 oxygens)			
Si	1.96	1.96	1.94
Al(iv)	0.04	0.04	0.06
Al(vi)	0.08	0.09	0.20
Cr	0.00	0.00	0.00
Fe	0.84	0.85	0.33
Ti	0.00	0.00	0.00
Mg	1.11	1.10	0.69
Mn	0.02	0.02	0.00
Ca	0.02	0.02	0.88
Na	0.00	0.00	0.09
K	0.00	0.00	0.00
Total	4.07	4.08	4.19
Mg(Mg+Fe)	0.57	0.57	0.68

Appendix C
Geothermometry Results

Sample #	Pair#	T (°C) Garnet core pairs								T (°C) Garnet rim pairs							
		Garnet-biotite @5 kbar					Garnet-hornblende @5 kbar			Garnet-biotite@ 5kbar					Garnet-hornblende @5 kbar		
		F&S '78	H&S '82	F&S w/ B '90	K&R '94	Avg	G&P '84	P '85	Avg	F&S '78	H&S '82	F&S w/ B '90	K&R '94	Avg	G&P '84	P '85	Avg
LWA-1.3	1	460.7	491.5	483.0	478.4	478.4											
	2	626.4	659.7	650.5	621.1	639.4											
	3									577.6	610.3	602.7	580.7	592.8			
LWA-2.2	1	531.0	594.7	594.2	584.8	576.2											
	2									605.1	673.9	674.0	655.3	652.1			
	3									581.5	647.6	646.0	632.1	626.8			
	4									626.4	693.9	694.3	673.5	672.0			
	5	482.8	544.1	542.6	541.6	527.8											
	6									532.4	594.3	592.9	589.5	577.3			
LWA-2.3	1									755.4	810.2	810.3	768.6	786.1			
	2	771.0	829.5	831.2	785.5	804.3											
	3														759.2	798.6	778.9
	4														627.9	654.4	641.2
	5														789.0	799.1	794.1
LWB-1.1	1														767.8	727.0	747.4
	2														618.9	616.3	617.6
	3									682.0	763.6	772.8	737.2	738.9			
	4	643.1	729.4	734.0	702.8	702.3											
	5									629.5	691.9	701.4	674.9	674.4			
	6									633.0	695.6	705.2	678.1	678.0			
	7						707.4	645.5	676.5								
	8														596.7	593.4	595.1
	9														614.4	580.1	597.3

Notes: For garnet-biotite thermometry: F&S '78, Ferry and Spear (1978); H&S '82, Hodges and Spear (1982); F&S w/ B '90, Ferry and Spear (1978) with Berman (1990) garnet model; K&R '94, Kleeman and Reinhardt (1994). For garnet-hornblende thermometry: G&P '84, Graham and Powell (1984); P '85, Perchuk et al (1985). Avg = simple average. * Indicates prograde garnet compositions, but not technically rims.

Appendix C
Geothermometry Results

Sample #	Pair#	T (°C) Garnet core pairs								T (°C) Garnet rim pairs							
		Garnet-biotite @5 kbar					Garnet-hornblende @5 kbar			Garnet-biotite@ 5kbar					Garnet-hornblende @5 kbar		
		F&S '78	H&S '82	F&S w/ B '90	K&R '94	Avg	G&P '84	P '85	Avg	F&S '78	H&S '82	F&S w/ B '90	K&R '94	Avg	G&P '84	P '85	Avg
LWB-1.2	1	737.1	757.7	731.3	682.8	725.7											
	2	604.2	624.1	600.6	573.6	600.6											
	3									575.4	593.1	577.2	556.5	575.6			
	4									479.6	496.5	482.0	471.3	482.4			
	5									607.7	627.2	604.7	577.3	604.2			
	6									739.1	761.3	736.2	687.0	730.9			
LWB-1.3	1									542.6	571.8	563.1	556.6	558.5			
	2									551.6	586.7	584.5	574.9	574.4			
	3	646.0	681.2	654.9	649.1	657.8											
	4	628.6	663.6	654.9	636.5	645.9											
	5	657.5	692.9	684.1	658.3	673.2											
	6	717.0	758.5	750.7	717.1	735.8											
	7	712.3	753.8	746.0	712.8	731.2											
	8	714.9	756.4	748.6	712.0	733.0											
	9									591.1	622.3	614.6	603.6	607.9			
	10									511.4	545.8	543.5	543.3	536.0			
	11									636.8	663.7	651.4	631.2	645.8			
LWB-1.5	1	624.9	644.6	617.7	576.6	616.0											
	2	605.4	626.1	601.6	563.0	599.0											
	3	787.7	809.1	780.5	715.9	773.2											
	4	711.1	732.4	705.5	660.0	702.3											
	5									809.6	831.3	801.7	733.0	794.0			
	6									730.0	751.5	723.7	675.0	720.1			
	7									785.9	808.5	781.2	716.6	773.1			
	8									709.6	732.0	706.2	660.8	702.2			
	9	582.8	604.9	580.8	552.9	580.4											

Notes: For garnet-biotite thermometry: F&S '78, Ferry and Spear (1978); H&S '82, Hodges and Spear (1982); F&S w/ B '90, Ferry and Spear (1978) with Berman (1990) garnet model; K&R '94, Kleeman and Reinhardt (1994). For garnet-hornblende thermometry: G&P '84, Graham and Powell (1984); P '85, Perchuk et al (1985). Avg = simple average. * Indicates prograde garnet compositions, but not technically rims.

Appendix C
Geothermometry Results

Sample #	Pair#	T (°C) Garnet core pairs								T (°C) Garnet rim pairs							
		Garnet-biotite @5 kbar					Garnet-hornblende @5 kbar			Garnet-biotite@ 5kbar					Garnet-hornblende @5 kbar		
		F&S '78	H&S '82	F&S w/ B '90	K&R '94	Avg	G&P '84	P '85	Avg	F&S '78	H&S '82	F&S w/ B '90	K&R '94	Avg	G&P '84	P '85	Avg
	10	553.5	578.5	558.9	532.2	555.8											
	11	617.6	643.2	622.5	590.7	618.5											
	12	705.5	731.6	709.5	665.9	703.1											
	13	780.2	806.6	783.2	721.5	772.9											
	14									626.5	650.2	627.4	594.7	624.7			
	15									786.8	812.0	787.1	724.4	777.6			
	16									594.5	617.3	596.0	568.1	594.0			
LWB-1.6	1	691.7	754.8	755.6	726.0	732.0											
	2	741.4	805.0	806.6	767.8	780.2											
	3									506.0	535.6	530.4	536.1	527.0			
	4									573.1	606.8	600.9	597.4	594.6			
	5									548.1	577.7	571.0	571.0	567.0			
	6	719.3	782.7	783.9	748.8	758.7											
	7	721.6	785.1	786.3	750.4	760.9											
	8									549.7	579.3	572.6	572.0	568.4			
	9									715.1	745.8	730.8	704.1	724.0	*		
	10									717.4	748.2	733.1	705.6	726.1	*		
	11									687.7	718.5	703.5	681.9	697.9	*		
LWB-2.6	1						718.0	713.9	716.0								
	2														652.7	644.5	649.0
	3						728.7	723.4	726.1								
	4						715.3	709.7	712.5								
	5														694.8	683.5	689.2
	6														719.3	706.3	712.8
LWB-6.1	1						748.1	744.0	746.1								
	2														739.4	738.1	738.8
	3														728.6	725.7	727.2

Notes: For garnet-biotite thermometry: F&S '78, Ferry and Spear (1978); H&S '82, Hodges and Spear (1982); F&S w/ B '90, Ferry and Spear (1978) with Berman (1990) garnet model; K&R '94, Kleeman and Reinhardt (1994). For garnet-hornblende thermometry: G&P '84, Graham and Powell (1984); P '85, Perchuk et al (1985). Avg = simple average. * Indicates prograde garnet compositions, but not technically rims.

Appendix C
Geothermometry Results

Sample #	Pair#	T (°C) Garnet core pairs								T (°C) Garnet rim pairs							
		Garnet-biotite @5 kbar					Garnet-hornblende @5 kbar			Garnet-biotite@ 5kbar					Garnet-hornblende @5 kbar		
		F&S '78	H&S '82	F&S w/ B '90	K&R '94	Avg	G&P '84	P '85	Avg	F&S '78	H&S '82	F&S w/ B '90	K&R '94	Avg	G&P '84	P '85	Avg
	4						664.1	646.0	655.1								
	5						603.7	585.3	594.5								
	6						711.9	700.0	706.0								
	7														665.5	658.2	662.0
	8														692.1	683.5	687.8
	9														698.2	691.6	694.9
LWB-6.2	1						571.4	497.2	525.3								
	2						567.1	493.2	530.2								
	3						562.2	488.7	525.5								
	4														588.4	574.9	581.7
	5														590.9	568.6	579.8
	6														614.0	571.9	593.0
	7						668.8	553.4	611.1								
	8						651.7	548.7	600.2								
	9						574.3	468.8	521.6								
	10														611.1	559.2	585.2
	11														602.2	537.7	570.0
	12														607.1	560.6	584.0
LWB-6.3	1						631.4	619.9	625.7								
	2						655.0	643.8	649.4								
	3						616.1	604.4	610.3								
	4						635.1	623.7	629.4								
	5														644.5	639.4	642.0
	6														599.2	593.8	596.5
	7														622.2	610.8	616.5
	8														661.2	652.7	657.0

Notes: For garnet-biotite thermometry: F&S '78, Ferry and Spear (1978); H&S '82, Hodges and Spear (1982); F&S w/ B '90, Ferry and Spear (1978) with Berman (1990) garnet model; K&R '94, Kleeman and Reinhardt (1994). For garnet-hornblende thermometry: G&P '84, Graham and Powell (1984); P '85, Perchuk et al (1985). Avg = simple average. * Indicates prograde garnet compositions, but not technically rims.

Appendix C
Geothermometry Results

Sample #	Pair#	T (°C) Garnet core pairs								T (°C) Garnet rim pairs							
		Garnet-biotite @5 kbar					Garnet-hornblende @5 kbar			Garnet-biotite@ 5kbar					Garnet-hornblende @5 kbar		
		F&S '78	H&S '82	F&S w/ B '90	K&R '94	Avg	G&P '84	P '85	Avg	F&S '78	H&S '82	F&S w/ B '90	K&R '94	Avg	G&P '84	P '85	Avg
	9						700.9	691.8	696.4								
	10						658.5	648.7	653.6								
	11														609.4	604.2	606.8
	12														626.5	618.1	622.3
LWB-6.4	1	556.0	586.5	572.9	561.9	569.3											
	2	659.4	691.0	676.4	645.4	668.1											
	3									661.2	693.5	679.4	647.9	670.5			
	4	701.8	729.8	712.2	675.6	704.9											
	5	705.5	733.5	715.9	676.6	707.9											
	6									628.8	664.8	656.6	630.1	645.1			
	7									631.9	668.0	659.8	630.8	647.6			
	8									662.0	697.3	687.1	653.5	675.0			

Notes: For garnet-biotite thermometry: F&S '78, Ferry and Spear (1978); H&S '82, Hodges and Spear (1982); F&S w/ B '90, Ferry and Spear (1978) with Berman (1990) garnet model; K&R '94, Kleeman and Reinhardt (1994). For garnet-hornblende thermometry: G&P '84, Graham and Powell (1984); P '85, Perchuk et al (1985). Avg = simple average. * Indicates prograde garnet compositions, but not technically rims.